

**The investigation of Optical Coherence Tomography as
a clinical tool to determine the extent of Molar Incisor
Hypomineralisation (MIH) Lesions**

**Submitted in partial fulfilment of the requirements for the
Degree of Clinical Doctorate in Dentistry (Paediatric Dentistry)**

Eastman Dental Institute

University College London

2012 – 2015

Submitted by:

Khalifa Mohamed Harith Al-Azri

B.Dent.Sc. (Ireland), B.A (Ireland), MFD-RCSI (Ireland)



eastman DENTAL
INSTITUTE

Project Supervisors:

Dr Laurent Bozec (Division of Biomaterials & Tissue engineering, Eastman Dental Institute – University College London)

Dr Susan Parekh (Department of Paediatric Dentistry, Eastman Dental Institute – University College London)

Dr. Maisoon Al-Jawad (Dental Physical Science Department, Queen Mary University of London)

Dr Richard Cook (Biomaterials & Tissue engineering Department at King's College London Dental Institute, King's College London)

Dr Frederic Festy (Biomaterials & Tissue engineering Department at King's College London Dental Institute, King's College London)

DECLARATION OF WORK

I, Khalifa Mohamed Harith Al-Azri confirm that the work presented in this thesis is my own. Where information has been derived from other sources, I confirm that this has been acknowledged and indicated in the thesis.

Khalifa Mohamed Harith Al-Azri

Eastman Dental Institute, University of College London

July 2015

ABSTRACT

Molar incisor hypomineralisation (MIH) is associated with abnormal mineralisation of enamel during tooth development. It is probably related to systemic upset during this stage of enamel formation. Diagnosing this condition at an early stage is essential in its management, due to complications such as hypersensitivity, post-eruptive breakdown and rapid carious progression in the affected teeth. The current diagnostic measures are clinical visual examination with the aid of indices which are used to describe the defects and radiographic examination of the affected teeth. These diagnostic tools have their limitations and therefore there is a need for better diagnostic tools to give more information about the extent of these defects into the enamel. Optical coherence tomography (OCT) was investigated in this project as an alternative diagnostic tool for MIH defects.

The aim of this study was to develop the use of OCT in diagnosing the MIH and correlating it with the conventional clinical methods. In addition, OCT was verified with imaging modalities used in investigating the ultrastructure of MIH affected FPMs such as X-ray microtomography (XMT) and synchrotron X-ray diffraction (SXRDR).

Ethical approval was obtained for the study. Teeth were prepared immediately after collection, and stored in a refrigerator at 4°C until imaged. MIH defects were categorised using the mDDE index, then radiographic images were taken. Teeth then imaged using OCT (VivoSight diagnostic™) in King's College London (KCL) Dental Institute where each surface was scanned separately. Teeth were taken to the Dental Physical Science Department, Queen Mary University of London (QMUL) where they were imaged using XMT (MuCat 2 scanner™). They were sectioned into thin sections of 300µm thick and polished down to 220-250µm. SXRDR was done on these sections on the BM28 (XMaS) beamline at the European Synchrotron Radiation Facility (ESRF), Grenoble, France and enamel diffraction patterns were obtained.

The incident light from OCT behaved differently when compared between control and MIH enamel as well as when different types of MIH defects were compared. More details about the ultrastructure of enamel and the extent of the MIH lesions were obtained from OCT images when compared to clinical examination using mDDE index and radiographs. An association between the OCT Images and the mineral density, obtained from XMT, was found. However, there was no change in enamel crystal orientation between MIH and healthy enamel, but the magnitude of the enamel crystal organisation was different in both types.

Optical Coherence Tomography proved to be a potential diagnostic tool in determining the extent of MIH defects and both XMT and SXRD helped in understanding OCT imaging.

ACKNOWLEDGEMENT

Alhamdulillah, with His gracious help, I managed to finish and submit this final thesis after three years of continuous hard work. First, I would like to express my deepest gratitude to my beloved wife, Rahma Al-Ruqaishi, for her patience and tolerance throughout the last three years, standing alone for the family back home while I was away for my study. To my four lovely children, Al Majd, Al Mudhafar, Mohamed and Al Mansoor. To my late father who would have been proud of me. A special thanks also dedicated to all my family members in Oman for the continuous pray and encouragement especially, my Mother and Mother in-law.

A warm appreciation to my supervisors from EDI-UCL, Dr Laurent Bozec and Dr Susan Parekh, for their excellent guidance and assistance until this final thesis is successfully completed. My gratitude is to my main supervisor in King's College London Dental Institute at Guy's hospital, Dr Richard Cook, for his guidance at the early stage of this project, while working with the OCT scanner. Also I would like to thank Dr Frederic Festy for his help at the time. Without Dr Maisoon Al-Jawad and Dr Samera Siddiqui from the Dental Physical Science Department, Queen Mary University of London (QMUL), this work would not be brought to this rich scientific research level. Their continuous help and support in understanding the advanced techniques used in this research and their endless collaboration is most appreciated. Also, to my friend Mohamed Al-Mosawi, a PhD student at the Dental Physical Science Department, QMUL.

I would like also to dedicate this thesis to my Programme Director, Dr Paul Ashley for his continuous support throughout the DDent programme. My sincere dedication of this thesis also goes to the man of the people and god-father of Oman, His Majesty the Sultan Qaboos Bin Said, Sultan of Oman, who has sponsored my scholarship as one of 1000 scholarships for doctors and dentists, through Oman Medical Specialty Board (OMSB). Thanks to the Ministry of Defence, represented by the Medical Services of the Armed Forces in the Royal Army of Oman for supporting my living expenses during my stay in London as well as the Ministry of Higher education for their ongoing support. Also, thanks to the Embassy of the Sultanate of Oman in London, represented by the Omani cultural attaché's office for their support.

My gratitude goes also to my senior colleague Mazlina Mohd Noor, who has kindly shared with me most of the samples used in this project. Thanks to Dr Graham Palmer, Dr Nicola Mordan and Dr George Georgiou at the biomaterials & tissue engineering

laboratory, EDI; and to Mr Peter Pelicki at KCL. Thank you very much all for your assistance.

To my lovely colleagues, Lama Dakkouri, Salwa Ibrahim and Soha Al-Qadi, who were supportive throughout our DDent journey that we experienced together. We had together moments of happiness and despair for the last three years. I would like also to thank my other DDent colleagues for their support.

To all the staff that I have met and worked with in the Unit of Paediatric Dentistry of the Eastman Dental Institute/Hospital, thank you very much.

Khalifa Mohamed Harith Al-Azri

Paediatric Dentistry,

Eastman Dental Institute, University of College London

July 2015

TABLE OF CONTENTS

DECLARATION OF WORK	3
ABSTRACT	4
ACKNOWLEDGEMENT	6
LIST OF FIGURES	12
LIST OF TABLES	17
ABBREVIATIONS.....	18
1 BACKGROUND.....	21
1.1 Molar Incisor Hypomineralisation.....	23
1.1.1 Prevalence	24
1.1.2 Aetiology.....	25
1.1.3 MIH Clinical Features	27
1.1.4 Managing children with MIH.....	27
1.1.5 The Ultrastructure of MIH teeth.....	28
1.2 Limitations of assessing the extent of MIH defects using existing methods: ..	29
1.2.1 Indices of enamel defects	29
1.2.2 The use of radiographic imaging.....	32
1.3 Optical Coherence Tomography (OCT).....	35
1.3.1 Principle of OCT	36
1.3.2 Applications of OCT.....	40
1.4 X-ray Microtomography	42
1.4.1 Principle of XMT	42
1.4.2 Applications of XMT.....	44
1.5 Synchrotron X-ray Diffractometry (SXR).....	45
1.5.1 Disclaimer.....	45
1.5.2 Principle of SXR.....	45
1.5.3 Diffraction Data Analysis.....	49
1.5.4 Applications of SXR	51
2 Aim and Objectives.....	53
2.1 Aim.....	53

2.2	Objectives.....	53
3	Patient Recruitment and Selection.....	54
3.1	Study registration and ethical approval.....	54
3.2	Participants and Samples.....	54
3.2.1	Patient identification.....	54
3.2.2	Sample collection and storage.....	55
4	Conventional methods in diagnosing MIH.....	56
4.1	Clinical Visual Assessment.....	56
4.1.1	Method.....	56
4.1.2	Result.....	58
4.2	Radiographic Assessment.....	61
4.2.1	Method.....	61
4.2.2	Results.....	62
4.3	Discussion.....	63
4.3.1	Clinical Visual Assessment.....	63
4.3.2	Radiographic Assessment.....	64
5	OCT as a diagnostic imaging tool.....	65
5.1	Optical Coherence Tomography scanner.....	65
5.2	Imaging teeth using OCT scanner.....	66
5.2.1	Method.....	66
5.2.2	Results of OCT imaging.....	68
5.2.3	En-face Reconstruction of the OCT images.....	74
5.3	Advanced Diagnostics Using OCT Signal Intensity Profiles.....	75
5.3.1	Method.....	75
5.3.2	Application of signal intensity profile.....	76
5.4	Comparison between Conventional Clinical Methods and OCT.....	80
5.4.1	Type 1 (white/creamy) MIH defect.....	81
	81	
5.4.2	Type 2 (yellow/brown) MIH defect.....	87
5.4.3	Type 8 (with PEB) MIH defect.....	93
5.5	Discussion.....	98

6	Correlation of OCT imaging with XMT and SXR	103
6.1	OCT and XMT	103
6.1.1	Disclaimer	103
6.1.2	Materials and Method	103
6.1.3	Data analysis	106
6.1.1	Results	108
6.1.1	Further Quantitative MD Analysis	117
6.2	OCT and SXR	119
6.2.1	Disclaimer	119
6.2.2	Method	119
6.2.3	Results	122
6.3	Discussion	137
7	Synopsis	142
7.1	Rational for a better diagnostics	142
7.2	The Use of Different Diagnostic Methods in MIH	142
7.2.1	The short falls and the limitations of the current diagnostic methods	142
7.3	A Novel approach	143
7.4	Correlating the OCT results with other advanced imaging techniques	144
8	Clinical relevance	147
9	Conclusion	149
10	Future work	150
11	Scientific Dissemination	152
11.1	Publications	152
11.2	Presentations	152
12	References	154
13	APPENDIX 1	168
14	APPENDIX 2	170
15	APPENDIX 3	172
16	APPENDIX 4	174
17	APPENDIX 5	176

18	APPENDIX 6	177
19	Appendix 7 Michelson Diagnostics' Manual on manipulating OCT images in image J	179
20	Appendix 8	183

LIST OF FIGURES

FIGURE 1.1 AN OCT B–SCAN IMAGE OF A FIRST PERMANENT MOLAR TOOTH TAKEN IN THE CURRENT STUDY.....	35
FIGURE 1.2 AN EXAMPLE OF AN OCT A-SCAN SIGNAL; LIGHT INTENSITY IN ARBITRARY UNIT (AU) IS PLOTTED AGAINST DEPTH IN TOOTH STRUCTURE IN MICRONS.	36
FIGURE 1.3 PRINCIPLE OF SWEEP SOURCE OCT	38
FIGURE 1.4 SCHEMATIC REPRESENTATION OF A SYNCHROTRON RADIATION SYSTEM.	46
FIGURE 1.5 SCHEMATIC REPRESENTATION DEPICTING THE EXPERIMENTAL SET UP FOR SAXS AND WAXS,.....	48
FIGURE 1.6 SIMPLIFIED GEOMETRIC CONSTRUCTION REPRESENTING THE CONDITIONS NECESSARY FOR DIFFRACTION.	49
FIGURE 1.7 A SCHEMATIC REPRESENTATION OF THREE TYPES OF DIFFRACTION PATTERNS THAT CAN BE OBTAINED FROM THREE TYPES OF CRYSTALS	50
FIGURE 1.8 GRAPHICAL REPRESENTATION OF THE FWHM ON A FITTED PEAK.....	50
TABLE 4.1 MDDE INDEX USED TO RECORD THE CHARACTERISATION OF DENTAL DEFECTS OF ENAMEL	57
TABLE 4.2 THE DEMOGRAPHIC DATA OF CONTROL FIRST PERMANENT MOLAR SAMPLES	58
TABLE 4.3 THE DEMOGRAPHIC DETAILS OF MIH AFFECTED FIRST PERMANENT MOLAR SAMPLES	59
FIGURE 4.1 SHOWS THREE TYPES OF MIH DEFECTS;	60
TABLE 4.4 THE MDDE INDEX SCORES FOR MIH AFFECTED FPMs.....	60
FIGURE 4.2 RADIOGRAPHIC IMAGES OF A CONTROL TOOTH.	61
FIGURE 4.3 RADIOGRAPHIC IMAGES OF A MIH TOOTH.....	62
FIGURE 4.4 RADIOGRAPHIC IMAGE OF A MIH TOOTH WITH TYPE 8 LESION	63
FIGURE 5.1 SHOWS THE VARIOUS PARTS OF THE OCT SCANNER.....	65
FIGURE 5.2 SHOWS A CLOSE VIEW OF OCT MACHINE DURING THE IMAGING PROCEDURE.	66
FIGURE 5.3 A DEMONSTRATION OF THE SCANNED AREA OF THE TOOTH SURFACE WITH ‘A’ BEING THE START OF THE SCAN AND ‘B’ IS WHERE IT ENDS.	68
FIGURE 5.4 AN OCT IMAGE OF PART OF A PALATAL SURFACE OF A CONTROL FPM TOOTH.	69

FIGURE 5.5 HISTOLOGICAL SECTION SHOWING THE ENAMEL SPINDLES AT THE ENAMEL-DENTINE JUNCTION.....	70
FIGURE 5.6 AN OCT IMAGE OF THE DISTAL SURFACE OF A CONTROL FPM	70
FIGURE 5.7 AN OCT IMAGE OF THE MESIAL SURFACE OF A CONTROL FPM TOOTH WITH A CAVITATED CARIOUS LESION.....	71
FIGURE 5.8 AN OCT IMAGE OF A BUCCAL SURFACE OF A MIH AFFECTED FPM TOOTH.	72
FIGURE 5.9 OCT IMAGE OF A DISTAL SURFACE OF A MIH AFFECTED TOOTH.	73
FIGURE 5.10 OCT OF A MESIAL SURFACE OF A MIH OF A FPM	73
FIGURE 5.11 OCT IMAGE STACK WAS RECONSTRUCTED INTO AN EN-FACE VERTICAL STACK OF FRAMES.....	75
FIGURE 5.12 SIGNAL INTENSITY PROFILE OF A CONTROL HEALTHY ENAMEL.....	77
FIGURE 5.13 BACK SCATTERED LIGHT INTENSITY PROFILES EXTRACTED FROM FOUR DIFFERENT SELECTED REGIONS IN AN OCT IMAGE OF A HEALTHY CONTROL ENAMEL.....	78
FIGURE 5.14 SIGNAL INTENSITY PROFILE OF A MIH ENAMEL.....	79
FIGURE 5.15 BACK SCATTERED LIGHT INTENSITY PROFILES EXTRACTED FROM FOUR DIFFERENT SELECTED REGIONS IN AN OCT IMAGE OF A MIH AFFECTED ENAMEL	79
FIGURE 5.16 PALATAL SURFACE OF MIH 35 WITH TYPE 1 (T1) MIH DEFECT	81
FIGURE 5.17 RADIOGRAPHIC IMAGE OF MIH 35 SHOWING THE BUCCAL AND PALATAL SURFACES OF THE TOOTH.....	82
FIGURE 5.18 OCT FRAMES CORRESPONDING TO THE LINES DRAWN ON THE CLINICAL PHOTOGRAPH OF MIH 35 SHOWN IN FIGURE 5.16.....	82
FIGURE 5.19 SCATTERING INTENSITY PROFILES TAKEN FROM OCT IMAGE PRESENTED IN FIGURE 18B.	83
FIGURE 5.20 (A) BUCCAL SURFACE OF MIH 32 SHOWING A DEMARCATED TYPE 1 MIH DEFECT (1) AND A DIFFUSE TYPE 2 DEFECT (2)	84
FIGURE 5.21 RADIOGRAPHIC IMAGE OF MIH 32 SHOWING THE BUCCAL AND PALATAL SURFACES OF THE TOOTH.	84
FIGURE 5.22 OCT FRAMES CORRESPONDING TO THE LINES ILLUSTRATED ON THE CLINICAL PHOTOGRAPH OF THE BUCCAL SURFACE OF MIH 32	85
FIGURE 5.23 SCATTERING INTENSITY PROFILES OF DEMARCATED TYPE 1 MIH DEFECT	86

FIGURE 5.24 (A) THE BUCCAL SURFACE OF MIH 32 SHOWING TWO TYPES OF DEFECTS MIH TYPE 1 (MARKED 1) AND MIH TYPE 2 (MARKED 2).....	87
FIGURE 5.25 OCT FRAMES CORRESPONDING TO THE LINES DRAWN IN FIGURE 5.24B	88
FIGURE 5.26 SHOWS INTENSITY PROFILES EXTRACTED FROM A B-SCAN IMAGE SHOWN IN FIGURE 5.25A	89
FIGURE 5.27 DISTAL SURFACE OF MIH 37 WITH TYPE 2 MIH DEFECT.....	90
FIGURE 5.28 THE RADIOGRAPHIC IMAGE OF MIH 37 SHOWING THE MESIAL AND DISTAL SURFACES OF THE TOOTH.	90
FIGURE 5.29 OCT FRAMES CORRESPONDING TO THE LINES DRAWN ON THE CLINICAL PHOTOGRAPH OF THE DISTAL SURFACE OF MIH 37 SHOWN IN FIGURE 5.27	91
FIGURE 5.30 INTENSITY PROFILE PLOTS OF THE EMARCATED TYPE 2 DEFECT IN FIGURE 5.29A	92
FIGURE 5.31 BUCCAL SURFACE OF MIH 38 WITH TYPE 8 (WITH PEB) DEFECT.....	93
FIGURE 5.32 RADIOGRAPHIC IMAGE SHOWING THE BUCCAL AND LINGUAL SURFACES OF MIH 38.....	94
FIGURE 5.33 OCT FRAMES CORRESPONDING TO THE LINES ON THE CLINICAL PHOTOGRAPH OF THE BUCCAL SURFACE OF MIH 38.....	94
FIGURE 5.34 BACK SCATTERED LIGHT INTENSITY PROFILES TAKEN FROM THE B-SCAN SHOWN IN FIGURE 5.33C.....	95
FIGURE 5.35 (A) THE OCCLUSAL SURFACE OF MIH 33 SHOWING PEB WHICH LOOKS YELLOW BROWN IN COLOUR; (B) THE DISTAL SURFACE OF THE OF THE TOOTH WITH MIH TYPE 2 OCCLUSALLY.	96
FIGURE 5.36 THE RADIOGRAPHIC IMAGE OF MIH 33 SHOWING THE MESIAL AND DISTAL SURFACES.....	96
FIGURE 5.37 OCT FRAMES CORRESPONDING TO THE LINES DRAWN ON THE DISTAL SURFACE OF MIH 33 SHOWN IN FIGURE 5.35B.....	97
FIGURE 6.1 A SCHEMATIC REPRESENTATION OF THE CURRENT XMT SYSTEM USED.	104
TABLE 6.1 SHOWS A LIST OF THE CONTROL AND MIH AFFECTED SAMPLES SCANNED WITH MUCAT SCANNER AT QMUL.....	105
FIGURE 6.2 A SCHEMATIC REPRESENTATION OF THE THREE AREAS OF ENAMEL FROM WHICH MD WAS OBTAINED.....	107
FIGURE 6.3 A CONTROL TOOTH SURFACE DIVIDED INTO THREE REGIONS.	107
FIGURE 6.4 THE AREA OF THE MIH ENAMEL DEFECT DIVIDED INTO THREE REGIONS.	108

TABLE 6.2 THE TYPES OF MIH LESIONS INVESTIGATED USING XMT SCANNING..	108
FIGURE 6.4 XMT SCAN OF C129 CONTROL TOOTH.....	109
FIGURE 6.5 COMPARISON OF OCT AND XMT IMAGES OF THE DISTAL SURFACE OF C129.....	110
FIGURE 6.6 XMT SCAN OF MIH 67.	111
FIGURE 6.7 COMPARISON OF OCT AND XMT IMAGES OF A TYPE 2 MIH DEFECT ON THE DISTAL SURFACE OF MIH 33 WHICH WAS VERY CLOSE TO A PEB REGION.....	112
FIGURE 6.8 AN OCT IMAGE TAKEN FROM A SCAN OF THE BUCCAL SURFACE OF MIH 38 WHICH HAD TYPE 8 LESION.	113
FIGURE 6.9 THE BUCCAL SURFACE OF MIH 50 WHICH HAD A DIFFUSE TYPE 1 DEFECT	114
FIGURE 6.10 A COMPARISON OF OCT AND XMT IMAGING OF THE DISTAL SURFACE OF MIH 50 WHICH HAS TWO TYPES OF MIH DEFECTS.....	115
FIGURE 6.11 DISTAL SURFACE OF MIH 67 SHOWING TYPE 2 MIH DEFECT.....	116
FIGURE 6.13 THE THREE AREAS OF ENAMEL FROM WHICH MD WAS OBTAINED.....	117
TABLE 6.3 SHOWS VALUES OF MD IN GCM^{-3} DISTRIBUTED IN THREE REGIONS ACROSS THE ENAMEL THICKNESS FROM THE ENAMEL SURFACE TO EDJ IN BOTH CONTROL AND MIH ENAMEL IN TWO EXAMPLES, C129 AND MIH 33.	118
FIGURE 6.14 BAR GRAPH SHOWING THE AVERAGE MINERAL DENSITY (MD) OF ENAMEL CLOSE TO THE SURFACE, IN THE MIDDLE OF ENAMEL THICKNESS AND CLOSE TO THE EDJ.	118
FIGURE 6.13 FOUR SAMPLE SLICES PREPARED FOR THE SXR D EXPERIMENT IN BM28 (XMAS) BEAMLINE AT ESRF, GRENoble, FRANCE.....	119
FIGURE 6.14 A) A SCHEMATIC REPRESENTATION OF THE EXPERIMENTAL SETUP AT THE XMAS BEAMLINE.....	120
FIGURE 6.15 SHOWS THE FOUR SAMPLE SLICES PREPARED FOR THE SXR D EXPERIMENT IN BM28 (XMAS) BEAMLINE AT ESRF, GRENoble, FRANCE.....	121
FIGURE 6.16 SHOWS FULL CROWN SCANNED AREAS TAKEN FOR THREE TEETH A) C108, B) MIH 50 AND MIH 67	122
FIGURE 6.17 THE THREE DIFFRACTION PATTERNS FROM THE SXR D EXPERIMENT OBTAINED WHEN SAMPLES WERE SUBJECTED TO THE MICRO-FOCUSSED BEAM.	123
FIGURE 6.18 EXAMPLES OF PEAKS OBTAINED FROM THE 002 DEBYE RING FROM AN ENAMEL DIFFRACTION PATTERN SHOWING GRAPHS OF INTENSITY (IN ARBITRARY UNIT OR AU) VERSUS AZIMUTHAL ANGLE (IN DEGREES) THROUGH THE 360°	123

FIGURE 6.19 THE RESULT OF THE FWHM OF THE CONTROL HEALTHY SAMPLE C108	125
FIGURE 6.20 THE RESULT OF THE FWHM OF THE MIH 50 SAMPLE.	127
FIGURE 6.21 THE RESULT OF THE FWHM OF THE MIH 67 SAMPLE.	128
TABLE 6.4 LIST OF THE MIH 67 TRACKS PRESENT ABOVE THE LEVEL OF THE DENTINE HORN (DH).....	129
FIGURE 6.22 FOUR TRACKS TAKEN FROM MIH 67 DISTAL SURFACE WHICH HAS DEMARCATED TYPE 2 DEFECT.	132
FIGURE 6.23 A COMPARISON BETWEEN THE FWHM OF THE SECOND PEAK FROM THE 002 DEBYE RING AND THE INTENSITY PROFILE PLOTS OF THE SHADED BLUE AREAS INDICATED IN THE OCT IMAGES IN FIGURE 6.19.....	133
FIGURE 6.24 THE OUTLINE OF THE OPAQUE DEFECT AS IT EXTENDS FROM THE CUSPAL REGION TO THE AREA OF THE DH..	134
FIGURE 6.25 SHOWS THE PREFERRED ORIENTATION OF ENAMEL CRYSTALS THROUGHOUT THE CROWN OF C108 SAMPLE USING THE 002 REFLECTION OF THE HYDROXYAPATITE CRYSTALLITE IN ENAMEL TAKEN FROM THE 2D DIFFRACTION IMAGES.	135
FIGURE 6.26 SHOWS THE PREFERRED ORIENTATION OF ENAMEL CRYSTALS THROUGHOUT THE CROWN OF MIH 50 SAMPLE USING THE 002 REFLECTION OF THE HYDROXYAPATITE CRYSTALLITE IN ENAMEL TAKEN FROM THE 2D DIFFRACTION IMAGES.	136
FIGURE 6.27 THE PREFERRED ORIENTATION OF ENAMEL CRYSTALS THROUGHOUT THE CROWN OF MIH 67 SAMPLE USING THE 002 REFLECTION OF THE HYDROXYAPATITE CRYSTALLITE IN ENAMEL TAKEN FROM THE 2D DIFFRACTION IMAGES.....	137
FIGURE 11.1 POSTER PRESENTATION DONE ON IADR GENERAL MEETING, BOSTON, USA, MARCH 2015	153

LIST OF TABLES

TABLE 1.1 CRITERIA USED IN DEVELOPMENTAL DEFECT IN ENAMEL INDEX, PROPOSED BY FDI WORKING GROUP IN 1982.....	30
TABLE 1.2 MODIFIED DDE INDEX FOR USE IN GENERAL PURPOSE EPIDEMIOLOGICAL STUDIES.....	32
TABLE 1.3 MEANS FOR REDUCING X-RAY EXPOSURE, TAKEN FROM (WHITE AND MALLYA, 2012)	34
TABLE 4.1 MDDE INDEX USED TO RECORD THE CHARACTERISATION OF DENTAL DEFECTS OF ENAMEL; THE CRITERIA MARKED IN BOLD ARE RELATED TO DEFECTS IN MIH	57
TABLE 4.2 THE DEMOGRAPHIC DATA OF CONTROL FIRST PERMANENT MOLAR SAMPLES.....	58
TABLE 4.3 THE DEMOGRAPHIC DETAILS OF MIH AFFECTED FIRST PERMANENT MOLAR SAMPLES.....	59
TABLE 4.4 THE MDDE INDEX SCORES FOR MIH AFFECTED FPMS.	60
TABLE 5.1 THE TYPES OF MIH DEFECTS PRESENT IN MIH AFFECTED FPMS.....	80
TABLE 6.1 SHOWS A LIST OF THE CONTROL AND MIH AFFECTED SAMPLES SCANNED WITH MUCAT SCANNER AT QMUL.....	105
TABLE 6.2 THE TYPES OF MIH LESIONS INVESTIGATED USING XMT SCANNING. THE TYPES HIGHLIGHTED IN BOLD FONT ARE THOSE TYPES WHICH WERE FURTHER INVESTIGATED USING SYNCHROTRON XRD.	108
TABLE 6.3 SHOWS VALUES OF MD IN GCM-3 DISTRIBUTED IN THREE REGIONS ACROSS THE ENAMEL THICKNESS FROM THE ENAMEL SURFACE TO EDJ IN BOTH CONTROL AND MIH ENAMEL IN TWO EXAMPLES, C129 AND MIH 33; N IS THE NUMBER OF REGIONS ON THE XMT IMAGE FROM WHICH LAC HAS BEEN EXTRACTED IN EACH AREA IN ENAMEL.	118
TABLE 6.4 LIST OF THE MIH 67 TRACKS PRESENT ABOVE THE LEVEL OF THE DENTINE HORN (DH).....	129
TABLE 7.1 SUMMARY OF THE FINDINGS OF OCT, XMT AND SXRD INVESTIGATIONS ON MIH AFFECTED TEETH ACCORDING TO DEFECT AND DEMARCATION TYPES.....	142

ABBREVIATIONS

Å	Angstrom
ALARA principle	As Low As Reasonably Achievable principle
BM	Bending Magnet
BW	Bite-wing radiograph
CCD device	Charge-Coupled Based Device
CEJ	Cemento-Enamel Junction
DDE index	Developmental Defects of Enamel index
DH	Dentine Horn
DICOM formats	Digital Imaging and Communications in Medicine formats
DNA	Deoxyribonucleic acid
DPT	Dental Panoramic Tomography
EAPD	European Academy of Paediatric Dentistry
EDH	Eastman Dental Hospital
EDJ	Enamel Dentine Junction
ESRF	European Synchrotron Radiation Facility
FDI	World Dental Federation
FD-LCI	Fourier domain Low Coherence Interferometry
fFD-LCI	frequency tuning Fourier domain Low Coherence Interferometry
FD-OCT	Fourier Domain OCT
FPM	First Permanent Molar
FWHM	Full Width at Half Maximum
HA	Hydroxyapatite crystals
ID	Insertion Device
LAC	Linear Attenuation Coefficient
LCI	Low Coherence Interferometry
LCPA	Long Cone Periapical radiograph
MD	Mineral Density

mDDE index	modified Developmental Defect of Enamel index
Micro-CT	Micro – Computerised Tomography
MIH	Molar-Incisor Hypomineralisation
µm	micro metre
NHS REC	National Health Services Research Ethics Committee
NIH	National Institutes of Health
NIR	Near-Infra Red
nm	Nano metre
OCT	Optical Coherence Tomography
OPL	Optical Path-Length
PEB	Post-Eruptive Breakdown
PLM	Polarized Light Microscopy
PS-OCT	polarisation sensitive Optical Coherence Tomography
QMUL	Queen Mary University of London
SAXS	Small-Angle X-ray Scattering
SD-OCT	Spectral Domain OCT
SEM	Scanning Electron Microscopy
sFD – LCI	spectral Low Coherence Interferometry Fourier domain
SNR	Signal-to-Noise Ratio
SLDs	Super luminescent Light Diodes
SXRD	Synchrotron X-Ray Diffraction
TIFF stack	Tagged Image File Format stack
TD-LCI	Time-Domain Low Coherence Interferometry
TD-OCT	Time Domain OCT
US	United States
WAXS	Wide-Angle X-ray Scattering
WSL	White Spot Lesion
XMT	X-ray Micro Tomography

XRD

X-ray diffraction

1 BACKGROUND

Enamel formation can be affected by genetic, environmental and systemic upsets. This can be displayed clinically in the enamel surface and in its ultrastructure. As a result, diagnosis of enamel defects requires full investigation into the patient's medical and family history, and thorough clinical examination. As enamel is not altered after its formation, any insult to this process will show clinically after the tooth erupts (Alaluusua, 2010). The most common type of enamel developmental defect is Molar-Incisor Hypomineralisation (MIH).

Enamel is said to have a transparent arrangement and is the strongest structure in the human body, due to its high mineral content and well-arranged structure (Margolis et al., 2006). The main constituent of enamel is hydroxyapatite (97%) with very small amounts of protein and water (Cox, 2010). The hydroxyapatites (HA) are described as neatly ordered, closely packed crystallites that is directed from the enamel dentine junction (EDJ) to the surface of the tooth (Simmer and Hu, 2001). They are nanorods measuring 50nm X 25nm in cross section and about 1mm long; clustered (about 1000 crystallites) to form enamel rods or prisms; these prisms are 5 µm in diameter and few millimetres long (Al-Jawad et al., 2007). It was revealed, using electron microscopy, that the HA crystallites at the head of the enamel rods are parallel to the long axis of the rod and are diverted away from the long axis in the tail region (Meckel et al., 1965, Simmer and Hu, 2001).

The prism's arrangement is developed in order to counteract masticatory forces (Jiang et al., 2003). When enamel prisms are viewed in polarised light microscopy, distinctive bands are seen, called 'Hunter-Schreger bands'. Lynch et.al interpreted these band arrangements in the enamel as features which have developed to enhance enamel resistance to all types of tooth wear, such as attrition, erosion and abrasion (Lynch et al., 2011).

Enamel is formed by ameloblasts, which are developed as a consequence of interactions between cells derived from the neural crest termed ectomesenchymal cells and the oral epithelium (Simmer and Hu, 2001). The stages of ameloblast morphological changes are induction, initial-secretory, secretory and maturation stages. In the inductive stage, the epithelial cells undergo morphologic and functional changes. During the secretory stage, large amounts of proteins are secreted by ameloblasts such as amelogenin, ameloblastin and enamelin (Tye et al., 2009).

However, in the maturation stage, enamel proteins are completely removed, through proteases such as matrix metalloproteinase-20, which are also secreted by ameloblasts (Tye et al., 2009).

Enamel minerals are deposited during the secretory stage. At this stage they are very long and thin, but constitute less than a fifth of the enamel matrix (Margolis et al., 2006). In the maturation stage, as enamel proteins and water are removed from the matrix, space is created for the enamel crystals (ribbon-like) to grow in thickness and width (Bei, 2009). The dimensions of the formed enamel prisms are the same as the dimensions of the ameloblasts (Lacruz et al., 2012).

Any interruption occurring in the late maturation stage of enamel formation causes an abnormality in the quality of the formed enamel rather than its quantity. This is called “hypomineralisation of enamel”. This condition is related to the reduced mineral content of the enamel and increased amount of enamel proteins compared to normal enamel. This can be due to either systematic (MIH) or genetic (Amelogenesis Imperfecta – hypomineralised type) causes.

MIH has become more evident as a clinical entity over recent years and its diagnosis and management are challenging. At present, the available diagnostic tools cannot determine accurately the extent of the lesion into enamel. This project will investigate the use of optical coherence tomography (OCT), which is a well-established diagnostic tool in medical specialities, such as ophthalmology and dermatology.

1.1 Molar Incisor Hypomineralisation

Weerheijm et al. defined MIH as “hypomineralisation of systemic origin of at least one First Permanent Molar (FPM) which is frequently associated with affected incisors” (Weerheijm et al., 2001). This definition was established after the condition was presented at the European Academy of Paediatric Dentistry (EAPD) Assembly in 2000, by four different groups of researchers. Each group had named the condition differently; consequently, a need for a consensus on the condition was required to avoid confusion. Some authors called these first permanent molars ‘hypomineralised FPMs’ (Beentjes et al., 2002), ‘idiopathic enamel hypomineralisation in FPM’ (Jälevik et al., 2000), ‘non-fluoride hypomineralisation in FPM’ (Leppäniemi et al., 2000) and ‘cheese molars’ (Weerheijm et al., 2000). MIH had been reported since the 1970s by Swedish dentists working in public dental services (Koch et al., 1987). First permanent molars were noted to have abnormal discolouration ranging from creamy-white to yellow-brown (Jälevik, 2010).

The first permanent molars start to develop in the fourth month of intra-uterine life, and start to mineralise immediately after birth (Alaluusua, 2010). The whole process of enamel formation takes about 33 months (Reid and Dean, 2006), with one third of this period dedicated to secretory and transitional stages, and the remaining two thirds dedicated to the maturation stage. The first three years of life are important for both FPM and permanent incisors development, and MIH can occur at any time during this period, but most importantly during the first year when early maturation starts (Alaluusua, 2010).

Enamel abnormalities vary in severity, with severely affected teeth undergoing a process called Post-Eruptive Breakdown (PEB), which is related to subsurface porosity (Daly and Waldron, 2009). Once the tooth comes to occlusion, it cannot withstand the occlusal forces and starts to break down (Alaluusua, 2010). However, incisors are affected to a lesser degree than FPMs and do not often show PEB. This is because they are not subjected to occlusal loads like FPMs (Fayle, 2003, Weerheijm, 2003).

There are three indices used to describe enamel defects. The first one was introduced by the world dental federation (FDI), in 1982 and was called the developmental defects of enamel (DDE) index. This index was difficult to use in a clinical set-up, due to its complexity and therefore in 1992, the FDI modified the index and called it the modified DDE index (mDDE). The index subdivided defective opacities into diffuse or

demarcated opacities, and identified them as qualitative defects of enamel. A defect must be more than 1mm in diameter to be included in the mDDE index. Lack of enamel thickness was termed hypoplasia, a quantitative enamel defect (Jalevik, 2010)

In 2003, at an EAPD meeting there was an agreement to develop a new index specifically for MIH that would be easier to use in epidemiological studies. The criteria required examining the twelve permanent teeth (FPMs and incisors), at the age of eight, and each tooth noted the presence of enamel demarcation, PEB, large restorations, extraction due to MIH and eruption failure of any of the twelve index teeth (Weerheijm et al., 2003). The DDE and mDDE indices will be described in detail in section 1.2.1.

Weerheijm et al. reported that MIH can involve the second primary molars, cusps of permanent canines and permanent second molars and the more teeth are involved, the more severe the condition (Weerheijm et al., 2003, Lygidakis et al., 2010).

1.1.1 Prevalence

Due to the use of different indices, criteria, age groups and sample range, there is a wide range of prevalence of MIH worldwide. Koch et al. reported a prevalence of 3.6% – 21.5% (Koch et al., 1987). Some authors think that MIH may have been concealed by caries rates in the past, but as caries levels in the population have decreased, MIH lesions became a clear entity (Ogden et al., 2007). Prevalences of less than 6% in Germany and Bulgaria (Dietrich et al., 2003, Kukleva et al., 2008) and 40.2% in Rio de Janeiro, Brazil (Soviero et al., 2009) have been reported. However, Lygidakis et al. reported a prevalence range of 2.8% - 25% taken from studies conducted between 1996 and 2008 (Lygidakis et al., 2010). They added that there was no data at present from North America. The MIH prevalence was reported to be 15.9% in Northern England (Balmer et al., 2012).

The distribution between boys and girls has been investigated and there was no strong evidence of any difference between the two genders (Willmott et al., 2008). Also, it was reported that children with severely affected FPMs will more likely have affected incisors (Jalevik et al., 2001a).

1.1.2 Aetiology

The aetiology of MIH is not well known. Authors who conducted systematic reviews about the causative factors of MIH concluded that evidence is either weak or moderate (Crombie et al., 2009, Alaluusua, 2010). These factors can be divided into prenatal, neonatal and postnatal causes.

1.1.2.1 Prenatal

Maternal illness during conception is thought to be one of the important causative factors related to MIH. Fredén and Grönvik found urinary infections during the last three months of pregnancy were related to enamel defects (Fredén and Grönvik, 1980). It was reported that children with MIH were more likely to be born to mothers with pregnancy illnesses (Whatling and Fearne, 2008, Lygidakis et al., 2008).

1.1.2.2 Neonatal

Children who had a history of abnormal delivery such as Caesarean section, lengthy or preterm birth may be more likely to have MIH (Alaluusua, 2010). This is thought to be a result of prolonged hypoxia, with reduced levels of oxygen affecting ameloblasts directly (Seow, 1996, Lygidakis et al., 2008). Babies with birth weights well below normal weight had more hypomineralisation than hypoplasia defects (Seow, 1996).

1.1.2.3 Postnatal

Jälevik et al. found a relationship between illness in the first year of life and MIH, but only in boys (Jalevik et al., 2001b). However, a study in the Netherlands found a correlation between illness in the first four years and MIH in children (Beentjes et al., 2002). Some of the conditions that are thought to predispose children to MIH postnatally include:

Hypocalcaemia

This may affect enamel development at all stages. Jälevik et al. suggested the reason may be that ameloblasts have an abnormal calcium processing ability (Jalevik et al., 2001b). The longer the duration of hypocalcaemia the more the effect on enamel

formation (Namiki et al., 1990). Conditions linked to hypocalcaemia include maternal diabetes and vitamin D deficiency (Alaluusua, 2010).

Childhood illnesses and high fever

As increased temperature is a common symptom for most of the childhood illnesses, it is difficult to ascertain if MIH is a result of the disease or the raised temperature (Alaluusua, 2010). However, Tung et al. showed in an experiment on rats, that a prolonged increase in temperature affected enamel formation (Tung et al., 2006). Diseases of childhood which have been documented in the literature to be linked to MIH include; infection of the middle ear, pneumonia, asthma, urinary tract infections and chicken pox (Beentjes et al., 2002, Jalevik et al., 2001b, Tapias-Ledesma et al., 2003, Whatling and Fearne, 2008).

Antibiotics

The same question poses itself; is it the use of antibiotics that causes these children to have MIH, or is it the disease for which the antibiotic was prescribed? Studies have investigated several antibiotics and found that children who were given Amoxicillin, Erythromycin or other macrolides were associated with MIH when compared to other antibiotics (Alaluusua, 2010). However, it must be remembered that these are also the most commonly prescribed antibiotics in childhood.

Environmental toxicants

Dioxins and Polychlorinated biphenyls are environmental pollutants that have been reported to affect enamel formation in high levels. Studies which looked at this effect demonstrated a dose related effect (Alaluusua et al., 2004, Jan et al., 2007). They found a relationship between pollutants' exposures (serum concentration) and the enamel defect in MIH. In another study in Slovenia, Jan and Vrbic found the prevalence of developmental defect of enamel was high in areas contaminated with Polychlorinated biphenyls (Jan and Vrbic, 2000).

Breastfeeding

Prolonged breastfeeding was associated to MIH in one study (Alaluusua et al., 1996) and they suggested that pollutants in breast milk, such as dioxins, could be the causative agents. However, other researchers did not find any association between MIH and breast feeding (Jalevik et al., 2001a, Whatling and Fearne, 2008).

1.1.3 MIH Clinical Features

The clinical features of MIH include opacities of large well defined areas ranging in colour from white creamy to yellow brown. PEB may or may not be a clinical feature depending on the severity of the condition. The incisor teeth do not usually exhibit PEB, as they are not subject to occlusal loading. A research group investigated the association between the clinical appearance of MIH teeth and laser fluorescence with the mineral density, using X-ray Microtomography (XMT) for mineral density (MD) and Diagnodent for the laser fluorescence (Farah et al., 2010a). They reported a correlation between colour of the teeth and laser fluorescence to enamel MD and concluded that the laser fluorescence (Diagnodent) can be used to clinically diagnose the severity of MIH enamel.

First permanent molars affected by MIH can be very sensitive to hot and cold stimuli (Willmott et al., 2008), therefore when treating patients with MIH affected FPM, local anaesthetic may not always be as effective (Weerheijm, 2003). This is due to the porous enamel leading to a clinically inflamed pulp (Jalevik and Klingberg, 2002). This was also reported by another study investigating pulps of MIH teeth and comparing them with controls. The authors concluded that even though their sample was small, the changes they found suggested the presence of inflammatory changes in the pulp (Rodd et al., 2007).

Caries can progress rapidly in MIH teeth making diagnosis difficult, especially if the tooth is badly broken down. A speculated reason for this is that children with very sensitive teeth have difficulty in brushing them resulting in poor oral hygiene around these teeth (Beentjes et al., 2002, Weerheijm, 2003).

1.1.4 Managing children with MIH

Children with MIH may have high levels of anxiety while having dental treatment done on affected teeth, due to hypersensitivity of teeth leading to frequent pain episodes, as well as their young age (Willmott et al., 2008, Jalevik and Klingberg, 2002). Diagnosis at an earlier stage is key in the management, to re-enforce teeth remineralisation levels and reduce their hypersensitivity. Caries prevention should be achieved in the same way as for other children of the same age for example, regular fluoride application and fissure sealants placement. If these teeth are already carious then they should either be restored or extracted if unrestorable. Maintenance is important to make sure there is

no further deterioration of these teeth. Leppäniemi et al. emphasized that these patients will need multidisciplinary management of the dentition (Leppaniemi et al., 2001).

1.1.5 The Ultrastructure of MIH teeth

The enamel in MIH has different physical and chemical characteristics when compared to sound enamel. Studies investigating the ultrastructure of FPMs in MIH are limited. Techniques that have been used include X-ray microtomography (XMT), polarising light microscopy (PLM) and scanning electron microscopy (SEM). Fearne et al. investigated MIH enamel using XMT and found that the extent of lower MD varied from one area in the enamel to another, ranging from the whole enamel being affected with low mineral concentration to only the enamel closer to the EDJ (Fearne et al., 2004).

Crombie et.al investigated both the physical and chemical features of MIH enamel (Crombie et al., 2013). They reported lower microhardness (Vickers) and mineral content (using transverse microtomography or TMR) compared to sound enamel. In addition, higher porosity (using PLM) and carbonate contents (determined by carbon dioxide release from acidic disintegration) were noted. They also found that the enamel structure in MIH was defective when examined by SEM, and that the whole thickness of enamel was involved. Although a difference between white/creamy or intact lesions and yellow/brown or broken down lesions was shown, this difference was not statistically significant. Interestingly, the thin surface layer in both intact and broken down lesions, measuring about 25µm, had characteristics values approaching those for normal enamel. Also, the cervical areas were spared as well as those areas which looked clinically sound (Crombie et al., 2013).

A study investigated the protein content of MIH enamel, found that yellow/brown and white/chalky lesions contained 15 – 21 fold and 8 – fold, more protein, respectively compared to normal enamel (Farah et al., 2010b). They found that MIH enamel contained higher levels of serum albumin (which inhibits crystal growth), antitrypsin and serum antithrombin (which inhibit kallikrin 4 proteolytic activity) compared to normal enamel (Farah et al., 2010b).

1.2 Limitations of assessing the extent of MIH defects using existing methods:

1.2.1 Indices of enamel defects

During a clinical examination, a clinician can assess the prognosis of MIH affected FPMs, for example, if the tooth has been affected by PEB or already restored or exhibiting signs and symptoms. It is important to determine the long term prognosis of FPMs, as planned extractions of affected teeth may be required. Indices have been developed to aid clinicians in assessing enamel defects.

1.2.1.1 The Developmental Defect of Enamel index

The developmental defect of enamel (DDE) index was first introduced in 1982 by the FDI working group (FDI, 1982). They stressed the need for classification based on the clinical appearance of teeth instead of the causative factor of the defects. Also, they recommended that the index should be suitable to be used in person, tooth or tooth surface levels. They used the criteria demonstrated in Table 1.1

Each sub category is assigned numbers for permanent teeth, and letters for primary teeth. They recommended that visual examination should be done using natural or artificial light, and a tactile examination with a probe to check for irregularities of the tooth surfaces. Also, to optimise the level of accuracy, teeth should receive prophylaxis. However, if there is any doubt on diagnosing the surface abnormality, it should be recorded as normal. If the lesion is clear, but cannot be categorised to any of the above categories then it should be scored as 'Other'. However, the index received a lot of criticism due to its complexity and discussion was raised for the FDI to review the index (FDI, 1992).

1. Type of Defect	Code	
	Permanent teeth	Primary teeth
Normal	0	A
Opacity (white/cream)	1	B
Opacity (yellow/brown)	2	C
Hypoplasia (pits)	3	D
Hypoplasia (grooves: horizontal)	4	E
Hypoplasia (grooves: vertical)	5	F
Hypoplasia (missing enamel)	6	G
Discoloured enamel(not associated with opacity)	7	H
Other defects	8	J
Combination of defects	Each is given a code individually same as mentioned above	
2. Number and demarcation of defects		
Single	1	A
Multiple	2	B
Diffuse, fine white, lines	3	C
Diffuse, patchy	4	D
3. Location of defect		
Gingival one-half	1	
Incisal one-half	2	
Gingival and incisal halves	3	
Occlusal	4	
Cuspal	5	
Whole surface	6	
Other combinations	7	

Table 1.1 Criteria used in Developmental Defect in Enamel index, proposed by FDI working group in 1982.

Modified from FDI Commission on Oral Health, Research and Epidemiology (1982)

1.2.1.2 The modified developmental defect of enamel index

In 1988 a committee was commissioned by the FDI to review the DDE Index, and modify the index accordingly. The modified developmental defect of enamel (mDDE) index was published in 1992 (FDI, 1992), as shown in Table 1.2, the proposed modifications were:

- Examination criteria
 1. In the DDE index it was recommended to examine teeth either dry or wet. Because drying teeth takes long time, it was decided to carry the examination on wet teeth instead.
 2. To decide whether a defect is present or not was very difficult, so it was decided that any defect less than 1mm will not be recorded.
 3. DDE index did not clarify how to deal with white spot lesions, white cuspal ridges etc.
 4. If the examination light is very bright it will make a glare which will make some opacity difficult to view. Therefore, the type of lighting needs to be specified.
 5. The position of the examiner is also said to be important when examining such enamel defects.

Table 1.2 shows the criteria used in mDDE index and codes given for each sub criteria. All of the points raised by epidemiological studies which used the DDE index were considered in the modified version of the index.

However, all indices are subject to criticism, due to subjectivity and problems with reproducibility. To overcome these problems, more objective measures to assess prognosis of MIH teeth are required.

Type of Defect	Code
Normal	0
Demarcated opacities	
white/cream	1
yellow/brown	2
Diffuse opacities:	
Diffuse-lines	3
Diffuse-patchy	4
Diffuse-confluent	5
Confluent/patchy + staining + loss of enamel	6
Hypoplasia:	
Pits	7
Missing enamel	8
Any other defects	9
Combinations	Code
Demarcated and diffuse	A
Demarcated and hypoplasia	B
Diffuse and hypoplasia	C
All three defects	D

Table 1.2 Modified DDE Index for use in general purpose epidemiological studies.

This table has been taken from the FDA working group report (1992).

1.2.2 The use of radiographic imaging

Generally, radiographic examination of teeth is an important part in the diagnostic process of any dental disease. It aids in visualising the oral structures and distinguishing them in health and disease. It helps to diagnose caries, periodontal disease, radicular or bony resorptions, bony tumours and cysts. In MIH, radiographic

imaging has a role in investigating the extent of the lesion into the tooth structure. However, in studies describing MIH condition, authors do not tend to give an account of the radiographic features of MIH affected teeth. This could be because MIH is diagnosed mainly clinically rather than radiographically.

The usual radiographic images prescribed in investigating the extent of MIH lesions into the tooth structure are dental panoramic tomography (DPT), bite-wing (BW) radiographs or long cone peri-apical (LCPA) radiographic images. DPT is an extra-oral image which shows the dentition in both dental arches as well as the adjacent bony structures. Whereas, BW and LCPA images are intra-oral images showing areas confined to the affected region. In BW radiographs, the posterior teeth in one side of the mouth are imaged at the same time making them the most suitable images when the crown is the area of interest (Vandenberghe et al., 2010, Wenzel, 2004). They mainly show the crown of the imaged teeth and possibly the area between the roots (the furcation area) as well as interdental alveolar bone. On the other hand, LCPA radiographs show the crowns and roots of the imaged teeth. They also show the quality of the bone around the teeth (Vandenberghe et al., 2010). One of the drawbacks of these radiographic images is that information from these images are masked by superimposition of other anatomical structures (Otis et al., 2000).

Radiographic imaging has potential risks associated with it due to increased patient's radiation exposure. For example, in the United States (US) radiographic imaging cost and radiation exposure has increased for the last thirty years due to the increase in its use in diagnosing a variety of clinical conditions (White and Mallya, 2012, Fazel et al., 2009, Brenner and Hall, 2007, Mettler et al., 2009). The contribution of the radiography and fluoroscopy to the effective dose in the US population in 2006 was reported to be 5% and half of this percentage was contributed to conventional dental imaging (US National Council on Radiation Protection and Measurements Report, 2009, White and Mallya, 2012).

The effects of radiation can be deterministic or stochastic. Deterministic effects occur from high exposure doses, result in cell death and have a threshold dose for it to occur, such as in radiotherapy, (White and Mallya, 2012). However, stochastic effects have no threshold or safe dose, and can occur from very low doses and they damage the cell's Deoxyribonucleic acid (DNA) causing cancer (White and Mallya, 2012, Ribeiro, 2012). This cancer risk was reported to be lifelong for the exposed individual (US National Research Council, 2006). However, it is presumed that the benefits of use of radiography in diagnosing medical and dental conditions balance its risks (Tubiana,

2000). Therefore, it is important to try and limit the unnecessary radiation exposures whenever possible. This can be achieved by using two principles, justification and optimization.

- Use selection criteria to assist in determining type and frequency of radiographic examinations
- Use E/F-speed film or digital imaging
- Use rectangular collimation for periapical and bitewing images
- Use rare-earth screens for panoramic and cephalometric imaging
- Stand at least 1.8m away from patient and away from the X-ray machine
- Reduce Cone Beam Computerised Tomography beam size to region of interest
- Any dentist still using short pointed aiming tubes should replace them with open-ended aiming cylinders
- Dentists still using manual film processing should use the time temperature method rather than 'sight' processing, or use an automatic processor

Table 1.3 Means for reducing X-ray exposure, taken from (White and Mallya, 2012)

Justification is important, so that the patient and the operator will not be exposed to a radiation dose unless this will add new information which will impact on patient management. If this is the case, the imaging should be optimised and every effort should be done to reduce the amount of radiation needed. This is known as the ALARA principle of exposure which stands for As Low As Reasonably Achievable (International Commission on Radiological Protection, 2008). Meanwhile, it is important to use methods that will decrease radiation exposure to patients in a particular radiographic examination. Table 1.3 shows the methods of reducing X-ray exposure when taking radiographic images in dental set-up.

Due to the risk of ionisation radiation of the radiographic imaging and consequent carcinogenic risk, it is important to investigate novel diagnostic technique which avoid the use of radiation to the patient.

1.3 Optical Coherence Tomography (OCT)

Optical Coherence Tomography is a 'non-destructive imaging system, using near infrared light to investigate the internal biological structures to a depth of up to 2-3 mm' (Jones et al., 2006b). OCT is based on the same concept as for ultrasound imaging, but uses light instead of sound. In both techniques an incident beam is used and a back scattered signal is measured (Jones et al., 2006b). It produces two-dimensional (2D) optical tomographic (XZ), cross-sectional depth images called *b*-scans (Figure 1.1). When multiple *b*-scan images are taken in the Y-plane direction a three-dimensional (3D) image (in the XYZ dimensions) can be obtained.

When measuring the backscattered signal from a surface, an *a*-scan is obtained which is basically a signal intensity as a function of position within the imaged tissue as shown in Figure 1.2 (Fried et al., 2002). In some studies that have used polarisation sensitive OCT (PS-OCT), which is a type of OCT where the backscattered light is polarised (Manesh et al., 2009b, Hee et al., 1992), this backscattered intensity signal was shown as a colour-coded scale instead.

Visible and near infrared wavelengths have been used in OCT (Fercher and Hitzenberger, 2002). OCT has depth (or axial) resolution in the order of 10 μ m (Baumgartner et al., 2000). However, it was reported that OCT has no detrimental biological effect (Delpy et al., 1988, Otis et al., 2000).

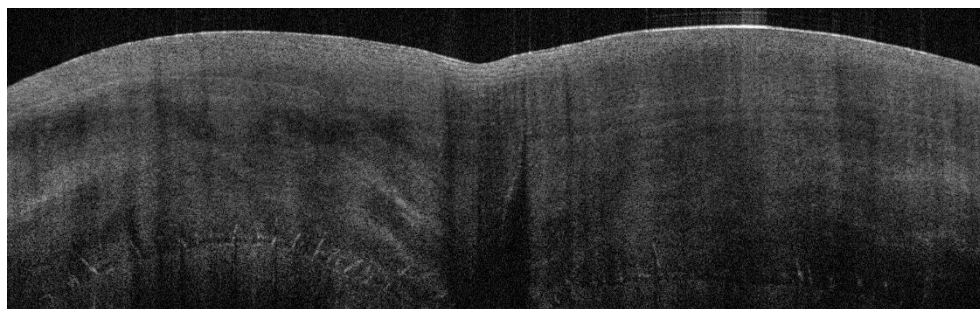


Figure 1.1 An OCT *b*-scan image of a first permanent molar tooth taken in the current study.

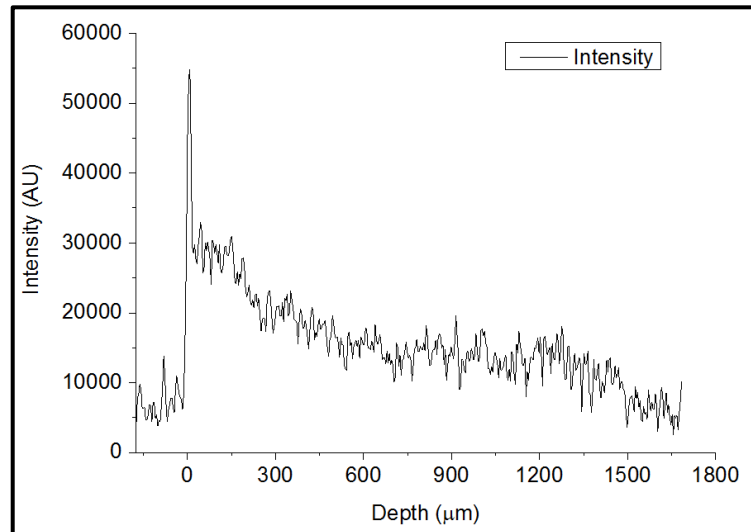


Figure 1.2 An example of an OCT *a*-scan signal; light intensity in arbitrary unit (AU) is plotted against depth in tooth structure in microns.

As light hits the enamel surface, a sharp peak of back scattered light is seen then as light travels further into the enamel structure it gets absorbed by the enamel and decays in an exponential pattern.

1.3.1 Principle of OCT

Most of the earlier investigations on OCT were done in ophthalmology, and in 1990, Fercher presented the first two dimensional representation of an in vivo human eye fundus contour using this technique (Fercher et al., 1993). OCT is based on Low Coherence Interferometry (LCI). Low Coherence Interferometry has two different techniques which are time-domain Low Coherence Interferometry (TD-LCI) and Fourier domain Low Coherence Interferometry (FD-LCI). The first technique records the depth structure of the sample using partial time-coherence interferograms. These interferograms are developed by the combination of sample sites and a reference beam back reflected at a moving reference mirror (Fercher, 2010).

On the other hand, FD-LCI can be achieved on a spectrometer (spectral or sFD-LCI) or on a tuneable laser (“frequency tuning” or fFD-LCI) (Fercher, 2010). Depth data can be obtained by a Fourier transform of the spectrum of light at the output of a Michelson interferometer (Fercher et al., 1995). Fercher et.al demonstrated that TD-LCI and FD-LCI are both comparable in terms of resolution (Fercher et al., 1991). Both techniques can be used to generate low coherence *a*-scan signals and *b*-scan images (Fercher et al., 1995, Fercher et al., 1999). However, it was demonstrated that the Fourier domain

OCT (FD-OCT) technique has better sensitivity than Time domain OCT (TD-OCT) (Leitgeb et al., 2003, de Boer et al., 2003, Choma et al., 2003).

Originally, multimode diode lasers were used as light sources for OCT. These light sources produced confusing results, this is due to their periodic coherence functions (Fercher and Roth, 1986). Later, superluminescent light diodes (SLDs) were used (Huang et al., 1991, Fercher et al., 1993). These SLD light sources gave much wider spectral emission resulting in an improved depth resolution. This was due to their monotonic coherence functions (Fercher, 2010). Other types including femtosecond Titanium-sapphire lasers and photonic crystal fibres which produced a very high resolution and sub-micrometre resolution, respectively (Drexler et al., 1999, Hartl et al., 2001, Povazay et al., 2002, Bourquin et al., 2003).

Current lasers substituted external-cavity tuneable laser diodes by cavity-tuning 'swept laser sources'. In these systems the spectral filtering is performed inside the laser cavity (Fercher, 2010). Nonetheless, SLDs are still the light sources of choice. Multiplexed SLDs have a wavelength range from 675nm to 1600 nm with an output range of up to 50mW and spectral widths of up to average wavelength of 100 nm.

There are many acquisition systems used in the OCT technique. In typical OCT systems (TD-OCT and FD-OCT), the images are acquired in planes normal to frontal plane in depth oriented cross-sections i.e. *b*-scan images. However, an en face OCT system produces frontal plane sections. This is a two dimensional acquisition system scanning with a slow change of the coherence is required in axial direction (Fercher, 2010). Another acquisition system used is full field OCT system which is ultrafast system with a reported speed of about 10 μ s (Dubois and Boccara, 2008). Linear OCT acquisition system is a substitute to the TD-OCT system. However, it has a lower resolution and sensitivity (Koch et al., 2004, Fercher, 2010). Other acquisition systems are endoscopic OCT, High depth-resolution OCT, high speed and volumetric OCT, high lateral resolution or adaptive optics OCT and depth of field OCT system. Each system has its particular applications.

Regarding optical signal property detection, there are many systems used. One of these systems is polarisation sensitive OCT (PS-OCT). This system is based on work done by Hee et al. (Hee et al., 1992). In this arrangement the sample is illuminated with circularly polarized light with two channels of a polarization sensitive detection unit used (Fercher, 2010). However, in differential phase contrast OCT system, optical path-length generated phase difference of the interferometric signal of two sample

beams was used and measured to be as little as 2 nm (Fercher, 2010). Other signal detection systems used were spectrometry, refractometry and system sensitivity.

Enamel and dentine are scattering materials. Light scattering in enamel was said to decrease by $1/\lambda^3$, where λ is the wavelength of the incident light (Darling et al., 2006). This is related to the size of the main scatterers in enamel (enamel crystals). Therefore Darling et al. suggested that the near-infra red (NIR) region of 780-1550nm results in an optimal imaging techniques, due to low scattering and absorption in enamel and dentine. If the NIR wavelength is longer, then the light is absorbed distinctly by the water in the tissue and consequently reducing the penetration of the NIR light (Darling et al., 2006, Fried et al., 2002)

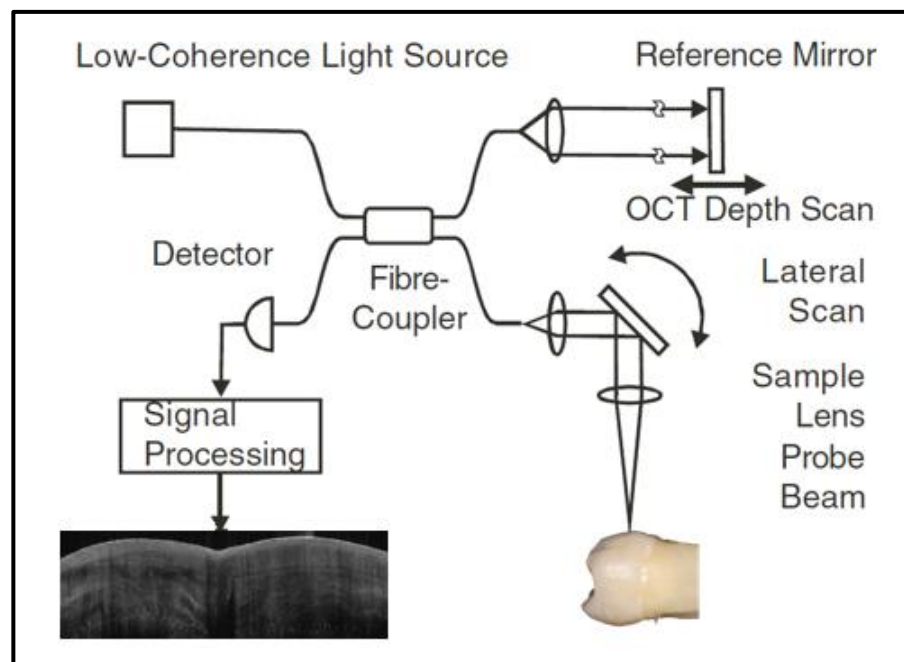


Figure 1.3 Principle of swept source OCT; taken and modified from (Fercher et al., 2003).

The principle on which a low coherence, frequency domain OCT system works is illustrated in Figure 1.3. A low-coherent light produced from the source is splitted into two beams at the fibre coupler; one is directed to a movable reference mirror arm and another to a sample arm. Both back-reflected beam from the reference arm and the back-scattered beam from the sample arm are recombined at the fibre coupler and transferred to a photo detector which is a Michelson interferometer. When the path length of back-reflected light from the tissue and the reference mirror was within the

coherence length of the source, an interference signal is identified (Otis et al., 2000). Due to the known reference mirror position, the depth into the sample structure can be determined (depth resolution). These depth resolved signals are called *a*-scan signals which are transferred into digital signal processing unit. In this processing unit, OCT *b*-scan image can be constructed from multiple *a*-scan signals (Fercher et al., 2003). Lateral scanning is done by the use of a sample lens which aid in moving light laterally across the surface of the sample (lateral resolution).

Refractive Index of dental structures

As light travels from one medium (or material) to another its speed changes and consequently light refraction occurs. The measure of change in light speed when it passes from air to another material or medium is called the refractive index. The larger the refractive index the slower the speed of light in the material. The refractive index of air is 1. In OCT, light travels from air to tooth structures and light refraction occurs.

Refractive index is a significant optical parameter of biological tissues (Meng et al., 2009). Light propagation in biological tissues depends on the tissues' refractive index, which gives an indication of the scattering properties of the tissue (Hariri et al., 2012). This scattering properties of the tissue is the ultimate result of refractive index variation between tissues (Knuttel et al., 2004). It has been reported that early carious lesions can change the enamel refractive index and consequently this change assists in diagnosing dental caries (Meng et al., 2009, Besic and Wiemann, 1972). Clinically, the occurrence of white spot lesions when enamel is dried is due to change in enamel refractive index (Kidd and Fejerskov, 2004)

Many studies have looked at methods to measure the refractive index of tooth using OCT. An example was the OCT-based focus-tracing method (Tearney et al., 1995, Haruna et al., 1998, Song et al., 2000). This method is practically difficult to do due to several focal point adjustments and precise calibration of the numerical aperture of the lens are required.

There was a simpler method which was based on optical path-length (OPL) matching (Meng et al., 2009, Hariri et al., 2013). It is easy, fast and had high accuracy (Meng et al., 2009). They reported the refractive indices of enamel, dentine and cementum to be 1.631 ± 0.007 , 1.540 ± 0.013 and 1.582 ± 0.01 respectively. These results coincided with other studies (Ohmi et al., 2000, Kienle et al., 2006, Hsieh et al., 2011).

Hariri et.al investigated the effect of structural orientation of enamel prisms and dentinal tubules on optical properties namely, the refractive index and OCT signal slope (from a-scan signal) using swept-source OCT (Hariri et al., 2012). They used OPL method in measuring the refractive index and found that the optical properties of enamel did not vary with enamel prism orientation (cross-cut enamel prisms compared to long-cut enamel prisms). However, dentinal tubules orientation significantly affected the optical properties.

1.3.2 Applications of OCT

The use of OCT in medical and dental fields has increased in the last twenty years. Its first application in medicine was in ophthalmology (Swanson et al., 1993, Fercher et al., 1993). Fercher et.al reported the advantages of OCT in contrast to non-optical techniques (Fercher, 2010). One of the advantages was that OCT has high depth and transverse resolutions. They described it as a contact-free and non-invasive technique. However, its disadvantage was its limited penetration into the imaged scattering tissue (Fercher, 2010). Besides its use in ophthalmology, it was used in gastroenterology and dermatology. Endoscopic OCT was reported to be a promising imaging modality for early diagnosis of tumours (Sergeev et al., 1997). In the meanwhile, standard OCT was reported to be a valuable tool in diagnosing some inflammatory and bullous dermatological conditions (Welzel, 2001).

In dentistry, OCT was used in investigating caries, artificial demineralisation and remineralisation in enamel and dentine. Jones et.al used PS-OCT to image artificial occlusal caries by investigating the magnitude of backscattered light with variations in the enamel volume (Jones et al., 2006b). They also used transverse sections from digital microradiography to obtain the quantitative mineral content profile and relative mineral loss. It was concluded that PS-OCT can measure artificial occlusal caries by observing the changes in backscattered and depolarisation of near infra-red light and the technique was promising in detecting and monitoring early enamel caries (Jones et al., 2006b). A study conducted by Fried et.al demonstrated that PS-OCT is an invaluable tool in imaging of interproximal, occlusal and early root caries and caries underneath composite fillings (Fried et al., 2002). Manesh et.al showed that PS-OCT can be used to detect remineralisation of dentine (Manesh et al., 2009b, Jones and Fried, 2006).

Another study investigated the use of OCT in evaluating the degree of demineralisation of in vitro microbiologically induced dentine caries (Azevedo et al., 2011). They used FD-OCT and concluded that OCT is an efficient method to detect the depths of carious lesions. Maia et.al used two types of OCT; TD-OCT and sFD-OCT with light source wavelengths of 1280 nm and 840 nm, respectively in evaluating caries in primary teeth (Maia et al., 2010). They concluded that there was a great potential for OCT to be used routinely in clinical practice for caries detection and monitoring. The same conclusion was reached by Amaechi et.al who looked at root caries using PS-OCT and correlated it with TMR (Amaechi et al., 2004). They added that the technique could replace conventional dental radiographs and avoid the hazard of ionising radiation. Feldchtein et.al demonstrated the use of OCT in imaging healthy oral soft and hard tissues (Feldchtein et al., 1998). They also imaged restorations such as amalgam, composite and compomer in vivo, and demonstrated the presence of defects underneath the composite and compomer restorations. In restoring carious teeth, they obtained images of smear layer and etched enamel surface (Feldchtein et al., 1998).

However, enamel defects such as MIH have not been investigated previously using OCT. As already discussed, this technique is promising and its merit is that it does not involve ionising radiation. However, it is important to correlate OCT findings with well-established techniques such as X-ray microtomography, Synchrotron X-ray diffraction when investigating such anomalies, to ensure the technique is effective. These imaging techniques are described in the following sections.

1.4 X-ray Microtomography

1.4.1 Principle of XMT

X-ray microtomography, also known as micro-computerised tomography (micro-CT) scan, have been in the market since the 1990s and was first described in 1982 by Elliot (Elliott and Dover, 1982). Its principle is the same as for the medical CT scan; XMT scanners are capable of reconstructing three dimensional images of variable sizes of up to a few centimetres (Davis et al., 2013). It is non-invasive and non-destructive technique that provides high resolution data (Huang et al., 2010, Huang et al., 2007). It is important to note that the radiation dose is very high in the XMT and it takes long time to image a specimen and therefore it is not suitable for clinical imaging and restricted to in vitro lab studies (Davis et al., 2013).

As the incident X-ray beam is directed on to a specimen, the degree of absorption of the x-ray beam by the specimen gets recorded on a detector, usually a charge-coupled based device or CCD device, (Salvo et al., 2003). The specimen is rotated in a small angle every time after it is being imaged and the process is repeated for 360°. The images are transferred onto software, where they can be reconstructed into a 3-D image. The imaging process takes up to 18 hours.

The XMT systems can be synchrotron based, in-house developed desktop or commercial systems; the earlier type produces monochromatic X-rays, while the later types produces cone-beam polychromatic X-rays (Huang et al., 2007, Kinney and Nichols, 1992, Cooper et al., 2004, Prymak et al., 2005). Examples of desktop X-ray micro-tomography systems are SkyScan™ and MuCat™ systems.

X-ray microtomography has been established to determine the MD with an accuracy of less than 1% and resolution between 5 and 30 µm (Wong et al., 2004). The basis of XMT depends on the x-ray attenuation passing through the object, and the resulting grey level of the reconstructed image in the quantification process (Huang et al., 2010, Huang et al., 2007, Clementino-Luedemann and Kunzelmann, 2006, Dowker et al., 2003, Wong et al., 2004, Anderson et al., 1996). Wong et.al reported the advantage of XMT over conventional physical cutting of the specimen (Wong et al., 2004). They mentioned that the thickness of the slice is constant in XMT and is dependent on the size of the X-ray beam only.

The x-ray source and the detector in XMT are immobilised while the sample is revolving on a platform with an upright axis. Besides the fact that 3D reconstruction can be done, local quantification of mineral density is feasible (Davis et al., 2013) as well as in vitro assessment of enamel lesion development (Huang et al., 2010, Dowker et al., 2003). When XMT was first described in the early 1980s, the main purpose was to quantify the mineral density of hard tissues (Elliott and Dover, 1982). As XMT evolved, most of its applications were mainly about investigating the structure and features of the imaged object rather than the density. Consequently, the commercial XMT scanner has evolved in terms of high spatial resolution instead of high accuracy and high contrast resolution (Davis et al., 2013).

There are four XMT scanner generations. In the first generation, a very narrow beam (pencil beam) is created using a source collimator and any scattered radiation are eliminated at the detector using a second collimator. An energy selective photon counting system is used to record photons in a narrow energy window. In this system the priority is the accuracy of the acquired image rather than the speed of acquiring it (Davis et al., 2010). The second generation scanners used a 2D detector instead of the point detector used in the first generation.

The main concern of the third generation XMT scanners was the structural quantification and the absolute precision of the X-ray linear attenuation coefficient (LAC) was not essential compared to the first generation. The source for the third generation systems is practically well distinct. They use area detectors increasing the number of detected photons. In this system, the arrangement of polychromatic X-ray source and energy integrating detector results in beam-hardening artefacts (Davis et al., 2010, Van de Castele et al., 2002). Another imaging problem with this system is the ring artefact.

In the fourth generation scanners, ring artefacts are overcome by using a fixed ring of detectors, such that each projection is effectively recorded by a single detector as the X-ray generator passes behind the subject. The time-delay integration CCD readout is used in a moving X-ray camera (Davis et al., 2010, Davis and Elliott, 1997). Example of this system is "MuCat™" scanners.

The x-ray spot size in XMT is small causing the XMT to have a low flux (Davis et al., 2013). There is a correlation between the image resolution, image contrast or signal-to-noise ratio (SNR), X-ray exposure and detectors' pixel count. In an attempt to improve the SNR, exposure time can be increased to some extent. However, if the exposure time is longer, a ring artefact appears on the image (Davis et al., 2013). To minimise

this artefact, the detector or the specimen are moved slightly between projections. On the other hand, those studies which investigated the structure of the specimen or generation of a 3D restricted component model, the noise in the system is not as important as when quantifying and measuring mineral density (Huang et al., 2007).

In an attempt to develop an XMT scanner with high SNR images, a scanner employed the principle of time-delay integration readout was developed (Davis et al., 2013, Davis and Elliott, 1997). Other advantages of this principle are that it helps to eliminate ring artefact and to acquire high range X-ray projections (Davis et al., 2010). Development of the design of these scanners, the processing of the data and correcting the hardening of the beam all contributed to the production of high SNR images of hard tissues and more accurate quantification of mineral density (Davis et al., 2013). However, dental researchers are getting more familiar with the commercial XMT scanners which are concerned more about the analysis of hard tissue structure and the visualisation of features rather than the mineral density quantification; in the meantime, the quality and accuracy of these scanners have improved recently (Davis et al., 2013).

Linear attenuation coefficient (LAC) is the logarithmic decline in intensity of the transmitted radiation per unit length. It has a unit of cm^{-1} . In XMT, LAC is measured throughout the sample giving a map of spatially varying LAC for that sample.

1.4.2 Applications of XMT

X-ray microtomography has mainly been used in vitro to investigate the mineral contents in normal, hypomineralised and demineralised enamel. Wong et.al investigated the mineral concentration distribution in primary molars using XMT (Wong et al., 2004). They found large variations in means and gradients of mineral concentration from the EDJ to the enamel surface and therefore concluded that in caries research, caries progression rates are affected by the baseline mineral concentration. Huang et.al have correlated mineral density using XMT with elastic modulus of natural enamel white spot lesions using nanoindentation (Huang et al., 2010). They found that the mineral density in the body of the white spot lesion was lower than that in sound enamel; however it increased towards the surface enamel in white spot lesion, but not to the level of normal enamel.

Hypomineralised enamel was investigated using XMT mineral concentration. Fearn et.al investigated hypomineralised enamel in first permanent molars and reported 20%

reduction in enamel mineral concentration in these teeth compared to normal enamel; and that the full thickness enamel was involved (Fearne et al., 2004). They found mineral concentration ingredient in hypomineralised enamel was opposite to that of normal enamel, suggesting a disturbance during the maturation stage of enamel formation (Fearne et al., 2004). Farah et.al have reported a strong correlation between the mineral density in MIH enamel and the colour of enamel opacity (from white/chalky to brown opacities) using XMT (Farah et al., 2010a). They mentioned that with every change in colour coding (moving from normal enamel to white/chalky to brown enamel colour) within a tooth there was 0.28 g/m³ decrease in mineral density.

1.5 Synchrotron X-ray Diffractometry (SXR)

1.5.1 Disclaimer

This part of the literature background has been written in collaboration with Dr Samera Siddiqui, from the Dental Physical Science Department, Queen Mary University of London (QMUL) at the time of writing this section.

1.5.2 Principle of SXR

Since X-rays was discovered by Röntgen in 1895, they have been used in medicine as well as in food and cosmetic industries. The internal structure of objects can be shown clearly as well as their chemical composition and physical characteristics using X-rays. X-rays are high frequency photons and have short wavelengths ranging from 0.1 to 100 Ångstrom (Å) (1×10^{-11} – 1×10^{-8} m), with energy range of 100 eV – 100 keV. In diffraction studies, the X-rays wavelength is between 0.5 and 2.5 Å depending on the crystal dimensions and shape (Cullity, 1978). X-rays interact with the irradiated material's atoms and are either scattered or absorbed and consequently, the x-ray energy is attenuated. This depends on the X-ray energy, the density of the irradiated material and its atomic number.

Synchrotron X-ray diffraction facilities offer a flux, energy range and resolution unachievable with conventional (laboratory) radiation sources. They are used in a variety of research disciplines such as material science, physics, chemistry and drug

industry. There are several of these facilities around the world, each have different levels of energy. However, the three most powerful third generation sources include, the European Synchrotron Radiation Facility (ESRF, Grenoble, France), the Advanced Photon Source (APS, Illinois, USA) and the Super Photon Ring 8GeV (SPring-8, Japan). The Diamond Light Source (DLS, UK) has a medium energy range compared to the first three. The SXR is a very novel and advanced technique which investigate the crystallographic arrangement of the enamel. As a result these facilities are on continuous demands.

The principle on which SXR works is that when electrons are accelerated and hit a target material, X-rays are produced. This process involves electron transition interaction. The X-ray sources are either monochromatic or polychromatic types, producing a single wavelength or multiple wavelengths, respectively. X-rays can be produced conventionally using X-ray tube or by synchrotron radiation. The difference between the two types of X-ray produced is that the synchrotron radiation has higher energy.

Synchrotron X-ray was first described in 1947. The principle of synchrotron is that particles are accelerated in an electromagnetic field to a speed reaching the speed of light; and guided in a circular track or ring. Synchrotron light, which is a bright light, is emitted as the particles deviate from the circular pathway along an orbit. Clusters of electrons are produced in the electron gun and guided into the linear accelerator then they are directed into a booster ring and accelerated to a speed close to the speed of light.

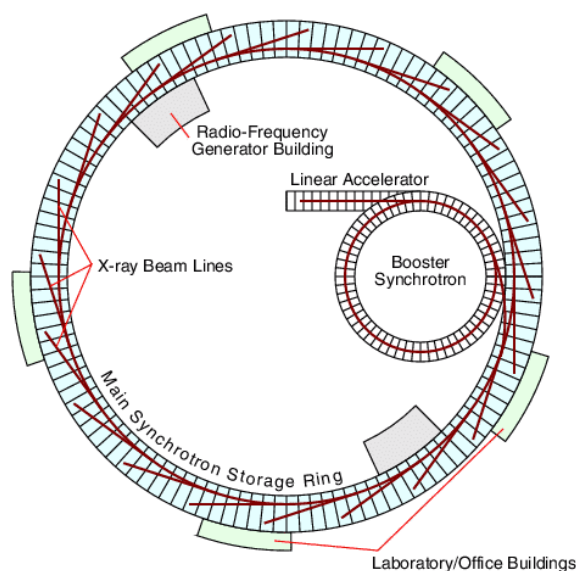


Figure 1.4 Schematic representation of a synchrotron radiation system.

(Image taken from <http://pd.chem.ucl.ac.uk/pdnn/inst2/work.htm>)

Electrons are injected into the storage ring and are accelerated more to be maintained in the circular motion by the strong electromagnetic fields. Figure 1.4 shows an example of a synchrotron radiation system.

When the electrons are forced to deviate from the straight line motion, radiation is emitted. This force is applied on the electrons by the use of magnet fields, bending magnet (BM) and insertion device (ID). They are situated in the straight lines of the orbit. These magnets serve two functions; they further increase the radiation intensity and adjusting the X-rays to the requirements of the beamline. Each beamline has unique properties according to the experimental requirements.

Due to the high energy from the synchrotron radiation (compared to the laboratory based), which is well collimated and contains a higher photon flux, the energy beams facilitate deeper penetration of the sample under investigation. The small wavelength allows investigation of very fine details of the sample. Modifications to beam size and other parameters can be done according to the specific experiment conducted allowing fast data collection with enhanced quality. Synchrotron facilities are on continuous demand.

X-ray diffraction is an important technique in investigating the arrangement of the atomic and molecular structures of a crystalline material. This technique is a powerful one which has been discovered by Laue in 1912. He concluded that uniformly arranged atoms in a crystal can act as scattering objects for X-rays. The wavelength of the electromagnetic waves should be the same as the distance between the atoms in the crystal. This results in X-rays diffraction. The X-rays used in diffraction have a short wavelength reaching a few angstroms (as in synchrotron radiation). This enables the researchers to obtain important chemical and physical information about crystals. For example, the chemical and phase compositions of a crystalline material, the texture (preferred orientation of crystallites), the crystallite size and presence of strain.

There are two types of scattering methods, Wide-angle X-ray scattering (WAXS) in which the distance between the sample and detector is short; and small-angle X-ray scattering (SAXS) in which the distance between the sample and detector is longer as shown in Figure 1.5. Consequently, the diffraction maxima is at larger angles in WAXS and at smaller angles at SAXS. The former is used for extracting information such as lattice planes in crystalline materials. However SAXS is used to study larger features such as the sizes of grains in crystalline and non-crystalline samples.

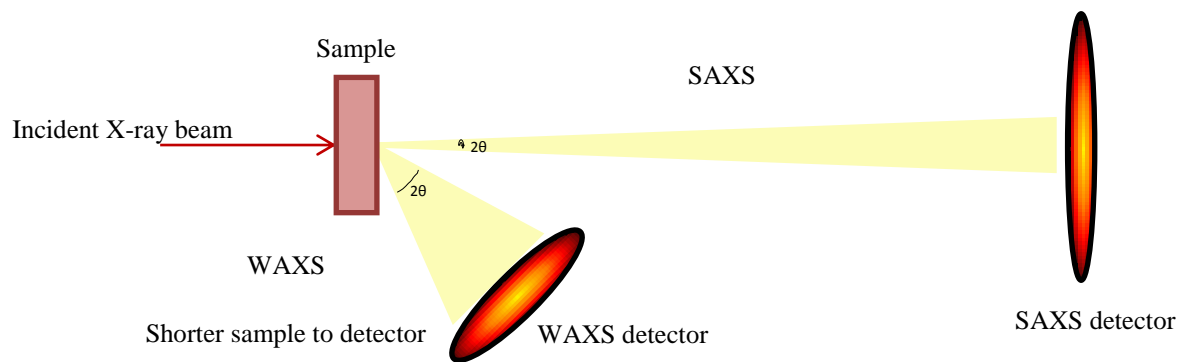


Figure 1.5 Schematic representation depicting the experimental set up for SAXS and WAXS, highlighting the difference in diffraction angle and sample to detector distance; courtesy of Dr Samera Siddiqui.

Principle of Diffraction

Crystalline materials consist of ordered atoms in three dimensional arrangement. These atoms are at distance 'd' from each other and organised in planes exhibiting periodicity (Figure 1.8). X-ray scattering from sequential planes in a crystal is called diffraction. If the X-ray Wavelength is the same as the distance between the atoms constructive interference occurs.

Braggs law (Bragg, 1928) shows that when parallel rays of an incident beam on lattice planes are scattered at angle θ a resultant reflections create coherent interference of the diffracted beam. Its basic form is

$$n\lambda = 2d\sin\theta$$

Where n = integer, λ = wavelength, d = distance between atomic layers in a crystal and θ = incidence angle

In powder diffraction, scattering of the diffracted beam from lattice planes of a polycrystalline material form continuous cones of intensity, known as Debye Scherrer cones. The direction of the diffracted beam can be used to determine the size and shape of the unit cell from an unknown crystal. The 2θ position of these cones defines the space d_{hkl} between diffracting atom planes hkl (Figure 1.6) and the intensity defines the type of atoms present in the plane.

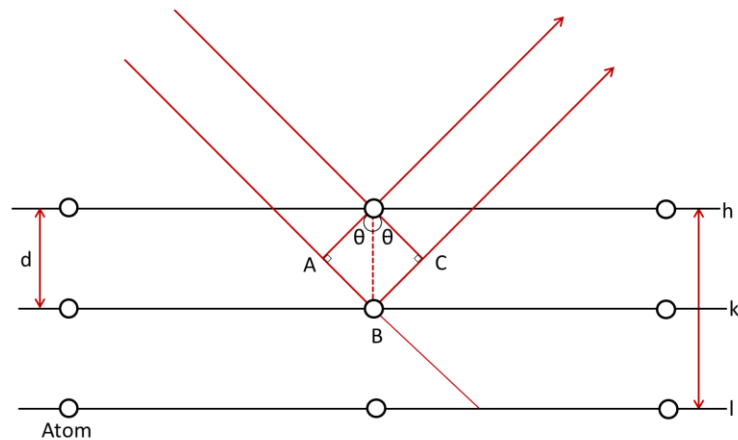


Figure 1.6 Simplified geometric construction representing the conditions necessary for diffraction; courtesy of Dr Samera Siddique.

1.5.3 Diffraction Data Analysis

The diffraction patterns obtained from SXRD gave information about the structure of the imaged specimen at the crystal level as shown in Figure 1.7. These information are obtained using profile fitting of the peaks present on the diffraction patterns. In this figure three examples of diffraction patterns are shown, from a single crystal (figure 1.7 (A)), a powder crystalline material (Figure 1.7 (B)) and a well crystallised material such as enamel (Figure 1.7 (C)). In the first example a single point intensity is obtained and as a result when the intensity is plotted against the azimuthal angle (in 360° direction), the resulting intensity profile is two vertical lines representing the diffraction pattern of the Debye ring (in this case two dots only).

The intensity of the powder material demonstrates a continuous Debye ring (Figure 1.7 (B)). This is because the crystals in the powdered material are randomly oriented with loss of a specific pattern of orientation for these crystals. As a result, a horizontal flat line is obtained when the intensity is plotted as a function of the azimuthal angle (Figure 1.7 (b)). However, in a well crystallised material, the 002 Debye ring consists of two peaks of intensity (Figure 1.7 (C)). This is because the well organised crystals have the same orientation producing a specific amount of intensity. Consequently, the intensity profile obtained would be in the form of two peaks when it is plotted against the azimuthal angle corresponding to the peaks present in the Debye ring (Figure 1.7 (c)).

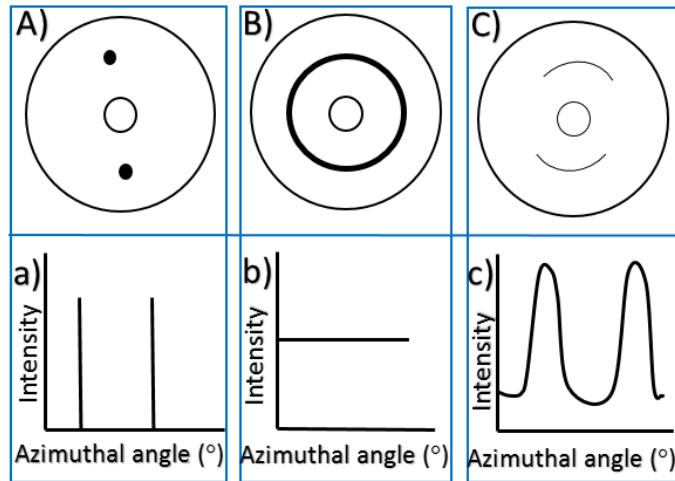


Figure 1.7 A schematic representation of three types of diffraction patterns that can be obtained from three types of crystals; A) from a single X crystal; B) Powder crystal; C) well crystallised material such as enamel; below each diffraction pattern a plot of the intensity obtained from each type as a function in the azimuthal angle, (a), (b) and (c), respectively.

The magnitude of crystallinity of a material can be measured by measuring the width of the intensity peaks present in the Debye ring from the intensity vs azimuthal angle plot shown in Figure 1.7 (C). This is done by using a Gaussian fitting curve of these peaks and extracting the Full Width at Half Maximum (FWHM) for each (Figure 1.8). This value is a measure of the peak's width, which in turn gives an indication of how closely the crystals are oriented compared to single crystals orientation (figure 1.7 (a)). Therefore, FWHM is an accurate measure of the material's texture. However, the direction of the crystal orientation can be obtained directly from the 002 Debye ring.

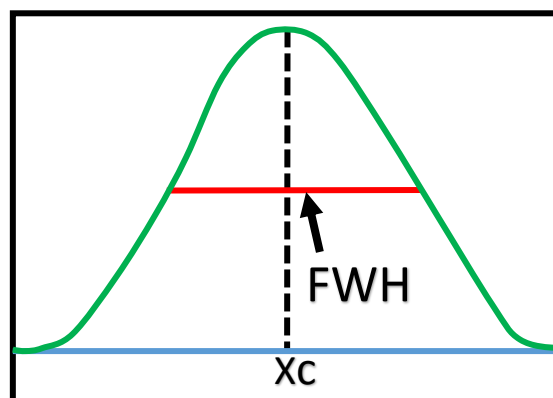


Figure 1.8 Graphical representation of the FWHM (arrow) on a fitted peak, which is a measure of the peak's width; Xc is the centre of the peak.

1.5.4 Applications of SXRD

Micro and nanoscopic techniques such as SEM and Atomic force microscopy (AFM) have been used to investigate enamel structure (Habelitz et al., 2001, Marshall et al., 2001, Gaiser et al., 2012). These techniques gave information about the qualitative properties of enamel, but did not provide any information about the subsurface structure. Even though they demonstrated the arrangement and structure of enamel prisms, they could not quantify the spatial dimensions of the HA crystallites (Simmons et al., 2011, Al-Jawad et al., 2007). Such information about enamel crystallites could be obtained from X-ray diffraction (XRD) techniques. When a sample is irradiated by low wavelength X-rays, the X-rays get deflected producing diffraction patterns which gives information about the structure of the sample crystals, molecules or atoms.

The crystallography of the HA crystals has been described in early XRD experiments. It was reported to be of space group P63/m (hexagonal) with the parameters of the lattice being $a = 9.441(2) \text{ \AA}$ and $c = 6.6.878(1) \text{ \AA}$ (Young and Mackie, 1980, Wilson et al., 1999, Wilson et al., 2004, Reyes-Gasga et al., 2013). These figures were obtained from ground enamel substance taken from different teeth and the spatial information and variability between teeth about the crystallites were missing (Seredin et al., 2013, Simmons et al., 2011, Tiznado-Orozco et al., 2009, Fried et al., 2002, Low, 2004).

Powder XRD technique averages larger amount of crystals compared to synchrotron XRD (SXRD). In the later technique, the beam spot is microfocussed, probing minute areas and distinguish any abnormality on a micron scale (Simmons et al., 2011). A study investigating tracks from the enamel surface to the EDJ using grazing-incidence SXRD, reported that the enamel crystals at the surface are well aligned compared to those near the EDJ (Low, 2004). Another advantage of SXRD over the powder XRD is that the SXRD is used on intact thin slice of enamel which gave more information about the spatial details of enamel crystallites (Al-Jawad et al., 2007, Simmons et al., 2011). Obtaining information in healthy enamel and abnormal enamel is crucial in understanding the phenotypic characteristics of the abnormal enamel noted in Mucopolysaccharidosis Type IVA and Type II (Al-Jawad et al., 2012).

A research group used powder XRD to investigate the size of the HA crystallites in enamel and dentine of a patient diagnosed with Mucopolysaccharidosis type I condition which is associated with Hurler's syndrome, a hereditary condition which affects the metabolism of glycosaminoglycans in the body (Güven et al., 2008). They did not find clear differences in the structure of HA crystal between normal control enamel and the

enamel from the Hurler's syndrome affected teeth. However, Mucopolysaccharidosis Type IVA and Type II were investigated by another research group using SXRD (Al-Jawad et al., 2012). They found that a distinct difference in mineral crystallite orientation distribution between affected teeth and normal counterparts.

A most recent study reported by Siddiqui et.al investigated the recovery of the crystallographic texture of enamel after remineralisation process using SXRD (Siddiqui et al., 2014). They concluded that, by following a particular remineralisation protocol it was possible to restore the demineralised enamel to the original healthy enamel state.

There are various techniques for investigating the structure, mineral density and the degree of crystallinity of enamel. The methods that were examined in this project were OCT, XMT and SXRD. However, there was no study that has looked at comparing these methods, especially for MIH affected enamel. Comparison of OCT with the conventional diagnostic methods of MIH affected enamel also has not been done before.

2 Aim and Objectives

2.1 Aim

To develop the use of Optical Coherence Tomography in dental clinical diagnostics of MIH and correlate the outputs with conventional clinical methods

2.2 Objectives

1. Understanding OCT as an imaging technique for teeth.
2. Comparison of OCT imaging with clinical measures (mDDE index) and radiographic imaging of MIH teeth.
3. Verifying the OCT results with imaging modalities used in investigating the ultrastructure of MIH affected FPMs such as XMT and SXR.

3 Patient Recruitment and Selection

A dental anomalies clinic was established in the Department of Paediatric Dentistry at the Eastman Dental Hospital (EDH) in 2011, on a monthly basis to ensure phenotypic data is recorded and to develop a database of anomalies patients.

3.1 Study registration and ethical approval

This research is part of a larger project to investigate dental anomalies. Ethical approval obtained from the National Health Services Research Ethics Committee (NHS REC) on the 11th of August 2011, R & D reference number 11/LO/0777. Project ID: 11/0223.

3.2 Participants and Samples

3.2.1 Patient identification

Two groups of paediatric patients were invited to participate in the project. The first group were paediatric patients in the Department of Paediatric Dentistry, Eastman Dental Hospital, who required extraction of FPMs, either as part of an orthodontic treatment plan or due to caries. This group acted as the control group. The inclusion criteria for patients in the control group were those who were fit and well, without any known illness or syndromes. However, the exclusion criteria were patients with any known relevant medical illnesses, patients with deep caries lesions or any other dental anomaly and patients who did not understand English sufficiently to consent for the study. Patients and parents in this group gave informed written consent, after being given sufficient time to ask questions (Appendices 3 and 4).

The second group was those patients who were diagnosed to have MIH, and scheduled for extractions of FPMs as part of their treatment plan. Patients and parents were approached and given full explanation about the study as well as an information leaflet (Appendices 1 and 2). They were given sufficient time to consider enrolling to

the project. Those who decided to participate were given consent forms (Appendices 3, 4 and 5).

Three copies of consent forms were signed by the participants. One copy was kept in a filing cabinet in the locked office of the secondary supervisor, another copy was filed in the patient's clinical file, and the last copy was given to the parents for their reference.

3.2.2 Sample collection and storage

The samples were obtained and stored in accordance with the Human Tissues Act 2004. All of the control samples collected from the patients were extracted as part of the treatment plan.

Each sample was given an I.D. number after extraction to ensure anonymity. Then they were stored in saline until taken to the laboratory, where they were debrided from soft tissue debris and any remaining blood cleaned under running water. Then samples were stored in 70% ethanol at room temperature for 48 hours for disinfection. After 48 hours, samples were transferred to 0.1% Thymol solution and stored in a locked fridge at 4° C at the Eastman Biomaterial Science Laboratory, as per department policy, until imaged.

4 Conventional methods in diagnosing MIH

In this chapter the use of the conventional methods of diagnosing MIH in clinical set-up are going to be described. These are visual and radiographic methods.

4.1 Clinical Visual Assessment

4.1.1 Method

The modified developmental defects of enamel index (mDDE) was used in characterising the hypomineralised enamel defects in MIH affected FPMs. Nine Clinicians, who were involved in the anomalies clinic, were calibrated to use the index in a training session. They were shown photographs of a variety of enamel and dentine defects. After one month, the assessment was repeated to determine reproducibility. At the end of the final training, 85% calibration was achieved.

Photographs of the samples were taken using Canon™ camera (DS6041) with Canon™ macro Ring lite flash (MR-14EX) for a uniform flash light. Each sample was photographed against a dark background to enhance the contrast between the sample and the background. There were five tooth surfaces photographed, starting with buccal surface then distal, lingual/palatal, mesial and occlusal surfaces. The tooth surfaces were wiped off excess moisture before imaging, but were not fully dried. Then, the photographs were uploaded immediately to a computer after each tooth was imaged and labelled according to tooth code with the tooth surface.

The modified DDE index was used to characterise the enamel surface of the teeth from the photographic images. A Dental anomalies proforma (Appendix 6) was used and each tooth was coded according to its location (L), demarcation (D), extent (E) and type of the lesion (T) as demonstrated in Table 4.1. Each of these codes were graded according to the severity of the defect ranging from grade one to grade three with grade one being less affected and grade three is more affected. For example, the location of the enamel defect was given three codes, code 1 if the defect was confined only to the Incisal half of the tooth surface, but if it is confined to the gingival half of the tooth it will be given code 2 and code 3 would be for a defect that involves the whole surface. This was done to be able to compare the mDDE codes with the OCT and radiographic images.

Criteria of the defect	Code	Description
Location	L1	Incisal ½
	L2	Gingival ½
	L3	Whole surface
Demarcation	D1	Demarcated
	D2	Diffuse
	D3	Both
Extent	E1	Less than 1/3 of the surface
	E2	1/3-2/3 of the surface
	E2	More than 2/3 of the surface
Type	T0	Normal
	T1	White/creamy opacity
	T2	Yellow/brown opacity
	T3	Hypoplasia (pits)
	T4	Hypoplasia (horizontal grooves)
	T5	Hypoplasia (vertical grooves)
	T6	Hypoplasia (missing enamel)
	T7	Discoloured enamel (not associated with opacity)
	T8	Post-eruptive breakdown
	T9	Other defects

Table 4.1 mDDE index used to record the characterisation of dental defects of enamel; the criteria marked in bold are related to defects in MIH

4.1.2 Result

4.1.2.1 Control and MIH Samples

Six control FPMs were collected from five different patients. The Patients' demographic details are illustrated in Table 4.2 . This low number of control teeth was because control FPMs were difficult to get as they were rarely indicated for extraction unless they were deemed to have poor prognosis due to dental caries or were extracted in compensation for a FPM on the same side of the mouth. Also, these carious teeth usually have scarce sound enamel as they were severely affected which rendered them unsuitable to be used as control teeth. This yielded 24 tooth surfaces to be investigated.

Patient ID	Age (years)	Gender	Ethnicity	Tooth notation	Sample ID
38	15	Female	White	UR6	C 106
39	12	Male	White	UR6	C 108
49	13	Male	Asian	UR6	C128
				LL6	C129
52	15	Male	Asian	UL6	C133
53	13	Male	African	LR6	C134

Table 4.2 The demographic data of control first permanent molar samples

Thirteen MIH affected FPMs were collected from four patients whose demographic details are shown in Table 4.3. As mentioned previously, these teeth were extracted as part of their treatment plans. This gave a total number of 52 tooth surfaces to be evaluated.

Patient ID	Age	Gender	Ethnicity	Tooth notation	Sample ID
67	9	Female	White	UR6	MIH 33
				UL6	MIH 34
				LL6	MIH 35
				LR6	MIH 36
64	10	Male	White	UR6	MIH 32
				UL6	MIH 37
				LL6	MIH 38
				LR6	MIH 39
72	12	Male	White	UR6	MIH 49
				UL6	MIH 50
				LL6	MIH 51
				LR6	MIH 52
101	11	Male	Asian	UR6	MIH 67

Table 4.3 The demographic details of MIH affected first permanent molar samples

4.1.2.2 The Modified Developmental Defects of Enamel Index

The mDDE index was used to characterise the phenotypic appearance of MIH affected FPMs as described previously. Each tooth was given a particular score depending on the overall appearance of the tooth when looking at the five tooth surfaces (Table 4.4). In the examples shown below, it can be observed that the lesions were located in the entire surface except in two samples where the occlusal half was mainly affected. The majority of the samples had both demarcated and diffuse lesions and at least two thirds of the tooth surfaces were involved in most of them. Nine samples had type 1 (chalky/white opacity) lesions, seven of them showed PEB. However, four samples showed type 2 (yellow/brown opacity) lesions with two of them having PEB. Examples of the three types of MIH (type 1, type 2 and type 8) are shown in Figure 4.1

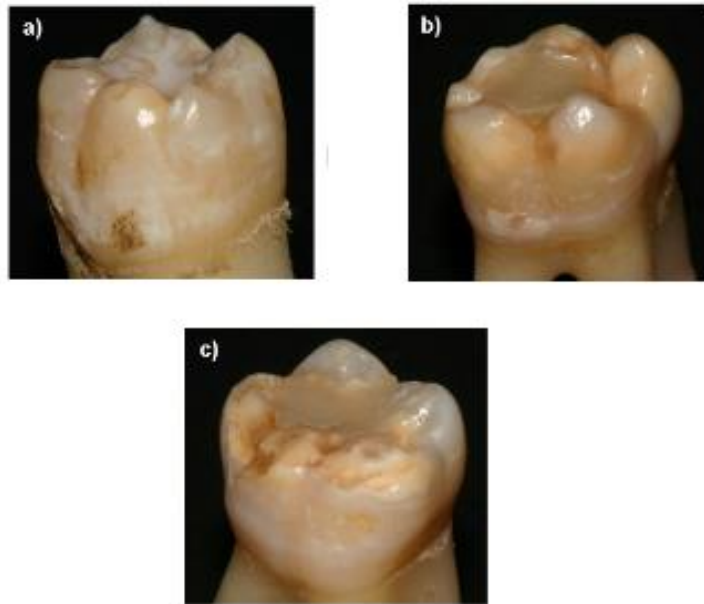


Figure 4.1 Shows three types of MIH defects; (a) is type 1 (chalky/white opacity) lesion, (b) is Type 2 (yellow/brown opacity) lesion; (c) is Type 1 lesion with Post eruptive breakdown (type 1 and 8).

Tooth Sample	Location (L)	Demarcation (D)	Extend of Defect (E)	Type of Defect (T)
MIH 32	L3	D3	E3	T2
MIH 33	L3	D3	E3	T1 and T8
MIH 34	L3	D3	E3	T2 and 8
MIH 35	L3	D3	E3	T1
MIH 36	L3	D2	E3	T1 and T8
MIH 37	L1	D1	E1	T2 and 8
MIH 38	L3	D3	E3	T1 and T8
MIH 39	L3	D3	E3	T1 and T8
MIH 49	L3	D3	E3	T1 and T8
MIH 50	L3	D3	E3	T1 and T8
MIH 51	L3	D2	E3	T1
MIH 52	L3	D3	E3	T2
MIH 67	L1	D2	E2	T1 and T8

Table 4.4 The mDDE index scores for MIH affected FPMs.

4.2 Radiographic Assessment

Radiographic assessment of teeth is an essential part of diagnosing dental diseases such as dental caries and periodontal disease. In MIH, radiographs are also used in investigating the extent of the lesions and the degree of tooth structure breakdown. This is especially important when planning the management of these teeth and possible extraction.

4.2.1 Method

Samples were radiographed after photographic images were taken. Radiographic images for control and MIH affected FPMs were taken at the same session using the same settings, such as exposure time, using intra-oral radiographic films. Radiographic films were developed after all images were taken. Each radiographic film was coded according to tooth code. Each tooth had two images taken. The first one was with the X-ray beam aimed in a bucco-lingual direction in an attempt to image the mesial and distal surfaces. The second view was taken with the X-ray beam aimed in a mesio-distal direction to image the buccal and lingual surfaces. These views are demonstrated in Figure 4.2 and Figure 4.3. The reason for taking two images was to correlate them with OCT images later.

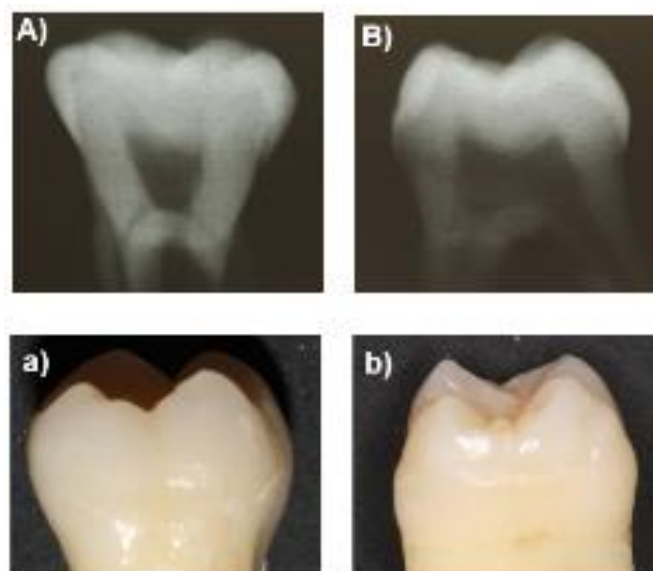


Figure 4.2 Radiographic images of a control tooth.

Image A is a mesio-distal view of the tooth shown in the clinical photograph (a) and image B is a bucco-lingual radiographic image of the same tooth which corresponds to the clinical photograph in (b).

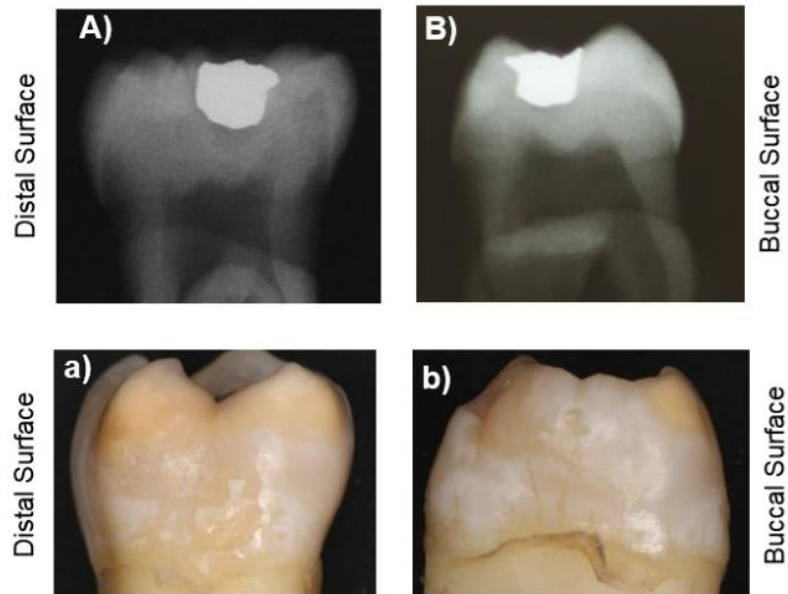


Figure 4.3 Radiographic images of a MIH tooth.

Image A is a mesio-distal view of the tooth shown in the clinical photograph (a) (distal surface is labelled) and image B is a bucco-lingual radiographic image of the same tooth which corresponds to the clinical photograph in (b) (buccal surface is labelled).

4.2.2 Results

From the radiographic images of control teeth, it can be seen that there is a clear contrast between enamel and dentine, with enamel being more radiopaque than dentine; and apparent continuity of the EDJ between them as shown in Figure 4.2. However, the degree of contrast is variable from one surface to another. The contrast in Figure 4.2B is better than in Figure 4.2A.

The radiographic features of MIH teeth relied on how severe the MIH lesion is, as well as its size and depth. If the lesion is mild as in type 1, it might not be visible and the radiographic features would resemble that of normal enamel as in the buccal surface shown in Figure 4.3 (images B and b). However, in the case of type 2 lesion as in the distal surface shown in Figure 4.3 (images A and a) the radiographic image does not show good contrast between enamel and dentine, and the lesions are not very clearly defined.

The most severe type of MIH lesion is the lesion that involves PEB. The tooth structure in this type is already compromised due to the loss of enamel structure. Radiographically, this results in radiolucency in the enamel and possibly dentine, as shown in Figure 4.4.

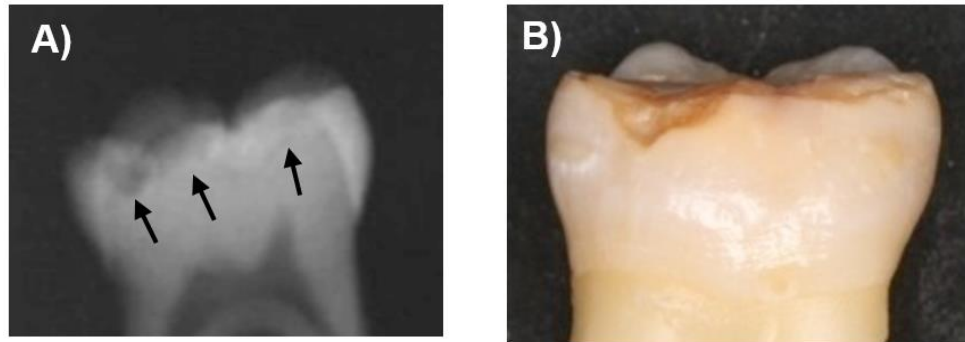


Figure 4.4 radiographic image of a MIH tooth with type 8 (with PEB) lesion

A, radiographic image of the MIH affected tooth shown in B; the arrows show the extent of the defect related to the PEB shown in B.

4.3 Discussion

4.3.1 Clinical Visual Assessment

Practitioners vary in their ability to diagnose MIH teeth in the dental chair. This is clearly evident from the wide range of prevalence in the condition worldwide. In this project, mDDE index was used which gave a comprehensive description about the extent and type of the enamel defect. The higher the score of each criteria of the index, the more severely affected the tooth. For example, a tooth which has scores L3, D3, E3 and T8 have the worst prognosis. Also, those teeth which have been given score T8, the enamel beneath the PEB is always of a yellow/brown discolouration type i.e. T2, as shown in Figure 4.1c.

The mDDE index is very useful way of diagnosing the severity of enamel defect in MIH affected FPMs. It has been established in research that the colour of the enamel defects can give an indication of the severity of the defect (Farah et al., 2010a). However, it is time consuming and the practitioner has to be calibrated to be able to use it. Globally, there is no consensus on the most efficient index to be used for characterising enamel defects in MIH. Even though mDDE index provided an important information about the severity of the defects, it does not give any information on the depth of the enamel affected unless there is a PEB indicating that the defect has extended deep into enamel exposing the underlying dentine.

4.3.2 Radiographic Assessment

Clinicians usually undertake radiographic assessment of oral and dental tissues to assess the degree and severity of a related condition. They always try to comply with the ALARA principle. This means that patient should be exposed to a minimal dose of X-ray radiation which produces a good quality image and minimises the chance for any further exposures. This is due to the ionising effect of the radiation on the patient. Beside this, radiographs usually give an underestimated picture about any given lesion. They are also 2D images of 3D objects such as teeth.

The radiographic images of control teeth can show clear contrast between enamel and dentine due to the different degree of X-ray absorption or scattering of both structures. This is because enamel is a well organised structure and highly mineralised compared to dentine. If the structure of enamel or dentine is altered, the degree of radiographic contrast between them is also affected.

As MIH is hypomineralisation of enamel, one expects this contrast to be altered and the enamel will be less radiopaque than in control sound enamel. However, from the radiographic images of MIH samples it can be seen that the degree of enamel opacity depended on the severity of MIH lesions. In MIH type 1 lesion, enamel structure appeared more or less like that of control enamel. In contrast, MIH types 2 and 8 enamel was less radiopaque or even radiolucent. The radiographic images are of low resolution and the details obtained from such images were scarce.

5 OCT as a diagnostic imaging tool

5.1 Optical Coherence Tomography scanner

The OCT scanner used in this project was a VivoSight™ OCT scanner which is a Multi-Beam Swept-source frequency Domain scanner, manufactured by Michelson Diagnostics, Kent, United Kingdom (Figure 5.1). It uses a class one laser which is a near-infra red (NIR) light with a wave length of 1305nm centrally with optical resolution (in tissue) of less than 7.5 μm laterally and less than 5 μm axially. The depth of focus is 1mm. The area to be scanned can be up to 6 mm x 6 mm (width x length) and an image depth of 1.2 mm - 2.0 mm depending on the tissue. It has a rate of scan of 10 kHz and frame rate can be up to 35 frames per second. The image can be presented as a vertical B scan, En-face image or 3D in TIFF (Tagged Image File Format) stack or DICOM (Digital Imaging and Communications in Medicine) formats. This scanner was originally intended to be used for dermatological purposes.

The components of the scanner is the Santec HSL-2000-12-MDL light source, Dell Precision T3600 processing system, monitor for image display and Spectrum M2i.4022 4-channel 20 MHz 1-bit data acquisition and a hand-held scanning probe. The hand-held scanning probe was mounted on an adjustable arm as shown in Figure 5.1. The vertical distance between the sample and the scanning probe was adjusted so that the optimum quality of the image is obtained.

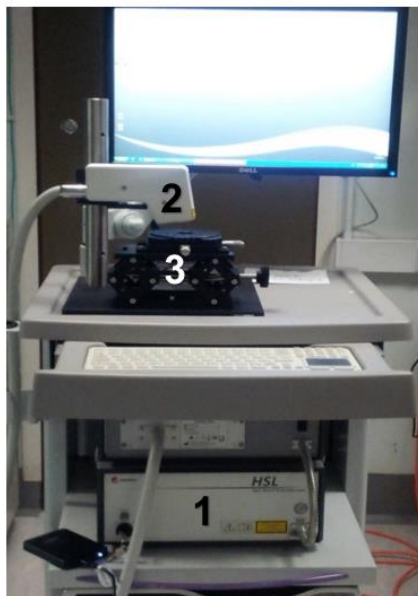


Figure 5.1 Shows the various parts of the OCT scanner.

1 Santec HSL-2000-12-MDL light source, 2 scanning probe, 3 mounting platform

5.2 Imaging teeth using OCT scanner

5.2.1 Method

OCT imaging was conducted in the Biomaterials, Biomimetic and Biophotonics Department at King's College London Dental Institute, King's College London.

Each sample was taken from the storage medium (0.1% thymol) and excess moisture was wiped off. Then it was mounted and stabilised on a glass slab using plasticin and placed on the mounting platform set below the mounted scanning probe as shown in Figure 5.2. The position of the sample was adjusted vertically and horizontally, using the adjustment screws attached to the mounting platform (Figure 5.2), in order to obtain a clearly focused image.

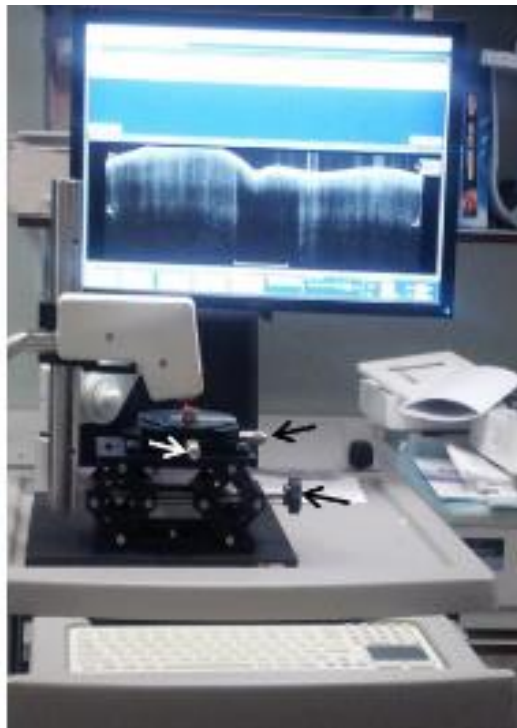


Figure 5.2 Shows a close view of OCT machine during the imaging procedure.

The sample is mounted on a glass slab and placed on the mounting platform below the scanning probe. The sample position can be adjusted using the screws indicated with the arrows.

The size of the imaged area, the number of frames taken and the distance between individual frames were the same when tooth surfaces were imaged for all samples. The maximum width of the OCT frame that can be scanned was 6mm, therefore this width was selected for all scans. These frames were possible to be collected along a maximum distance of 6mm in an occlusal direction (the distance between A and B in Figure 5.3). However, there were two methods of OCT imaging acquisition in the OCT scanner software. Free run acquisition where a single image could be captured at one time.

The second method was taking multiple frames of a particular area. Multiple frames can be captured using either the manufacturer's pre-set system or can be accustomed by the operator. The pre-set system can be either multi-one (captures 60 consecutive *b*-scan images with 100 μ m distance between them and a scanning widow of 6mm x 6mm) or multi-two (captures 500 consecutive *b*-scan images with 4 μ m distance between them and a scanning widow of 2mm x 2mm). In this study an accustomed set-up was used instead, in an attempt to collect the maximum information from the examined tooth surfaces.

The scan started at or close to the cemento-enamel junction (CEJ) cervically and ended at the cusps occlusally as shown in Figure 5.3. The order in which the surfaces of the teeth imaged was buccal, distal, lingual/palatal and mesial. The occlusal surface was not imaged due to its morphology. As the maximum depth of OCT imaging is between 1.2mm - 2mm, only the occlusal cusps would be imaged instead of the entire occlusal surface. Also, most of the MIH samples' occlusal surfaces were either broken down or heavily restored.

OCT images were viewed using imageJ software, which is a public domain, Java-based image processing program; developed at the National Institutes of Health (NIH) (Maryland, USA). It was designed with an open architecture that provides extensibility via Java plugins and recordable macros (image J information page on NIH web site). The latest version of imageJ (when the project was started) was used in the analysis which was imageJ 1.47 with 64 bit Java (2013).

There were two methods used to analyse the OCT images obtained. The first method was a qualitative analysis in which the enamel structure in MIH and control teeth was investigated. The second method was the investigation of the back scattered light signal intensity as it travels through the depth of enamel structure. Comparison of both methods was done for MIH and control enamel as well as for different types of MIH defects.

5.2.2 Results of OCT imaging

A total of nineteen teeth were scanned using OCT. Thirteen teeth were MIH affected FPMs and six were control. Consequently, the number of scanned surfaces was 52 MIH and 24 control surfaces giving a total of 76 tooth surfaces. The OCT scanning area on each surface was 6 mm x 6 mm (Figure 5.3) and the depth of scan was approximately 2 mm deep.

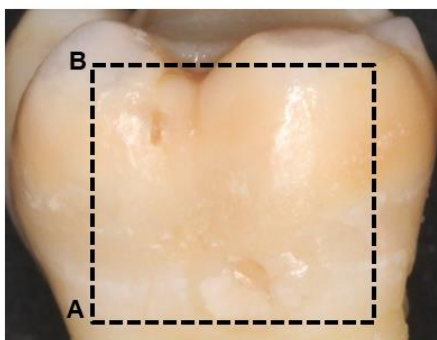


Figure 5.3 A demonstration of the scanned area of the tooth surface with 'A' being the start of the scan and 'B' is where it ends.

As discussed previously, the settings used for each scan acquisition were the same throughout the scanning procedure of all tooth surfaces. Beside the size of the imaged area mentioned for each tooth surface, the number of frames of images captured was 600 frames with a distance of 10 μ m (0.01 mm) between the frames. Each scanning frame measured 1482 pixels X 460 pixels corresponding to 6000 μ m (6 mm) X 1840 μ m (1.84 mm) with each 1 pixel corresponding to about 4 μ m. The images were exported from OCT software as 16 bit TIFF™ images.

5.2.2.1 Control Healthy enamel

An example of a control tooth surface scanned by OCT is shown in Figure 5.4. Both the clinical photograph and OCT image are demonstrated here. The position where the OCT frame or slice has been taken is indicated with a solid line across the clinical photographic image (labelled AB). From the clinical photograph, we can see that the surface is free of any defects.

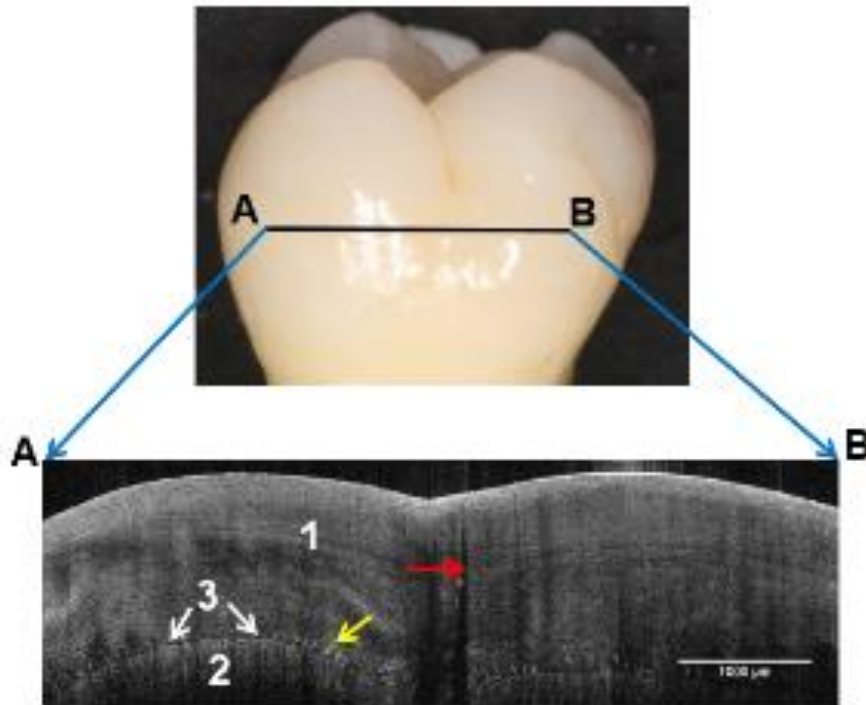


Figure 5.4 An OCT image of part of a palatal surface of a control FPM tooth.

The position at which the image was taken is marked on the tooth surface by the solid dark line (AB). It clearly shows Enamel structure (1), dentine (2), EDJ (3), and enamel crack (red arrow). Also, there are numerous small opaque structures (yellow arrow) which resemble enamel spindles in histological sections of enamel. The dimensions of the image are 1482 pixels X 460 pixels corresponding to 6000 μm X 1820 μm .

In the OCT image, enamel and dentine can be seen clearly. The enamel dentine junction is clearly visible between them and the structure of enamel shows a uniform scattering. The structure of dentine is distinct from enamel. There is also a small crack (red arrow in Figure 5.4) and interestingly the area below the crack is dark. There are numerous small opaque structures related to the EDJ, resembling enamel spindles in histological sections (Figure 5.5).

Another example of an OCT image of a control tooth is demonstrated in Figure 5.6. Unlike the OCT image of the previous example, just enamel is shown in this image. This is because of the enamel thickness in this area of the surface. From the clinical photograph, it can be seen that the OCT image is located just above the middle of the surface where it is bulbous and the enamel is thick. Another feature of this image is the presence of increased surface brightness related to the buccal side of the OCT image indicated by the white arrows and the areas underneath these regions look darker than the rest of the enamel structure. This is due to the increased scattering of the incident light.

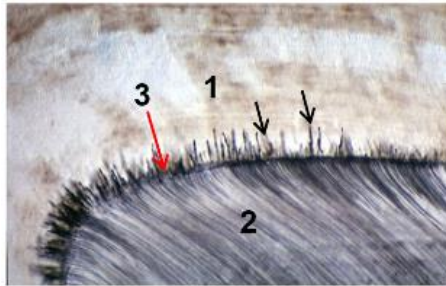


Figure 5.5 Histological section showing the enamel spindles (dark arrows) at the enamel-dentine junction (EDJ) (red arrow).

(1) Enamel, (2) dentine, (3), EDJ; enamel spindles are thought to be residual tubules formed when odontoblastic processes extend across the dentinoenamel junction during tooth formation. Taken from:

http://course.jnu.edu.cn/yxy/eruption/zuzhitupu/Cards/tth/09_bb.html

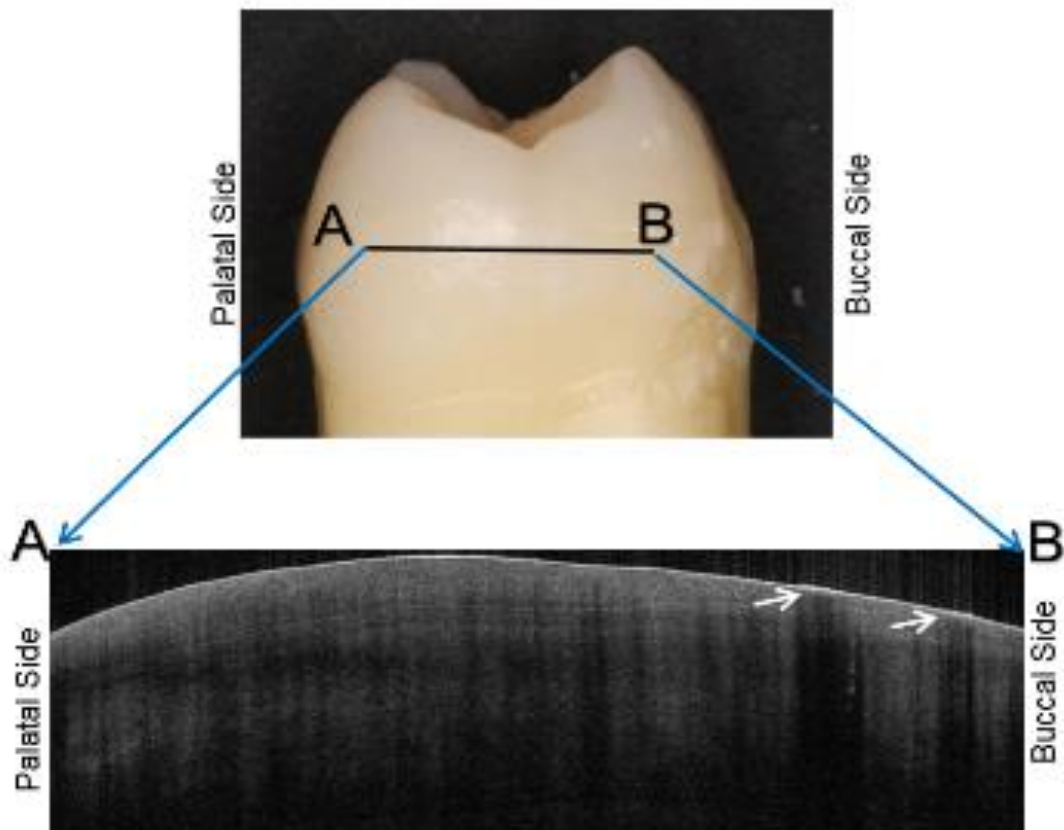


Figure 5.6 An OCT image of the distal surface of a control FPM

In this image only the structure of enamel is shown which looks homogenous except at the regions of the white arrows. The arrows indicate areas of increased surface brightness and the enamel beneath these areas is dark.

A third example of control enamel is shown in Figure 5.7. It has been taken from a mesial surface of a control tooth. From the clinical photograph, there is a cavitated carious lesion corresponding to the interproximal contact area. In this example, only enamel is shown in the OCT image. The enamel in the middle of the OCT scan is carious enamel where there is an increased brightness along the depth of enamel in comparison with the adjacent enamel. The enamel surface shows a sign of cavitation.

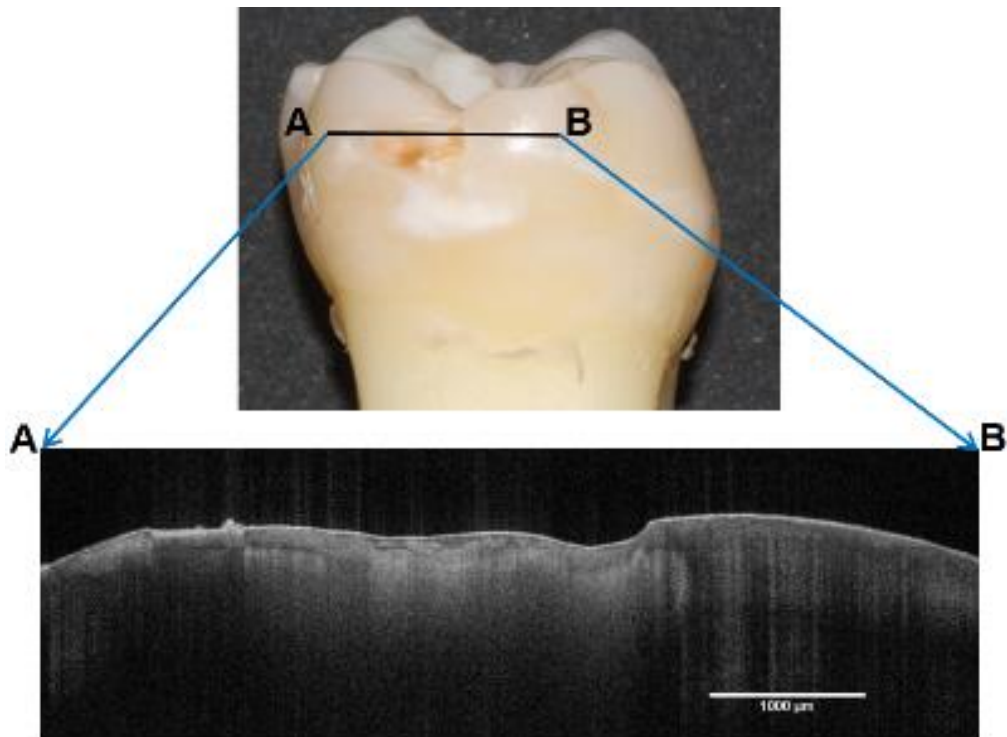


Figure 5.7 An OCT image of the mesial surface of a control FPM tooth with a cavitated carious lesion. Enamel structure shows brighter enamel region compared to the rest of the enamel.

5.2.2.2 MIH Affected Enamel

An OCT image of a MIH lesion is shown in Figure 5.8. Enamel, dentine and EDJ are shown clearly on the distal side of the OCT image as in control. The most prominent feature in this image is the subsurface crack which is about 3000 μ m (3mm) in length and extends close to the EDJ in depth. The tooth structure beneath the crack is dark and details of enamel, dentine and EDJ in the area are not clear. This crack is one of a

series of horizontal fracture lines visible on 200 consecutive frames of OCT images in this region, corresponding to 2000 μm (2mm). The number of enamel spindle-like structures which were related to the EDJ were fewer in this image unlike that for the control counterpart.

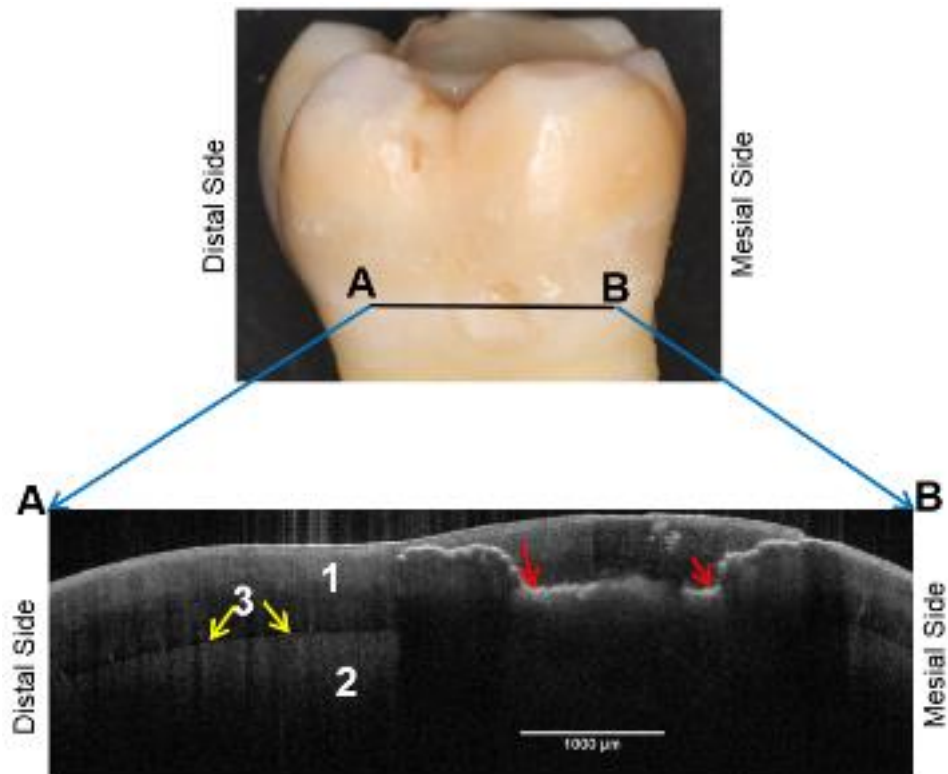


Figure 5.8 An OCT image of a buccal surface of a MIH affected FPM tooth.

It clearly shows Enamel structure (1), dentine (2), EDJ (3), and an enamel fracture line (red arrows). The fracture line is running across the enamel measuring nearly 3000 μm (3mm) extending down close to the EDJ.

A second example of MIH image is demonstrated in Figure 5.9. Only enamel is shown in this image, as at this level of the crown the enamel is thick. In contrast to the clinical photograph which shows mild MIH defect of enamel (in the region of the frame), the OCT image shows a huge defect in enamel extending the full width of the image. This may be a sign of enamel delamination which may progress to PEB which is already present at the buccal cusp.

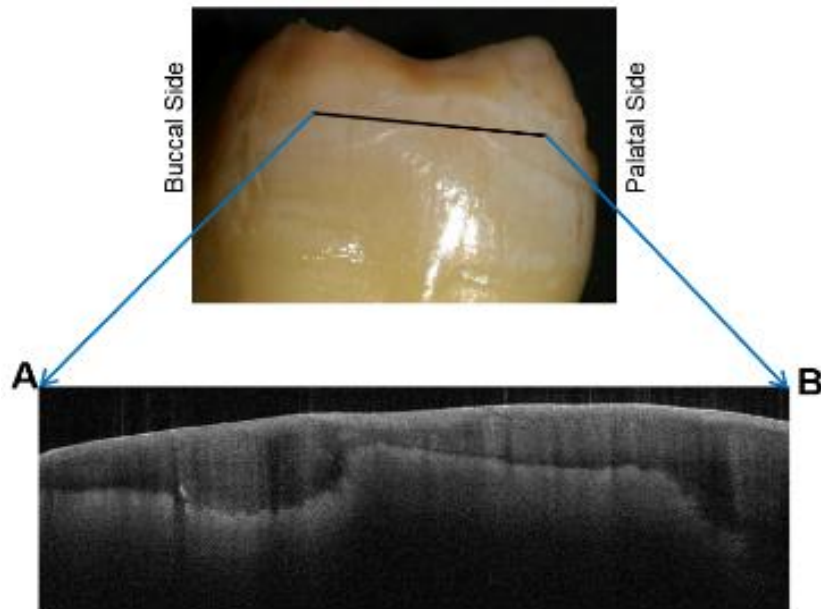


Figure 5.9 OCT image of a distal surface of a MIH affected tooth.

The clinical photograph shows an intact surface where the scan has been taken. However, the OCT image shows a huge defect extending the full width of the distal surface in that scanned area.

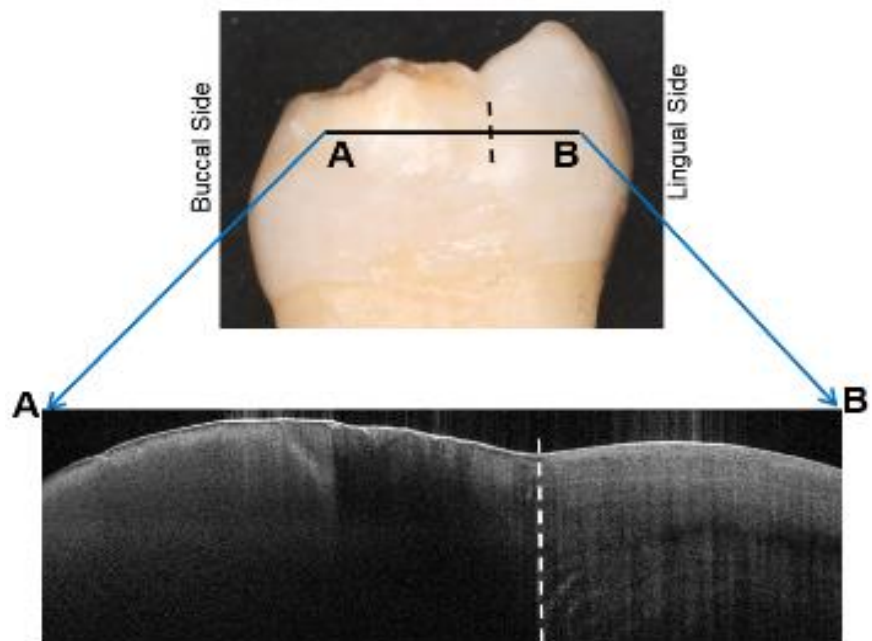


Figure 5.10 OCT of a mesial surface of a MIH of a FPM

The clinical photograph shows a demarcated MIH lesion related to the buccal cusp which shows PEB. The OCT image shows normal enamel structure related to the lingual side of the image. However, the buccal side shows clearly abnormal enamel structure correlating to the demarcated MIH lesion in the clinical photograph. This side has bright and dark regions.

A third example is shown (Figure 5.10) which shows an OCT image of a demarcated lesion related to a PEB of a mesio-buccal cusp on the mesial surface of MIH affected FPM. The lingual side of the OCT image looks like a normal control enamel unlike the buccal side which has different scattering pattern. The boundary between the normal and abnormal enamel is indicated by the broken line on the photographic and OCT images. There are two regions of the MIH lesion one is bright and the other is dark which interacted with light differently. In the dark region, the surface area of the enamel seems to be broken compared to the other areas of the enamel surface. However, in the bright area there was a thin dark layer immediately beneath the surface and the appearance of the rest of the enamel seems distinct when compared to the normal enamel on the lingual side.

5.2.3 En-face Reconstruction of the OCT images

Full stacks of B-scans were computed using image J to create an en-face reconstruction. This was done to evaluate the extent of the MIH lesion at a given depth in the tooth. Frames in this reconstruction are not vertical B-scans anymore, but horizontal planes made by stacked rows of pixels. Each pixel in every row is taken from the same z-axis depth of the original B-scans. The stack is moving vertically in the construction in the z-plane. To keep the original scanning area, corrective factors for the aspect ratio of individual frame was needed and the resultant image needed to be re-scaled. Therefore the following formulae were used (taken from Michelson Diagnostics VivoSight scanner manual, Appendix 7):

$$X_scale = \frac{y}{x} \times \text{factor}$$

$$Y_scale = \text{factor}$$

$$Z_scale = 1$$

Where: x is the number of pixels in the x-direction (shown in image J software)

y is the number of pixels in the y direction (shown in image J software)

The factor is added to enlarge the image, usually 2, but depends on the number of slices in the image

En-face reconstruction was performed on a full scan of 600 frames taken for MIH affected enamel shown in Figure 5.9 to evaluate the extent of the subsurface lesion.

The b-scan image shown in Figure 5.11 (a) was taken from the B-scan OCT stack which shows the MIH defect. However, Figure 5.11b and c are reconstructed frames and the dot-dash-dot lines in Figure 5.11 (a) indicate the corresponding depth of both reconstructed frames. Figure 5.11 (b) shows that the surface of the imaged enamel is not flat. The bright area represents enamel and the dark area is air. In the deeper en-face plane (Figure 5.11(c)), the lesion becomes apparent (star symbol in Figure 5.11(c)). A significant crack is visible in all the frames: B-scan and the 2 reconstructed frames as indicated by the solid white arrows which was used as a reference in this case to confirm correlation between the two types of images presented

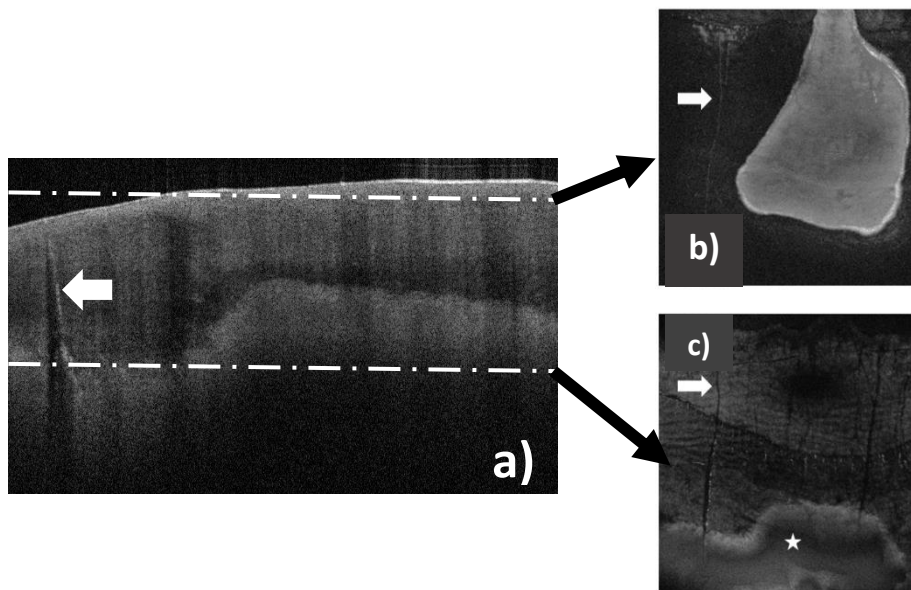


Figure 5.11 OCT image stack was reconstructed into an en-face vertical stack of frames; a) a vertical B-scan of MIH affected enamel, the dot-dash-dot lines indicate the depth at which the horizontal en-face planes shown in (b) and (c) were taken, the solid white arrow indicates a crack in enamel; b) an enface horizontal plane showing the increased back scattering of light (bright area) indicative of enamel compared to the dark area (air); c) a lower horizontal plane of the enface reconstruction showing the MIH lesion (star), the crack line in (a) is indicated by solid white arrows in (b) and (c).

5.3 Advanced Diagnostics Using OCT Signal Intensity Profiles

5.3.1 Method

Scattering profiles as a function of the enamel depth were measured on selected B-scans of both control and MIH teeth. An attempt was made to avoid enamel structure

with any sign of fracture or broken down surface as they affect the scattering property of the enamel. Regions with increased surface reflectivity were also avoided. The width of the selected regions was taken as the width of ten pixels in X-axis which corresponded to 40.5 μ m.

The OCT images were exported from OCT software and were managed using image J software. A signal intensity profile (*a*-scan signal) was obtained using this software. The distance measurement was changed to micrometres (μ m). It is known that the width of the OCT image measures 6,000 μ m which corresponds to 1,482 pixels (shown in image J) and as a result one pixel is equivalent to about 4.05 μ m (This was confirmed with Michelson Diagnostics, UK). Therefore, a rectangular region of interest was selected with a 40.5 μ m width. Additionally, scattering profiles were extracted from single frames and plotted as a function of the sample's depth using Origin Pro 9.0™ (OriginLab Corporation, Northampton, MA 01060, USA).

5.3.2 Application of signal intensity profile

The healthy and MIH enamels were investigated by this method. In both types of enamel the signal intensity profiles showed sharp increase (spike-like) in the intensity profile as the light hits the tooth surface. These profiles provide a direct representation of the scattering of light photons as they travel through the enamel layer and any disruption in the enamel structure resulted in altered scattering which could be measured in the profile.

5.3.2.1 Signal Intensity Profile of Healthy Enamel

An example of healthy enamel's signal intensity profile is shown in figure 5.12. The selected region is highlighted in yellow on the *b*-scan OCT frame (figure 5.12 b and c). It can be seen from the *b*-scan image that the enamel structure is uniformly scattering. The signal intensity profile in 5.12d shows initially a non-scattering phase where light travels in air. However, at the air/surface interface a sharp scattering peak is observed as photons encounter a medium with a greater refractive index i.e. enamel ($n\sim 1.63$) compared to air ($n=1$).

Following the strong air/surface scattering peak, the profile presents an exponential decay profile as photons travel through the enamel. From this intensity profile it can be

seen that the total distance travelled by photons in enamel and dentine was about 1800 μm . The blue arrows in figure 5.12b, c and d indicate the position of the EDJ. In figure 5.12d, there is a slight increase in back scattered light intensity as light photons hit the EDJ.

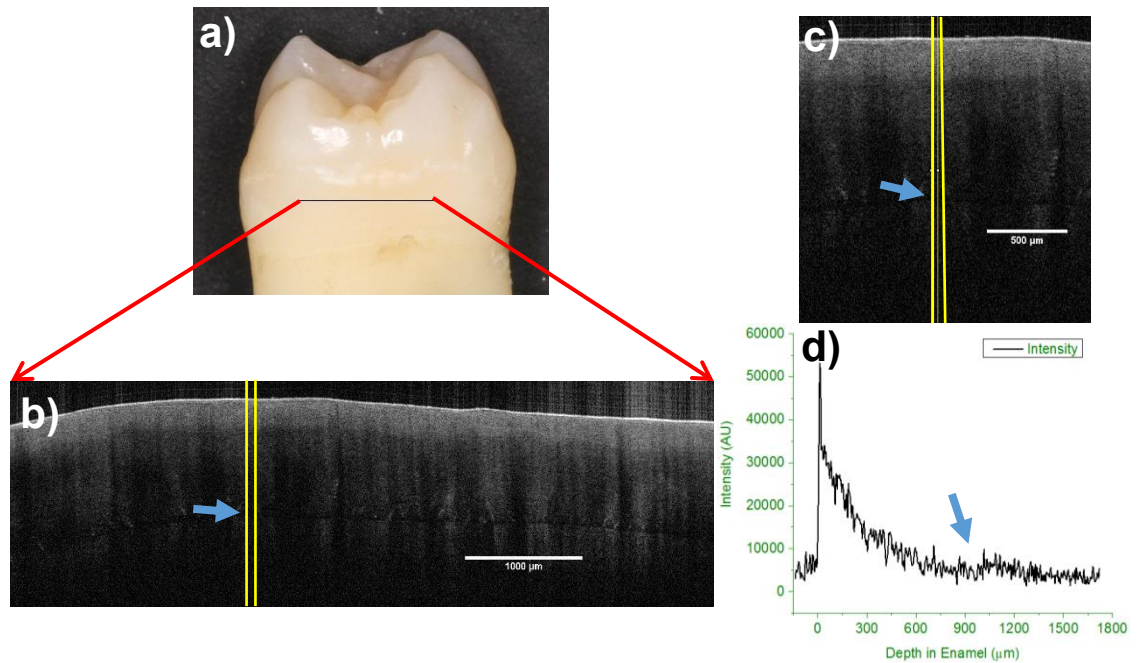


Figure 5.12 Signal intensity profile of a control healthy enamel.

a) mesial surface of a control FPM; b) OCT *b*-scan image taken from the same surface, the selected region is highlighted with yellow vertical lines; c) a magnification of the selected region; d) the signal intensity profile of the selected region in b and c (AU arbitrary unit); the blue arrows in b, c and d indicate the position of the EDJ.

5.13a shows scattering intensity profile plot taken from different regions on a single OCT image of control healthy enamel. It can be seen that the decay of the scattering profiles in healthy enamel (figure 5.13b) may present some small variations which are due to localised interruptions in the enamel structural and chemical homogeneity. It is also necessary to consider that the non-scattering phase prior to the enamel-air scattering peak will vary from one profile to another as one needs to take into account the curvature of the enamel surface whilst recording the profiles (as shown by the gray arrow in figure 5.13b).

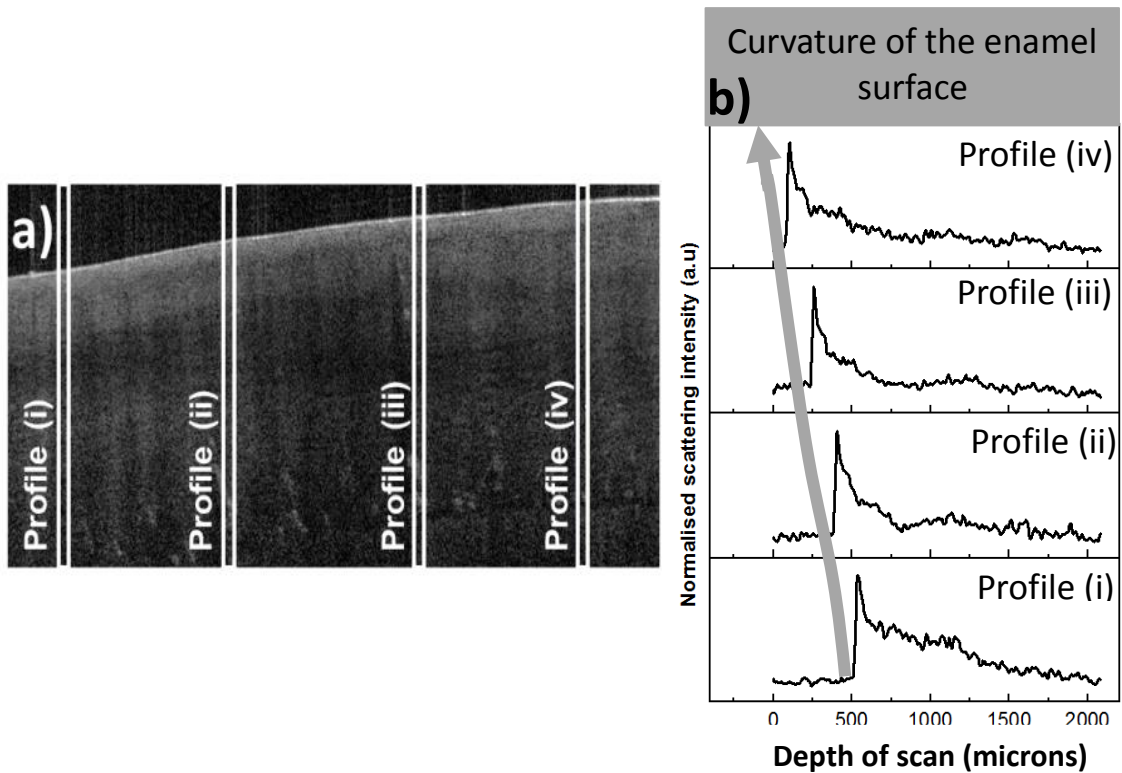


Figure 5.13 Back scattered light intensity profiles extracted from four different selected regions in an OCT image of a healthy control enamel; (a) 10 pixels wide selected regions (i-iv); (b) the intensity profile plots in function of depth of scan, the gray arrow following the intensity peaks on the profiles follow the enamel surface curvature which is apparent on the OCT image.

5.3.2.2 Signal Intensity Profile of MIH Affected Enamel

The same approach was performed on a b-scan image obtained from MIH affected tooth as presented in figure 5.14. A similar enamel-air scattering peak was obtained as for the control healthy enamel. However, as the overall shape of the profile dramatically changed whilst penetrating deeper in the enamel layer. The photons were scattered at a higher level for a considerable amount of depth after which there was an exponential decay of the scattering intensity of light.

Several profiles were recorded at different locations within the B-scan as shown in figure 5.15(a) and b. The overall shape of the profiles has changed whilst penetrating deeper into enamel layer. In the profiles presented in Figure 5.15 (b), one or more strong scattering peaks can be observed at various distance from the enamel-air interface.

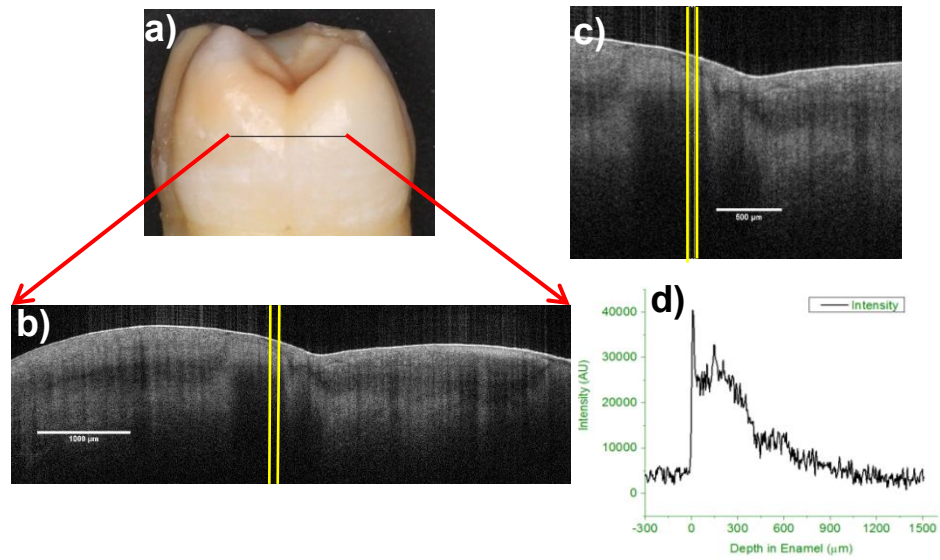


Figure 5.14 Signal intensity profile of a MIH enamel.

a) Distal surface of a MIH affected FPM; b) OCT *b*-scan image taken from a scan of the same surface, the selected region is highlighted with yellow vertical lines; c) a magnification of the selected area; d) the signal intensity profile of the selected region in b and c (AU arbitrary unit).

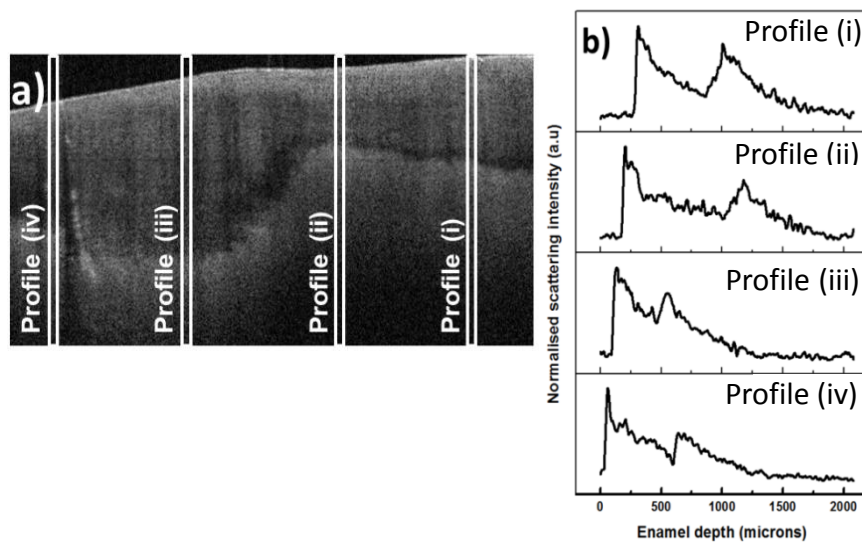


Figure 5.15 Back scattered light intensity profiles extracted from four different selected regions in an OCT image of a MIH affected enamel; (a) 10 pixels wide selected regions (i-iv); (b) the intensity profile plots in function of depth of scan, all intensity profiles show one or more strong scattering peaks in depth of enamel.

5.4 Comparison between Conventional Clinical Methods and OCT

The use of the clinical and radiographic methods in diagnosing MIH was discussed in chapter 4. When mDDE index was used in characterising the MIH defects in enamel, these defects were creamy/white (type1/T1), yellow/brown (type2/T2) or defects with a PEB (type8/T8). However, many MIH affected FPMs had combinations of these types of defects.

Although the index was applied in chapter 4 at the tooth level, in this chapter it will be applied to the tooth surfaces instead to facilitate the comparison between the use of the index and radiographic images with the use of OCT. This comparison will focus more on the type of the defect present on each surface and the demarcation type. For example, type 1 MIH would be investigated in the two situations of diffuse and demarcated.

Table 5.1 The types of MIH defects present in MIH affected FPMs

(T1 or type1: creamy/white defect; T2 or type2: yellow/brown; T8 or type8: defects with a PEB; 0 is a surface with a normal appearance)

Tooth Sample	Buccal	Distal	Lingual / Palatal	Mesial
MIH 32	T1 & T2	T1 & T2	T1	T1 & T2
MIH 33	T1 & T8	T2	T1 & T8	0
MIH 34	T1, T2 & T8	T1, T2 & T8	T1 & T2	T2 & T8
MIH 35	T1 & T2	T1 & T2	T1 & T2	T1
MIH 36	T2 & T8	T1 & T2	T1 & T2	T1 & T2
MIH 37	T1, T2 & T8	T2	T1 & T2	T2 & T8
MIH 38	T8	T2 & T8	T1	T2 & T8
MIH 39	T8	T2	T1 & T2	T2
MIH 49	T1, T2 & T8	T1 & T8	T1 & T2	T1 & T2
MIH 50	T1, T2 & T8	T1, T2 & T8	T1 & T2	T1
MIH 51	T1 & T2	T1	T1	T1
MIH 52	T1 & T2	T1	T1	T1 & T2
MIH 67	T1	T1	T1	T1

Table 5.1 shows the types of defects present in each surface of the MIH affected FPMs. One surface was apparently normal (mesial surface of MIH 33). Buccal surfaces of MIH 38 and 39 had T8 defects only. The rest of the surfaces have combinations of types as already mentioned. In each type of the defects, clinical picture along with the radiographic image and the corresponding OCT image will be looked at in detail as well as the back scattered intensity profiles of each. Type 1 defect will be investigated first then Type 2 and finally Type 8.

5.4.1 Type 1 (white/creamy) MIH defect

5.4.1.1 Diffuse Type 1 Defect

The white creamy MIH defect present on the palatal surface of MIH 35 shown in Figure 5.16 can be characterised according to mDDE index to be located on the whole surface of the tooth (L3), diffuse (D2) and extending at least two thirds of the surface (E3). Cervically, there seems to be some sort of a breakdown in the enamel which could possibly be caused by an extraction forceps when the tooth was extracted. The radiographic image in Figure 5.17 shows the palatal surface of the same tooth (labelled). The radiographic appearance of the enamel is different from the normal enamel in that it seems less radiopaque. However, the radiographic image does not give accurate information on the location of this radiolucency on the palatal surface.

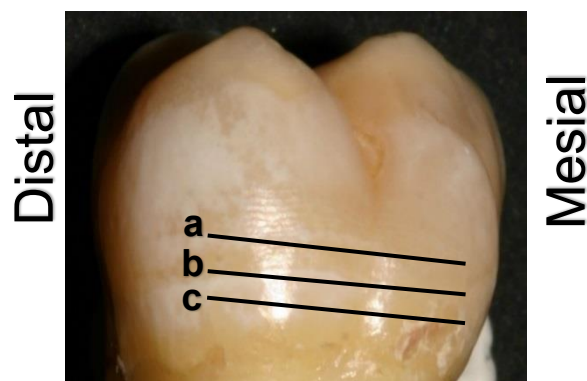


Figure 5.16 Palatal surface of MIH 35 with type 1 (T1) MIH defect; a, b and c are the positions of the frames shown in figure 5.18

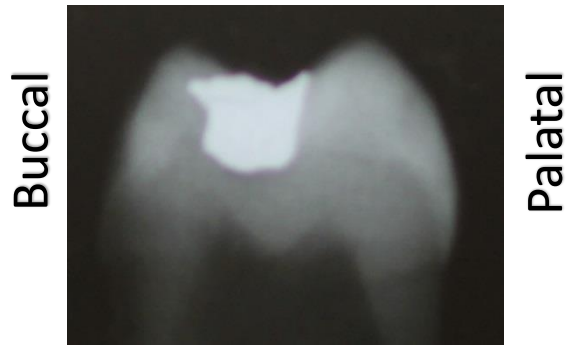


Figure 5.17 radiographic image of MIH 35 showing the buccal and palatal surfaces of the tooth

Three representative OCT frames or b-scans were chosen to demonstrate the appearance of this type of MIH defect (diffuse type 1 defect) (Figure 5.18). The position from which these OCT frames were taken is shown by dark lines in Figure 5.16. From these OCT frames it can be seen that the defect is mainly affecting the distal half of the tooth surface while part of the mesial half is spared especially in figures 5.18a and 5.18b. In figure 5.18c the enamel is broken in the mesial side of the OCT frame which corresponds to the clinical picture in Figure 5.16.

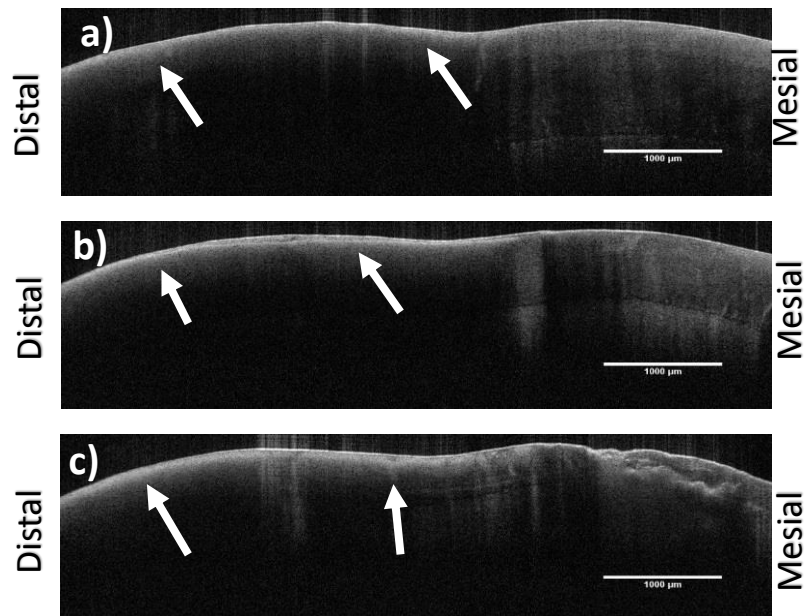


Figure 5.18 OCT frames corresponding to the lines drawn on the clinical photograph of MIH 35 shown in figure 5.16

The higher intensity of scattered light photons is confined to the enamel close to the surface on the distal side of the OCT frames corresponding to the creamy/white MIH defect present clinically.

The appearance of the white creamy type 1 defect is distinctive in these OCT frames in that there is an increased scattering of light photons just below the enamel surface as shown by the solid white arrows in the three b-scan images. Due to the high level of scattering present in these regions, there is a huge amount of shadowing occurring below which makes it difficult to evaluate the interaction of light with enamel layer below this high scattering region.

Scattering intensity profile plots were taken from four different areas on the *b*-scan OCT image demonstrated in Figure 5.18b and presented in Figure 5.19. These profile plots confirm that the light is mainly scattered just below the surface enamel. It can be seen that there are at least two peaks of back scattered light (profiles i-iii in figure 5.19b) as well as the fast decay of the scattered intensity caused by the shadowing effect found in the *b*-scan images.

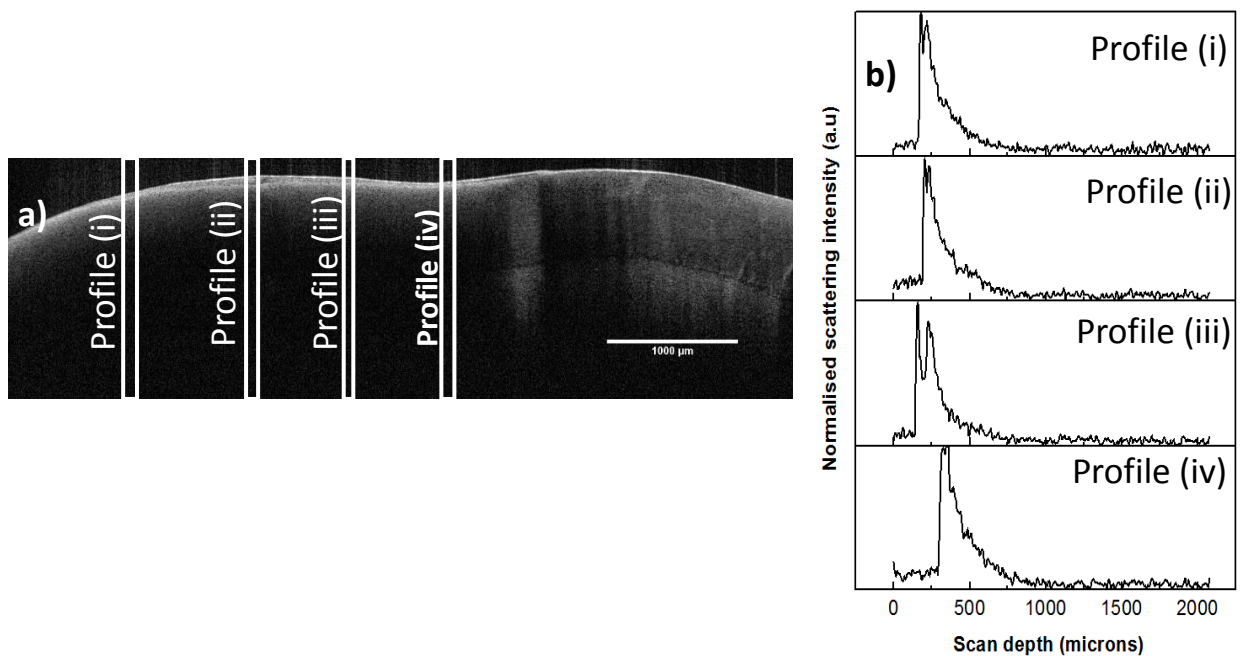


Figure 5.19 Scattering intensity profiles taken from OCT image presented in figure 18b; a) the selected regions (i-iv) where the profile plots were taken; b) profile plots of the selected areas (i-iv), it can be clearly seen that that the light highly scattered at the surface with a very rapid signal decay going into the depth of enamel.

5.4.1.2 Demarcated Type 1 Defect

An example of demarcated type 1 defect is found in the buccal surface of MIH 32 shown in Figure 5.20. It can be characterised using mDDE index as involving the whole surface of the tooth (L3) and extends to more than two thirds of the surface (E3).

However, it has two types of defects, type 1 white creamy defect (labelled (1) in figure 5.20A) which is demarcated (D1) and type 2 yellow brown defect (labelled 2 in figure 5.20A) which is diffuse (D2). In this section, the demarcated type 1 defect will be considered in detail. The description of this defect using mDDE index does not give us enough information on the extent of the lesion deep into enamel. It superficially describes the defect extent across the surface.

The radiographic image of the tooth in Figure 5.21 shows the buccal surface (labelled). This image does not give a lot of information about the defect. It gives two dimensional view of the defect.

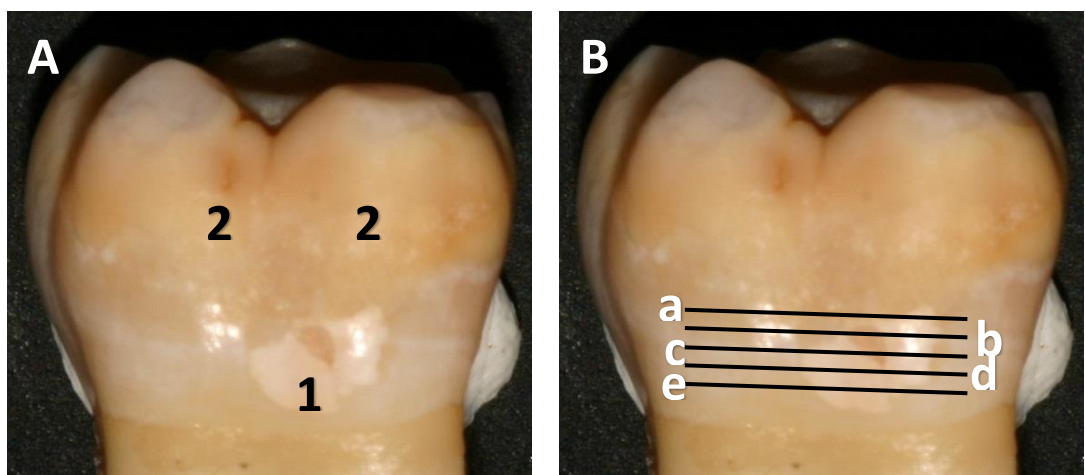


Figure 5.20 (A) Buccal surface of MIH 32 showing a demarcated type 1 MIH defect (1) and a diffuse type 2 defect (2); (B) the position of the OCT frames shown in figure 5.22

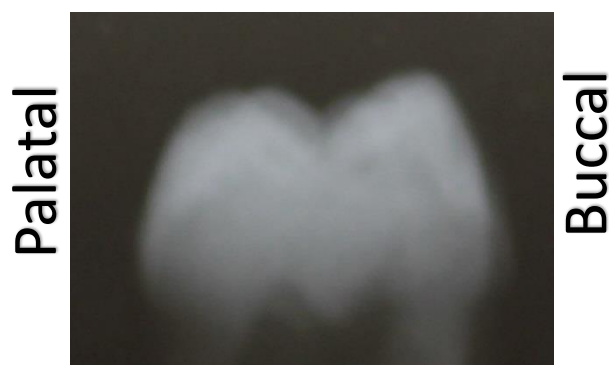


Figure 5.21 radiographic image of MIH 32 showing the buccal and palatal surfaces of the tooth.

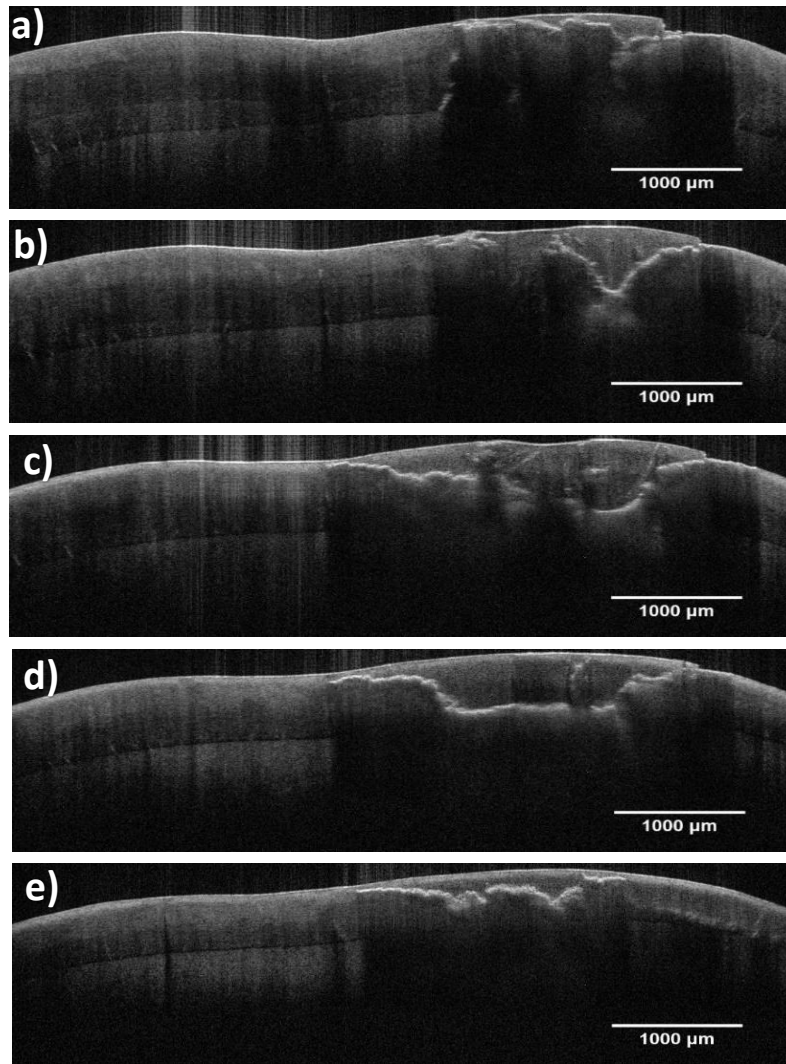


Figure 5.22 OCT frames corresponding to the lines illustrated on the clinical photograph of the buccal surface of MIH 32 in figure 6.4(B)

The demarcated type1 MIH defect demonstrated subsurface breakdown with horizontal fracture lines extending through the width of the defect. The image suggests that the enamel overlying the fracture lines is soon to be lost causing PEB (as in ‘a’ above) .

Figure 5.22 shows the OCT frames demonstrated on the clinical photograph shown in figure 5.20. These frames sweep across 6mm (6000µm) of the buccal surface crossing the demarcated type 1 defect. Each OCT frame in Figure 5.22 shows a 2D view of the defect. Figures 5.22a and 5.22e are located at the occlusal and cervical ends of the defect, respectively. In these frames the defect, represented by horizontal fracture lines in enamel, is shallow measuring approximately 400 µm in depth and is 2100 µm long. When the scanned images close to the centre of the lesion are viewed i.e. figures 5.22b, 5.22c and 5.22d, the depth of the lesion reaches to a maximum dimensions in

the OCT image shown in figure 5.22c. Its depth is 750 μm in enamel and has a maximum length of 3300 μm . The defect was scanned over 200 OCT frames, corresponding to a distance of 2000 μm . As a result the extent of the lesion can be evaluated in three dimensional as illustrated here. The length of the lesion (in the X-dimension), its depth (in the Z- dimension) and its extent across the surface or the number of frames (the Y- dimension) all can be measured using image J software.

The appearance of the fracture lines across this type of lesion gives a prognostic impression that this tooth might lose the enamel structure above the fracture over time and consequently lead to future post-eruptive break down (surface PEB already started as visible in figure 5.22a). The intensity of the back scattered light from this enamel defect is illustrated in Figure 5.23. It can be seen that the inhomogeneity in the enamel overlying the fracture lines as well as the fracture lines (demonstrated in figure 5.23a) are the causes of the increased light scattering. There are significant scattering peaks observed, some of them are as high as the air/surface peaks as seen in figures 5.23b (profiles i and iv). Another thing to note is that light scattering extends deeper into enamel when compared to that in the diffuse type 1 defect.

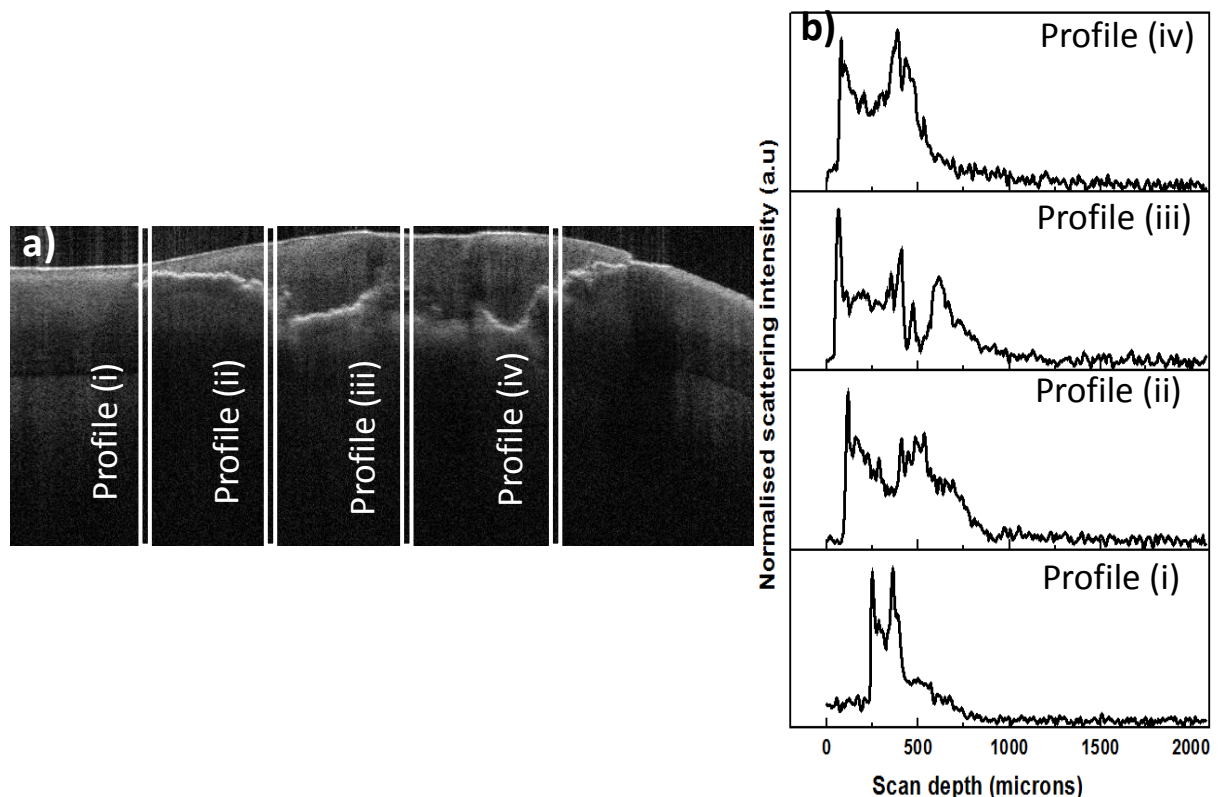


Figure 5.23 Scattering intensity profiles of demarcated type 1 MIH defect; a) the regions from which the profiles (i-iv) were taken; the amount of scattering of photon increased with depth of the lesion into enamel, also due to the nature of the defect the pattern of the light scattering is different from that of the diffuse type one in that it occurs along a deeper enamel layer and to a variable degree.

5.4.2 Type 2 (yellow/brown) MIH defect

5.4.2.1 Diffuse Type 2 Defect

This defect type can be seen on the buccal surface of MIH 32 shown in Figure 5.20 and 5.24. This surface has two distinct defects. The yellow brown defect (marked 2 in figure 5.20A and 5.24A) involved the occlusal half of the surface (L1), diffuse (D2) and it extends up to two thirds of the surface (E2). The radiographic appearance is as described in the above section and shown in figure 5.21. Figure 5.24B shows the position of the OCT frames on the buccal surface.

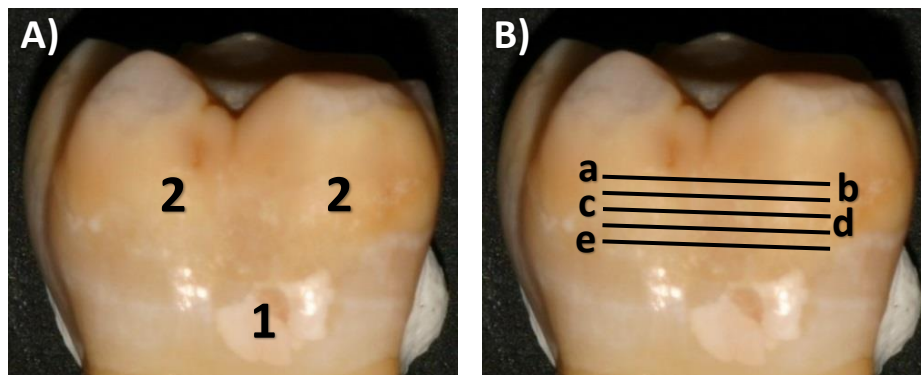


Figure 5.24 (A) The buccal surface of MIH 32 showing two types of defects MIH type 1 (marked 1) and MIH type 2 (marked 2); (B) shows the positions where the OCT frames shown in figure 6.9 were taken from.

The OCT frames shown in figure 5.25 show the appearance of the diffuse type 2 defect present on the surface. The white arrows in figures 5.25a, 5.25b and 5.25c indicate the defect extension into enamel. The image contrast at the surface appears gradually brighter than the surrounding enamel (as indicated by the blue solid arrows in figures 5.25b-e). The area below this bright band of subsurface enamel has significant shadowing, rendering the enamel below dark, with difficulty in assessing the quality of the enamel structure.

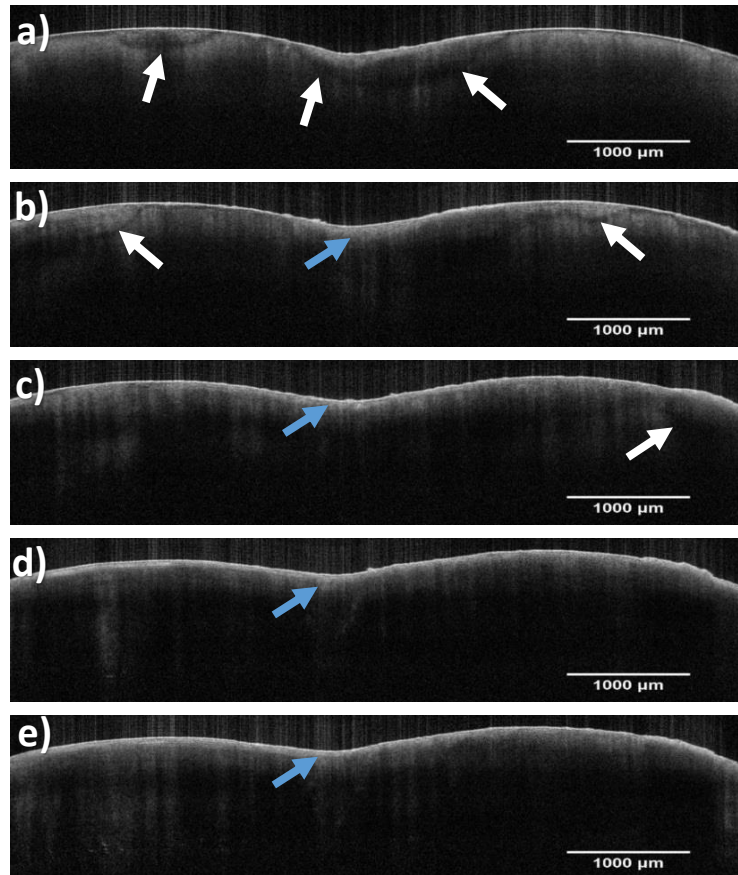


Figure 5.25 OCT frames corresponding to the lines drawn in figure 5.24B; white arrows demonstrate the defect at the region close to the cuspal area; blue arrows indicate a bright band close to the surface which is distinctive to the surrounding enamel and there is a significant shadowing underneath this bright band.

Selected areas on the b-scan demonstrated in figure 5.25a were chosen and the back scattered light intensity profiles were plotted against the depth of scan. The intensity profile plots confirm the increased scattering of light confined to the enamel close to the surface. However, the amount of light scattering and the depth to which the scattering occurred varied from one region to another. For example, in profiles (i, ii and iii) there was one sharp and narrow peak which corresponded to air/surface interface and a second blunt and broad peak corresponding to the scattered light photons caused by the MIH affected enamel structure. However, in profile (iii) the initial air/surface peak is continuous with the subsurface scattering of light. The four types of profile plots can give the clinician an idea about the position of enamel disruption and its extent.

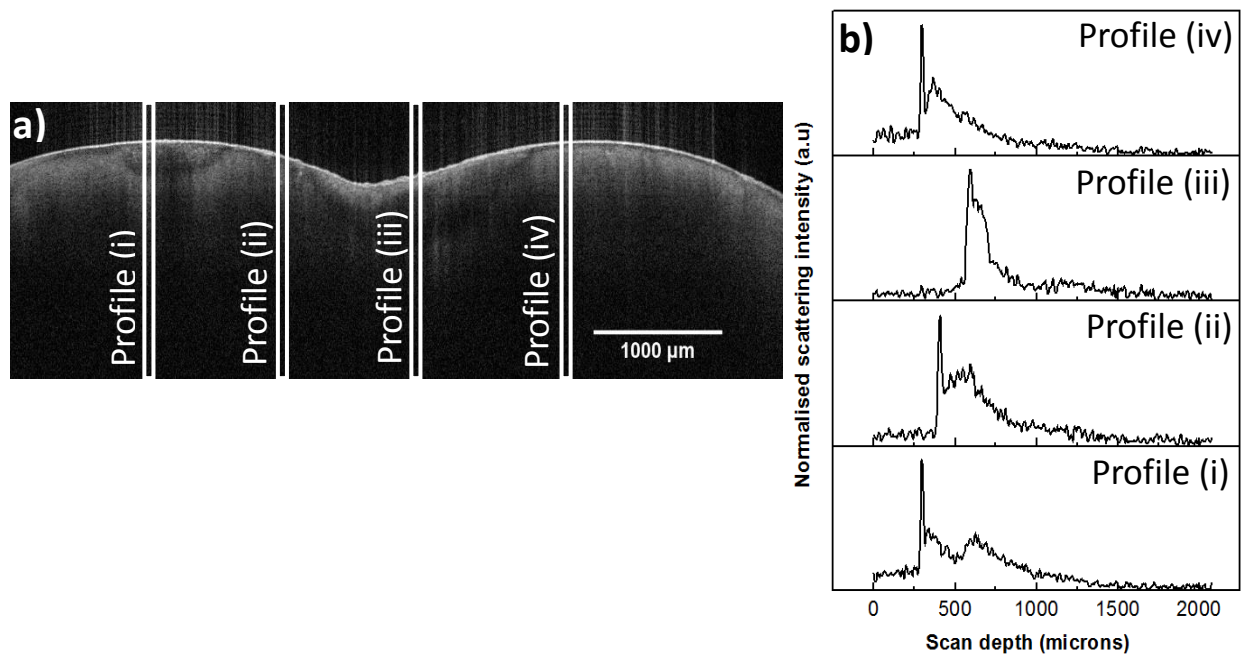


Figure 5.26 Shows intensity profiles extracted from a b-scan image shown in figure 5.25a; a) the areas from where the profiles have been taken; b) the intensity profiles showing increased scattering of light at higher level than in healthy enamel.

5.4.2.2 Demarcated Type 2 Defect

This type of defect is shown in figure 5.27 (black arrows). The distal surface of MIH 37 is shown in this figure. According to mDDE index, the defect is localised to the occlusal half of the surface (L1), demarcated (D1), and extends to about a third of the surface (E1). This defect consists of two demarcated defects very close to each other. The radiographic image of this surface is shown in figure 5.28. The image does not show the defect clearly.

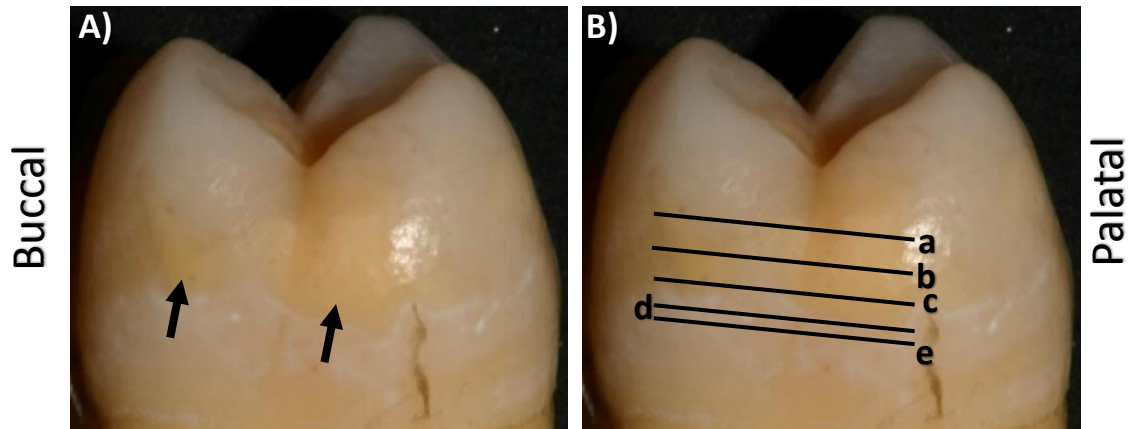


Figure 5.27 Distal Surface of MIH 37 with type 2 MIH defect. The lines 'a' to 'e' indicate the regions from which OCT frames shown in figure 6.12 have been taken.

There are two demarcated defects present, one on the buccal part of the surface and the other extends to the palatal part.



Figure 5.28 The radiographic image of MIH 37 showing the mesial and distal surfaces of the tooth; the image does not demonstrate clearly the presence of the defect on the surface.

The OCT frames showing these demarcated defects are demonstrated in figure 5.29. It can be seen that the defects are progressing as the OCT scan move occlusally (moving from figure 5.29e to figure 5.29a). The palatal defect (white arrows) is visible in all the *b*-scan images; initiating close to the EDJ and progresses to the surface of the enamel. Then as it spreads across the palatal side of the distal surface, it exhibits featureless appearance with loss of normal scattering of light that would be expected in normal enamel (which can be seen close to the defect on the buccal side of the distal surface in figure 5.29a and on the buccal sides of figure 5.29d and e).

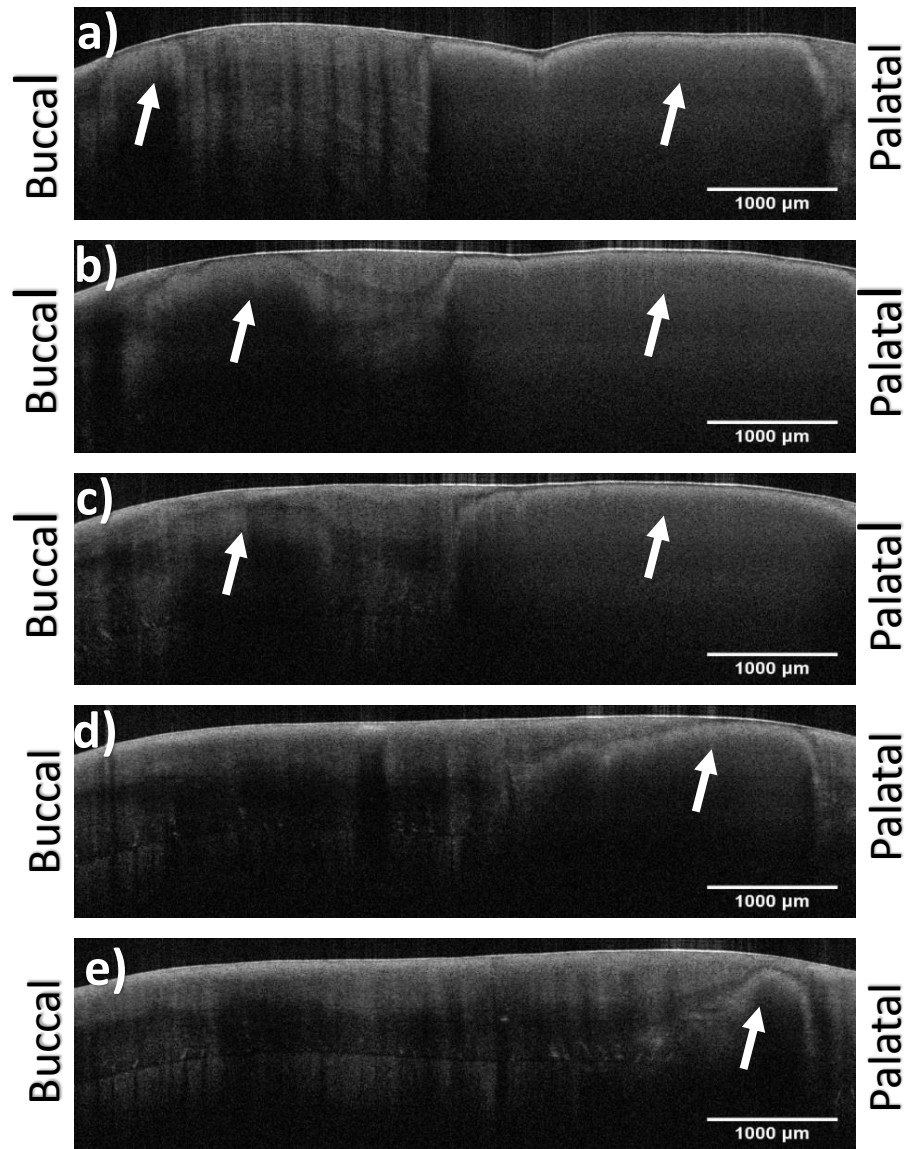


Figure 5.29 OCT frames corresponding to the lines drawn on the clinical photograph of the distal surface of MIH 37 shown in figure 5.27; the white arrows indicate the location of the defects.

The progression of the defect can be clearly demonstrated as the order of the frames moves occlusally (from e to a). The palatal defect has a featureless appearance as it progresses occlusally.

Another feature of the appearance of this type of defect is that there is a very thin dark line immediately beneath the enamel surface (figures 5.29a-c) which seems to have formed as a result of the progression and coalescence of the defect onto the surface (can be visualised as the frames move from figure 5.29e to c). The defect on the buccal side of the surface (arrows) extends to fewer numbers of frames (figures 5.29a-c) and coalesces with the defect on the palatal side before it starts to diminish.

Intensity profile plots taken from the *b*-scan image in figure 5.29a are illustrated in figure 5.30. The profiles were extracted from three different regions on the image, from the buccal defect (profile (i)), a normal looking enamel (profile (ii)) and from the palatal defect (profiles (iii) and (iv)). The scattering patterns were different in all three regions. The profile from region (i) shows that light photons were scattered to high level close to the level of the air-surface peak. The enamel seems severely disrupted causing a very broad peak of light scattering which is present across nearly 500 μ m in the depth of enamel after which there is less scattering of light. Profile (ii) is of the healthy looking enamel which can be seen on the b-scan image (figure 5.30a). The scattering of light in this area resembles that of normal enamel already described earlier with a gradual decay of the back reflected light intensity with very minimal light scattering beyond the air/surface peak.

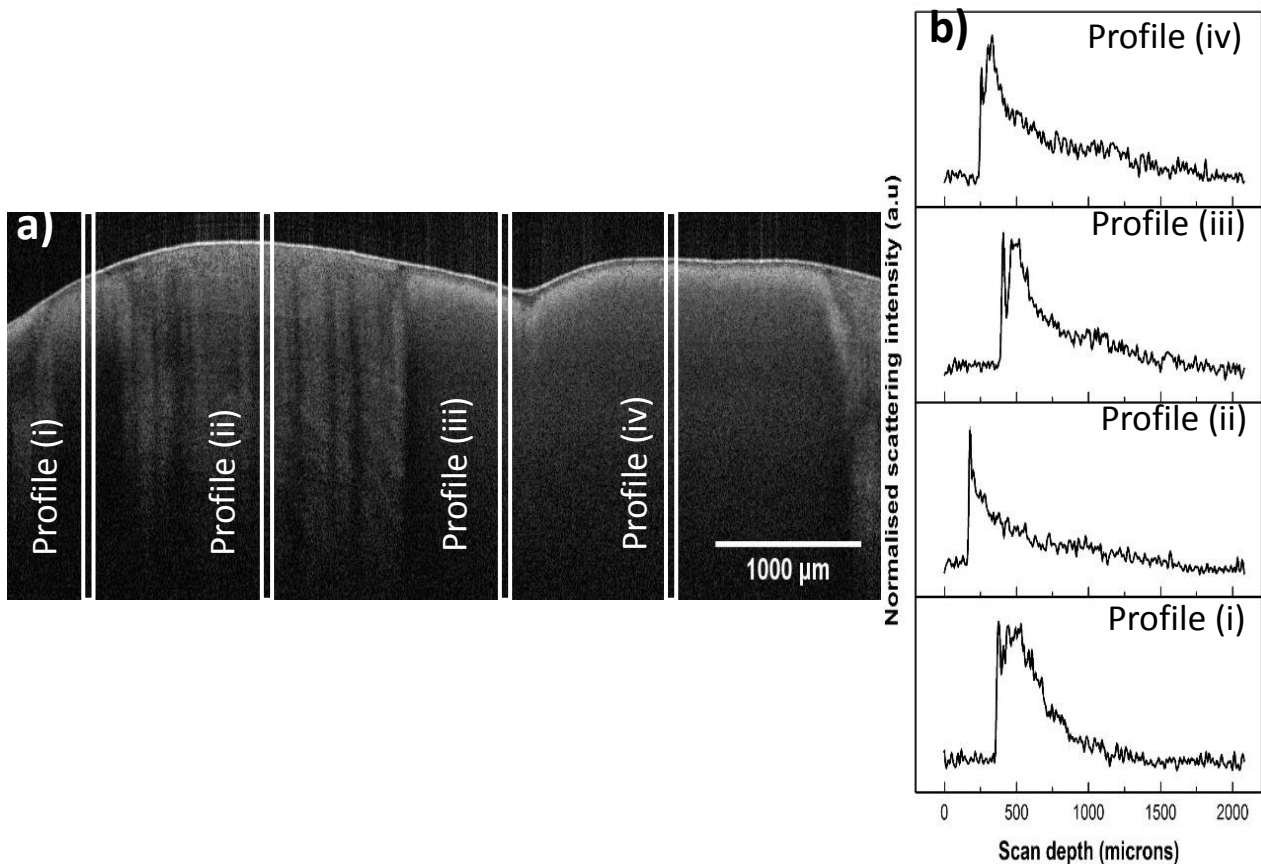


Figure 5.30 Intensity profile plots of the emarcated type 2 defect in figure 5.29a ; a) b-scan image with the selected regions for the profiles to be plotted; b) the intensity profiles taken from different regions on the image, profile (i) was taken from the defect on the buccal side showing significant light scattering caused by the defect; however profiles (iii) and (iv) were taken from the palatal side of the defect and both profiles show air/surface peak and immediately following it there is a second broader peak with the light photons decay at higher level than expected; profile (iii) is taken from apparently normal enamel in the region and shows a scattering pattern of light in healthy enamel.

The profile plots taken from the palatal side of the defect behaved somewhat differently. After air-surface interface peak there was a second peak immediately below the surface which was either of the same magnitude (profile iii) or even higher (profile iv). This second peak was not as broad as the one demonstrated by the intensity profile taken from the defect on the buccal side. The decay pattern of the back scattered light was the same as for the other two profiles taken from other regions in this *b*-scan. However, the back scattered light decayed with a higher intensity level. This means that even though the back scattered light is decaying exponentially the amount of disruption in the enamel structure is so high that it scattered light even at higher depths in enamel. In fact, this is clearly visible from the appearance of the enamel as the bright area mainly confined to the subsurface region and from there, there was a gradient distribution of brightness down the enamel depth.

5.4.3 Type 8 (with PEB) MIH defect

There were two surfaces affected with type 8 defects, the buccal surfaces of MIH 38 and MIH 39. As an example to this defect type, the buccal surface of MIH 38 is shown in figure 5.31. The defect is confined occlusally to the buccal cusps with a yellow brown halo around it. Characterising the defect using mDDE index, it is given L1 as it is present in the occlusal half of the tooth. The defect is demarcated given score D1 and its extent is less than a third of the tooth (E1). Figure 5.31b indicates the position of the OCT frames selected close to the PEB region occlusally. Radiographically, there is a radiolucency of the composite filling and the breakdown of the buccal cups (figure 5.32).

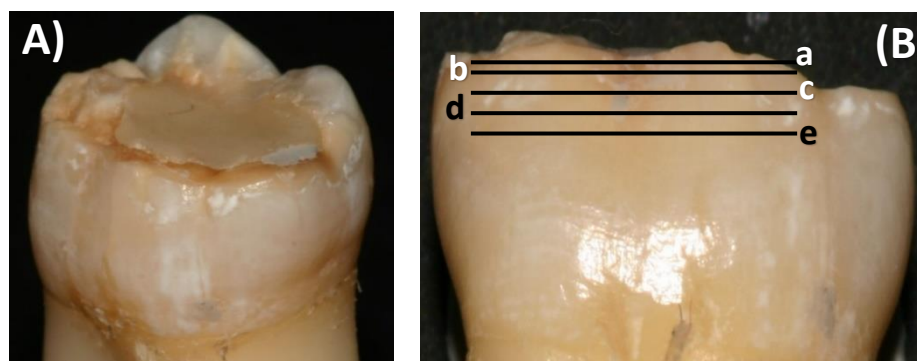


Figure 5.31 Buccal surface of MIH 38 with type 8 (with PEB) defect.

A, a view of the tooth from an angle to show the defect; B the buccal surface with lines from a to e indicating the position of the OCT frames shown in figure 5.33.



Figure 5.32 Radiographic image showing the buccal and lingual surfaces of MIH 38.

The OCT images illustrated in figure 5.33 show the appearance of the defect (white arrows) in enamel, even though the enamel surface close to the PEB area seems unaffected.

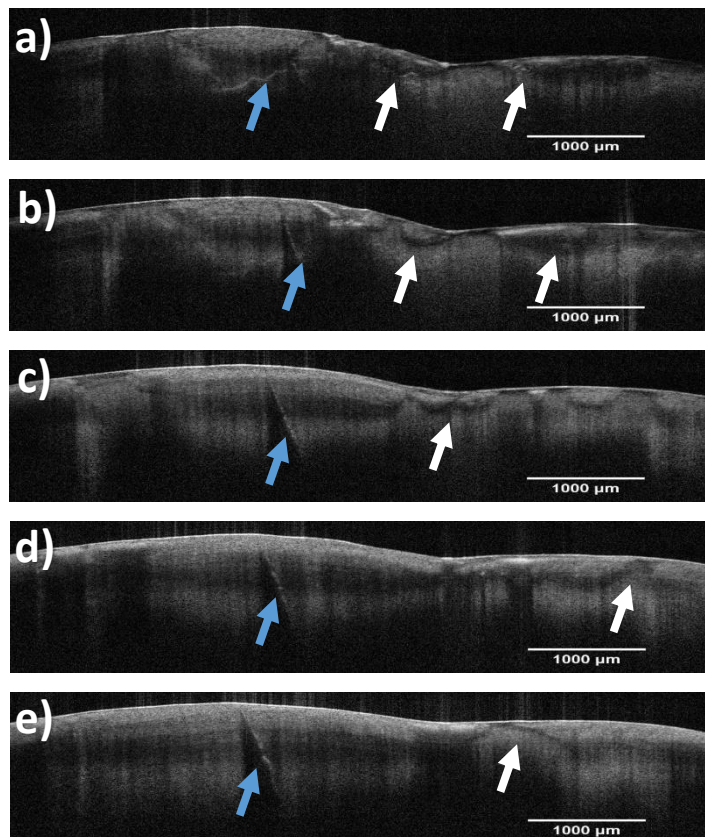


Figure 5.33 OCT frames corresponding to the lines on the clinical photograph of the buccal surface of MIH 38

The enamel close to the surface seems to be affected more (white arrows); the blue arrows indicate a fracture line extending into the enamel surface which could have propagated from the PEB area close to the OCT frame shown in 'a'.

However, an interesting finding in these *b*-scan images is the presence of a fracture line in enamel (blue arrows) which propagates from the area close to the PEB (figure 5.33a) down into the more cervical area (figure 5.33e), suggesting that the surface is weakened by the breakdown which occurred occlusally.

The intensity profiles shown in figure 5.34b show increased scattering of light in the areas which have visible enamel defects in the *b*-scan image. The intensity of back reflected light behaved in several different ways. The amount of scattered light was less at the subsurface region but was sustained at higher level before the intensity decays. Sharp single back reflected peaks can be seen in areas where there is shadowing or darkening in the enamel immediately below the surface (profiles i and iv). However, in profile (iii) the sharp peak of the air-surface interface is immediately followed by an even higher scattering peak of the subsurface enamel even though the dark subsurface layer is also present. This is most likely due to the degree of disorganised subsurface enamel in this region. The same applies to the area where profile (ii) has been taken from, in which there is two significant scattering peaks the second one is being due to the defect present in this area. After the second peak, there is a slight increase in the scattering of light before the intensity of light photons decay exponential.

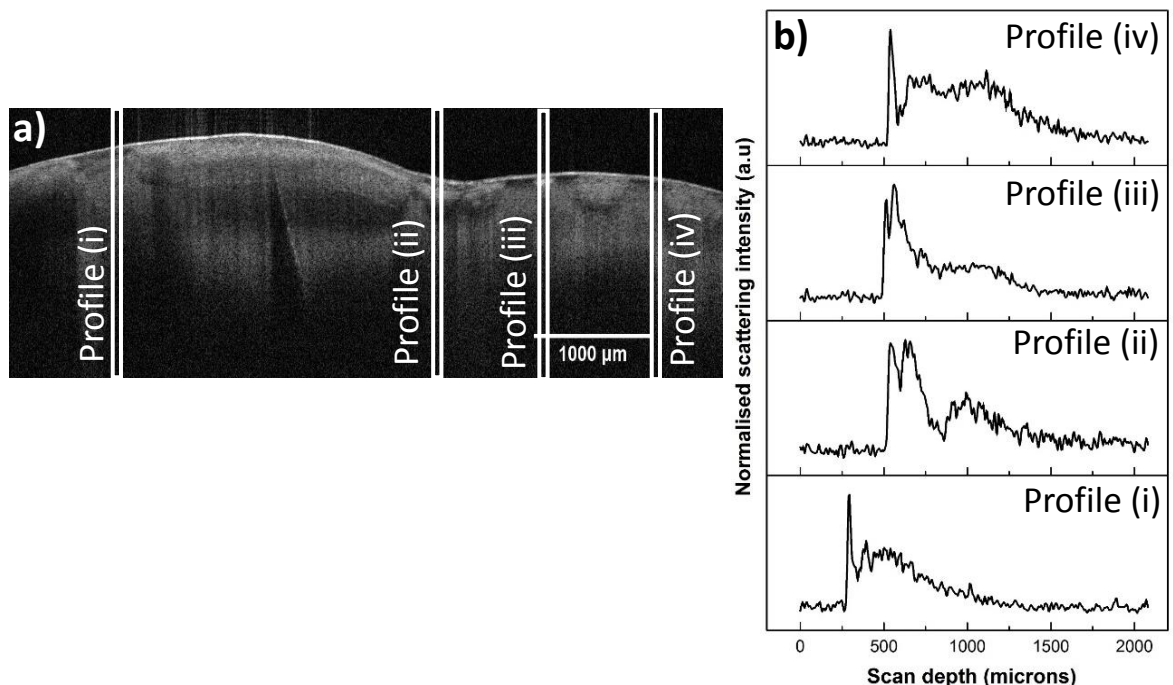


Figure 5.34 back scattered light intensity profiles taken from the *b*-scan shown in figure 5.33c; a) the position of the regions from which the profiles were plotted; b) these profiles were taken from areas which showed signs of disturbed enamel structure in the *b*-scan image; the increased light scattering presents in these profiles supports the idea that those regions were of disrupted enamel.

A second example to be discussed in this section is a surface which has type 2 defect, but closely related to PEB in the occlusal surface (type 8). The distal surface of MIH 33 is shown in figure 5.35B. The MIH defect present on this surface is located on the occlusal half (L1), demarcated (D1), and it extends to less than a third of the surface (E1). The radiographic image shown in figure 5.36 shows the close proximity of the distal surface to the occlusal PEB.

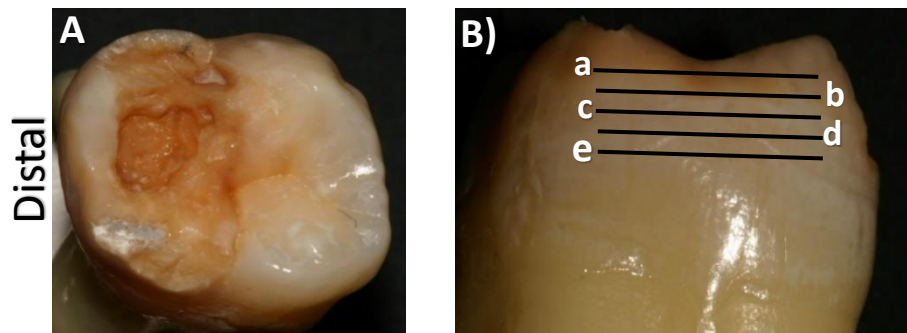


Figure 5.35 (A) the occlusal surface of MIH 33 showing PEB which looks yellow brown in colour; (B) the distal surface of the of the tooth with MIH type 2 occlusally.



Figure 5.36 The radiographic image of MIH 33 showing the mesial and distal surfaces.

The OCT images shown in figure 5.37 demonstrate the extent of the defect deep into enamel. Although clinically the yellow brown defect is limited to the first two frames (figures 5.35B (lines 'a' and 'b')) the defect has extended cervically to undermine healthy looking enamel (when looking at the lesion from the distal surface). The breakdown in enamel seemed to begin from the EDJ (the arrow in figure 5.37e) and as the breakdown and disruption continued occlusally, the EDJ has started to disappear (the arrow in figure 5.37d). From this point the defect becomes established dividing the thickness of enamel into two layers a superficial and deep which can get separated

from each other. For instance, if exposed to high load e.g. occlusal forces, leading to PEB.

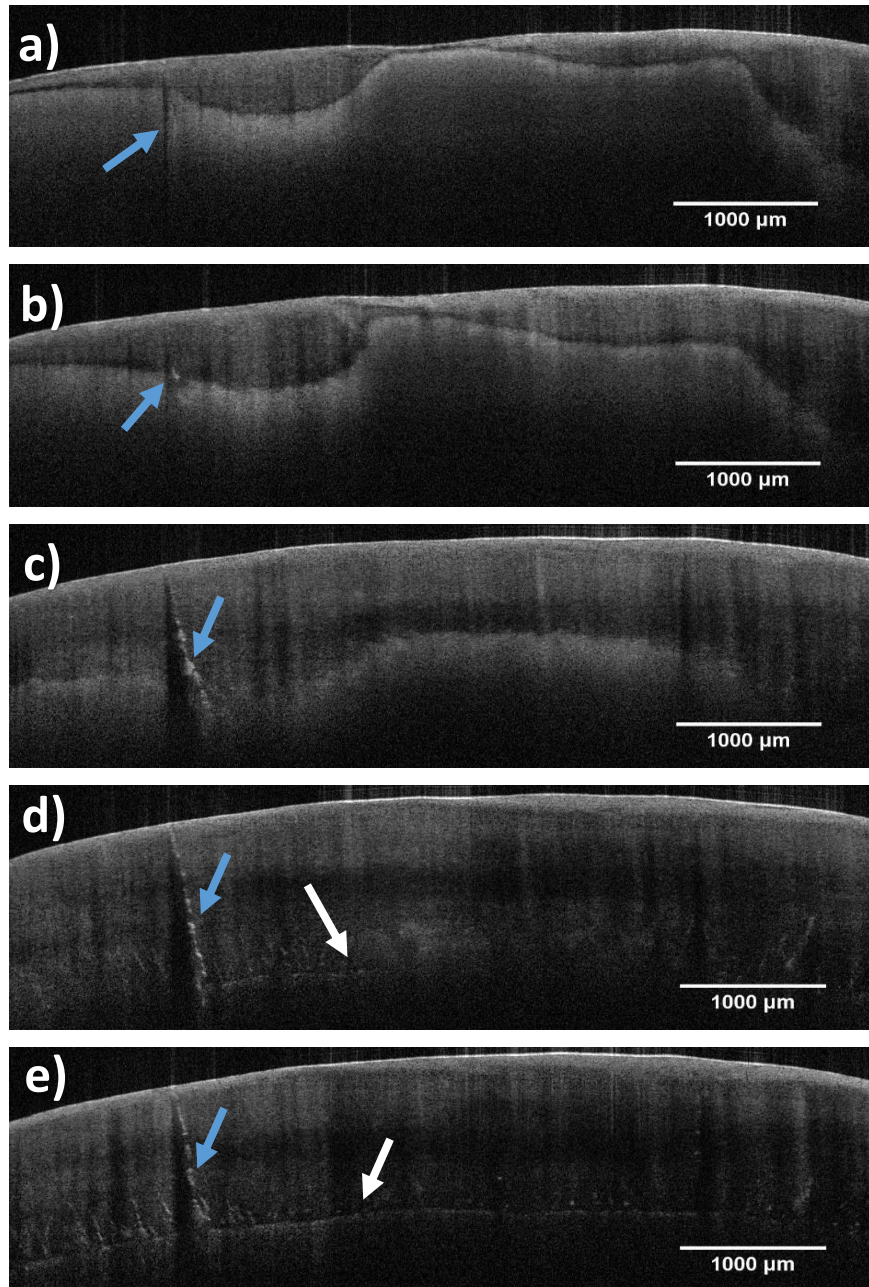


Figure 5.37 OCT frames corresponding to the lines drawn on the distal surface of MIH 33 shown in figure 5.35B. The enamel defect shows delamination like appearance. The arrows in d and e indicate the position of EDJ; in (d) the EDJ disappears due to the presence of the defect (white arrow); (e) there is a wide gap between dentine and enamel at the EDJ.

Another important feature present in figure 5.37 is the presence of a crack (blue arrow) extending from the enamel surface to the EDJ and can be seen throughout the OCT scan (figure 5.37a-e) of the surface. This is important in that it helps clinicians to determine the prognosis of the tooth as it weakens the structure of the tooth. The back scattered intensity profiles of this scan is already illustrated in figure 5.15b and the en-face images in figure 5.11 b and c.

5.5 Discussion

Optical coherence tomography scanning

OCT is a non-destructive imaging system that shows tooth structure to a depth of nearly 2mm. In this study, the maximum image dimension that can be captured was used. Consequently, the sections or frames obtained from OCT scanning were very thin (10 μ m) which are very difficult to obtain by the physical cutting of a tooth. This enables the investigator to detect abnormalities in the ultrastructure of teeth. However, the OCT scanning done in this research was not lesion oriented which lead to some lesions either missed or partially imaged when the surface was scanned.

The duration of taking a full scan of 600 OCT frames was about 1-2 minutes which makes the OCT technique a handy and easy to use clinical diagnostic tool. It does not involve ionising radiation hazard and this is an important merit of OCT over radiographic imaging currently used clinically. In the literature, the use of OCT has been reported for assessing restorations, demineralisation and remineralisation of dental hard tissues (Fried et al., 2002, Amaechi et al., 2004, Feldchtein et al., 1998).

Some important points might be considered when using OCT imaging on teeth in general and specifically when imaging MIH affected teeth. The current OCT imaging scanner is a dermatological one and is intended for imaging skin and not dental hard tissues. This has few implications. First, it is difficult to be used intraorally in vivo when imaging first permanent molars as these teeth are situated further back in the mouth and the current scanning probe need to be modified to be used in this case. However, it can be used on the anterior teeth which are more accessible.

The second implication is that the wavelength of the laser used in the VivoSight scanner is 1305nm which might not be suitable for imaging teeth. It was mentioned before that Darling et al. suggested that a near-infra red region of 780-1550nm results

in an optimal imaging techniques due to low scattering and absorption in enamel and dentine. If the wavelength is longer then the light is absorbed by the water in the tissue and consequently reducing the penetration of the NIR light (Darling et al., 2006, Fried et al., 2002). A possible future research is to evaluate the behaviour of MIH affected enamel in the wavelength range of 780-1550nm reported by Darling et.al (2006).

Diagnostic potential of OCT

A common finding in healthy and MIH affected teeth in this research project was the presence of enamel fractures or cracks which propagated and extended up to the full thickness of enamel. The irregular appearance of the enamel cracks in MIH effected teeth may be due to the weakened structure of these teeth which facilitate the propagation of such cracks. The minor cracks or enamel spindle-like structures associated with the EDJ of both types of teeth is another interesting feature when teeth were imaged with OCT.

The behaviour of the scattering of light photons when travelled in the depth of dental enamel is complex and depends on the structure of the enamel. This is evident when the quality of OCT images was looked at (qualitative assessment of the images). The appearance of healthy enamel OCT images was different from those of the MIH affected enamel; and those of the different types the MIH defects appeared also different from each other. This is a significant diagnostic finding of OCT imaging. Clinicians can use this technique to differentiate between the different enamel defect types. However, the disadvantage of OCT is that the increased scattering of enamel shown by the bright areas in OCT images cause shadowing underneath these areas. This makes further assessment of the enamel below these areas difficult.

En-face reconstruction of the images is a promising advancement of this imaging technique and aids in visualising the enamel structure and defects in an enhanced way. The ability to clearly visualise and locate the MIH defect gives the potential for OCT technique to be used in a 3D visualisation and reconstruction of the enamel defects and to highlight areas of disruption within the enamel. This reconstruction would be an important development in both diagnostic and prognostic evaluation of enamel conditions as it enables non-destructive subsurface imaging of teeth. Volumetric assessment of the enamel defect could be permitted in future by this method of re-construction.

The intensity of the back scattered light as light photons travel along the depth of the enamel was also investigated. This method was considered by several researchers

(Jones et al., 2006b, Manesh et al., 2009a, Manesh et al., 2009b) in an attempt to highlight the effect of certain procedures such as demineralisation and remineralisation on dental hard tissues. The change in the enamel ultrastructure due to these processes causes a change in the scattering of light. In this study *a*-scan signals of OCT were extracted from the *b*-scan images in an attempt to observe the behaviour of light as it travels through the depth of normal and MIH affected enamel, which may lead towards a more systematic diagnostic dental application of the technique using the intensity of back scattered light. The width of the selected regions was taken to be 40.5µm. This was done to get an average measurement representative of the area under investigation, instead of a line selection which was done by other researchers before (Jones et al., 2006b). Another merit of this width is reducing the signal to noise ratio or SNR and as a result obtaining a smoother intensity profiles. Another thing to mention is that the scattered intensity values were normalised using origin software as the scattering peak intensities were considerably variable between individual profiles.

In this research project, different intensity profiles were taken from several regions in a single OCT *b*-scan image. Each profile showed distinctive behaviour of light scattering which resulted from the enamel being heterogeneously disrupted. However, the decay of the scattering profiles in healthy enamel presented some small variations which could be due to localised interruptions in the enamel structural and chemical homogeneity. An example of scattering variations which was small is the one seen at the EDJ. This slight increase in scattering intensity could be due to change in refractive index between enamel ($n \sim 1.63$) and dentine ($n \sim 1.54$) or due to their different ultrastructure.

The intensity profiles of MIH affected enamel showed that there were more than one peak of intensity instead of only one air-enamel peak that is normally seen in healthy enamel. The presence of these scattering peaks indicates that the structure of the enamel is grossly disrupted. Diagnostically, these scattering peaks can be used as indicators of enamel defects. The depth at which these peaks are located below the air-enamel layer is also significant as this will provide information to clinicians about the extent of the lesion. This investigation of the scattering profiles may lead to future construction of intensity profile bank which can act as a reference in aiding clinicians to diagnose MIH affected enamel.

The use of signal intensity profiles in comparing the reflectivity of enamel has been investigated before and was correlated with the ultrastructure of enamel. It is well established in the literature that the ultrastructure of MIH enamel is different from that

of its healthy counterpart. The MIH enamel has an increased porosity compared to control healthy enamel (Crombie et al., 2013) and Jones et.al suggested that the porosity of the carious enamel controls the reflectivity of the lesion (Jones et al., 2006a). Therefore, MIH enamel porosity can be one of the causes of the different signal intensity profiles compared to that of normal enamel. Another cause of this variation is the decrease in MIH mineral enamel density which was reported to cause increased reflectivity (Jones et al., 2006b). Therefore, this technique could be possibly used in distinguishing the different types of enamel investigated.

When conventional diagnostic techniques were compared with OCT imaging, the latter technique gave a better description of the MIH defects either qualitatively or by the use of the intensity profiles of back scattered light. Conventional techniques either gave account of the external appearance of MIH defects (mDDE index) or showed images with low resolution of these defects (radiographic images) compared to OCT resolution. Moreover, it was possible to measure the dimensions of certain defects from OCT images (with the aid of image J software) directly to detect the extent of the lesions into the depth of enamel.

Conclusion

This project's findings were in line with what already reported in the literature. For example, Baumgartner et.al compared conventional OCT with PS-OCT and concluded that both techniques were able to give sufficient information on tooth structures; and the location and depth of the carious lesions can be measured by both techniques (Baumgartner et al., 2000). However, Hariri et.al used the signal intensity profiles in investigating the optical properties of enamel and dentine (Hariri et al., 2012).

However, due to the different patterns of interaction of light photons with enamel structure when the various types of enamel were imaged, an attempt to understand the behaviour of light in these circumstances is important. The question which poses itself is that whether this interaction is occurring at the level of the enamel crystals, rods (or prisms) or from enamel as a bulk material.

The correlation between light interaction (in terms of back scattered light intensity) with the ultrastructure of dental hard tissues was investigated by Jones et.al (2006b). They correlated a reduction in mineral density in artificial occlusal caries with reflectivity increase using TMR (Jones et al., 2006b). Another research team investigated the effect of dentine remineralisation on its light reflectivity using PS-OCT and compared it

to dentine demineralisation regions (Manesh et al., 2009a, Manesh et al., 2009b). They used TMR and PLM to correlate between light reflectivity and dentine structure.

In the current research project, the ultrastructure of enamel in terms of the amount of mineral density, the orientation of enamel crystals in enamel prisms or rods were investigated in an attempt to correlate the OCT findings with enamel ultrastructure. This correlation will be presented in the next chapter and a comparison between the OCT findings with the results from XMT (mineral density) and SXRD (enamel crystal orientation) will be discussed in detail.

6 Correlation of OCT imaging with XMT and SXR

6.1 OCT and XMT

6.1.1 Disclaimer

All the data related to the XMT presented in this section were obtained by Dr David Mills and Dr Samera Siddiqui (a PhD student at the time of the experiment) in the Dental Physical Science Department, Queen Mary University of London (QMUL).

6.1.2 Materials and Method

6.1.2.1 MuCat 2 Scanner

The XMT system used in this research (Figure 6.1) was “MuCat 2™” which is a fourth generation XMT scanner that has been developed from the first generation scanner first developed by Elliott (Elliott and Dover, 1982), in QMUL at the Dental Physical Science Department especially for dental research (Davis et al., 2013). It uses a 225 kV microfocus X-ray generator with 5 µm focal spot size (X-tek, Nikon Metrology, Tring, Hertfordshire, UK) in which the source or X-ray filament and targets can be demounted and changed (Davis et al., 2013). The camera or the detector was a Spectral Instrument (Tucson, Arizona) 800S series cooled CCD system with a 16 megapixel Fairchild CCD485 sensor coupled via a fibre-optic faceplate to a columnated CsI scintillator from Applied Scintillation Technologies (Harlow, Essex, UK).

MuCat 2™ uses time delay integration (TDI) where the camera is moved through the X-ray shadow while the CCD is being read out at a simultaneous speed. The CCD is mounted at 90° to the usual TV set-up. This helps in overcoming the ring artefact mentioned in chapter 1. The advantage of this mode is that the width of the recorded image can be larger than the width of the CCD, limited only by the X-ray field.

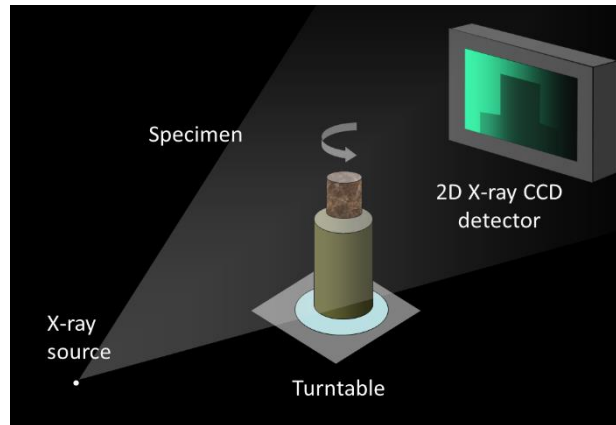


Figure 6.1 A schematic representation of the current XMT system used (adapted from Wong et.al 2006).

The mechanical stages in which the camera and the specimen were mounted were manufactured by Physique Instrument (Karlsruhe/Palmbach, Germany). The pixel size for the Fairchild CCD485 chip was $15\mu\text{m}$ which were binned 2×2 on-chip and a further 2×2 after TDI readout giving a $60\mu\text{m}$ recorded pixel size. The image recorded can be as high as 1000 pixels and is of a width of up to 2700 pixels.

The exposure time in TDI mode is defined to be the time needed for the CCD to move a distance equivalent to its own width. Therefore, the duration of the image acquisition depends on the width of the recorded image. It is usual for the detector to get saturated if the exposure time is too long. Therefore, it is crucial to average individual exposures in a process called frame averaging. The MuCat Scanner was also calibrated to minimise beam hardening during imaging of the sample.

It is important to point out that XMT is used to investigate the structure of the scanned sample as well as to measure the mineral content of a particular material. These will be looked at in detail in the next sections.

6.1.2.2 Procedure

Six FPMs have been taken to QMUL to be imaged using the MuCat scanner (Table 6.1). As mentioned in the disclaimer section, the scans were done in collaboration with the Dental Physical Science Department at QMUL and done by Dr. David Mills and Dr. Samera Siddique. Two control and four MIH affected FPMs were scanned. Each sample took up to nearly 14 hours to scan. The voxel size used was $15\mu\text{m}$ on a 75

pixels grayscale. The scans were taken with a 180 μ A current and a voltage of 90kV at a temperature of 26°C \pm 0.1°C. The crown of the teeth was imaged only.

Sample	Size	Number of Projections	Time (hours, minutes)
C129	854x784x640	1431	13h,11 mins
C133	491x194x640	1395	12h, 53mins
MIH 33	784x774x670	1503	13h, 50 mins
MIH 38	904x944x666	1287	11h, 52 mins
MIH 50	934x904x666	1395	12h, 51 mins
MIH 67	814x824x670	1395	12hrs, 52 mins

Table 6.1 shows a list of the control and MIH affected samples scanned with MuCat scanner at QMUL.

The attenuated intensity of transmitted beam was measured when the sample is placed in the path of the incident X-ray beam (figure 6.1) using the CCD detector and consequently, tomographic data could be obtained. The number of projections, duration of exposure, resolution of the image and current were determined by the size of the sample and its density. The rotation of the sample as the measurement was taken allowed a three dimensional reconstruction of the sample images. In each projection taken at every angle across 360°, the rotation centre was determined by the use of the average of mass for each projection.

Images were reconstructed by converting the 2D projections obtained from each sample through the 360° to a 3D array of X-ray LAC. This was done by the application of a modified Feldkamp cone back projection algorithm (Feldkamp et al., 1984) to the corrected projections which was done in QMUL.

6.1.3 Data analysis

The three dimensional images of the obtained projections were viewed using a software called Tomview™ (version 1.1, copy right 2003, Graham Davis, QMUL) which was especially created for viewing and manipulating the XMT images. Using this software. It was possible to extract the values of the enamel LACs and consequently, calculating the mineral density of enamel in the samples.

Quantifying the mineral density (MD) in each sample using the LAC values distribution was done by using the following equation:

$$MD = \frac{\mu_{LAC}}{\mu_m} \times \rho$$

Where μ_{LAC} is the measured LAC of the sample

μ_m is LAC of a pure HA of the mineral

ρ is the density of pure HA.

The density of pure sample of HA was measured by Davis et.al to be 3.16 g cm^{-3} as well as the LAC of pure HA which measured to be 3.12 cm^{-1} (Davis et al., 2013) with high accuracy. These values were used in calculating the mineral density in the sample using the above formula after obtaining the measured LAC using Tomview software.

Mineral Density Mapping

Two dimensional projections were extracted from Tomview into bitmap images format and then imported in turn into image J where images were further analysed (Appendix 8). From the MuCat scan set-up, each 1 cm^{-1} LAC corresponded to 75 pixels gray scale and as a result, it was feasible to colour map the mineral density using image J on the imported images. Comparison between OCT images and MD mapping was done on the same areas.

Further Quantitative MD Analysis

The MD of control enamel was further compared with that of MIH affected enamel quantitatively. This comparison was done in three areas across the enamel in both types; close to the surface, in the middle third of enamel thickness and close to the EDJ (Figure 6.2). The values of LAC from each area were extracted from XMT images

using Tom view™ version 2 and exported into MS Excel spread sheet which in turn was transferred to SPSS® IBM® version 22 software. This process was repeated in three regions across the tooth surface by randomly selecting an XMT image from the occlusal, middle and cervical thirds of the tooth surface (Figure 6.3). The mean of MD, for example, at the surface enamel was obtained from these three randomly selected XMT images. The same was done for the mean MD at the middle of the enamel thickness and that close to the EDJ. It is important to mention that the three XMT images chosen from the MIH enamel were selected from three different regions across the lesion area and not across the whole the surface enamel (Figure 6.4).

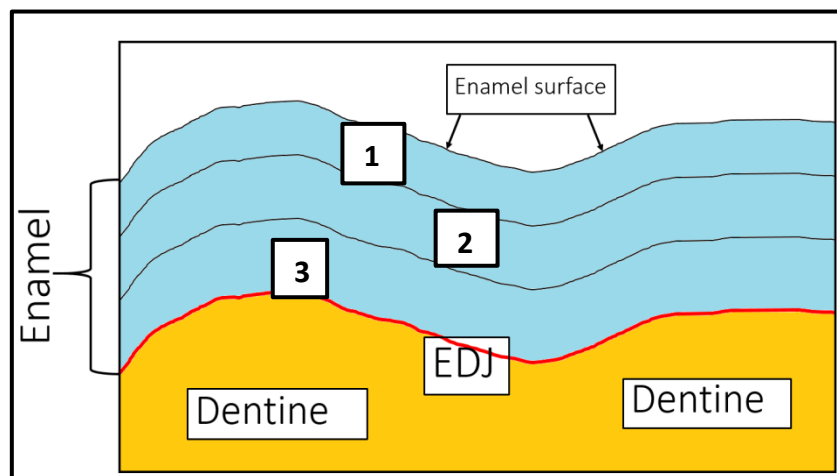


Figure 6.2 A schematic representation of the three areas of enamel from which MD was obtained; area (1) is close to the surface, area (2) in the middle of the enamel thickness and area (3) close to the EDJ.

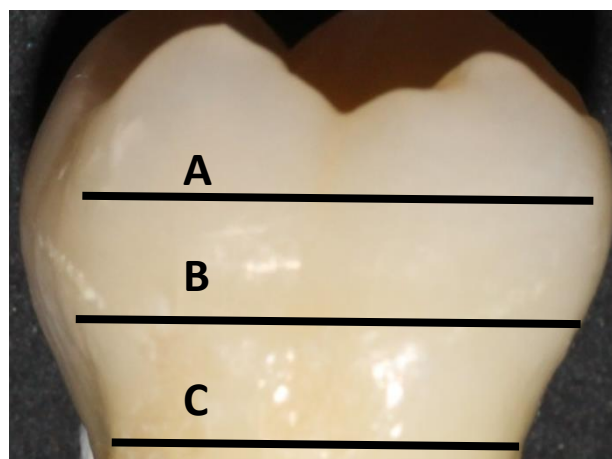


Figure 6.3 A control tooth surface divided into three regions (A) is the occlusal third of the surface, (B) is the middle third and (C) is the cervical third. From each region an XMT image was randomly selected and MD was obtained using Tom view™ software.

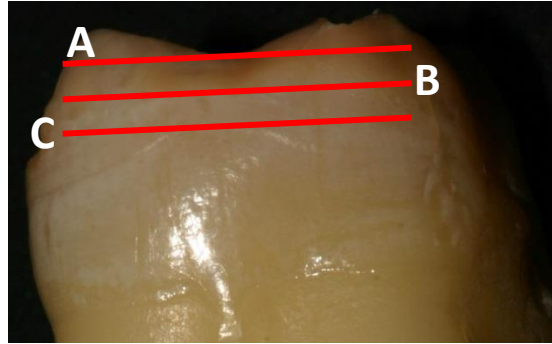


Figure 6.4 The area of the MIH enamel defect was divided into three regions (A-C). From each region an XMT image was randomly selected and MD was obtained using Tom view™ software.

6.1.1 Results

Mineral Density Mapping

Two control and four MIH affected teeth were imaged using XMT technique. The type of lesions investigated are listed in table 6.2 which included a variety of MIH defects. Both XMT and OCT images are presented for direct comparison between them.

Sample	Surface	Defect type
MIH 33	Distal	Type 2 Demarcated close to a PEB
MIH 38	Buccal	Type 8
MIH 50	Buccal	Type1 diffuse
MIH 50	Buccal	Type 2 demarcated
MIH 50	Distal	T1 diffuse and T2 demarcated
MIH 67	Distal	Type 2 demarcated

Table 6.2 The types of MIH lesions investigated using XMT scanning. The types highlighted in bold font are those types which were further investigated using synchrotron XRD.

A colour scale of MD is incorporated with each XMT image with red being the lowest MD of 2 gcm^{-3} and the highest is blue comprising a MD of 3.16 gcm^{-3} which is the density of pure HA.

MD of Control FPM

Before starting to present the XMT results of the MIH affected samples, it is important to present the results of the control ones, so any difference between the two types will be appreciated. Figure 6.5 shows the distribution of MD in selected regions in the crown of C129 sample, at a lower (figure 6.5(A)), middle (figure 6.5(B)) and high levels of the crown (figure 6.5(C)). It can be seen that in the sections presented the enamel MD is in the range of 2.75 to 3.16 gcm^{-3} except in areas close to the EDJ where it measures as low as 2.5 . However, in certain areas where there is carious lesion or demineralisation in enamel (e.g. the palatal fissure in figure 6.5(B) and the mesial surface in figure 6.5(C)) the MD is $\leq 2.25 \text{ gcm}^{-3}$.

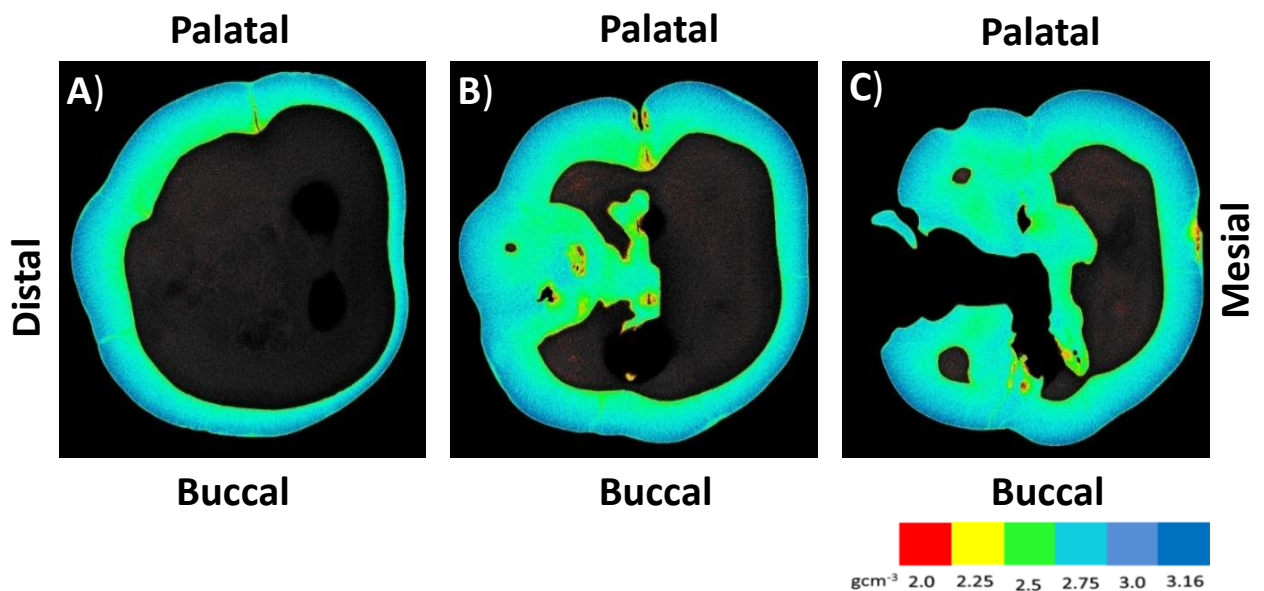


Figure 6.5 XMT scan of C129 control tooth; A) XY scan at a lower level of the tooth; B) in the middle of the tooth and C) at an occlusal level of the tooth; from the three XMT images, distribution of mineral density in the depth of enamel can be seen clearly; areas of decalcifications/early carious lesions have lower MD.

Another example is demonstrated in figure 6.6 with a comparison between OCT and XMT images of the same sample. The distal surface of C129 is shown in this figure. The appearance of the enamel in the OCT images is of a typical healthy enamel with a uniform scattering of light present throughout the depth of the enamel. The XMT images show the distribution of MD in the regions shown in OCT. There is a noticeable gradient in mineral density present from enamel surface to the EDJ with the higher MD being mainly close to the enamel surface which varies to up to 3.16 gcm^{-3}

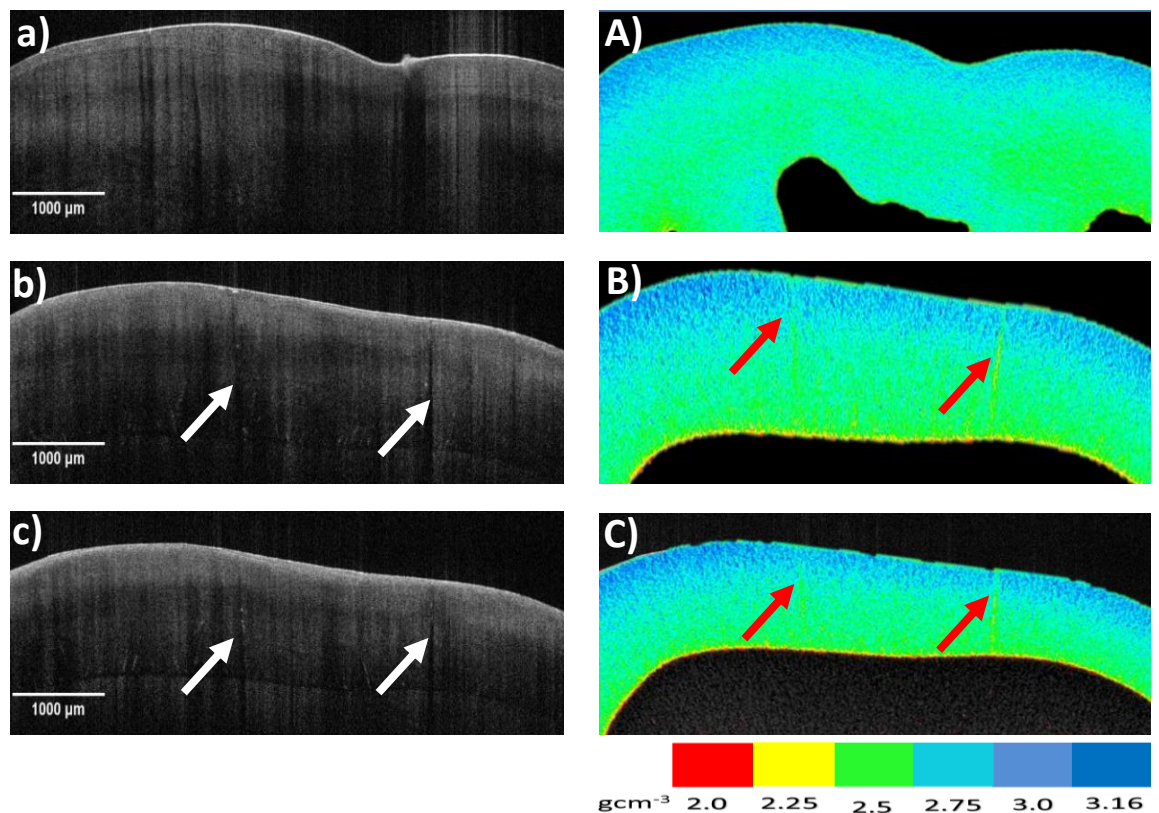


Figure 6.6 Comparison of OCT and XMT images of the distal surface of C129; the OCT images show the uniform scattering of the light; the XMT images show the MD distribution in enamel with a gradient moving from the enamel surface to the EDJ; the red and white arrows shown indicate fracture lines present in enamel that can be identified in both imaging techniques.

Deeper into enamel the MD goes down to 2.5 gcm^{-3} . In figures 6.6 (B) and (C) the mineral density in the region of the EDJ is $\leq 2.25 \text{ cmg}^{-3}$ (the presence of the yellow and red colours in this region). Enamel fracture lines can be seen in both OCT and XMT images (white and red arrows, respectively).

MD of MIH affected FPMs

The two dimensional (XY) images of MIH 67 are shown in figure 6.7 which represent as cross sectional images of the tooth. The three images presented were taken from three different regions in the tooth. Generally, there is very small band of high MD at the surface compared to the size of this area found in the control sample and measures up to 2.75 gcm^{-3} . Overall, the MD of this sample is in the region of $2.25\text{-}2.5 \text{ gcm}^{-3}$. Figure 6.7(B) shows two lesions present on the tooth, a mesial carious lesion and a distal MIH defect. The MD in the carious lesion present on the mesial surface of the tooth is as low as 2 gcm^{-3} . However, the MD of the MIH defect on the distal surface of the tooth is measuring 2.25 gcm^{-3} .

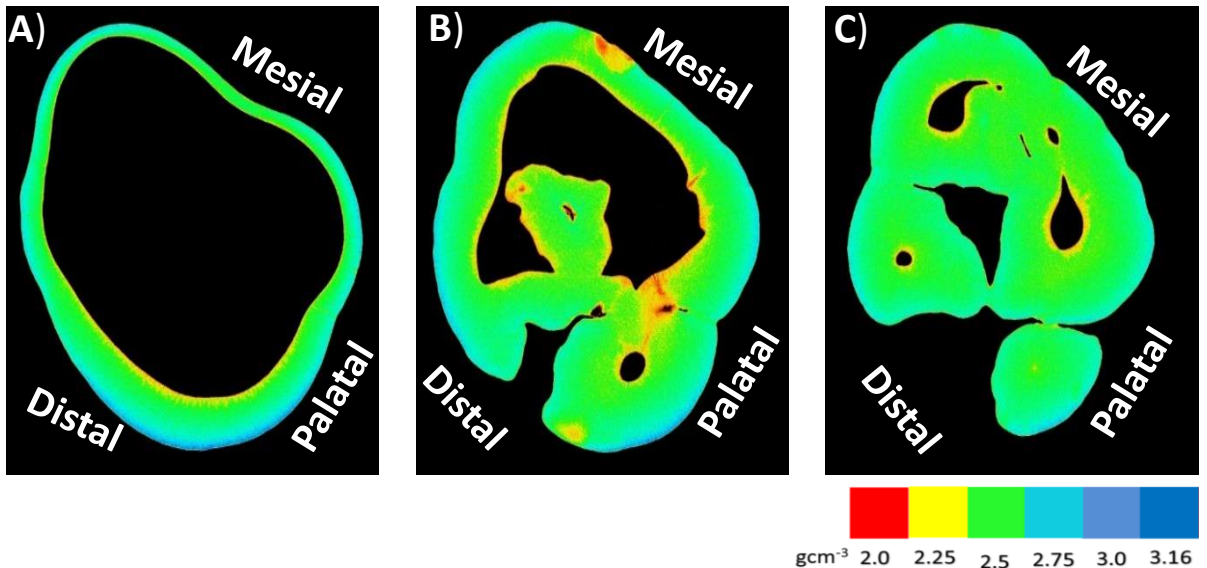


Figure 6.7 XMT scan of MIH 67; A) XY scan at a low level of the tooth crown; B) at a higher level of the tooth crown and C) at an occlusal level of the tooth crown; from the three XMT images it can be seen the reduced mineral density compared to that of the C129 demonstrated in figure 6.3, in general the level of MD ranges between 2.25 and 2.5 gcm^{-3} ; the mesial surface in (B) is carious showing a localised area of reduced MD distinctive of the surrounding enamel.

Demarcated Type 2 lesion present close to a region of PEB

The OCT images of the distal surface of MIH 33 has been Compared with XMT mineral density colour mapping (Figure 6.8). It can be clearly seen that the lesion in the XMT images follow the same outline as that in OCT images with the presence of two layers, a superficial and a deeper layer. However, from the XMT image it can be seen that the

MD of the superficial layer is higher than that of the deeper layer with the former layer has a MD in the range of 2.75-3.16 gcm^{-3} and the deeper layer has a MD of 2.25 - 2.5 gcm^{-3} . This arrangement is the same as that of the control sample discussed above. However, the difference between the two samples' MDs is that the superficial layer of enamel which has higher MD is irregular and in some areas very thin or absent.

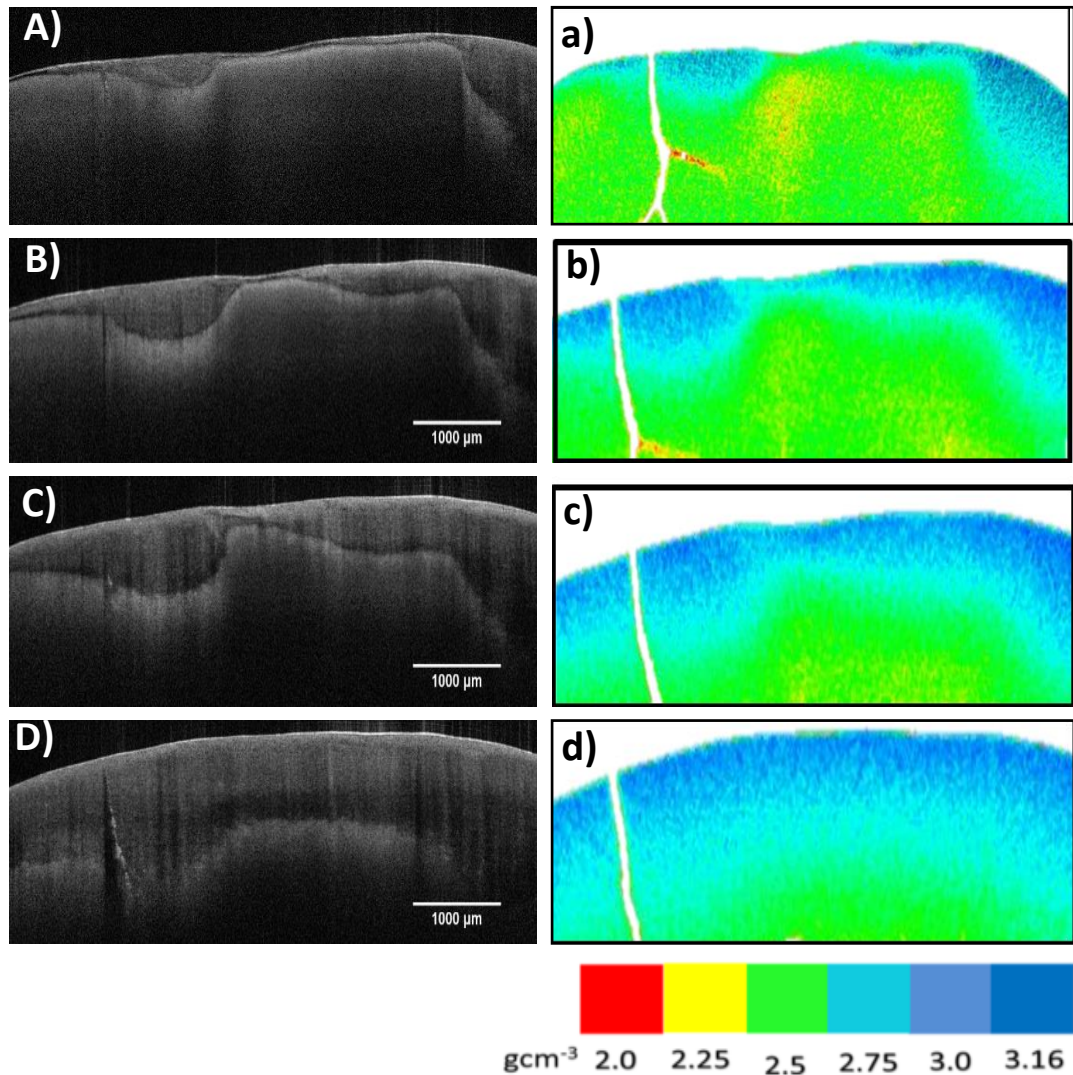


Figure 6.8 comparison of OCT (A-D) and XMT (a-d) images of a type 2 MIH defect on the distal surface of MIH 33 which was very close to a PEB region. From the OCT images there are two regions in enamel layer which are divided by a demarcated line (more clearly seen in images A-C); the XMT images indicate that these two regions have in fact different MDs, the superficial layer has higher MD (in the region of 2.75-3.16 gcm^{-3}) while the deeper layer has lower MD (2.25 - 2.5 gcm^{-3}); the fracture line can be seen in both groups of imaging.

From figure 6.8 it can also be seen that there is a gradient in the MD with the area between the two layers described above predominantly of the value of 2.75 gcm^{-3} . Another thing to mention is the presence of a crack on the left side of the OCT images has become an established fracture in the XMT. Unfortunately, this surface was eventually lost.

Buccal Surface with Type 8 Defect

Another example is that of the buccal surface of MIH 38 which had PEB occlusally (type 8) already discussed in the previous chapter (figure 6.9). Earlier it was thought that the localised demarcated areas at the enamel surface were part of the MIH lesion, however from the XMT MD colour mapping, it can be seen that those areas which were thought to be the MIH lesions are in fact areas of higher MD compared to the enamel around them. The surface layer which has higher MD is irregular and deficient in many areas at the surface. Focal areas of a lower MD in the range of $2\text{-}2.25 \text{ gcm}^{-3}$ can also be noticed in this type of MIH.

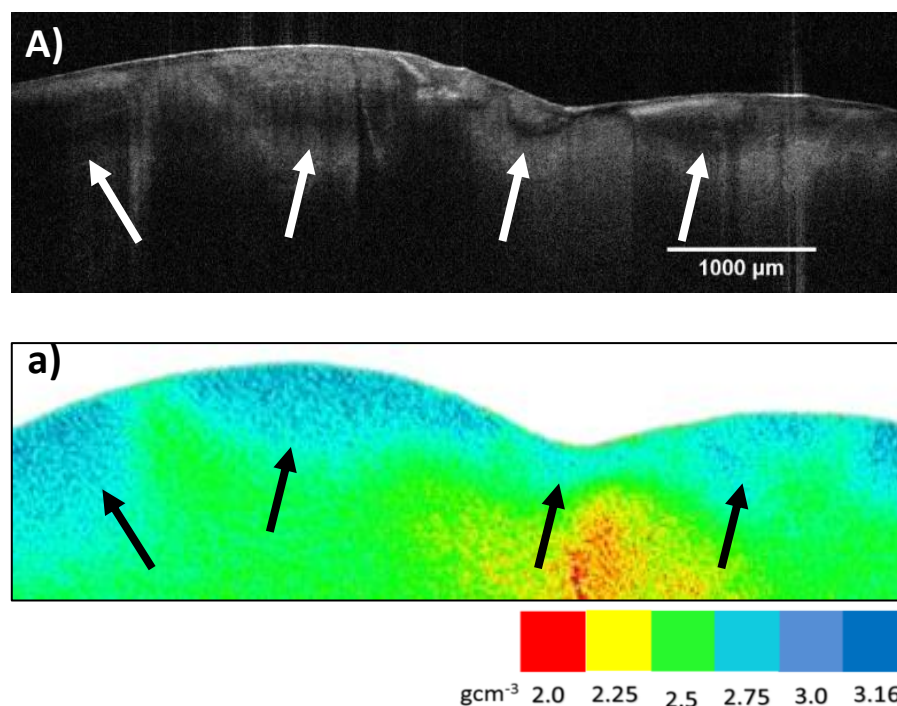


Figure 6.9 (A) An OCT image taken from a scan of the buccal surface of MIH 38 which had type 8 lesion, the white arrows show what was thought to be the MIH defect in the enamel; **(a)** an XMT image of the same area showing areas of higher MD and below it areas of low MD of as low as 2gcm^{-3} ; the black arrows correspond to the areas indicated by the white arrows in (A).

Diffuse Type 1 defect

Diffuse type1 MIH defect on the buccal surface of MIH 50 was compared in both imaging modalities (figure 6.10). The XMT of this type of defect showed that reduced MD was confined to the surface enamel with a value of 2.5 gcm^{-3} in this area (figure 6.10(B)). This was comparable to the enamel MD at the EDJ (figure 6.10(B), red arrow). The increased intensity of back scattered light at the surface seen in figure 6.10(A) (white arrows) seems to correspond to this reduced MD at the enamel surface in the XMT image (figure 6.10(B), white arrows).

Also, it can be seen from the OCT image that the EDJ is visible on the left of the image and consequently, this area was judged to be less affected with the MIH defect. This can be confirmed from the XMT image which shows that the corresponding region has higher MD compared to the region indicated with the white arrows and only the very superficial surface layer has reduced MD. The brown arrows in both images show cracks in enamel which served to act as a reference in correlating the two images.

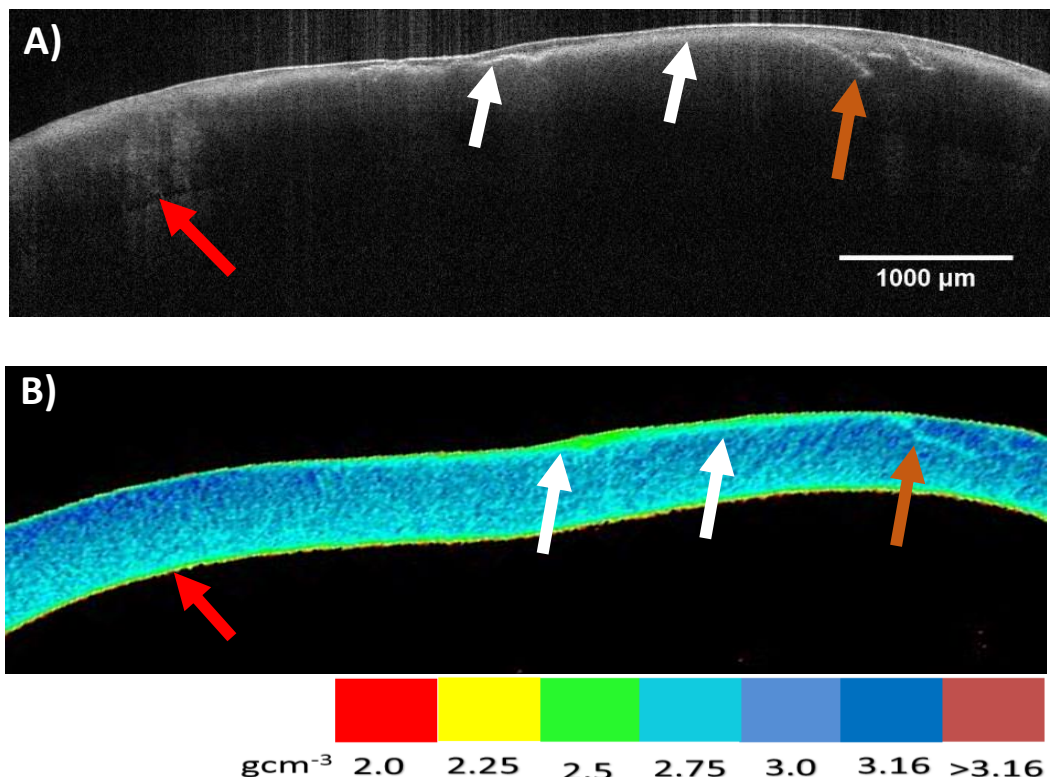


Figure 6.10 The buccal surface of MIH 50 which had a diffuse type 1 defect; the reduced MD is confined to the surface enamel (the middle white arrows) this surface mineral density is almost comparable to the enamel MD close to the EDJ (red arrows); the brown arrows indicate cracks in enamel in both OCT and XMT images which were used as a reference in correlating the two images.

Demarcated type 2 and diffuse type 1 Defects

The distal surface of the same tooth (MIH 50) had two types of MIH defects, diffuse type 1 and demarcated type 2 defects (figure 6.11). The mineral densities of both defects were very different with type1 defect (white arrows) having higher MD reaching 3.16 gcm^{-3} . On the other hand, the mineral density on the demarcated type 2 is very low in some areas, which was as low as 2 gcm^{-3} .

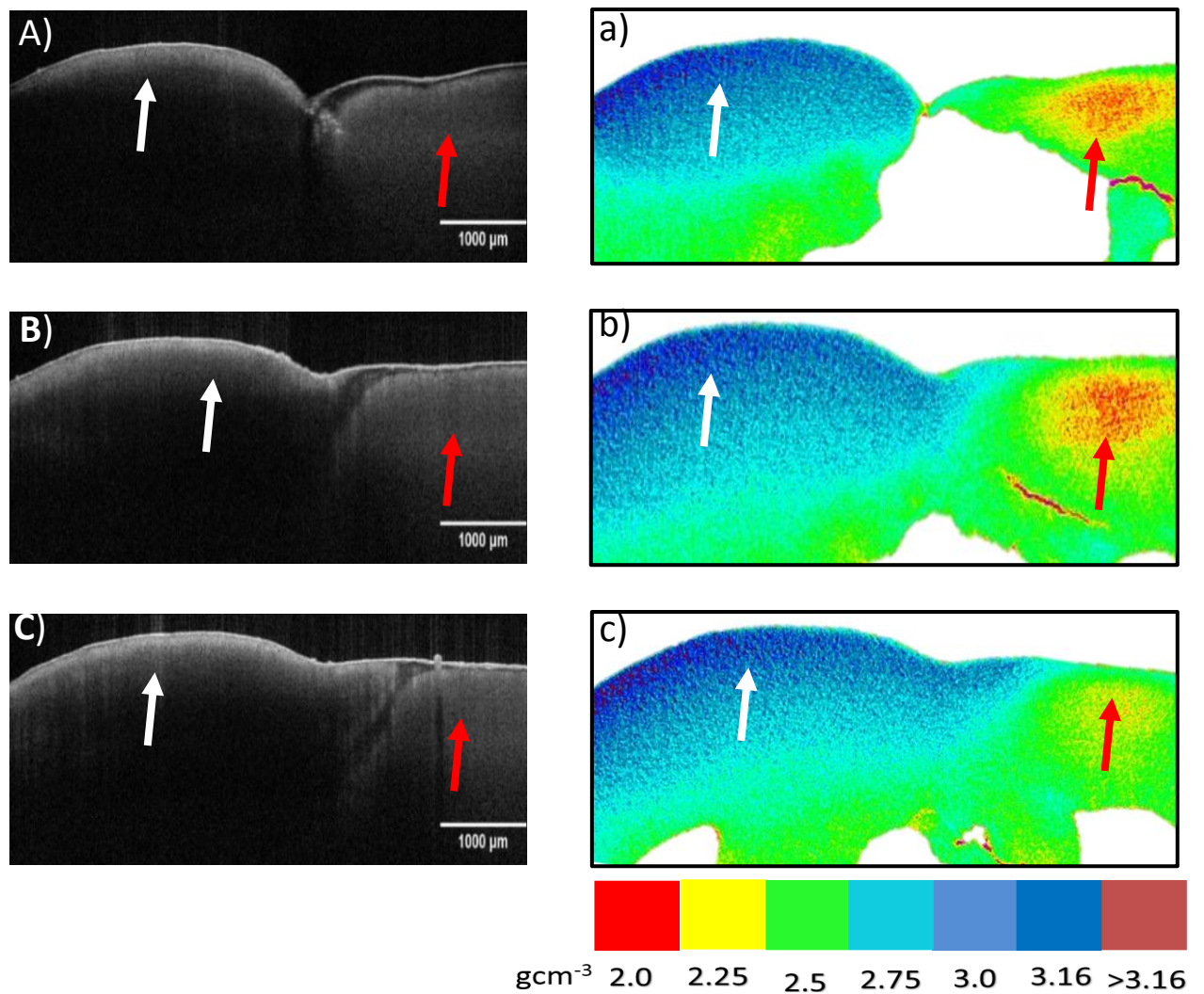


Figure 6.11 A comparison of OCT and XMT imaging of the distal surface of MIH 50 which has two types of MIH defects, type 1 on the left side of the images and type 2 in the right side of the images. The MD of the two defects are different with type 1 having more MD than type 2.

Demarcated Type 2 defect

The distal surface of MIH 67 had type 2 MIH defect (figure 6.12 white arrows). This defect seems to have a low MD as in the other defects already described. It is in the region of $2.25\text{-}2.5\text{gcm}^{-3}$. However, this surface had less MD in general which was well below the level of healthy enamel measuring just $2.5 - 2.75 \text{gcm}^{-3}$. In the OCT image, there is a region which is highly scattering (red arrow in OCT image (D) in figure 6.12). In the XMT image, there is no prominent feature on the enamel surface that can be seen on this region that causes this increased scattering. However, very small sized red spots which are difficult to see without magnifying the image can be seen in XMT image (d) in figure 6.12, red arrows.

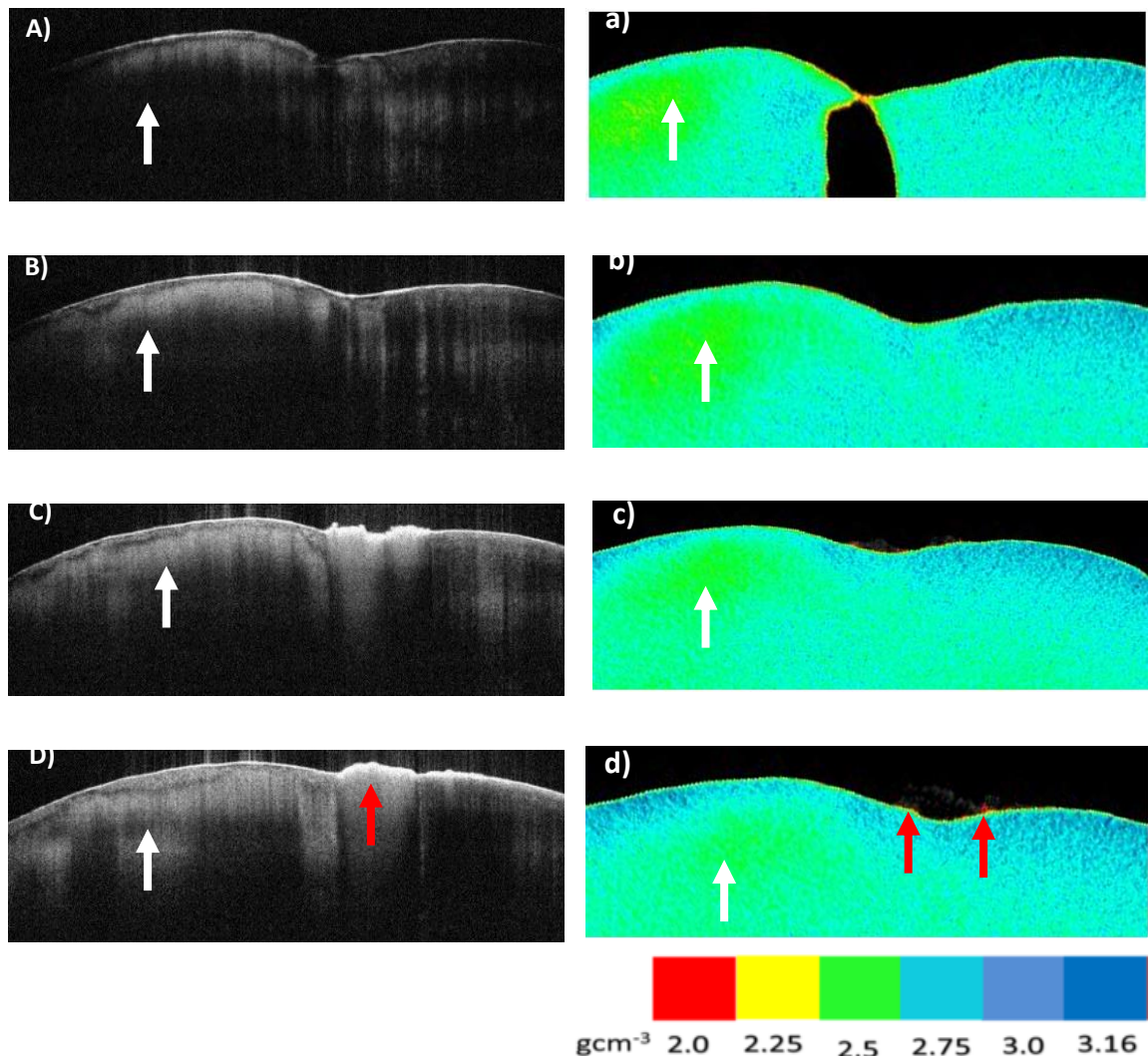


Figure 6.12 Distal surface of MIH 67 showing type 2 MIH defect (white arrows); as seen in other defects it has a reduced MD, but the tooth surface generally has reduced MD which is mainly in region of $2.5 - 2.75 \text{gcm}^{-3}$; the red arrows in image (d) indicate the position of the highly scattering region in image (D) which is not clearly seen in the XMT image (d).

6.1.1 Further Quantitative MD Analysis

The thickness of control and MIH affected enamel was divided into three areas as illustrated in figures 6.13A and 6.13B, respectively. LAC values were extracted from these areas in three regions across tooth surface as described previously. The mean value for MD, the total number of LAC values (n), the minimum and maximum MD values obtained and the standard deviation for each area are illustrated in table 6.3. The lowest number of LAC values was taken from surface enamel of MIH sample (n=278), whereas the highest number was from the enamel close to the EDJ in the control enamel (n=510). In general, the number of LAC values from control enamel are more than that from MIH enamel. On moving from the enamel surface to the EDJ on both control and MIH enamel, there is a downward trend in enamel MD. Also, in all areas of enamel across its thickness the MD of control enamel is higher than that in MIH enamel. For example, the average MD at the surface of control enamel is 3.01 g/cm^{-3} compared to 2.89 g/cm^{-3} at the surface of MIH affected enamel. However, the MD of enamel close to the EDJ is 2.77 g/cm^{-3} and 2.47 g/cm^{-3} for control and MIH enamel, respectively. This is clearly demonstrated by figure 6.14. It is also clearly seen that in MIH enamel the MD at the surface is considerably higher than that in the rest of the enamel.

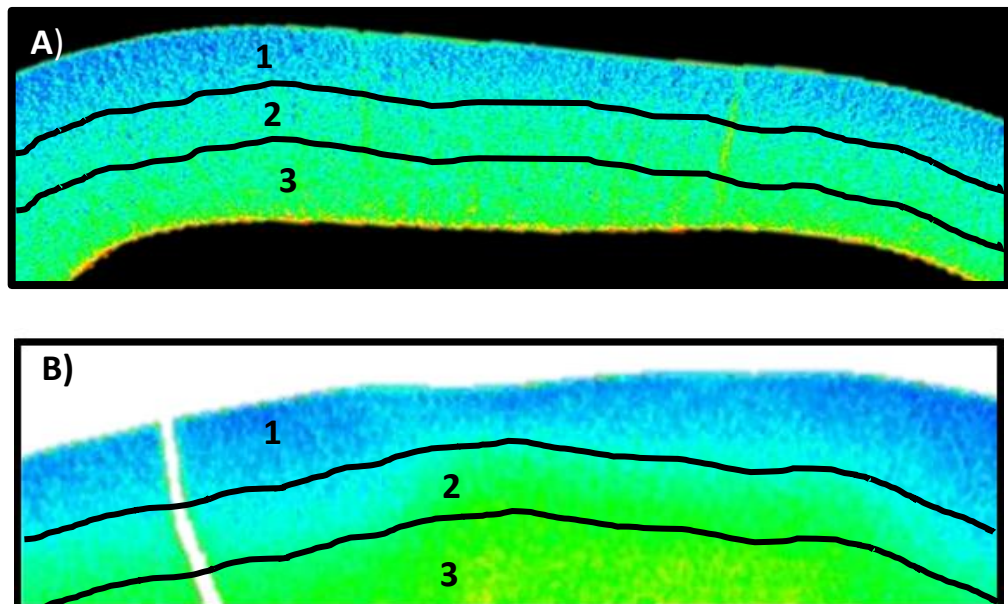


Figure 6.13 The three areas of enamel from which MD was obtained; areas (1, 2 and 3) in control (A) and MIH enamel (B).

	MD of enamel close to the surface		MD in the middle of enamel thickness		MD of enamel close to the EDJ	
	Control	MIH	Control	MIH	Control	MIH
n	337	278	438	386	510	344
Mean	3.01	2.89	2.86	2.52	2.77	2.47
Standard Deviation	0.84	0.11	0.87	0.12	0.1	0.13
Minimum	2.72	2.58	2.54	2.18	2.33	1.56
Maximum	3.24	3.15	3.11	2.79	3.02	2.79

Table 6.3 Shows values of MD in gcm⁻³ distributed in three regions across the enamel thickness from the enamel surface to EDJ in both control and MIH enamel in two examples, C129 and MIH 33; n is the number of regions on the XMT image from which LAC has been extracted in each area in enamel.

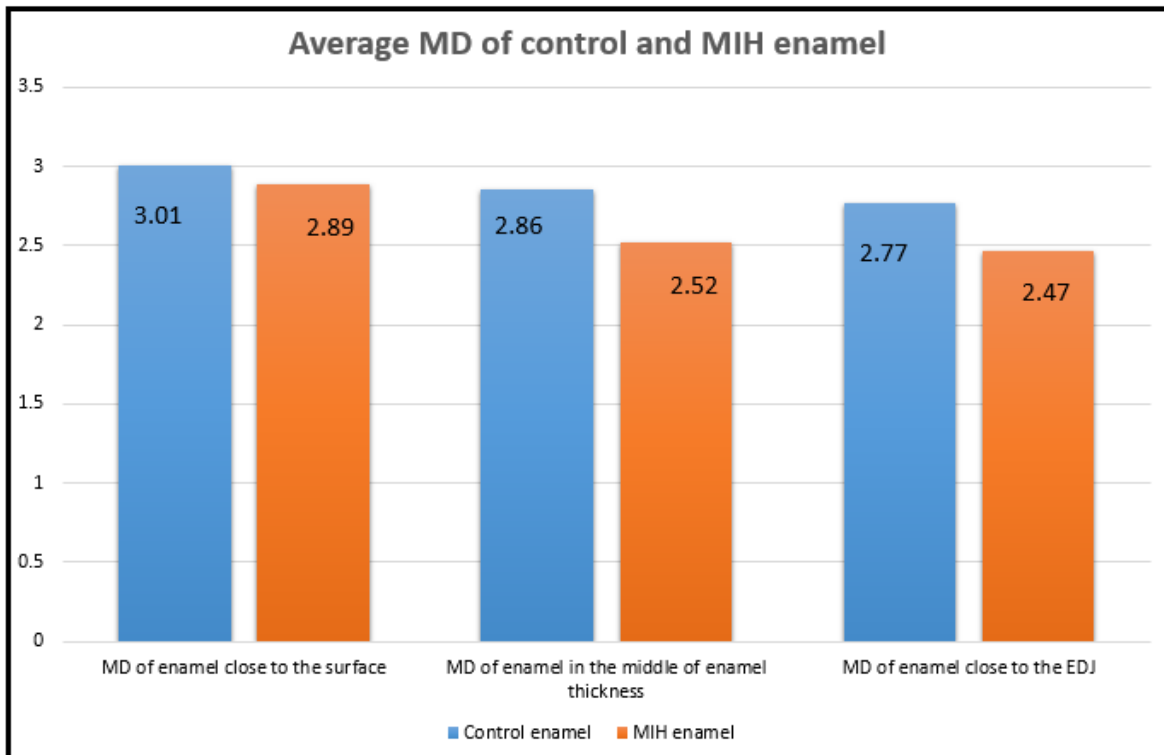


Figure 6.14 Bar graph showing the average mineral density (MD) of enamel close to the surface, in the middle of enamel thickness and close to the EDJ. The MD in control enamel is higher than in MIH enamel in all three areas across the enamel surface.

6.2 OCT and SXR

6.2.1 Disclaimer

This experiment was done in collaboration with Dr. Maisoon Al-Jawad and Dr. Samera Siddiqui from the Dental Physical Science Department, Queen Mary University of London (QMUL). The Data analysis of the experiment was done in collaboration with Mr. Mohamed Al-Mosawi, a PhD student from the same institution.

6.2.2 Method

Synchrotron X-ray diffraction experiment was conducted on the BM28 (XMaS) beamline at the European Synchrotron Radiation Facility (ESRF), Grenoble, France. Four samples were used for the experiment (figure 6.10); one control healthy FPM and three MIH affected FPM. The MIH affected FPMs were selected, so that the defects were of diffuse type1 (MIH 50), demarcated type 2 (MIH 67) and type 8 (MIH 38). The first two samples had their defects present on the distal surfaces, the later one had the buccal surface affected with PEB. Both MIH 50 and MIH 67 were matched control with the C108.

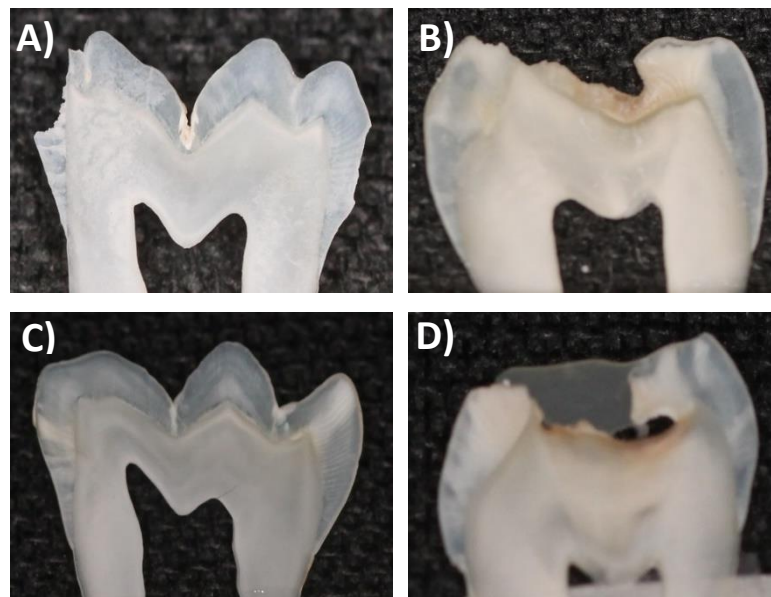


Figure 6.15 Four sample slices prepared for the SXR experiment in BM28 (XMaS) beamline at ESRF, Grenoble, France; A) C108 control FPM, B) MIH 50, C) MIH 67 and D) MIH 38; some surface enamel was lost from C108 on preparing the slice (A).

All four samples were sectioned using Accutom-5 (Accutom-5; Struers, Ballerup; Denmark) at QMUL, Dental Physical Science Department's laboratory under continuous water irrigation. Very thin sections were taken longitudinally in the mesio-distal direction of MIH 50, MIH 67 and C 108 and in the bucco-lingual direction of MIH 38; measuring 400 μm in thickness using 300 μm cutting blade. Then each section was polished manually down to between 220 μm and 240 μm using polishing papers. The tooth slices were then mounted on a card board using an adhesive tape and made ready to be used for the SXRD experiment.

The experimental set-up is shown in figure 6.11 (a) and (b) with the samples placed on a travelling platform which moves in the x and y axes. The X-ray beam had a wavelength of 0.82 \AA which is equivalent to the energy of 15.1keV. The distance between the sample and detector was 145cm allowing a 2θ range of $4^\circ - 24^\circ$. If this distance was increased more counting time would be needed and consequently, the number of diffraction patterns would be reduced as well as the resolution of the texture distribution maps.

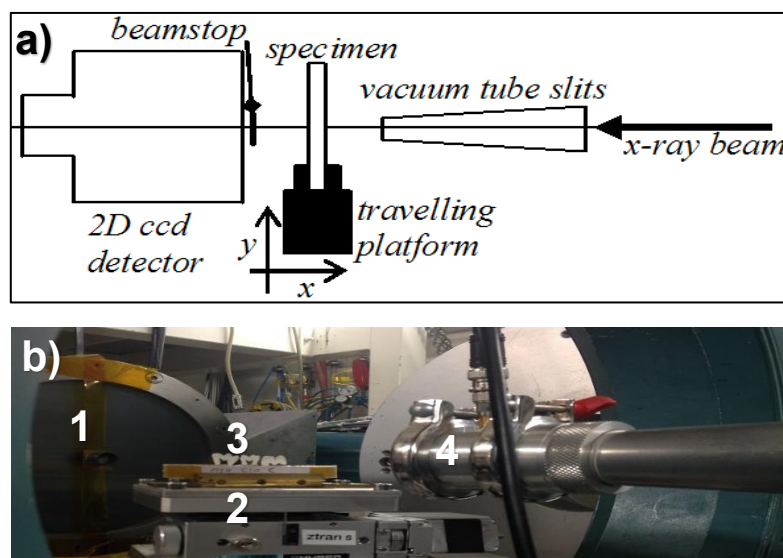


Figure 6.16 a) A schematic representation of the experimental setup at the XMaS beamline. Taken from (Al-Jawad et al., 2007); b) three samples mounted on the travelling platform ready for the experiment; 1 is a 2D CCD detector; 2 a travelling platform; 3 mounted samples and 4 the X-ray beam with a focussing slit at its end).

A vacuum tube slit focussed an incoming X-ray beam to a 20 $\mu\text{m} \times 20\mu\text{m}$ beam spot on to the mounted samples. A mar CCD two dimensional detector with a 2048 \times 2048 pixels was mounted behind the samples and at right angle to the beam, so images can be collected in transmission geometry to identify changes across small regions of

interest. The alignment of the position of the beam on the slices was done with the aid of the cross hairs of a telescope which was situated in line with the centre of the beam. Diffraction patterns were obtained as the microfocussed X-ray beam moved across selected enamel tracks (figure 6.12). Each diffraction pattern took 32 s counting time and 8 s CCD camera processing, an overall time of 40 s for each pattern.

After all diffraction patterns were obtained across all selected enamel tracks, a full crown diffraction patterns were obtained for C108, MIH 50, and MIH 67 (figure 6.13). This was taken by changing slit size to $150\mu\text{m} \times 150\mu\text{m}$ and each diffraction patterns took a total time of 5 s. The grid size for each tooth varied according to the tooth crown size. The total number of diffraction patterns collected for the tracks were 6,323 patterns. However, the number of diffraction patterns taken for the full crown was 1,778 patterns for C108, 2,171 patterns was for MIH 50 and 2,865 patterns was taken for MIH 67.

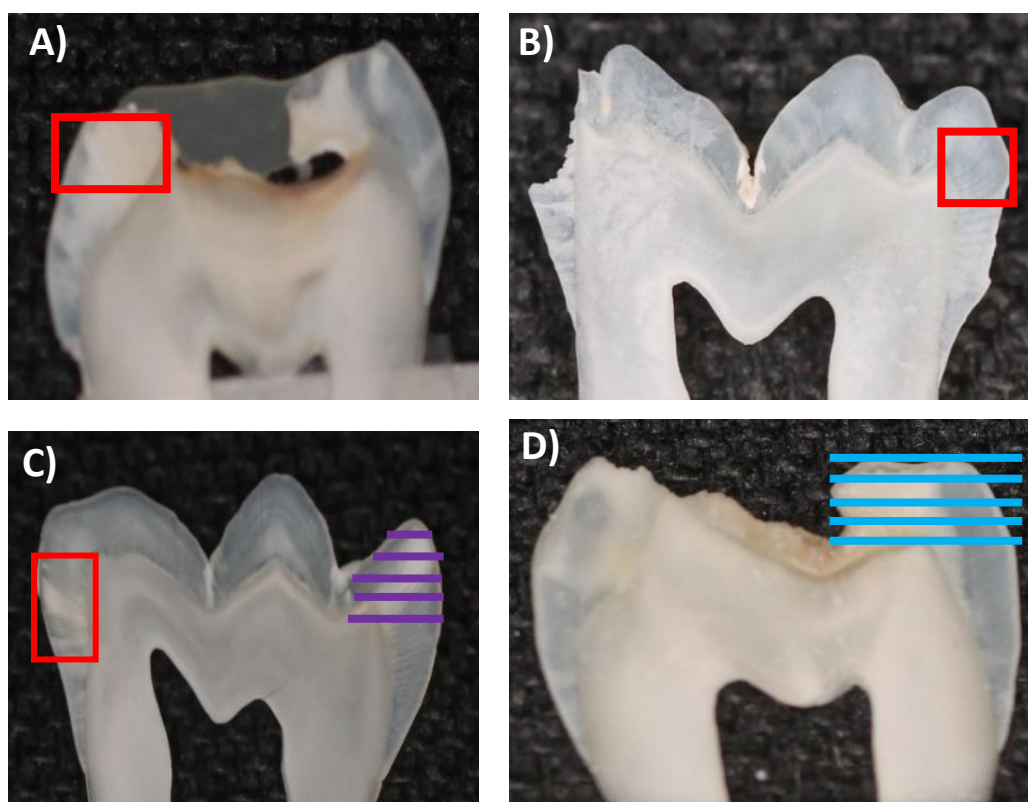


Figure 6.17 shows the four sample slices prepared for the SXR experiment in BM28 (XMaS) beamline at ESRF, Grenoble, France; A) MIH 38, B) C108 control FPM, C) MIH 67 and D) MIH 50. Boxes indicate tracks taken very close to each other, while individual tracks were more distant from each other up to $400\mu\text{m}$, all scanned areas had a track situated at the dentine horn.

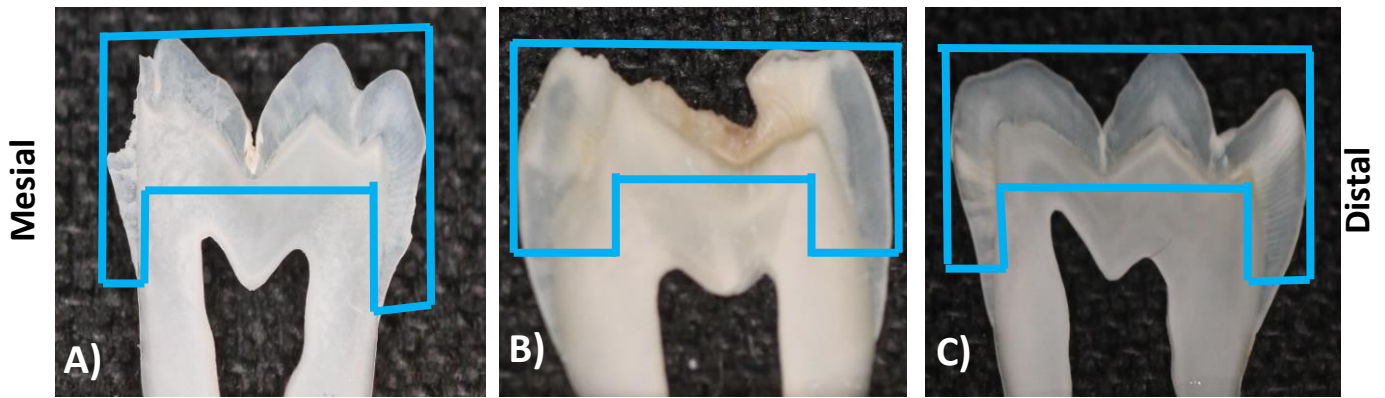


Figure 6.18 shows full crown scanned areas taken for three teeth A) C108, B) MIH 50 and MIH 67; the imaged areas were mainly confined to enamel (boxed areas)

Processing of the Diffraction Images

Diffraction images were pre-processed using the ESRF software package FIT2D (Hammersley, 1997). Diffraction images from enamel only were processed. The 002 Debye ring was selected and analysed by extracting its two peaks by using this software. As a result graphs of intensity (in arbitrary unit) versus the Azimuthal angle (in degrees) were obtained showing two peaks of intensity. These graphs were fitted to the Gaussian curve using a written in-house automated batching procedure using MatLab R2015b (MathWorks, Inc.). The MatLab analysis was done in collaboration with Mr. Mohamed Al-Mosawi from the Dental Physical Science Department at QMUL. Full Width at Half Maximum (FWHM) of peaks were extracted which is a measure of the peaks' width. Any increase in the width of these peaks compared to the control would mean a decrease in the texture of the enamel. The direction of the preferred orientation of the crystals was determined directly from the Debye ring's reflection (figure 6.14).

6.2.3 Results

There were three types of diffraction patterns obtained in the experiment, from air, enamel and dentine (figure 6.14). Enamel diffraction patterns show more crystallinity with the presence of the Debye ring (indicated with red arrows in figure 6.14B), unlike those from dentine (figure 6.14C) which have a broader peak indicating the presence of smaller crystallites and less variation in intensity around the 002 ring meaning that dentine has reduced texture compared to enamel. The determination of the preferred crystal orientation from the Debye ring can be done as illustrated in figure 6.14D.

An example of raw data of intensity peaks obtained from the 002 ring is shown in figure 6.15(A) and another example of fitted peaks in figure 6.15(B). The results of the diffraction patterns obtained from the experiment will be presented in two sections. The first section will be presenting the results from selected tracks in enamel. The second section will be looking at the data obtained from the full crowns scans.

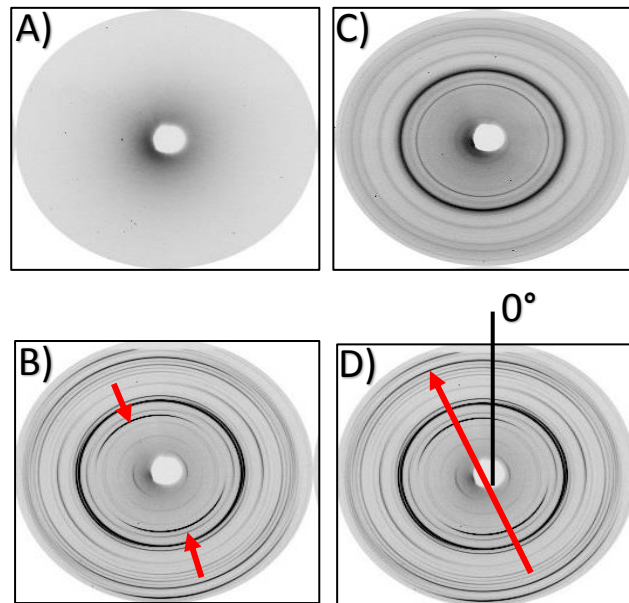


Figure 6.19 the three diffraction patterns from the SXR D experiment obtained when samples were subjected to the micro-focussed beam; A) air diffraction pattern, B) enamel diffraction patterns showing crystallinity, the arrows are indicating the Debye 002 ring which is distinctive for enamel crystals; C) dentine diffraction pattern with loss of crystallinity; D) is the determination of the preferred orientation of the crystals from the Debye ring (0° is shown) taken from AL-Jawad et.al 2007).

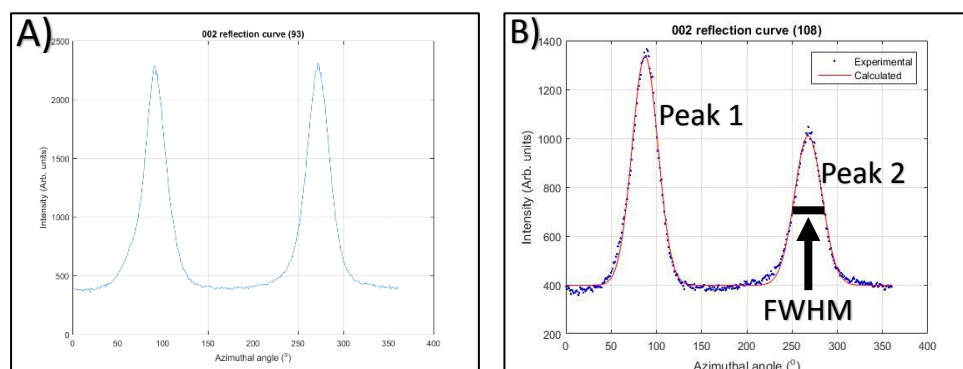


Figure 6.20 Examples of peaks obtained from the 002 Debye ring from an enamel diffraction pattern showing graphs of intensity (in arbitrary unit or AU) versus Azimuthal angle (in degrees) through the 360° ; A) graph of unfitted raw data; B) fitted graph peaks 1 and 2 of a different diffraction pattern the red line indicate the Gaussian fitting curve of the peaks. The FWHM is indicated by the horizontal black line (arrow) which is a measure of the width of the peak quantifying the magnitude of the enamel texture.

6.2.3.1 Selected Enamel Tracks Results

In every sample, one of the selected tracks was present at the dentine horn (DH). The only tracks which were comparable were those from C108, MIH50 and MIH 67, because they were taken from the distal surface whereas the track from MIH 38 was taken from the buccal surface. Figures 6.16 – 6.18 show the position of the tracks on the tooth slice (a), FWHM of the diffraction patterns obtained from the region of the enamel surfaces extending to the DH of the three samples (graph (b) in all three figures). The preferred orientation of the crystals is indicated with arrows crossing the Debye rings in the diffraction patterns (c). These diffraction patterns were taken from every fourth pattern in the track, as the number of patterns in every track was up to 200 patterns. The corresponding OCT image is shown as well with a shaded area indicating the location of the tooth slice on the image (D). With every corresponding OCT image a back scattered intensity profiles are provided to be compared with the FWHM graphs of each track.

When looking at the three FWHM graphs in all three figures, it can be noted that in general the FWHM fluctuate in the region of 20-30 and therefore a line was drawn at FWHM of 30 indicating that any value below this line is within normal range suggesting normal enamel texture and anything above it means the enamel has less texture.

Enamel track of C108 at Dentine horn

The position of the enamel track at the DH in C108 slice is shown in (figure 6.16(a)). The FWHM is fluctuating within the range of 20 – 30 in figure 6.16(b)). It slightly exceeds this range at the surface where there is air/enamel surface interface and in enamel close to the EDJ where it reaches around 40 degrees. On the meanwhile, the preferred crystal orientation changes slightly on moving from the EDJ to the enamel surface (figure 6.16(c)).

The OCT image in figure 6.16(d) shows that enamel has a uniform scattering characteristic with the absence of regions of increased light scattering. The appearance of the C108 tooth slice (figure 6.16 (a)) confirms this homogeneity of the enamel structure. The back scattered light intensity profile of the area corresponding to the position of the tooth slice on the OCT image is also shown in figure 6.16 (d). It can be seen that the profile obtained shows a gradual decrease in intensity to a depth of 625 μ m from the surface where it stays at the same level for the following 200 μ m after

which it drops in an exponential manner. The overall pattern of the profile is a gradual decline in the intensity of back scattered light.

The full length of the enamel track (1400 μm) is in fact inside the OCT depth scan window (1750 μm) and changes in the magnitude of the enamel texture (as shown by the FWHM) are not correlating well with changes in scattering intensity of enamel. However, the FWHM graph is flat and mainly in the region of the 20-30 of width, meaning that the enamel is highly textured. This can be clearly seen in the OCT *b*-scan image as the tooth structure is homogenous with absence of highly scattering structures.

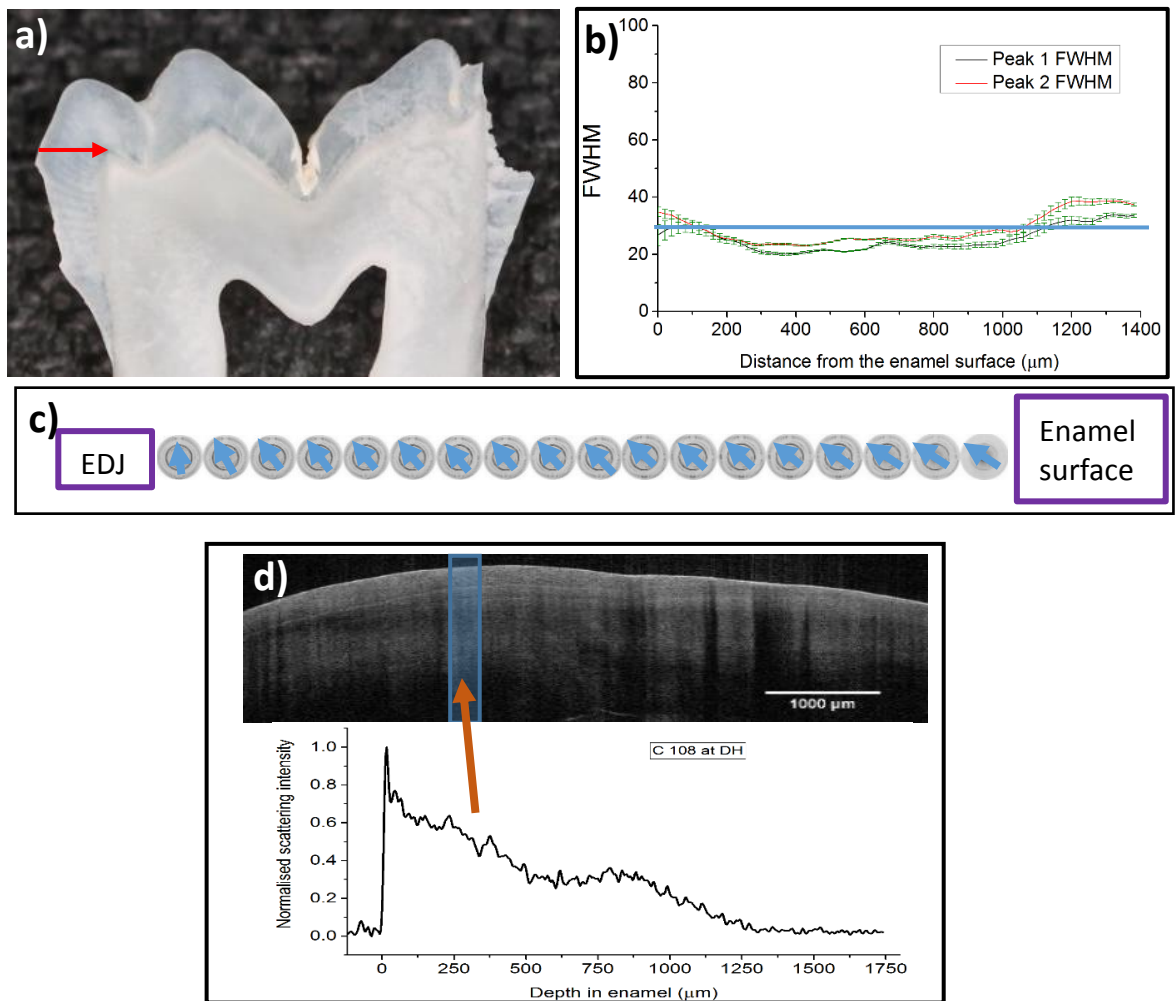


Figure 6.21 The result of the FWHM of the control healthy sample C108; a) the position of the enamel track at the dentine horn indicated with a red arrow; b) the FWHM graph of the track as a function of the distance from the enamel surface; c) the preferred crystal orientation obtained from every four diffraction patterns along the track; d) the OCT image corresponding to the position of the track at the DH, the shaded area corresponds to the position of the tooth slice in the OCT image and the back scattered light intensity profile of the area is shown. It is important to note that the SXR scale is a physical scale while the depth scale in the OCT intensity profile is an optical scale.

Enamel track of MIH 50 at Dentine horn

The enamel track at the DH in MIH 50 is demonstrated on the tooth slice in figure 6.17 (a). There are two types of MIH defects present on this sample, MIH type 1 confined to the surface and type 2 which is present on the occlusal surface of the tooth and extending to the area of the DH. The area between the two defects along the current track seems translucent and close to the appearance of healthy enamel.

The FWHM graph for this track shows distinctive peaks of increased FWHM in the same regions as for C108, but extending to a higher level (figure 6.17(b)). However, in the first 100µm from the enamel surface there is a low value FWHM of 11-12 before an abrupt increase in FWHM to around 40. Close to the EDJ the FWHM had also increased to nearly 50. The appearance of the enamel structure at this region already described conforms to the pattern of the FWHM graph. On the other hand, there is a slight change in the preferred crystal orientation at the EDJ compared to that at the enamel surface (figure 6.17(c)). This seems to be almost the same as for C108.

The OCT image corresponding to this enamel track is shown in figure 6.17 (d) and it shows an increased scattering of light at the surface, but the enamel structure below this region is not clearly visible due to the highly scattering enamel at the surface. The back scattered light intensity profile shown along with OCT *b*-scan image confirms that at the first 1250µm from the surface there is a second scattering peak present which has a lower magnitude when compared to the first air/enamel interface peak. A rapid decline in the back scattered light is seen immediately after the second peak. It is important to mention that type 2 MIH defect that is present at the DH and shows an increase in the FWHM at the end of the track close to the DH lies at the end of the OCT window of scan. Comparison between the FWHM graph and the back scattered intensity profile, the area of high scattering intensity present corresponds to a low FWHM (in the first ~ 200µm below the surface) which indicates an area of high texture organisation. However, the region below this depth shows high FWHM and consequently is of low texture and the scattering of which is not seen and a decay in intensity is seen instead. Hence the area where there is a second peak in intensity in the OCT profile (at 125microns) is an area of rapidly- changing FWHM.

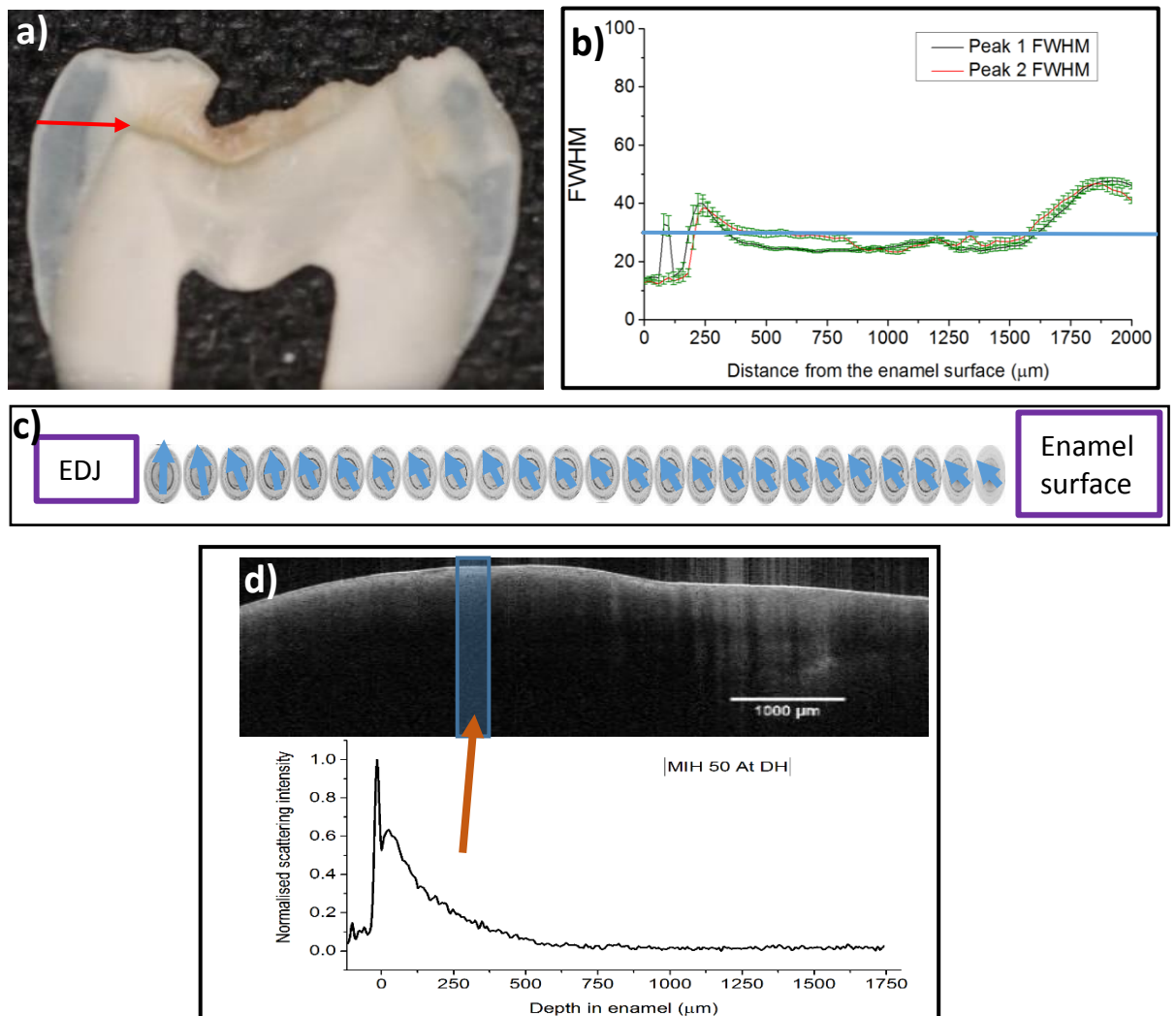


Figure 6.22 The result of the FWHM of the MIH 50 sample; a) the photographic image of the tooth slice with the position of the enamel track at the dentine horn indicated with a red arrow; b) the FWHM graph of the enamel diffraction patterns obtained from the same track as a function of the distance from the enamel surface; c) the preferred crystal orientation of every four diffraction patterns from the EDJ to the enamel surface; d) the OCT image corresponding to the position of the track at the DH, the shaded area corresponds to the position of the tooth slice in the OCT image, below is the back scattered intensity profile of the shaded region. It is important to note that the SXRD scale is a physical scale while the depth scale in the OCT intensity profile is an optical scale.

Enamel track of MIH 67 at Dentine horn

This track is shown in figure 6.18 (a). It is closely related to the MIH type 2 defect running from cusp of the tooth to the DH in a diagonal direction. The track crosses the defect at the area of the DH. The FWHM graph in figure 6.18 (b) shows a slight rise in FWHM at the surface which drops quickly down to around 20 degrees at 400μm from

the surface where it stays at this level for some distance. A second rise in FWHM is seen at around 1800 μm where it goes up to 45 degrees and then drops back to 20. At the end of the track there is a final rise to 40. The rise in FWHM as 1800 μm is coincident with the visual appearance of the enamel in this region that can be seen clearly as more opaque in the photographic image of the tooth slice in figure 6.18(a).

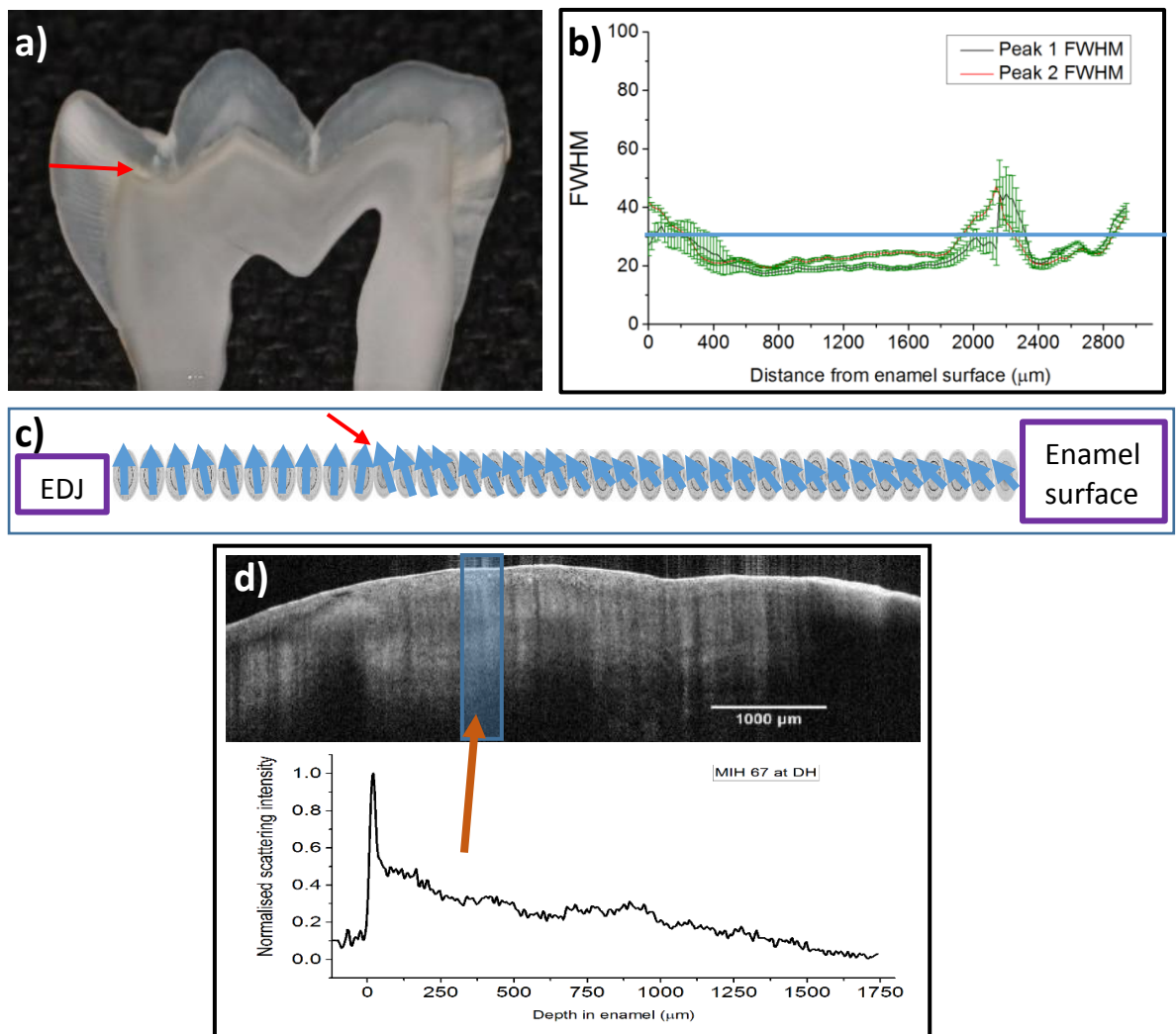


Figure 6.23 The result of the FWHM of the MIH 67 sample; a) the photographic image of the 240 μm thick slice with the position of the enamel track at the dentine horn indicated with a red arrow; b) the OCT image corresponding to the position of the track at the DH, the shaded area corresponds to the position of the tooth slice in the OCT image; c) the FWHM graph of the enamel diffraction patterns obtained from the same track as a function of the distance from the enamel surface; d) the preferred crystal orientation of every four diffraction patterns from the EDJ to the enamel surface. It is important to note that the SXR scale is a physical scale while the depth scale in the OCT intensity profile is an optical scale.

The preferred crystal orientation seems almost the same as for the previous two samples. However, in MIH 67 there is a sudden unexpected change in the preferred crystal orientation (red arrow in figure 6.18(c)). This seems to be co-incident with the enamel lesion present on the tooth slice in this region.

The OCT image (figure 6.18(d)) shows a slight change in light scattering at the surface. However, the deeper enamel does not seem too much affected. The second peak present in FWHM which starts at a distance of 1800 μm lies outside the OCT window of scan. This is confirmed by the back scattered intensity profile where the maximum depth of scan is 1750 μm . The pattern of light scattering profile seems to resemble that of a control healthy enamel with no sign of any scattering feature along the position of the tooth slice that may correspond to the increase in FWHM at the surface.

Further MIH 67 Distal Tracks

The MIH lesion on the distal surface of the MIH 67 sample seems to be an interesting MIH defect. As mentioned earlier it starts at the external surface of the tooth and ends at the dentine horn in an oblique direction (figure 6.10 (c) and figure 6.18). The tracks of the diffraction patterns were taken across this region. The distance between each track was 400 μm . However, the track which was discussed earlier was at the dentine horn and the tracks above this level are discussed in this section. Table 6.3 lists these tracks and the distance between them and the DH. At the end of this section, a comparison between the back scattered intensity profiles are compared with the FWHM graphs of the second peak. One peak was selected for the ease of comparison as the two peaks behaved almost in an identical way.

MIH 67 Tracks	Distance from the DH
Track A	1600 μm
Track B	1200 μm
Track C	800 μm
Track D	400 μm

Table 6.4 list of the MIH 67 tracks present above the level of the dentine horn (DH).

Track A

This enamel track crosses the lesion close to the cuspal region (figure 6.19A (a)). It started on the occlusal enamel surface and ended at the distal enamel surface. The distal enamel surface will be referred to as the 'enamel surface'. From the position of the track (red line in figure 6.19 Track A (a)), nearly half of the track involves the MIH enamel defect. The OCT image of the area of the track (figure 6.19 Track A (b)) does not show the whole depth of the enamel, but the area close to the surface shows fluctuation in the intensity of back reflected light related to the lesion (blue shaded area). The FWHM graph in figure 6.19 Track A (c) show that close to the enamel surface (<200 μ m) the two peaks extracted from the Debye ring of the enamel diffraction pattern behaved differently. Peak one had a lower and constant FWHM at 20 degrees while the second peak starts with a FWHM of around 35 degrees and gradually dropped to 20. Both peaks have the same width of 20 degrees until a distance of about 1200 μ m from which Peak's width have increased to around 45. The crystal orientation along the track is shown in figure 6.19 Track A (d). Its direction changes gradually as moving from the enamel surface towards the other end of the track.

Track B

This track is a longer track than track A, due to the enamel thickness in this area (figure 6.19 Track B (a)). The OCT image (figure 6.19 Track B (b)) shows an increased scattering region very close to the enamel surface. The amount of enamel shown in this image is more than that for track A in image 6.19 Track A (b). From figure 6.19 Track B (c), it can be seen clearly that the overall width of the two peaks present in the FWHM graph fluctuates around 25 degrees. However, it reaches almost 40 degrees at a distance of 1800-1900 μ m from the enamel surface. There is a final rise in FWHM at the end of the track. The texture orientation of the of enamel crystals is behaving in the same way as for track A.

Track C

The position of this track is shown in figure 6.19 Track C (a). The length of this track is the same as for track B. The OCT image shows scattering of light throughout the depth of the enamel. With a thicker distinct subsurface layer compared to that seen in the region of track A and B as shown in figure 6.19 Track A (b) and figure 6.19 Track B (b),

respectively. The FWHM graph in figure 6.19 Track C (c) shows the same increase in width of peak 2 at the surface, but to a higher level of around 45 degrees. An upward trend is seen in both peaks starting at a distance of around 750 μ m from enamel surface reaching a peak at a distance of 1500 μ m with a width of nearly 40. From this region the FWHM has fluctuated around a value of 30 before it drops to 20. The texture orientation of the of enamel crystals is behaving in the same way as for tracks A and B (figure 6.19 Track C (d)).

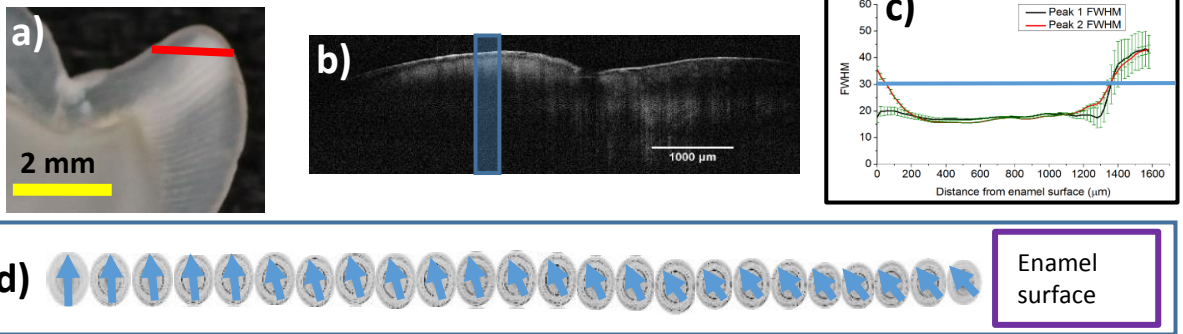
Track D

Track D is shown on the tooth slice in figure 6.19 Track D (a). The MIH defect is almost in the middle third of the track. The OCT image of the region of the track (figure 6.19 Track D (b)) shows the light scattering is almost uniform throughout the depth of enamel and the subsurface band that was present in the images of the previous tracks is no longer present. However, this area exhibits a higher scattering intensity than in other track regions. The FWHM graph in figure 6.19 Track D (c) shows the same width of the peaks seen at the surface as in other tracks with a gradual decrease to below 20 at a distance of 500 μ m from the enamel surface. From this region, there is an upward trend in the width of the peaks on moving along the track. The preferred crystal orientation in this track is not different from that seen in other tracks (figure 6.19 Track D (d)).

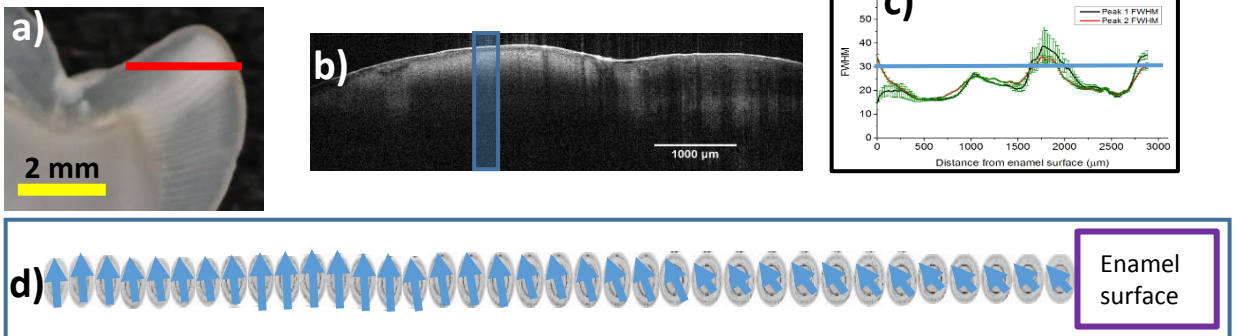
As already mentioned, a comparison between the FWHM of the second peak and the back scattered light intensity profiles are compared in an attempt to see if there was any correlation that can be found between the two. Another comparison is made at the same time which is to find out if there is a correlation between the FWHM and the opacity/translucency pattern of the defect seen on the photograph of tooth slice. This is done by comparing the series of FWHM graphs. These comparisons are shown in figure 6.20.

The FWHM graphs show fluctuations across the enamel tracks (figure 6.20) especially in track B, C and D. The fluctuation regions are highlighted to identify them from the rest of the regions in the graphs. These shaded areas in tracks B, C, and D start at about 1400 μ m from the surface and end up at around 2800 extending across nearly 1400 μ m. The pattern of these areas (shown by the two blue large arrows in figure 6.20) seems to some extent to conform to the shape of the MIH defect shown in figure 6.22 (blue lines stand for the defect margins).

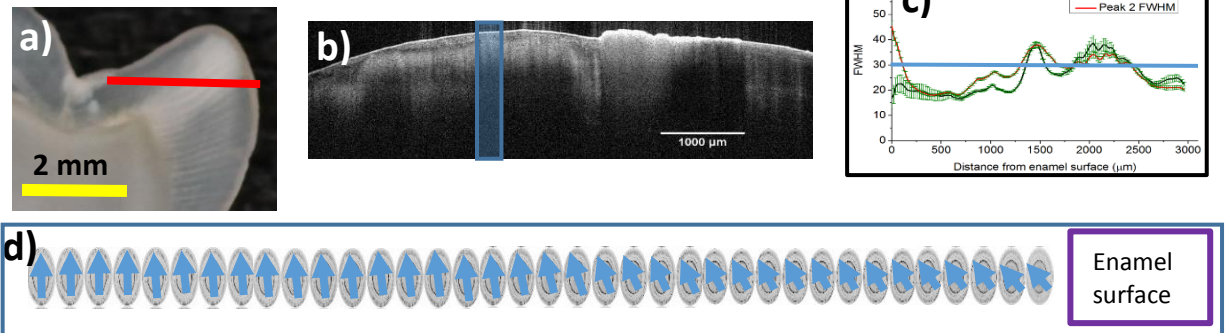
Track A



Track B



Track C



Track D

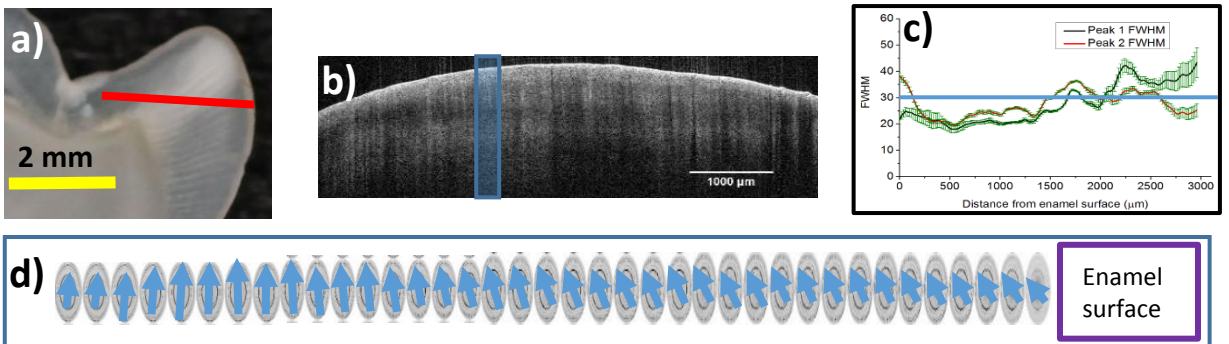


Figure 6.24 four tracks taken from MIH 67 Distal surface which has demarcated Type 2 Defect; Track A is the highest track and Track D is the lowest and the closest one to the dentine horn; in all tracks: a) shows a red line indicating the position of the track; b) OCT image at the level of the track and the shaded area is the position of the tooth slice; c) the FWHM graph; d) the preferred crystal orientation. It is important to note that the SXR scale is a physical scale while the depth scale in the OCT intensity profile is an optical scale.

The back reflected light intensity profiles in the track areas show a second peak immediately after the first air/enamel interface intensity peak (figure 6.20). However, this second peak is more noticeable in tracks A and B, and in track C it is flat. On the other hand, it is absent in track D and there is no sign of increased scattering after the enamel/air interface peak. The presence of the second peak in the intensity profiles of tracks A,B and C which extends to the first 500 μm from the enamel surface corresponds to the presence of the increased FWHM in this region in the FWHM graphs in figure 6.20. Meanwhile, the increase in FWHM in track D did not correlate to the intensity profile for the same track. Even though there was fluctuations in FWHM in the FWHM graphs, these fluctuations are not seen in the intensity profiles. However, the intensity profile of track D shows slight fluctuation which is negligible.

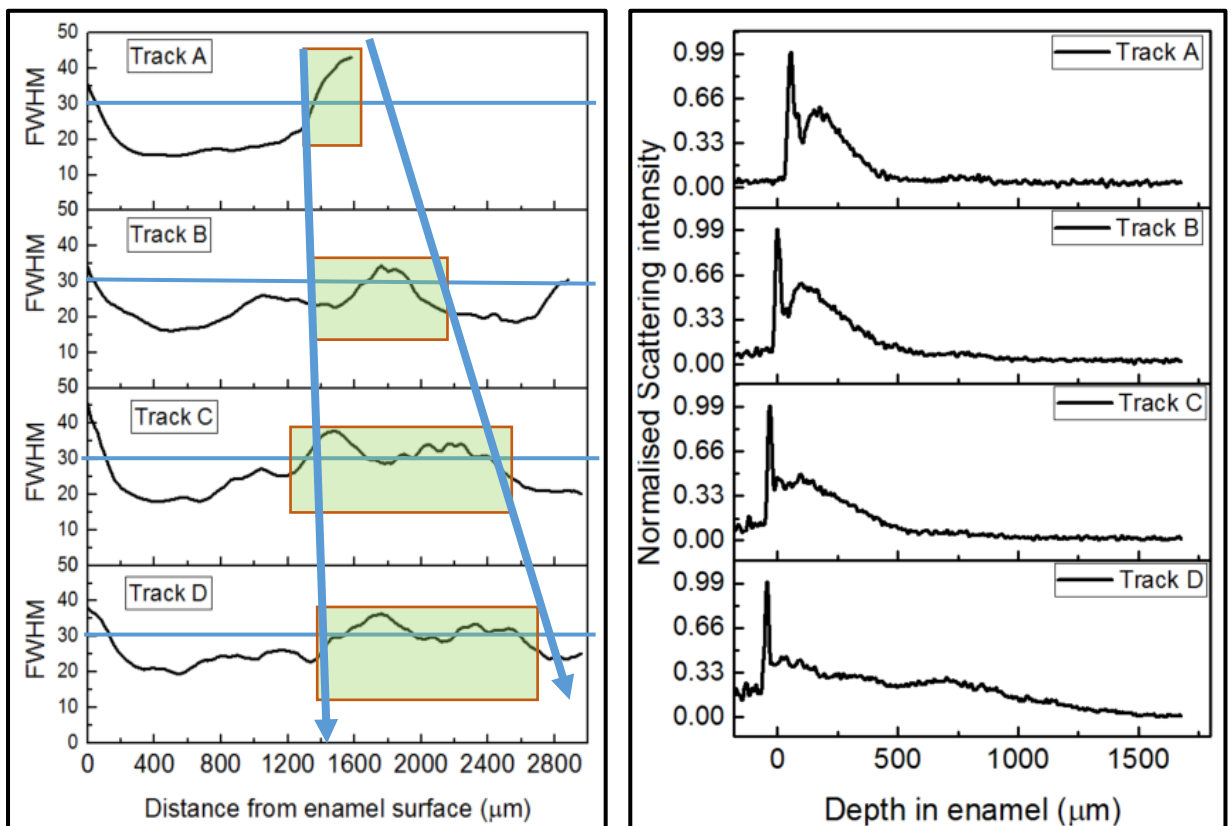


Figure 6.25 A comparison between the FWHM of the second peak from the 002 Debye ring and the intensity profile plots of the shaded blue areas indicated in the OCT images in figure 6.19; the area of fluctuating FWHM are shaded to indicate this area along the enamel track and to see if it correlate with the defect pattern, the two blue arrows indicate of the outline of shaded areas on the enamel tracks. It is important to note that the SXR scale is a physical scale while the depth scale in the OCT intensity profile is an optical scale.

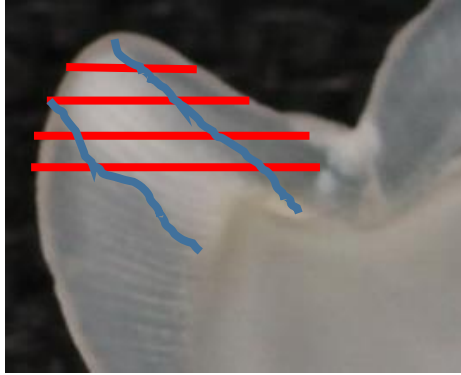


Figure 6.26 The outline of the opaque defect as it extends from the cuspal region to the area of the DH (blue lines). The pattern in which the tracks cross the defect is clearly seen.

6.2.3.2 Full crown texture results

A map of the preferred orientation angles extracted from the 002 Debye ring reflection was superimposed into a composite image of each tooth. These orientation angles are shown in every second diffraction pattern for clarity.

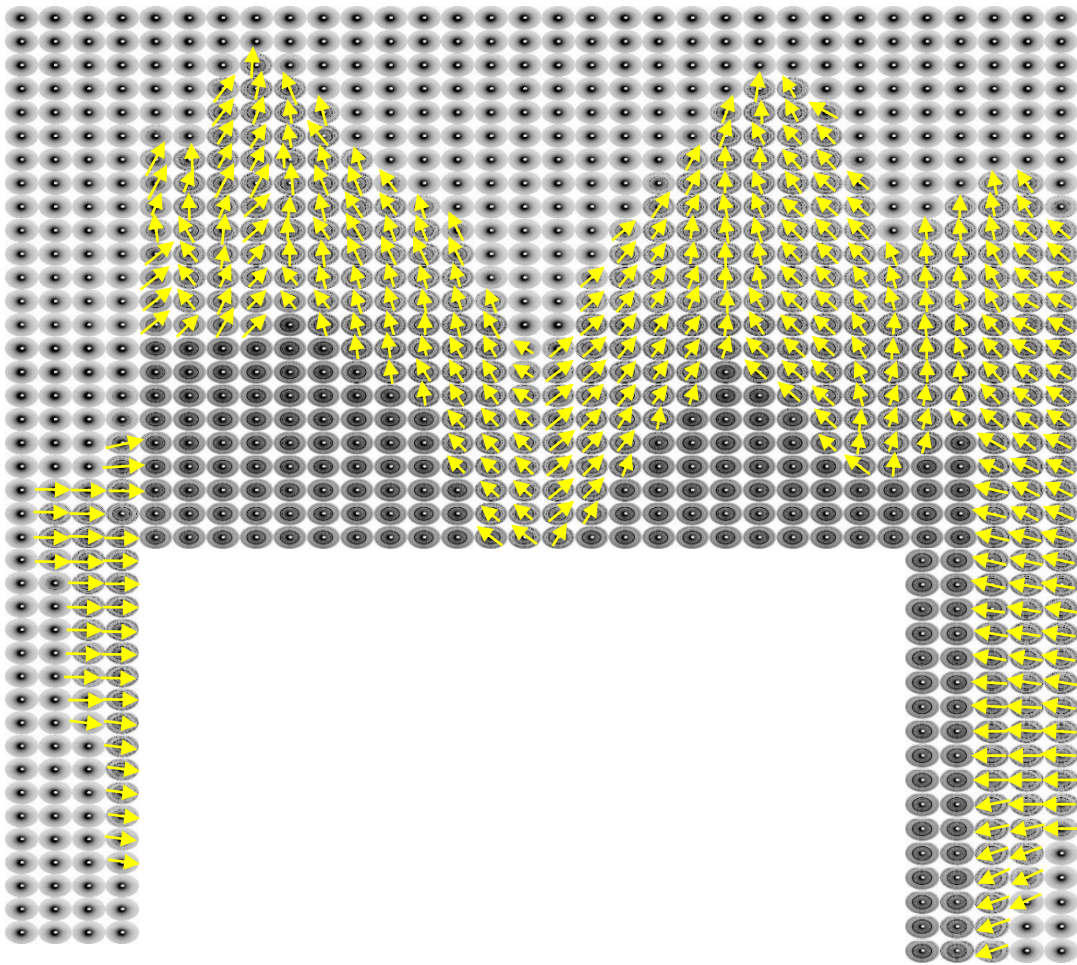


Figure 6.27 shows the preferred orientation of enamel crystals throughout the crown of C108 sample (yellow arrows) using the 002 reflection of the hydroxyapatite crystallite in enamel taken from the 2D diffraction images.

Figure 6.22 shows the orientation angles map of C108 sample. In the cervical third of both mesial and distal surfaces of the tooth slice, it can be seen that the preferred orientation or texture is perpendicular to the EDJ throughout the enamel thickness. There is a slight change in orientation in the middle third of the distal surface on moving from the cervical region. Due to loss of enamel on the mesial surface of the tooth, it was not possible to assess the preferred orientation on this surface. However, on the occlusal third of both surfaces, the preferred orientation of the crystals is mainly directed towards the centre of the cusps. In the fissure region the crystal orientation is directed away from the fissure.

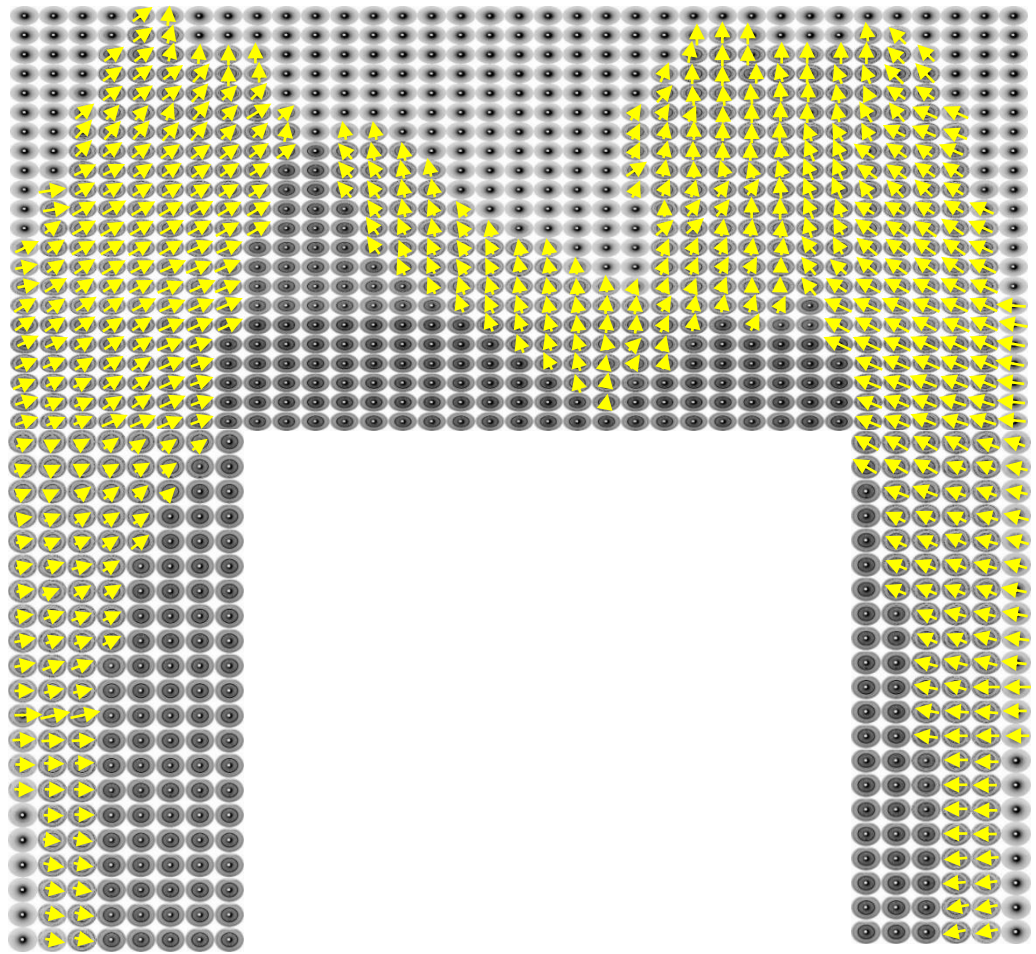


Figure 6.28 shows the preferred orientation of enamel crystals throughout the crown of MIH 50 sample (yellow arrows) using the 002 reflection of the hydroxyapatite crystallite in enamel taken from the 2D diffraction images.

Figure 6.23 shows the texture mapping of the MIH 50. The preferred orientation of the enamel crystals in the mesial and distal sides of enamel is almost the same as the one seen in C108 except that the crystal orientation at the distal side of the occlusal surface is at right angle to the occlusal surface.

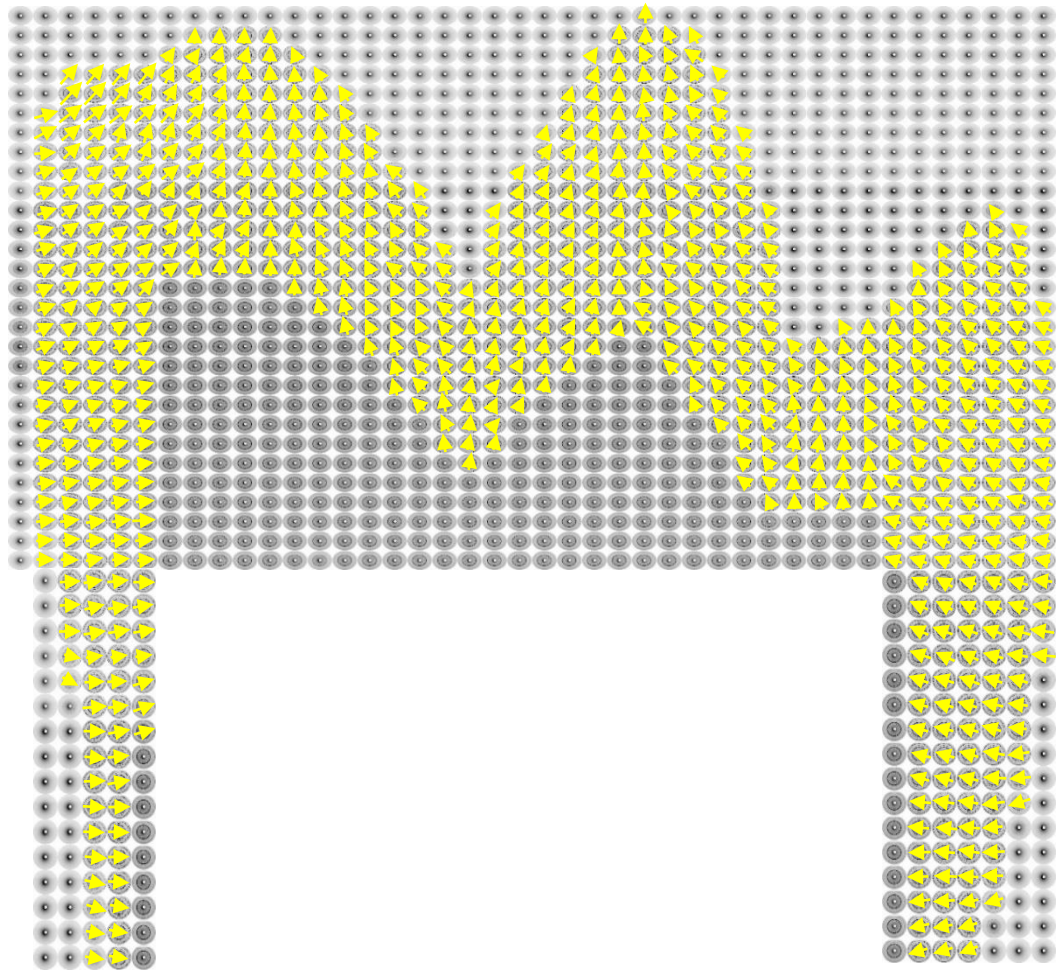


Figure 6.29 The preferred orientation of enamel crystals throughout the crown of MIH 67 sample (yellow arrows) using the 002 reflection of the hydroxyapatite crystallite in enamel taken from the 2D diffraction images.

The texture mapping for MIH 67 is shown in figure 6.24. In this sample, the texture orientation is almost the same as in C108 and MIH 50.

6.3 Discussion

X-ray Microtomography

X-ray Microtomography technique gave an insight into the structure of MIH enamel as well as a better understanding of the behaviour of the Optical Coherence Tomography

imaging modality when imaging MIH affected teeth. It has evaluated the MD of enamel in both control and MIH affected FPMs. This evaluation was done both quantitatively and qualitatively by presenting colour mapping of the XMT images representing the MD values.

The values used in calculating the MD of enamel were taken from the MD measurement done by Davis et.al (2013). They reported that the density of 100% HA is 3.17 - 3.16 gcm⁻³ using XMT which was 0.7% higher than the calculated density of the discs of pure HA. They also reported that the LAC of pure HA was 3.12 – 3.13 cm⁻¹. The error in calculating the density using XMT with the current calibration technique was 1-2% (Davis et al., 2015), compared to 15% with the use of the conventional calibration technique (Davis et.al. 2013).

Control enamel MD measured to be in 2.75 - 3.16 gcm⁻³ close to the surface. However, the MD close to the EDJ was lower with a value of 2.5 gcm⁻³. This MD gradient was reported in the literature by several authors. Farah et.al has reported that MD was highest midway between DEJ and outer enamel in healthy teeth measured by XMT and it was in the range of 2.37 – 2.62 gcm⁻³ (Farah et al., 2010a). Other researchers reported somewhat similar range of MD of healthy enamel in the range of 2.4 – 2.99 gcm⁻³ (Huang et al., 2007, Wong et al., 2004, Clementino-Luedemann and Kunzelmann, 2006, Dowker et al., 2003, Dowker et al., 2004, Anderson et al., 1998). The MD gradient was reported to increase from the EDJ to the enamel surface (Fearne et.al, 2004). However, Farah et.al found that the range of MD of enamel they reported increased in going from the cervical region to the cusps of the teeth (Farah et al., 2010a); and Wong et.al reported a an increasing gradient from the EDJ to the surface in primary teeth with an average of 3,66 gcm⁻³ per 1µm (Wong et.al, 2004).

In this study the MD in MIH affected FPMs was measured to be in the region of 2.25 and 2.75 gcm⁻³ with an increasing gradient going from the EDJ to the enamel surface. Other authors reported a decreasing MD going from the EDJ to the surface enamel (Fearne, 2004; Farah 2010), with Fearne et.al reported MD of 1.9 at the DEJ and 2.3 gcm⁻³ at the surface. Most of the studies in the literature compared healthy enamel with white spot lesion and only few which compared it with MIH affected enamel.

The MD gradient across the distance between the EDJ and the enamel surface was evenly distributed in healthy enamel. However, this is not the case in MIH affected enamel. The gradient of MD distribution across the MIH affected enamel was disrupted to the extent that only thin layer of high MD could be seen at the surface with the rest of the enamel being of low MD. This finding lead to another important finding when

comparing the XMT and OCT images of MIH lesions. In OCT, in some MIH lesions there was two distinct regions in enamel a superficial region and deep one. The superficial region is always of higher MD and the deeper region is of lower MD, with the higher MD region may become totally absent. These areas of absent high mineral density were in fact the regions where the MIH defect was clinically visible as a demarcated lesion on the tooth surface. In this regards, the appearance of the MIH lesions in both techniques were easily matched. These findings were supported by the quantitative MD analysis which confirmed the presence of mainly two areas of different MD when moving from enamel surface to the EDJ; with enamel close to surface having higher MD than the rest of the enamel.

When diffuse type one defect was compared in OCT and XMT the finding was different. The surface enamel had a low MD compared to the rest of the enamel thickness which was of higher MD (figure 6.8). This was not the case when the diffuse type 1 defect on the distal surface of MIH 50 investigated. In fact, it had a higher mineral density than any other part of the surface in the imaged region. The reason for this could be the aetiology of this defect which could be due to fluorosis instead of MIH. Fluorosis is a mineralisation defect of enamel due to high amount of fluoride exposure of the individual during tooth development and therefore it is associated with high level of fluoride intake (Weerheijm, 2004). Fluorosis usually has a diffuse appearance (Weerheijm, 2004) and as a result it can easily be mistaken with a MIH lesion.

The comparison between the OCT and XMT images had yielded an important correlation of both imaging techniques. However, OCT can be used for MIH diagnosis, but not XMT. This is due the high radiation hazard associated with XMT as it uses X-ray radiation. As described earlier, XMT imaging takes very long time up to 14 hours of scan.

Synchrotron X-ray Diffraction

Synchrotron X-ray diffraction is an advance technique which looked at the level of crystal orientation in enamel. This was investigated to find out if the behaviour of light observed, when teeth were imaged with OCT, is due to the organisation of enamel crystal. In this experiment, it was important to identify and select an appropriate control specimen to match the MIH affected specimens. Each sample and its control have to be matched with regards to tooth type, tooth location and tooth surfaces investigated. This is because the crystal orientation is different from one tooth type to another and

spatially within a tooth (both inter- and intra- heterogeneity) (Al-Jawad et.al, 2007; Simmons et.al, 2011). In the current research project, it was possible to compare C108, MIH 50 and MIH 67 because they were appropriate sample-control pairs. However, MIH 39 was not matched with a proper control and as a result the data obtained were not included here.

Two types of data were looked at, data obtained from the enamel tracks and those obtained from the full crown of the tooth slices. The analysis of both these data showed that the lesions do not affect the crystal organisation direction shown by the preferred crystal orientation or texture. The crystal orientation obtained from the enamel tracks coincided with the directions obtained from the full crowns.

The magnitude of the enamel texture is presented here using FWHM. There was a sharp increase in FWHM at surface in most of the MIH tracks which means that there is a sharp magnitude of texture which correlated to high scattering of back reflected light in OCT. Therefore we can use OCT in measuring the sharp gradient of FWHM or the crystal organisation. The analysis of the enamel track at DH in C108 the FWHM graph showed a flat line which correlated with the OCT image appearance which had a uniform light scattering appearance as well as the Intensity profile which showed a gradual decrease in back scattered light intensity in down the depth of enamel. However, in MIH 50 the FWHM showed variation along the enamel track. An interesting finding is that the first 200 μ m from the enamel surface showed reduced FWHM. This indicates that the enamel crystals in this region is well organised with high texture. This could well correlate with the high MD found in this region from the XMT analysis (figure 6.9) and possibility that this surface is affected with fluorosis instead of diffuse type 1 enamel defect. The disadvantage of the OCT imaging that it is not possible visualise the area below a highly scattering region can be well appreciated in this case as well as in other enamel tracks shown.

The changes in FWHM in MIH 67 enamel track cannot be correlated well with the OCT image or the scattered intensity profile. This could be due to the different scales in OCT and SXR. In OCT the scale is an optical one while in SXR it is a physical scale. By converting the OCT optical scale to physical scale, better correlation can be achieved.

The comparison done between the FWHM of the four tracks in MIH 67 showed that it is possible to detect a MIH lesion by detecting the crystallite organisation magnitude. On the other hand, there is inconclusive results from the data presented in terms of the difference between type 1 and type 2 MIH enamel. This could be because we did not

have enough samples or maybe there is no difference structurally or crystallographically between the two types of MIH.

Conclusion

The changes seen in OCT images are due to changes in MD of enamel as well as a change in the magnitude of the enamel texture, but not the direction of the enamel crystallites. The shadowing present underneath some MIH defects prevent a proper correlation of these lesion using SXR. More future investigation of MIH enamel with SXR is needed with more sample-control pairs.

7 Synopsis

7.1 Rational for a better diagnostics

Molar incisor hypomineralisation is a condition that affects both first permanent molars and permanent incisors. Its aetiology is uncertain, but more likely to be a multifactorial in origin. Many factors that have systemic effect when these teeth are developing were included as causative factor. The effect of MIH on children can be as soon as these teeth erupt especially, if they are severely affected with symptoms of pain and sensitivity to heat and cold. This renders the oral hygiene to be poor as these children abstain from brushing and consequently these teeth become carious. Managing children with MIH is a complex process and requires a multidisciplinary approach. These children are usually have increased anxiety level because of the symptoms they have, as a result the behaviour management of these children should not be underestimated by the treating clinician. Therefore, this condition needs to be diagnosed at an early stage before a PEB can occur and the tooth becomes symptomatic. The need for regular reviews and monitoring of these affected teeth is part of this process with possible radiographic assessment which exposes the child to ionising radiation.

7.2 The Use of Different Diagnostic Methods in MIH

7.2.1 The short falls and the limitations of the current diagnostic methods

Clinical examination

The clinical use of the indices of developmental defects is the conventional method in describing the enamel defects in general. An example of these indices is the mDDE index. It qualitatively describes enamel defects and it is not specific for MIH. Along with the use of this index clinicians also rely on radiographic images in diagnosing such defects. Both methods have limitations which render the determination of the actual extent of the MIH lesion into the enamel difficult to determine.

Clinical examination with the aid of the mDDE index gave an account of the extent of the lesion across the surface of the enamel and no account was provided by the index of how deep is the enamel involved. Even though Farah et.al correlated the degree of discolouration with the reduction in enamel MD with yellow brown lesions having less MD than white creamy defects (Farah et.al, 2010), making the categorisation of the defects according to the defect's colour a reliable indicator of the prognosis of each lesion.

Radiographic examination

Radiographic imaging is part of the diagnostic process. The ability of a radiograph to detect the extent of the defect depends on the degree of MIH defect severity. This severity depends on the type of the defect and the extent of the enamel destruction. The more severely the enamel is affected, the more radiographic involvement can be seen. Also, tooth structures seen in radiographic images are usually superimposed on each other. Another thing to mention is the risk of ionising radiation associated with radiographic examination which is an important factor that needs to be considered and any radiographic imaging needs to be justified and optimised according to the ALARA principle. Finally, the resolution of these images is low with only gross view of the tooth structures can be seen.

7.3 A Novel approach

The need for a new diagnostic imaging modality which can give more information on the structure and extent of the enamel defects and does not involve ionising radiation is very demanding. Optical coherence tomography was investigated in this research project. This is the first time this imaging technique is utilised in diagnosing MIH affecting enamel. There was no prior information available from the literature that described such technique in diagnosing the condition. In this context, this was an exploratory project which showed the potential use of such a novel technique in investigating the diagnostic and prognostic potential of MIH which is commonly seen nowadays clinically.

Each tooth surface was investigated regardless of the extent of the lesion in an attempt to understand the interaction of light with tooth structure. This increased the sample

size to four times the number of teeth used. In return it was possible to characterise control healthy enamel from the MIH affected enamel. Also, with the use of OCT it was possible to view microscopic structures that could not be seen with the use of the conventional radiographs such as enamel fracture lines.

When MIH affected tooth surfaces were imaged using OCT, each type of the MIH defects interacted distinctively with the incident light. This was also true for the degree of demarcation of the defects. Table 7.1 shows a summary of the appearance of each type of the defects and the degree of demarcation along with a summary of the findings of the other advanced imaging techniques investigated in this study, as well as the findings obtained from the control healthy enamel. In some defect and demarcation types it was possible to clearly see the outline of the defect and the surrounding enamel as in demarcated type two defects. However, in demarcated type 1 defect it was possible to see the outline of the defect, but the enamel structure beneath it was difficult to visualise. Both diffuse type1 and type2 defects showed increased scattering intensity at the surface, but the enamel structure beneath these areas was not clearly visible and dark. Type 8 defects showed focal dark areas associated with fracture lines.

7.4 Correlating the OCT results with other advanced imaging techniques

To understand these OCT findings, it was important to investigate the present samples with other advanced imaging modalities used in dental research. The first imaging technique was X-ray microtomography or XMT which is used to investigate both the structure and mineral content or density (MD) in a mineralised structure. Comparison between healthy control and MIH affected samples was done and it was found that the mineral content of the MIH affected FPMs was lower than that of a healthy control. Also, a gradual MD gradient was found in a healthy control enamel unlike in MIH affected enamel where this gradient was sometimes absent with full thickness of enamel has low MD. Correlation between OCT images and XMT images for the same regions of MIH lesions was done and it was possible to match between images of the two imaging modalities. In fact, it gave us somewhat a clear explanation of the appearance of OCT imaging seen for each type of enamel (Table 7.1).

The second imaging modality with which the structure of the healthy and MIH affected enamel was investigated was Synchrotron X-ray Diffraction or SXR. In this technique,

enamel was investigated at its crystal level and their spatial orientation was determined. The direction of the enamel crystallites did not change when it was compared between that in MIH enamel and control enamel in same surface of the tooth. However, the magnitude of the crystalline organisation of the enamel (by looking at the FWHM values obtained from the diffraction patterns) varied between MIH and control enamel. It was also possible to use the FWHM values as indicators of the MIH enamel defects in a track of SXRD diffraction patterns in enamel.

Table 7.1 Summary of the findings of OCT, XMT and SXR D investigations on MIH affected teeth according to defect and demarcation types

Tooth/defect Type	Demarcation Type	Appearance in OCT image	XMT findings	SXR D findings
Control healthy FPMs	-	<ul style="list-style-type: none"> • Enamel and possibly dentine structures clearly seen in OCT image • No high scattering structures present throughout the tooth structure except the tooth surface, but not as scattering as in the some types of enamel defects. • Presence of enamel cracks and cracks/enamel spindles close to the EDJ. 	<ul style="list-style-type: none"> • The MD is uniformly distributed across the enamel surface, with an increasing gradient from the EDJ to the enamel surface. • This MD distribution corresponded well to the uniform scattering of enamel in OCT 	<ul style="list-style-type: none"> • The direction of crystal orientation showed gradual change across the distance from the enamel surface • The magnitude of the crystal direction in the form of the FWHM of the diffraction patterns showed minimal change across the distance from the enamel surface • This corresponded well with the uniformity of the enamel appearance in OCT
Type 1 (Creamy white)	Diffuse	<ul style="list-style-type: none"> • Thin subsurface area showing an increase scattering of light • The enamel structure beneath this area is not visible making the evaluation of enamel structure difficult 	<ul style="list-style-type: none"> • The enamel close to the surface has low MD and the enamel below this had normal level of MD • The lesion showed high MD which lead to the conclusion that it could be due to fluorosis 	<ul style="list-style-type: none"> • The direction of the enamel crystals was the same as that of the control enamel • The FWHM at the surface showed that the sample has a highly textured enamel while the OCT b-scan and a-signal showed a typical view of a type 1 MIH defect; this might reinforce the idea that the defect investigated is fluorosis defect and not MIH • The dark subsurface region made correlation of the pattern of the FWHM beyond the subsurface region difficult.
Type 1 (Creamy white)	Demarcated	<ul style="list-style-type: none"> • Subsurface horizontal fracture lines • The area beneath the fracture lines cannot be evaluate due as it is dark • The extent of the lesion can be evaluated 	<ul style="list-style-type: none"> • Was not investigated as the imaged samples did not have such lesion 	<ul style="list-style-type: none"> • Was not investigated
Type 2 Yellow/Brown	Diffuse	<ul style="list-style-type: none"> • There is a subsurface layer with slightly increased scattering intensity, but not as highly scattering as that of the diffuse type 1 defect • The lesion beneath this area is dark in appearance • Can be seen as lines of delamination across the enamel if the lesion is closely related to a PEB, but surface in which the lesion is present is affected with PEB • A layer of featureless enamel with the absence of the normal scattering feature of enamel and seems to be more slightly brighter than normal enamel 	<ul style="list-style-type: none"> • Was not investigated as the imaged samples did not have such lesion 	<ul style="list-style-type: none"> • Was not investigated
Type 2 Yellow/Brown	Demarcated	<ul style="list-style-type: none"> • The lesion has foci of dark areas and enamel fracture lines related to PEB 	<ul style="list-style-type: none"> • The appearance of the lesion was mainly related to the enamel MD gradient • The thickness of the mineralised enamel close to the surface was variable • Areas in which this layer was diminished or absent the lesion was clinically visible. 	<ul style="list-style-type: none"> • The direction of the enamel crystals was the same as that of the control enamel • The increased back reflected light intensity correlated with increase in FWHM at the surface. • The dark subsurface region in some OCT images of the defect made correlation of the pattern of the FWHM beyond the subsurface region difficult. • It was possible to map the defect using the FWHM of consecutive enamel tracks passing through the defect • Did not have a matching control
Type 8	-	<ul style="list-style-type: none"> • The lesion has foci of dark areas and enamel fracture lines related to PEB 	<ul style="list-style-type: none"> • The same findings as for demarcated Type 2 Defects 	

8 Clinical relevance

The use of OCT in clinical medicine has shown that this technology is an invaluable technique in clinical diagnostics. It is currently used in many medical fields since the 1990s such as ophthalmology, dermatology and endoscopy. However, in dentistry the main use of OCT is in dental research such as in *in vitro* demineralisation, remineralisation and erosion studies. It has not been investigated for potential clinical use especially for clinically diagnosing dental diseases. However, all dental studies involving OCT came to the same conclusion that OCT is an invaluable imaging tool.

MIH defects are variable in their presentation and severity. The current clinical measures that are used to diagnose the condition have their merits and limitations, and OCT can be an additional potential diagnostic aid. OCT has the advantage that it does not involve ionising radiation and it can be used at the chair side with real time imaging of the teeth. As a result, diagnosing conditions such as MIH can be done at the same time as conventional clinical examination which would take minimal clinical time. The prognosis of the affected teeth can also be evaluated in the mean while. OCT can also be used in imaging teeth after removal of the defective enamel and before restoring teeth to ensure that all defective enamel has been completely removed and the restoration will be placed on healthy enamel. This consequently enhances the durability of the restoration placed.

Our findings in this project are important in that they open the door for such techniques to be implemented in the clinical set-up in the future. We managed to assess the extent of MIH lesions in enamel in the case of the demarcated lesions and those lesions with PEB. The possibility of a complete data base in future, containing the profiles of the intensity of back scattered light of all MIH defects is another important thing to aid clinicians in diagnosing such defects.

With the current findings from the XMT imaging technique, it can be seen that the different scattering properties of the MIH defects, is likely to be related to the changes in mineral density of the enamel in relation to the defects. This information can be obtained non-invasively at the chair side which makes OCT a very effective and handy tool in evaluating MD changes in enamel.

It is important to emphasise that OCT may not totally replace the current diagnostic tools due to its limitations. The current OCT scanning probe is not intended to be used intra-orally. In fact it is a dermatological probe which could be used in the anterior teeth, but not for imaging the posterior teeth due to its bulkiness. At the moment this is

the biggest limitation for the imaging technique to be used in diagnosing MIH in FPMs. Also, increased scattering of light makes the evaluation of the full thickness of enamel difficult especially in the diffuse types of defects. Another limitation is that the depth of the scan in OCT, which is limited to 2mm. This is insufficient in areas where the enamel thickness is more than 2mm. Intra-orally, the buccal and lingual/palatal surfaces are accessible for imaging whereas the mesial and distal surfaces are difficult to image. This fact is important to consider and if these surfaces are involved the use of radiographic image is inevitable. However, imaging the occlusal surfaces is complicated by its topography. Lastly, the cost of OCT scanner is another limitation, because currently the scanner is very costly compared to the current diagnostic techniques.

9 Conclusion

Optical Coherence Tomography imaging technique can be used to investigate the extent of MIH lesions in most of the types of the lesions. Correlating this technique with XMT and SXRD enabled us to understand the behaviour of light in interacting with the tooth structure at the mineral content of the enamel and at level of the HA crystal orientation.

10 Future work

With the current results from OCT, the shortcomings of this technique needs to be investigated and looked at in future research. As mentioned earlier, the behaviour of light as it travels through the enamel structure seems complex. The different light wavelengths in the range of the near infra-red region, 850-1500nm, need to be investigated. This is important to investigate to resolve the disadvantage of the lack of viewing the entire enamel structure when imaging diffuse MIH types 1 and 2. Another option is by investigating these types of MIH defects using other types of OCT such as PS-OCT. This type is used by researchers to minimise the effect of the increased surface scattering. Any future OCT investigation of the MIH defects should focus on the defects mainly, and not imaging the whole tooth surface as was done in the current research project.

Going one step further in the use of OCT in clinical dental research is design of an intra-oral OCT scanning probe convenient for both the patient and the clinician. This design could be the same as that of a light curing machine used in curing composite filling material. This advancement in OCT would mean that a real time examination of the patients with MIH affected teeth at the chair side could be done. This step will lead to another important one, which is the use of this technique in clinical trials. Until an intra-oral probe is available, MIH in the anterior teeth could be investigated which are accessible to be scanned by the current probe. However, this scanner is large and difficult to manipulate in the clinical set-up.

The future potential use of OCT is to monitor dental restorations such as dental fillings, veneers and implants. It can also be used in monitoring plaque level on tooth surfaces. Erosion is one the conditions that have been looked at by researchers using OCT. As OCT scanner is used to diagnosed and monitor inflammatory and bullous dermatological conditions, it can be used to diagnose these conditions in oral medicine. Oral cancerous and precancerous conditions can also be diagnosed using OCT.

As part of the proposed future work, comparison between XMT and OCT depth profiles in both MIH and control enamel can investigated. Doing so, means that we will be able to do more quantitative analysis and consequentially, do statistical analysis to investigate the relationship between enamel MD and back scattered light intensity profiling.

With regards to the results obtained from the SXRD experiment. They were not conclusive when the types of MIH were compared. Therefore, a proper sample-control

pairing should be carried out. This pairing should be in tooth notation and tooth surfaces and be done in the three MIH types. Also, care should be done in preparing the samples to avoid any loss of enamel during the preparation process.

11 Scientific Dissemination

11.1 Publications

First article is in preparation for submission on September 2015

Title: The use of Optical Coherence Tomography to diagnose enamel defects

Name of Authors: Mr Khalifa Al-Azri

Dr Laurent Bozec

Dr Susan Parekh

Dr Richard Cook

Dr Maisoon Al-Jawad

Dr Frederic Festy

Journal: Journal of Dental Research (JDR)

Preparation for a second article which will be on the correlation of OCT, XMT and SXRD which will be done after October 2015

11.2 Presentations

11.2.1 Poster presentation at the International Association of Dental Research (IADR) in Boston, USA in March 2015 as shown on the next page.

Title: Advanced imaging towards better diagnostics of Molar Incisor Hypomineralisation

11.2.2 Oral Presentation at the 7th Scientific Meeting of the Head and Neck Optical Diagnostics and Intervention Society (HNODIS), accredited by the Royal College of Surgeons of England, London, UK in July 2015

Title: Correlation between optical coherence tomography, X-ray Microtomography and synchrotron X-ray diffraction for the diagnosis of enamel defects

Advanced imaging towards better diagnostics of Molar Incisor Hypomineralisation

4122

K. Al-Azri^{1*}, M. Al-Jawad², R. Cook³, F. Festy³, S. Siddiqui², S. Parekh¹, L. Bozec¹

¹ Eastman Dental Institute, University College London (UCL), London, UK.

² Institute of Dentistry, Queen Mary University of London (QMUL), London, UK

³ King's College London Dental Institute, King's College London (KCL), London, UK

* k.al-azri.12@ucl.ac.uk



Introduction

Molar Incisor Hypomineralisation (MIH) can be defined as qualitative defect of systematic origin of the enamel, involving one or more first permanent molars (FPMs), which is frequently associated with affected incisors.¹ The available diagnostic methods for MIH are clinical and radiographic examinations. However, these cannot accurately determine the extent of MIH lesions into enamel which may lead to an inaccurate prognosis. Optical Coherence Tomography (OCT) is a non-invasive and ionising radiation free technique that has been used in dentistry but not to diagnose MIH.

Aim and Objectives

- Investigate the effectiveness of OCT in assessing the extent of MIH
- Compare OCT results with imaging modalities used in investigating the ultrastructure of MIH affected FPMs, such as X-ray micro tomography (XMT) synchrotron X-ray diffraction (SXRD) and light microscopy.

Materials and methods

Ethical approval obtained and 18 teeth were collected, 9 control and 9 MIH-affected FPMs. The MIH defects were characterised using the modified developmental defects of enamel (mDDE) index. All teeth were then imaged radiographically and using OCT (VivoSight, Michelson Diagnostics, Kent, UK), XMT (Mucata2 scanner, Institute of Dentistry, QMUL) and light microscopy, before being sectioned and polished down to a thickness of 220-250 μm . SXRD was conducted on these sections at the European Synchrotron Radiation Facility (XMaS beamline, ESRF, Grenoble, France).

Results

An example of MIH affected FPM which was investigated by all imaging techniques used in the study is discussed in this section.

A) Conventional methods in diagnosing MIH affected FPMs

1) Clinical Assessment

The FPM shown in fig.1a has type 1 enamel defect (white/chalky) on the distal surface, confound to the occlusal half and is demarcated.

2) Radiographic Assessment

Radiographically, the enamel defect could not be seen clearly (fig. 1b), yet this assessment can be used to evaluate the extent of the defect.

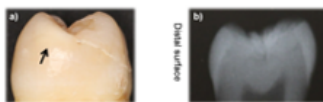


Fig. 1 a) The distal surface of a MIH affected FPM with type 1 (creamy/white) enamel defect (arrow); b) the radiographic image of the tooth.

B) OCT imaging

- non-destructive imaging system, using near infrared laser ($\lambda=1305 \text{ nm}$ - rate of scan of 10 kHz) to produce a light scattering image of the enamel ultrastructure.
- The surface area imaged by OCT was 6 mm X 6 mm and the depth of scan was approximately 2 mm as shown in fig.2. Each OCT scan consists of 600 vertical frames taken over the 6mm window.
- Healthy enamel shows a homogenous scattering throughout the enamel layer, whereas MIH affected enamel present strong localised area of scattering, which suggests superficial or internal breakdown in the enamel ultrastructure (fig. 3)

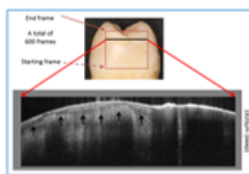


Fig. 2 An outline of the scanned area on a MIH affected FPM. The defect is indicated with black arrows.

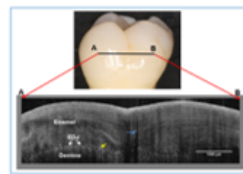


Fig. 3 An OCT image of a control FPM. Yellow arrow is enamel spindle-like structures. Blue arrow is a crack in enamel.

C. OCT imaging compared to other imaging modalities

- The XMT and light microscopy images (fig. 4) of the MIH defect show clearly the extent of the defect into enamel.



Fig. 4 a) a 220-250 μm tooth section through the defect; b) light microscopy image, c) a corresponding XMT image of the defect.

- From XMT, there is reduced mineral density related to subsurface enamel (dark area). This reduction in mineral density is less pronounced for the deeper enamel.
- The change in lattice parameter in a single track of SXRD diffraction patterns passing through the enamel defect was investigated (fig. 5).

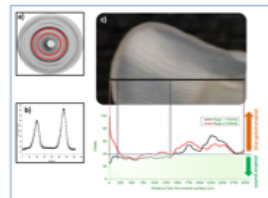


Fig. 5 Synchrotron X-ray diffraction (SXRD) of MIH enamel: a) a 2D diffraction pattern of enamel, b) 1D profile of the 2D pattern; c) a track taken at the level of the dentine horn (dark line) and below is a FWHM graph along the track. The green shaded area (FWHM $\leq 4\sigma$) corresponds to sound enamel and the region above is disrupted enamel.

- Full Width Half Maximum (FWHM) of the two peaks present in the 1D graph was taken as a measure of the degree of the enamel texture. The higher the FWHM value the broader the peaks and the less textured is the enamel². The increase in FWHM of the track shown in fig. 5c is related to the 250 μm below the surface and the deeper part of the track (deeper than 1500 μm).

Discussion

- This is the first time that there has been a correlation between Visual assessment, X-ray radiography, OCT, XMT and SXRD performed on the same sample(s).
- Conventional methods of diagnosing MIH affected teeth do not give sufficient information on the extent of the enamel defects.
- The abnormality of enamel structure in MIH teeth was demonstrated in OCT images by increased scattering.
- The XMT showed reduced mineral density related to the enamel defect shown as darker areas.
- The increased FWHM in SXRD correlated with the subsurface defect seen in OCT image.
- OCT imaging can be used in vivo with a micro-scale resolution to view detailed enamel structure and consequently, determine the prognosis of these teeth. However, OCT imaging is limited to a depth of 2mm only.

Conclusion

The change of the enamel ultrastructure as a result of Molar-Incisor Hypomineralisation is present at all scales, from the hydroxyl-apatite crystals in the enamel rod (SXRD) to the mineralization content of affected area (XMT) and even to the colour of the enamel (visual). However, this study efficiently proved that the contrast obtained from OCT imaging can be used to assess the extent of MIH defects, thus supporting the potential use of OCT as a diagnostic tool in dentistry, as other x-ray based techniques cannot be translated efficiently (or safely) to the patients' chair.

References

1. Weerheijm, K. L., Jalevik, B. & Alaluusua, S. 2001. Molar-Incisor hypomineralisation. *Caries Res*, 35, 350-1
2. Siddiqui S, Anderson P, Al-Jawad M. Recovery of Crystallographic Texture In Remineralized Dental Enamel. *PLoS One*. 2014;9(10)

Acknowledgement

Ministry of Higher Education, Oman
The Royal Army of Oman, Oman



Figure 11.1 Poster presentation done on IADR general meeting, Boston, USA, March 2015

12 References

- AL-JAWAD, M., ADDISON, O., KHAN, M. A., JAMES, A. & HENDRIKSZ, C. J. 2012. Disruption of enamel crystal formation quantified by synchrotron microdiffraction. *J Dent*, 40, 1074-80.
- AL-JAWAD, M., STEUWER, A., KILCOYNE, S. H., SHORE, R. C., CYWINSKI, R. & WOOD, D. J. 2007. 2D mapping of texture and lattice parameters of dental enamel. *Biomaterials*, 28, 2908-2914.
- ALALUUSUA, S. 2010. Aetiology of Molar-Incisor Hypomineralisation: A systematic review. *European archives of paediatric dentistry : official journal of the European Academy of Paediatric Dentistry*, 11, 53-8.
- ALALUUSUA, S., CALDERARA, P., GERTHOUX, P. M., LUKINMAA, P. L., KOVERO, O., NEEDHAM, L., PATTERSON, D. G., TUOMISTO, J. & MOCAREILI, P. 2004. Developmental dental aberrations after the dioxin accident in seveso. *Environmental Health Perspectives*, 112, 1313-1318.
- ALALUUSUA, S., LUKINMAA, P. L., KOSKIMIES, M., PIRINEN, S., HOLTITA, P., KALLIO, M., HOLTINEN, T. & SALMENPERA, L. 1996. Developmental dental defects associated with long breast feeding. *European Journal of Oral Sciences*, 104, 493-497.
- AMAECHI, B. T., PODOLEANU, A. G., KOMAROV, G., HIGHAM, S. M. & JACKSON, D. A. 2004. Quantification of root caries using optical coherence tomography and microradiography: a correlational study. *Oral health & preventive dentistry*, 2, 377-82.
- ANDERSON, P., ELLIOTT, J. C., BOSE, U. & JONES, S. J. 1996. A comparison of the mineral content of enamel and dentine in human premolars and enamel pearls measured by X-ray microtomography. *Archives of Oral Biology*, 41, 281-290.
- ANDERSON, P., LEVINKIND, M. & ELLIOTT, J. C. 1998. Scanning microradiographic studies of rates of in vitro demineralization in human and bovine dental enamel. *Archives of Oral Biology*, 43, 649-656.
- AZEVEDO, C. S. D., TRUNG, L. C. E., SIMIONATO, M. R. L., FREITAS, A. Z. D. & MATOS, A. B. 2011. Evaluation of caries-affected dentin with optical coherence tomography. *Brazilian oral research*, 25, 407-13.
- BALMER, R., TOUMBA, J., GODSON, J. & DUGGAL, M. 2012. The prevalence of molar incisor hypomineralisation in Northern England and its relationship to socioeconomic status and water fluoridation. *International Journal of Paediatric Dentistry*, 22, 250-257.

- BAUMGARTNER, A., DICHTL, S., HITZENBERGER, C. K., SATTMANN, H., ROBL, B., MORITZ, A., FERCHER, Z. F. & SPERR, W. 2000. Polarization-sensitive optical coherence tomography of dental structures. *Caries Research*, 34, 59-69.
- BEENTJES, V. E. V. M., WEERHEIJM, K. L. & GROEN, H. J. 2002. Factors involved in the etiology of hypomineralized first permanent molars. *Nederlands tijdschrift voor tandheelkunde*, 109, 387-90.
- BEI, M. 2009. Molecular Genetics of Ameloblast Cell Lineage. *Journal of Experimental Zoology Part B-Molecular and Developmental Evolution*, 312B, 437-444.
- BESIC, F. C. & WIEMANN, M. R. 1972. DISPERSION STAINING, DISPERSION, AND REFRACTIVE INDEXES IN EARLY ENAMEL CARIES. *Journal of Dental Research*, 51, 973-&.
- BOURQUIN, S., AGUIRRE, A. D., HARTL, I., HSIUNG, P., KO, T. H., FUJIMOTO, J. G., BIRKS, T. A., WADSWORTH, W. J., BUNTING, U. & KOPF, D. 2003. Ultrahigh resolution real time OCT imaging using a compact femtosecond Nd : Glass laser and nonlinear fiber. *Optics Express*, 11, 3290-3297.
- BRAGG, W. H. S. 1928. *An introduction to crystal analysis*, London, G. Bell & Sons.
- BRENNER, D. J. & HALL, E. J. 2007. Current concepts - Computed tomography - An increasing source of radiation exposure. *New England Journal of Medicine*, 357, 2277-2284.
- CHOMA, M. A., SARUNIC, M. V., YANG, C. H. & IZATT, J. A. 2003. Sensitivity advantage of swept source and Fourier domain optical coherence tomography. *Optics Express*, 11, 2183-2189.
- CLEMENTINO-LUEDEMANN, T. N. R. & KUNZELMANN, K.-H. 2006. Mineral concentration of natural human teeth by a commercial micro-CT. *Dental Materials Journal*, 25, 113-9.
- COOPER, D. M. L., MATYAS, J. R., KATZENBERG, M. A. & HALLGRIMSSON, B. 2004. Comparison of microcomputed tomographic and microradiographic measurements of cortical bone porosity. *Calcified Tissue International*, 74, 437-447.
- COX, B. 2010. A multi-scale, discrete-cell simulation of organogenesis: Application to the effects of strain stimulus on collective cell behavior during ameloblast migration. *Journal of Theoretical Biology*, 262, 58-72.
- CROMBIE, F., MANTON, D. & KILPATRICK, N. 2009. Aetiology of molar-incisor hypomineralization: a critical review. *International Journal of Paediatric Dentistry*, 19, 73-83.

- CROMBIE, F. A., MANTON, D. J., PALAMARA, J. E. A., ZALIZNIAK, I., COCHRANE, N. J. & REYNOLDS, E. C. 2013. Characterisation of developmentally hypomineralised human enamel. *Journal of Dentistry*, 41, 611-618.
- CULLITY, B. D. 1978. *Elements of X-ray diffraction*, Reading, Mass. ; London, Addison-Wesley.
- DALY, D. & WALDRON, J. M. 2009. Molar incisor hypomineralisation: clinical management of the young patient. *Journal of the Irish Dental Association*, 55, 83-6.
- DARLING, C. L., HUYNH, G. D. & FRIED, D. 2006. Light scattering properties of natural and artificially demineralized dental enamel at 1310 nm. *Journal of Biomedical Optics*, 11.
- DAVIS, G., EVERSHED, A., ELLIOTT, J. & MILLS, D. 2010. Quantitative X-ray microtomography with a conventional source. *Developments in X-Ray Tomography Vii*, 7804.
- DAVIS, G. R. & ELLIOTT, J. C. 1997. X-ray microtomography scanner using time-delay integration for elimination of ring artefacts in the reconstructed image. *Nuclear Instruments & Methods in Physics Research Section a-Accelerators Spectrometers Detectors and Associated Equipment*, 394, 157-162.
- DAVIS, G. R., EVERSHED, A. N. Z. & MILLS, D. 2013. Quantitative high contrast X-ray microtomography for dental research. *Journal of Dentistry*, 41, 475-482.
- DAVIS, G. R., EVERSHED, A. N. Z. & MILLS, D. 2015. Characterisation of materials: determining density using X-ray microtomography. *Materials Science and Technology*, 31, 162-166.
- DE BOER, J. F., CENSE, B., PARK, B. H., PIERCE, M. C., TEARNEY, G. J. & BOUMA, B. E. 2003. Improved signal-to-noise ratio in spectral-domain compared with time-domain optical coherence tomography. *Optics Letters*, 28, 2067-2069.
- DELPY, D. T., COPE, M., VANDERZEE, P., ARRIDGE, S., WRAY, S. & WYATT, J. 1988. ESTIMATION OF OPTICAL PATHLENGTH THROUGH TISSUE FROM DIRECT TIME OF FLIGHT MEASUREMENT. *Physics in Medicine and Biology*, 33, 1433-1442.
- DIETRICH, G., SPERLING, S. & HETZER, G. 2003. Molar incisor hypomineralisation in a group of children and adolescents living in Dresden (Germany). *European journal of paediatric dentistry : official journal of European Academy of Paediatric Dentistry*, 4, 133-7.

- DOWKER, S. E. P., ELLIOTT, J. C., DAVIS, G. R. & WASSIF, H. S. 2003. Longitudinal study of the three-dimensional development of subsurface enamel lesions during in vitro demineralisation. *Caries Research*, 37, 237-245.
- DOWKER, S. E. P., ELLIOTT, J. C., DAVIS, G. R., WILSON, R. M. & CLOETENS, P. 2004. Synchrotron x-ray microtomographic investigation of mineral concentrations at micrometre scale in sound and carious enamel. *Caries Research*, 38, 514-522.
- DREXLER, W., MORGNER, U., KARTNER, F. X., PITRIS, C., BOPPART, S. A., LI, X. D., IPPEN, E. P. & FUJIMOTO, J. G. 1999. In vivo ultrahigh-resolution optical coherence tomography. *Optics Letters*, 24, 1221-1223.
- DUBOIS, A. & BOCCARA, A. C. 2008. Full-Field Optical Coherence Tomography. *Optical Coherence Tomography: Technology and Applications*, 565-591.
- ELLIOTT, J. C. & DOVER, S. D. 1982. X-RAY MICROTOMOGRAPHY. *Journal of Microscopy-Oxford*, 126, 211-213.
- FARAH, R., DRUMMOND, B., SWAIN, M. & WILLIAMS, S. 2010a. Linking the clinical presentation of molar-incisor hypomineralisation to its mineral density. *International Journal of Paediatric Dentistry*, 20, 353-360.
- FARAH, R. A., MONK, B. C., SWAIN, M. V. & DRUMMOND, B. K. 2010b. Protein content of molar-incisor hypomineralisation enamel. *Journal of Dentistry*, 38, 591-596.
- FAYLE, S. A. 2003. Molar incisor hypomineralisation: restorative management. *European journal of paediatric dentistry : official journal of European Academy of Paediatric Dentistry*, 4, 121-6.
- FAZEL, R., KRUMHOLZ, H. M., WANG, Y., ROSS, J. S., CHEN, J., TING, H. H., SHAH, N. D., NASIR, K., EINSTEIN, A. J. & NALLAMOTHU, B. K. 2009. Exposure to Low-Dose Ionizing Radiation from Medical Imaging Procedures. *New England Journal of Medicine*, 361, 849-857.
- FDI 1982. Commission on Oral Health, Research and Epidemiology
An epidemiological index of developmental defects of dental enamel (D.D.E index). *Int Dent J*, 32, 159-167.
- FDI 1992. Commission on Oral Health, Research and Epidemiology; (1992); A review of the developmental defects of dental enamel index (D.D.E index). *Int Dent J*, 42, 411-426.
- FEARNE, J., ANDERSON, P. & DAVIS, G. R. 2004. 3D X-ray microscopic study of the extent of variations in enamel density in first permanent molars with idiopathic enamel hypomineralisation. *British Dental Journal*, 196, 634-638.

- FELDCHEIN, F. I., GELIKONOV, G. V., GELIKONOV, V. M., IKSANOV, R. R., KURANOV, R. V., SERGEEV, A. M., GLADKOVA, N. D., OURUTINA, M. N., WARREN, J. A. & REITZE, D. H. 1998. In vivo OCT imaging of hard and soft tissue of the oral cavity. *Optics Express*, 3, 239-250.
- FELDKAMP, L. A., DAVIS, L. C. & KRESS, J. W. 1984. Practical cone-beam algorithm. *Journal of the Optical Society of America A*, 1, 612-619.
- FERCHER, A. & HITZENBERGER, C. 2002. Optical Coherence Tomography. In: Wolf E, editor. *Progress in Optics*. Amsterdam: Elsevier Science B.V., 215–302.
- FERCHER, A. & ROTH, E. 1986. Ophthalmic Laser Interferometry. *Proc SPIE*, 658, 48–51.
- FERCHER, A. F. 2010. Optical coherence tomography - development, principles, applications. *Zeitschrift Fur Medizinische Physik*, 20, 251-276.
- FERCHER, A. F., DREXLER, W., HITZENBERGER, C. K. & LASSER, T. 2003. Optical coherence tomography - principles and applications. *Reports on Progress in Physics*, 66, 239-303.
- FERCHER, A. F., HITZENBERGER, C. & JUCHEM, M. 1991. MEASUREMENT OF INTRAOCULAR OPTICAL DISTANCES USING PARTIALLY COHERENT LASER-LIGHT. *Journal of Modern Optics*, 38, 1327-1333.
- FERCHER, A. F., HITZENBERGER, C. K., DREXLER, W., KAMP, G. & SATTMANN, H. 1993. IN-VIVO OPTICAL COHERENCE TOMOGRAPHY. *American Journal of Ophthalmology*, 116, 113-115.
- FERCHER, A. F., HITZENBERGER, C. K., KAMP, G. & ELZAIAT, S. Y. 1995. MEASUREMENT OF INTRAOCULAR DISTANCES BY BACKSCATTERING SPECTRAL INTERFEROMETRY. *Optics Communications*, 117, 43-48.
- FERCHER, A. F., LEITGEB, R., HITZENBERGER, C. K., SATTMANN, H. & WOJTKOWSKI, M. 1999. Complex spectral interferometry OCT. In: ALTSHULER, G. B., ANDERSSONENGELS, S., BIRNGRUBER, R., BJERRING, P., FERCHER, A. F., GESCHWIND, H. J., HIBST, R., HONIGSMANN, H., LAFFITTE, F., STERENBORG, H. J. C. & KATZIR, A. (eds.) *Medical Applications of Lasers in Dermatology, Cardiology, Ophthalmology, and Dentistry II, Proceedings Of*.
- FREDÉN, H. & GRÖNVIK, M. 1980. Prenatal urinary infection and materialisation of permanent teeth. *Tandläkartidningen*, 72, 1382-1383.
- FRIED, D., XIE, J., SHAFI, S., FEATHERSTONE, J. D. B., BREUNIG, T. M. & LE, C. 2002. Imaging caries lesions and lesion progression with polarization sensitive optical coherence tomography. *Journal of Biomedical Optics*, 7, 618-627.

- GAISER, S., DEYHLE, H., BUNK, O., WHITE, S. N. & MUELLER, B. 2012. Understanding Nano-Anatomy of Healthy and Carious Human Teeth: a Prerequisite for Nanodentistry. *Biointerphases*, 7.
- GUVEN, G., CEHRELI, Z. C., ALTUN, C., SENCIMEN, M. S., IDE, S., BAYARI, S. H. & KARACAY, S. 2008. Mucopolysaccharidosis type I (Hurler syndrome): oral and radiographic findings and ultrastructural/chemical features of enamel and dentin. *Oral Surgery Oral Medicine Oral Pathology Oral Radiology and Endodontology*, 105, 72-78.
- HABELITZ, S., MARSHALL, S. J., MARSHALL, G. W. & BALOOCH, M. 2001. The functional width of the dentino-enamel junction determined by AFM-Based nanoscratching. *Journal of Structural Biology*, 135, 294-301.
- HAMMERSLEY, A. 1997. FIT2D: an introduction and overview. *ESRF Internal Report*, ESRF97HA02T.
- HARIRI, I., SADR, A., NAKASHIMA, S., SHIMADA, Y., TAGAMI, J. & SUMI, Y. 2013. Estimation of the enamel and dentin mineral content from the refractive index. *Caries Research*, 47, 18-26.
- HARIRI, I., SADR, A., SHIMADA, Y., TAGAMI, J. & SUMI, Y. 2012. Effects of structural orientation of enamel and dentine on light attenuation and local refractive index: An optical coherence tomography study. *Journal of Dentistry*, 40, 387-396.
- HARTL, I., LI, X. D., CHUDOBA, C., GHANTA, R. K., KO, T. H., FUJIMOTO, J. G., RANKA, J. K. & WINDELER, R. S. 2001. Ultrahigh-resolution optical coherence tomography using continuum generation in an air-silica microstructure optical fiber. *Optics Letters*, 26, 608-610.
- HARUNA, M., OHMI, M., MITSUYAMA, T., TAJIRI, H., MARUYAMA, H. & HASHIMOTO, M. 1998. Simultaneous measurement of the phase and group indices and the thickness of transparent plates by low-coherence interferometry. *Optics Letters*, 23, 966-968.
- HEE, M. R., HUANG, D., SWANSON, E. A. & FUJIMOTO, J. G. 1992. POLARIZATION-SENSITIVE LOW-COHERENCE REFLECTOMETER FOR BIREFRINGENCE CHARACTERIZATION AND RANGING. *Journal of the Optical Society of America B-Optical Physics*, 9, 903-908.
- HSIEH, Y.-S., HO, Y.-C., LEE, S.-Y., LU, C.-W., JIANG, C.-P., CHUANG, C.-C., WANG, C.-Y. & SUN, C.-W. 2011. Subgingival calculus imaging based on swept-source optical coherence tomography. *Journal of biomedical optics*, 16, 071409.
- HUANG, D., SWANSON, E. A., LIN, C. P., SCHUMAN, J. S., STINSON, W. G., CHANG, W., HEE, M. R., FLOTTE, T., GREGORY, K., PULIAFITO, C. A. &

- FUJIMOTO, J. G. 1991. OPTICAL COHERENCE TOMOGRAPHY. *Science*, 254, 1178-1181.
- HUANG, T. T. Y., HE, L.-H., DARENDELILER, M. A. & SWAIN, M. V. 2010. Correlation of mineral density and elastic modulus of natural enamel white spot lesions using X-ray microtomography and nanoindentation. *Acta Biomaterialia*, 6, 4553-4559.
- HUANG, T. T. Y., JONES, A. S., HE, L. H., DARENDELILER, M. A. & SWAIN, M. V. 2007. Characterisation of enamel white spot lesions using X-ray microtomography. *Journal of Dentistry*, 35, 737-743.
- INTERNATIONAL COMMISSION ON RADIOLOGICAL PROTECTION 2008. Radiological Protection in Medicine Annals of the ICRP 2008. Publication 105.
- JALEVIK, B. 2010. Prevalence and Diagnosis of Molar-Incisor- Hypomineralisation (MIH): A systematic review. *European archives of paediatric dentistry : official journal of the European Academy of Paediatric Dentistry*, 11, 59-64.
- JALEVIK, B., KLINGBERG, G., BARREGARD, L. & NOREN, J. G. 2001a. The prevalence of demarcated opacities in permanent first molars in a group of Swedish children. *Acta Odontologica Scandinavica*, 59, 255-260.
- JÄLEVIK, B., KLINGBERG, G., NORÉN, J. G. & BARREGÅRD, L. 2000. Epidemiological study of idiopathic enamel hypomineraliation in permanent first molars. *European Academy of Paediatric Dentistry Congress Abstract number 99. Eur J Paediatr Dent*, 1:128.
- JALEVIK, B. & KLINGBERG, G. A. 2002. Dental treatment, dental fear and behaviour management problems in children with severe enamel hypomineralization of their permanent first molars. *International journal of paediatric dentistry / the British Paedodontic Society [and] the International Association of Dentistry for Children*, 12, 24-32.
- JALEVIK, B., NOREN, J. G., KLINGBERG, G. & BARREGARD, L. 2001b. Etiologic factors influencing the prevalence of demarcated opacities in permanent first molars in a group of Swedish children. *European Journal of Oral Sciences*, 109, 230-234.
- JAN, J., SOVCIKOVA, E., KOCAN, A., WSOLOVA, L. & TRNOVEC, T. 2007. Developmental dental defects in children exposed to PCBs in eastern Slovakia. *Chemosphere*, 67, S350-S354.
- JAN, J. & VRBIC, V. 2000. Polychlorinated biphenyls cause developmental enamel defects in children. *Caries Research*, 34, 469-473.

- JIANG, Y., SPEARS, I. R. & MACHO, G. A. 2003. An investigation into fractured surfaces of enamel of modern human teeth: a combined SEM and computer visualisation study. *Archives of Oral Biology*, 48, 449-457.
- JONES, R., DARLING, C., FEATHERSTONE, J. D. B. & FRIED, D. 2006a. Remineralization of in vitro dental caries assessed with polarization-sensitive optical coherence tomography. *Journal of biomedical optics*, 11, 014016.
- JONES, R. S., DARLING, C. L., FEATHERSTONE, J. D. B. & FRIED, D. 2006b. Imaging artificial caries on the occlusal surfaces with polarization-sensitive optical coherence tomography. *Caries Research*, 40, 81-89.
- JONES, R. S. & FRIED, D. 2006. Remineralization of enamel caries can decrease optical reflectivity. *Journal of Dental Research*, 85, 804-808.
- KIDD, E. A. M. & FEJERSKOV, O. 2004. What constitutes dental caries? Histopathology of carious enamel and dentin related to the action of cariogenic biofilms. *Journal of dental research*, 83 Spec No C, C35-8.
- KIENLE, A., MICHELS, R. & HIBST, R. 2006. Magnification - a new look at a long-known optical property of dentin. *Journal of Dental Research*, 85, 955-959.
- KINNEY, J. H. & NICHOLS, M. C. 1992. X-RAY TOMOGRAPHIC MICROSCOPY (XTM) USING SYNCHROTRON RADIATION. *Annual Review of Materials Science*, 22, 121-152.
- KNUTTEL, A., BONEV, S. & KNAAK, W. 2004. New method for evaluation of in vivo scattering and refractive index properties obtained with optical coherence tomography. *Journal of Biomedical Optics*, 9, 265-273.
- KOCH, G., HALLONSTEN, A. L., LUDVIGSSON, N., HANSSON, B. O., HOLST, A. & ULLBRO, C. 1987. EPIDEMIOLOGIC-STUDY OF IDIOPATHIC ENAMEL HYPOMINERALIZATION IN PERMANENT TEETH OF SWEDISH CHILDREN. *Community Dentistry and Oral Epidemiology*, 15, 279-285.
- KOCH, P., HUTTMANN, G., SCHLEIERMACHER, H., EICHHOLZ, J. & KOCH, E. 2004. Linear optical coherence tomography system with a downconverted fringe pattern. *Optics Letters*, 29, 1644-1646.
- KUKLEVA, M. P., PETROVA, S. G., KONDEVA, V. K. & NIHTYANOVA, T. I. 2008. Molar incisor hypomineralisation in 7-to-14-year old children in Plovdiv, Bulgaria--an epidemiologic study. *Folia medica*, 50, 71-5.
- LACRUZ, R. S., HACIA, J. G., BROMAGE, T. G., BOYDE, A., LEI, Y., XU, Y., MILLER, J. D., PAINE, M. L. & SNEAD, M. L. 2012. The Circadian Clock Modulates Enamel Development. *Journal of Biological Rhythms*, 27, 237-245.

- LEITGEB, R., HITZENBERGER, C. K. & FERCHER, A. F. 2003. Performance of fourier domain vs. time domain optical coherence tomography. *Optics Express*, 11, 889-894.
- LEPPÄNIEMI, A., LUKINMAA, L. & ALALUUSUA, S. 2000. Nonfluoride hypomineralisation in permanent first molars. *European Academy of Paediatric Dentistry Congress Abstract number 100. Eur J Paediatr Dent*, 1:128.
- LEPPANIEMI, A., LUKINMAA, P. L. & ALALUUSUA, S. 2001. Nonfluoride hypomineralizations in the permanent first molars and their impact on the treatment need. *Caries Research*, 35, 36-40.
- LOW, I. M. 2004. Depth-profiling of crystal structure, texture, and microhardness in a functionally graded tooth enamel. *Journal of the American Ceramic Society*, 87, 2125-2131.
- LYGIDAKIS, N. A., DIMOU, G. & MARINOU, D. 2008. Molar-incisor-hypomineralisation (MIH). A retrospective clinical study in Greek children. II. Possible medical aetiological factors. *European archives of paediatric dentistry : official journal of the European Academy of Paediatric Dentistry*, 9, 207-17.
- LYGIDAKIS, N. A., WONG, F., JALEVIK, B., VIERROU, A. M., ALALUUSUA, S. & ESPELID, I. 2010. Best Clinical Practice Guidance for clinicians dealing with children presenting with Molar-Incisor-Hypomineralisation (MIH): An EAPD Policy Document. *European archives of paediatric dentistry : official journal of the European Academy of Paediatric Dentistry*, 11, 75-81.
- LYNCH, C. D., O'SULLIVAN, V. R., DOCKERY, P., MCGILLYCUDDY, C. T., REES, J. S. & SLOAN, A. J. 2011. Hunter-Schreger Band patterns and their implications for clinical dentistry. *Journal of Oral Rehabilitation*, 38, 359-365.
- MAIA, A. M. A., FONSECA, D. D. D., KYOTOKU, B. B. C. & GOMES, A. S. L. 2010. Characterization of enamel in primary teeth by optical coherence tomography for assessment of dental caries. *International Journal of Paediatric Dentistry*, 20, 158-164.
- MANESH, S. K., DARLING, C. L. & FRIED, D. 2009a. Nondestructive Assessment of Dentin Demineralization Using Polarization-Sensitive Optical Coherence Tomography After Exposure to Fluoride and Laser Irradiation. *Journal of Biomedical Materials Research Part B-Applied Biomaterials*, 90B, 802-812.
- MANESH, S. K., DARLING, C. L. & FRIED, D. 2009b. Polarization-sensitive optical coherence tomography for the nondestructive assessment of the remineralization of dentin. *Journal of Biomedical Optics*, 14.

- MARGOLIS, H. C., BENIASH, E. & FOWLER, C. E. 2006. Role of macromolecular assembly of enamel matrix proteins in enamel formation. *Journal of Dental Research*, 85, 775-793.
- MARSHALL, G. W., BALOOCH, M., GALLAGHER, R. R., GANSKY, S. A. & MARSHALL, S. J. 2001. Mechanical properties of the dentinoenamel junction: AFM studies of nanohardness, elastic modulus, and fracture. *Journal of Biomedical Materials Research*, 54, 87-95.
- MECKEL, A. H., GRIEBSTEIN, W. J. & NEAL, R. J. 1965. Structure of mature human dental enamel as observed by electron microscopy. *Arch Oral Biol*, 10, 775-783.
- MENG, Z., YAO, X. S., YAO, H., LIANG, Y., LIU, T., LI, Y., WANG, G. & LAN, S. 2009. Measurement of the refractive index of human teeth by optical coherence tomography. *Journal of biomedical optics*, 14, 034010.
- METTLER, F. A., JR., BHARGAVAN, M., FAULKNER, K., GILLEY, D. B., GRAY, J. E., IBBOTT, G. S., LIPOTI, J. A., MAHESH, M., MCCROHAN, J. L., STABIN, M. G., THOMADSEN, B. R. & YOSHIZUMI, T. T. 2009. Radiologic and Nuclear Medicine Studies in the United States and Worldwide: Frequency, Radiation Dose, and Comparison with Other Radiation Sources-1950-2007. *Radiology*, 253, 520-531.
- NAMIKI, Y., TAKAHASHI, M. & SUGA, S. 1990. Disturbed formation of dental hard tissues due to calcium deficiency. *Odontology*, 78, 813-839.
- OGDEN, A. R., PINHASI, R. & WHITE, W. J. 2007. Gross enamel hypoplasia in molars from subadults in a 16th-18th century London graveyard. *American Journal of Physical Anthropology*, 133, 957-966.
- OHMI, M., OHNISHI, Y., YODEN, K. & HARUNA, M. 2000. In vitro simultaneous measurement of refractive index and thickness of biological tissue by the low coherence interferometry. *Ieee Transactions on Biomedical Engineering*, 47, 1266-1270.
- OTIS, L. L., EVERETT, M. J., SATHYAM, U. S. & COLSTON, B. W. 2000. Optical coherence tomography: A new imaging technology for dentistry. *Journal of the American Dental Association*, 131, 511-+.
- POVAZAY, B., BIZHEVA, K., UNTERHUBER, A., HERMANN, B., SATTMANN, H., FERCHER, A. F., DREXLER, W., APOLONSKI, A., WADSWORTH, W. J., KNIGHT, J. C., RUSSELL, P. S. J., VETTERLEIN, M. & SCHERZER, E. 2002. Submicrometer axial resolution optical coherence tomography. *Optics Letters*, 27, 1800-1802.

- PRYMAK, O., TIEMANN, H., SOTJE, I., MARXEN, J. C., KLOCKE, A., KAHL-NIEKE, B., BECKMANN, F., DONATH, T. & EPPLE, M. 2005. Application of synchrotron-radiation-based computer microtomography (SR μ CT) to selected biominerals: embryonic snails, statoliths of medusae, and human teeth (vol 10, pg 688, 2005). *Journal of Biological Inorganic Chemistry*, 10, 828-828.
- REID, D. J. & DEAN, M. C. 2006. Variation in modern human enamel formation times. *Journal of Human Evolution*, 50, 329-346.
- REYES-GASGA, J., MARTINEZ-PINEIRO, E. L., RODRIGUEZ-ALVAREZ, G., TIZNADO-OROZCO, G. E., GARCIA-GARCIA, R. & BRES, E. F. 2013. XRD and FTIR crystallinity indices in sound human tooth enamel and synthetic hydroxyapatite. *Materials Science & Engineering C-Materials for Biological Applications*, 33, 4568-4574.
- RIBEIRO, D. A. 2012. Cytogenetic biomonitoring in oral mucosa cells following dental X-ray. *Dento-maxillo-facial radiology*, 41, 181-4.
- RODD, H. D., BOISSONADE, F. M., DAY, P. F. & DENT, M. P. 2007. Pulpal status of hypomineralized permanent molars. *Pediatric Dentistry*, 29, 514-520.
- SALVO, L., CLOETENS, P., MAIRE, E., ZABLER, S., BLANDIN, J. J., BUFFIERE, J. Y., LUDWIG, W., BOLLER, E., BELLET, D. & JOSSEROND, C. 2003. X-ray micro-tomography an attractive characterisation technique in materials science. *Nuclear Instruments & Methods in Physics Research Section B-Beam Interactions with Materials and Atoms*, 200, 273-286.
- SEOW, W. K. 1996. A study of the development of the permanent dentition in very low birthweight children. *Pediatric Dentistry*, 18, 379-384.
- SEREDIN, P., KASHKAROV, V., LUKIN, A., IPPOLITOV, Y., JULIAN, R. & DOYLE, S. 2013. Local study of fissure caries by Fourier transform infrared microscopy and X-ray diffraction using synchrotron radiation. *Journal of Synchrotron Radiation*, 20, 705-710.
- SERGEEV, A. M., GELIKONOV, V. M., GELIKONOV, G. V., FELDCHEIN, F. I., KURANOV, R. V., GLADKOVA, N. D., SHAKHOVA, N. M., SNOPOVA, L. B., SHAKHOV, A. V., KUZNETZOVA, I. A., DENISENKO, A. N., POCHINKO, V. V., CHUMAKOV, Y. P. & STRELTZOVA, O. S. 1997. In vivo endoscopic OCT imaging of precancer and cancer states of human mucosa. *Optics Express*, 1, 432-440.
- SIDDIQUI, S., ANDERSON, P. & AL-JAWAD, M. 2014. Recovery of Crystallographic Texture in Remineralized Dental Enamel. *Plos One*, 9.
- SIMMER, J. P. & HU, J. C. 2001. Dental enamel formation and its impact on clinical dentistry. *Journal of dental education*, 65, 896-905.

- SIMMONS, L. M., AL-JAWAD, M., KILCOYNE, S. H. & WOOD, D. J. 2011. Distribution of enamel crystallite orientation through an entire tooth crown studied using synchrotron X-ray diffraction. *Eur J Oral Sci*, 119 Suppl 1, 19-24.
- SONG, G. J., WANG, X. Z., REN, H. W., ZHANG, W. Z., ZHANG, L. Y. & FANG, Z. J. 2000. Simultaneous measurements of the thickness and refractive index of microstructures in obscure specimen by optical coherence tomography. *Optik*, 111, 541-543.
- SOVIERO, V., HAUBEK, D., TRINDADE, C., DA MATTA, T. & POULSEN, S. 2009. Prevalence and distribution of demarcated opacities and their sequelae in permanent 1st molars and incisors in 7 to 13-year-old Brazilian children. *Acta Odontologica Scandinavica*, 67, 170-175.
- SWANSON, E. A., IZATT, J. A., HEE, M. R., HUANG, D., LIN, C. P., SCHUMAN, J. S., PULIAFITO, C. A. & FUJIMOTO, J. G. 1993. IN-VIVO RETINAL IMAGING BY OPTICAL COHERENCE TOMOGRAPHY. *Optics Letters*, 18, 1864-1866.
- TAPIAS-LEDESMA, M. A., JIMENEZ, R., LAMAS, F., GONZALEZ, A., CARRASCO, P. & GIL DE MIGUEL, A. 2003. Factors associated with first molar dental enamel defects: a multivariate epidemiological approach. *Journal of dentistry for children (Chicago, Ill.)*, 70, 215-20.
- TEARNEY, G. J., BREZINSKI, M. E., SOUTHERN, J. F., BOUMA, B. E., HEE, M. R. & FUJIMOTO, J. G. 1995. DETERMINATION OF THE REFRACTIVE-INDEX OF HIGHLY SCATTERING HUMAN TISSUE BY OPTICAL COHERENCE TOMOGRAPHY. *Optics Letters*, 20, 2258-2260.
- TIZNADO-OROZCO, G. E., GARCIA-GARCIA, R. & REYES-GASGA, J. 2009. Structural and thermal behaviour of carious and sound powders of human tooth enamel and dentine. *Journal of Physics D-Applied Physics*, 42.
- TUBIANA, M. 2000. Radiation risks in perspective: radiation-induced cancer among cancer risks. *Radiation and Environmental Biophysics*, 39, 3-16.
- TUNG, K., FUJITA, H., YAMASHITA, Y. & TAKAGI, Y. 2006. Effect of turpentine-induced fever during the enamel formation of rat incisor. *Archives of Oral Biology*, 51, 464-470.
- TYE, C. E., PHAM, C. T., SIMMER, J. P. & BARTLETT, J. D. 2009. DPPI May Activate KLK4 during Enamel Formation. *Journal of Dental Research*, 88, 323-327.
- US NATIONAL COUNCIL ON RADIATION PROTECTION AND MEASUREMENTS REPORT 2009. Ionizing radiation exposure of the population of the United States. Report No. 160.

- US NATIONAL RESEARCH COUNCIL 2006. Health risks from exposure to low levels of ionizing radiation BEIR VII – Phase 2. *Washington DC: National Academies Press.*
- VAN DE CASTEELE, E., VAN DYCK, D., SIJBERS, J. & RAMAN, E. 2002. An energy-based beam hardening model in tomography. *Physics in Medicine and Biology*, 47, 4181-4190.
- VANDENBERGHE, B., JACOBS, R. & BOSMANS, H. 2010. Modern dental imaging: a review of the current technology and clinical applications in dental practice. *European radiology*, 20, 2637-55.
- WEERHEIJM, K. L. 2003. Molar incisor hypomineralisation (MIH). *European journal of paediatric dentistry : official journal of European Academy of Paediatric Dentistry*, 4, 114-20.
- WEERHEIJM, K. L. 2004. Molar incisor hypomineralization (MIH): clinical presentation, aetiology and management. *Dental update*, 31, 9-12.
- WEERHEIJM, K. L., DUGGAL, M., MEJARE, I., PAPAGIANNOLIS, L., KOCH, G., MARTENS, L. C. & HALLONSTEN, A. L. 2003. Judgement criteria for molar incisor hypomineralisation (MIH) in epidemiologic studies: a summary of the European meeting on MIH held in Athens, 2003. *European journal of paediatric dentistry : official journal of European Academy of Paediatric Dentistry*, 4, 110-3.
- WEERHEIJM, K. L., GROEN, H. J. & BEENTJES, V. E. V. M. 2000. Prevalence in 11-year-old Dutch children of cheese molars. *European Academy of Paediatric Dentistry Congress Abstract number 101. Eur J Paediatr Dent*, 1:129.
- WEERHEIJM, K. L., JALEVIK, B. & ALALUUSUA, S. 2001. Molar-incisor hypomineralisation. *Caries Research*, 35, 390-391.
- WELZEL, J. 2001. Optical coherence tomography in dermatology: a review. *Skin Research and Technology*, 7, 1-9.
- WENZEL, A. 2004. Bitewing and digital bitewing radiography for detection of caries lesions. *Journal of dental research*, 83 Spec No C, C72-5.
- WHATLING, R. & FEARNE, J. M. 2008. Molar incisor hypomineralization: a study of aetiological factors in a group of UK children. *International Journal of Paediatric Dentistry*, 18, 155-162.
- WHITE, S. & MALLYA, S. M. 2012. Update on the biological effects of ionizing radiation, relative dose factors and radiation hygiene. *Australian Dental Journal*, 57 Suppl 1, 2-8.
- WILLMOTT, N. S., BRYAN, R. A. E. & DUGGAL, M. S. 2008. Molar-incisor-hypomineralisation: a literature review. *European archives of paediatric*

dentistry : official journal of the European Academy of Paediatric Dentistry, 9, 172-9.

- WILSON, R. M., ELLIOTT, J. C. & DOWKER, S. E. P. 1999. Rietveld refinement of the crystallographic structure of human dental enamel apatites. *American Mineralogist*, 84, 1406-1414.
- WILSON, R. M., ELLIOTT, J. C., DOWKER, S. E. P. & SMITH, R. I. 2004. Rietveld structure refinement of precipitated carbonate apatite using neutron diffraction data. *Biomaterials*, 25, 2205-2213.
- WONG, F. S. L., ANDERSON, P., FAN, H. & DAVIS, G. R. 2004. X-ray microtomographic study of mineral concentration distribution in deciduous enamel. *Archives of Oral Biology*, 49, 937-944.
- YOUNG, R. A. & MACKIE, P. E. 1980. Crystallography of Human Tooth Enamel - Initial Structure Refinement. *Materials Research Bulletin*, 15, 17-29.

Parent Information Leaflet



Research team:
Dr Susan Parekh,
Dr Agnes Bloch Zupan,
Dr Peter Brett,
Dr Laurent Bozec
Mashaal Abdullatif
Nurjehan Ibrahim
Nabilah Harith
Amanda O'Donnell

Contact details:
Dr Susan Parekh
Tel: 020 3456 1067
Fax: 020 3456 2329

Unit of Paediatric Dentistry
The Eastman Dental Hospital and Institute
256 Gray's Inn Road
London WC1X 8LD
s.parekh@eastman.ucl.ac.uk
Website: www.uclh.nhs.uk

If you need a large print, audio or translated copy of this document, please contact us on 020 3456 1067. We will try our best to meet your needs.

If you wish to discuss this study with a member of the research team or an independent expert who is not part of the research team, please ask Dr Susan Parekh

Thank you for taking the time to read this leaflet.

© University College London Hospitals NHS Foundation Trust

University College London Hospitals 
NHS Foundation Trust

A study of the genetics and the physical properties of dental anomalies

Publication date: 07/07/11
Date last reviewed:
Version number **2**

A Study of the genetics and the physical properties of dental anomalies

UCL Hospitals cannot accept responsibility for information provided by external organisations.

Invitation

Your child is being invited to take part in a research study. Before you make a decision, it is important that you know why the research is being done and what it would involve from your child. Please take time to read the following information carefully and discuss it with others if you wish. Ask us if anything is not clear at any time before or after participating. If you need more information we are willing to spend more time to satisfy you before taking any decision.

What is the purpose of the study?

To gather more information about dental anomalies, such as enamel defects (Amelogenesis Imperfecta), and dentine defects (Dentinogenesis Imperfecta). We want to use this information to improve our knowledge of genetics and how they affect the properties of the teeth.

Why has my child been chosen?

We are asking all patients who have been diagnosed with dental anomalies and members of their families with the same or other dental conditions to participate in the study

Does my child have to take part?

No. It is up to you to decide. If you do decide to participate we will ask you to sign a consent form. If you, or your child, change your mind, you are free to withdraw at any time, without giving a reason. The standard of care your child receives will not be affected in any way.

What will happen to me if my child takes part?

We will ask you and your child some questions about your child's teeth, take photographs, and a saliva sample. The saliva sample will be used to link your child's DNA with the physical properties of their teeth. We will also measure the colour of the front teeth using a machine called the spectroshade™ micro, which rests gently on the teeth and uses a light to record the shade of the tooth (see information sheet provided). If any teeth need to be extracted as part of your child's treatment, these will be collected for laboratory testing of the teeth. Your child will not need to do anything else. If any member of your family has similar teeth, we will invite them to take part as well, as this will help to detect the common dental genes in families. If you do not want other members of your family to participate, you can refuse and your child's treatment will not be affected in any way.

What are the possible disadvantages or risks of taking part?

There are no risks anticipated. None of your answers will affect your treatment in any way.

What are the possible benefits?

We cannot promise the study will help you, but the information we get might help treat young people with dental anomalies in the future.

What will happen with the results?

Any samples that we collect will be stored using a

study ID number, so that they cannot be directly linked to your child. We hope to publish the results of the study on completion.

Will taking part in the study remain confidential?

Yes. We will keep your information in confidence. This means we will only tell those who have a need or right to know. The safety and security of the data will be the responsibility of the principal investigator (Dr Susan Parekh). The information will also be stored in a database developed by Strasbourg University (phenodent database), who we work closely with. All information will be anonymised before putting on the phenodent database.

What happens if something goes wrong?

In the event that something does go wrong and you are harmed during the research and this is due to someone's negligence then you may have grounds for a legal action for compensation against UCLH NHS Trust, but you may have to pay your legal costs. The normal National Health Service complaints mechanisms will still be available to you (if appropriate).

Who has reviewed the study?

All research in the NHS is looked at by independent group, called a Research Ethics Committee to protect your safety, rights, wellbeing and dignity. This study has been reviewed and given favourable opinion by the Joint Research Ethics Committee. Thank you for reading this, please ask any questions if you need to.



Research team:
Dr Susan Parekh,
Dr Agnes Bloch Zupan,
Dr Peter Brett,
Dr Laurent Bozec
Mashaal Abdullatif
Nurjehan Ibrahim
Nabilah Harith
Amanda O'Donnell

Contact details:
Dr Susan Parekh
Tel: 020 3456 1067
Fax: 020 3456 2329
Unit of Paediatric Dentistry
The Eastman Dental Hospital and Institute
256 Gray's Inn Road
London WC1X 8LD
s.parekh@eastman.ucl.ac.uk
Website: www.uclh.nhs.uk

If you need a large print, audio or translated copy of this document, please contact us on 0207 915 1022. We will try our best to meet your needs.

If you wish to discuss this study with a member of the research team or an independent expert who is not part of the research team, please ask Dr Susan Parekh

Thank you for taking the time to read this leaflet.

© University College London Hospitals NHS Foundation Trust
University College London Hospitals 
NHS Foundation Trust
A study of the genetics and the physical properties of dental anomalies

Publication date: 08/08/11
Date last reviewed
Version number **3**

UCL Hospitals cannot accept responsibility for information provided by external organisations.

Patient's Information Leaflet



A Study of the genetics and the physical properties of dental anomalies

<p>Invitation</p> <p>You are being invited to take part in a research study. Before you make a decision, it is important that you know why the research is being done and what it would involve from you. Please take time to read the following information carefully and discuss it with others if you wish. Ask us if anything is not clear at any time before or after participating. If you need more information we are willing to spend more time to satisfy you before taking any decision.</p>	<p>What will happen to me if I take part?</p> <p>We will ask you some questions about your teeth and your medical history, and examine your teeth, take photographs, and a saliva sample. The saliva sample will be used to link your DNA with the physical properties of your teeth. If you require any teeth to be extracted as part of your treatment, these will be collected for laboratory testing of the teeth. You will not need to do anything else. If any member of your family has similar teeth, we will invite them to take part as well, as this will help to detect the common dental genes in families. If you do not want other members of your family to participate, you can refuse and your treatment will not be affected in any way.</p>	<p>way.</p> <p>Will my taking part in the study remain confidential?</p> <p>Yes. All information that is collected about you during the research will remain strictly confidential and will be seen only by the investigators named on this sheet. The safety and security of the data will be the responsibility of the principal investigator (Miss Susan Parekh). This information will be recorded in such a way that it is completely anonymous and you cannot be individually identified in anyway.</p>
<p>What is the purpose of the study?</p> <p>To obtain and gather more information about dental anomalies, such as Enamel defects (Amelogenesis Imperfecta AI), and dentine defects (Dentinogenesis Imperfecta DI). We want to use this information to improve our knowledge of genetics and the properties of the teeth, to provide better support and long term care.</p>	<p>What are the possible disadvantages or risks of taking part?</p> <p>There are no risks anticipated. None of your answers will affect your treatment in any way.</p>	<p>The information will also be stored in a database developed by Strasbourg University (phenodent database), who we work closely with. All information will be anonymised before putting on the phenodent database.</p>
<p>Why has I have been chosen?</p> <p>We are asking all patients who have been diagnosed with dental anomalies and members of their families with the same or other dental conditions to participate in the study</p>	<p>What are the possible benefits?</p> <p>The information from this study will hopefully be used to help us expand our knowledge about the genetics of dental anomalies, and relate this to the appearance of the teeth, identify affected families and provide better support and treatment.</p>	<p>Who has reviewed the study?</p> <p>All research in the NHS is looked at by independent group, called a Research Ethics Committee to protect your safety, rights, wellbeing and dignity. This study has been reviewed and given favourable opinion by the Joint Research Ethics Committee. If you would like to see a summary of the findings from the study when it is completed, please tell Miss Parekh or any of the other dentists you see.</p>
<p>Do I have to take part?</p> <p>No. It is up to you to decide. If you do decide to participate we will ask you to sign a consent form. If you change your mind, you are free to withdraw at any time, without giving a reason. The standard of care you will receive will not be affected in any way.</p>	<p>What will happen with the results?</p> <p>Any samples that we collect will be stored using a study ID number, so that they cannot be directly linked to you. We hope to publish the results of the study on completion. All confidential information will be coded and you will not be identifiable in any</p>	

University College London Hospitals 
 NHS Foundation Trust

The Eastman Dental Hospital
 256 Gray's Inn road
 London
 WC1X 8LD

Version 1
 Study Number:....
 Patient Identification Number for this trial:

Telephone: 020 3456 - 7899
 Direct Line: 020-3456 - 1067
 Fax: 020-3456-2329
 Web-site: www.uclh.nhs.uk

PARENT CONSENT FORM

Title of Project:

A Study of the genetics and the physical properties of dental anomalies.

Name of Researchers: Dr Susan Parekh, Dr Agnes Bloch-Zupan, Dr Peter Brett, Dr Laurent Bozec, Miss Amanda O'Donnell, Mashael Abdullatif, Nurjehan Mohamed Ibrahim and Nabilah Narith.

- | | |
|--|--------------------------|
| | Please initial box |
| 1. I confirm that I have read and understood the information sheet dated 21/12/10 (version 1) for the study. I have been allowed some time to think about this, ask questions, and have had these answered in a way that I understand. | <input type="checkbox"/> |
| 2. I understand that my child's is voluntary and that I am free to withdraw at any time, without giving any reason, without their medical care or legal rights being affected. | <input type="checkbox"/> |
| 3. I understand that sections of any medical notes may be looked at by the researchers and responsible individuals from regulatory authorities where it is relevant to my child taking part in research. I give permission for these individuals to have access to my child's records. | <input type="checkbox"/> |
| 4. I give permission to the investigators to pass clinical data collected from my child's examination to my General Practitioner or General Dental Practitioner | <input type="checkbox"/> |
| 5. I understand that the samples taken from my child may be stored and used for the purpose of further research at a later date. I understand that these results will also remain anonymous. | <input type="checkbox"/> |
| 6. I understand that (this project or future research) will include genetic research aimed at understanding the genetic influences on dental defects in children. | <input type="checkbox"/> |
| 7. I agree for my child to take part in the above study. | <input type="checkbox"/> |

Name of Patient	Date	Signature of parent
-----------------	------	---------------------

Name of Person taking consent	Date	Signature
-------------------------------	------	-----------

When completed, 1 for patient; 1 for researcher site file; 1 (original) to be kept in medical notes



UCL Hospitals is an NHS Foundation Trust comprising: The Eastman Dental Hospital, The Heart Hospital, Hospital for Tropical Diseases, National Hospital for Neurology and Neurosurgery, The Royal London Homoeopathic Hospital and University College Hospital (incorporating the former Middlesex and Elizabeth Garrett Anderson Hospitals).



For further information about this study please contact Dr Susan Parekh

Phone : 020 3456 1067 email: s.parekh@eastman.ucl.ac.uk

UCLH welcomes feedback from their patients who have been involved in research. In the first instance, you should inform the Principal Investigator. If you are not satisfied with the response of the research team then you should address your complaints to the UCLH complaints manager at UCLH postal address or through our website <http://www.uclh.nhs.uk/Contact+us/>. To help us identify the research study you have been involved in, please mention the title and the name of the research doctor or principal investigator. You can find this information on the Patient Information Sheet.

University College London Hospitals 
 NHS Foundation Trust

Version 1
 Study Number:.....
 Patient Identification Number for this trial:

The Eastman Dental Hospital
 256 Gray's Inn road
 London
 WC1X 8LD

Telephone: 020 3456 7899
 Direct Line: 020-3456-1067
 Fax: 020-3456-2329
 Web-site: www.uclh.nhs.uk

PATIENT CONSENT FORM

Title of Project:

A Study of the genetics and the physical properties of dental anomalies.

Name of Researchers: Dr Susan Parekh, Dr Agnes Bloch-Zupan, Dr Peter Brett, Dr Laurent Bozec, Miss Amanda O'Donnell, Mashael Abdullatif, Nurjehan Mohamed Ibrahim and Nabilah Narith.

Please initial box

1. I confirm that I have read and understood the information sheet dated 21/12/10 (version 1) for the study. I have been allowed some time to think about this, ask questions, and have had these answered in a way that I understand.
2. I understand that my participation is voluntary and that I am free to withdraw at any time, without giving any reason, without my medical care or legal rights being affected.
3. I understand that sections of any medical notes may be looked at by the researchers and responsible individuals from regulatory authorities where it is relevant to my part in the research. I give permission for these individuals to have access to my records.
4. I give permission to the investigators to pass clinical data collected from my examination to my General Practitioner or General Dental Practitioner
5. I understand that the samples taken from me may be stored and used for the purpose of further research at a later date. I understand that these results will also remain anonymous.
6. I understand that (this project or future research) will include genetic research aimed at understanding the genetic influences on dental defects in children.
7. I agree for to take part in the above study.

Name of Patient

Date

Signature of patient

Name of Person taking consent

Date

Signature

When completed, 1 for patient; 1 for researcher site file; 1 (original) to be kept in medical notes



S Parekh Version 1

UCL Hospitals is an NHS Foundation Trust comprising: The Eastman Dental Hospital, The Heart Hospital, Hospital for Tropical Diseases, National Hospital for Neurology and Neurosurgery, The Royal London Homoeopathic Hospital and University College Hospital (incorporating the former Middlesex and Elizabeth Garrett Anderson Hospitals).



For further information about this study please contact Dr Susan Parekh

Phone : 020 3456 1067 email: s.parekh@eastman.ucl.ac.uk

UCLH welcomes feedback from their patients who have been involved in research. In the first instance, you should inform the Principal Investigator. If you are not satisfied with the response of the research team then you should address your complaints to the UCLH complaints manager at UCLH postal address or through our website <http://www.uclh.nhs.uk/Contact+us/>. To help us identify the research study you have been involved in, please mention the title and the name of the research doctor or principal investigator. You can find this information on the Patient Information Sheet.

17 APPENDIX 5

Consent form for the Phenodent database

You/ your child have been asked to participate in the database project entitled "Diagnosing Dental Defects database D [4] / Phenodent.

The establishment of this registry has received the favorable opinion of CCTIRS 11.09.2008, and authorization of the CNIL on 18/05/2009 (Registration No. 908416).

I can at any time obtain additional information from Miss Susan Parekh (primary investigator) or Prof. Agnes Bloch-Zupan, Project Manager, the Reference Centre of dental manifestations of rare diseases, Department of Oral Health Care, University Hospital Strasbourg, Hôpital Civil, 1 place Hospital, F-67000 Strasbourg Cedex France or email: agnes.bloch@chru-strasbourg.fr

I authorize the registration of anonymous data and pictures in the database yes no
and my ethnic background (via the collection of country and city of birth) yes no
This information may also be used for teaching purposes

For data files, I authorize the possible dissemination of all images, yes no
or only intraoral pictures yes no

YOUR AGREEMENT TO PARTICIPATE IN THIS REGISTRY

My signature certifies that I clearly understood the information regarding my participation in this registry

Name of Patient

Date

Signature

Name of Parent

Date

Signature

Name of Person
taking consent

Date

Signature

This document is to be performed in two original copies:
A copy kept by the person giving consent (or by the holders of parental authority if minor)
The other copy to be kept by the primary investigator, Miss Susan Parekh

18 APPENDIX 6

Dental anomalies proforma

study ID:.....
 Date of clinic:..... Pt sticker:
 Clinician name:.....

Ethnicity: White Mixed Black Asian Chinese Other.....
 Referred by: GDP CDS HDS GP Other:.....
 c/o: Nil pain sens appearance Other:.....

Relevant medical history:.....

 Fluoride history: supp Y/N water Y/N toothpaste child/adult
 Dental history: restrn Y/N ext Y/N LA Y/Nsed Y/N GA Y/N
 Family history (inc family tree): Plaque score:

Extra-oral features: Skeletal pattern I II III
 Hair: normal/sparse skin:.....
 face:..... hands/nails:..... Other:.....

Intra-oral features: lips gingivapalate mucosa saliva

Teeth present (chart):

	17	16	5	4	3	2	1	1	2	3	4	5	26	27
	47	46	5	4	3	2	1	1	2	3	4	5	36	37

Eruption: early Y/N delayed Y/N infraoccluded Y/N impacted Y/N
 General/local Mild/mod/sev; teeth:..... Teeth:.....

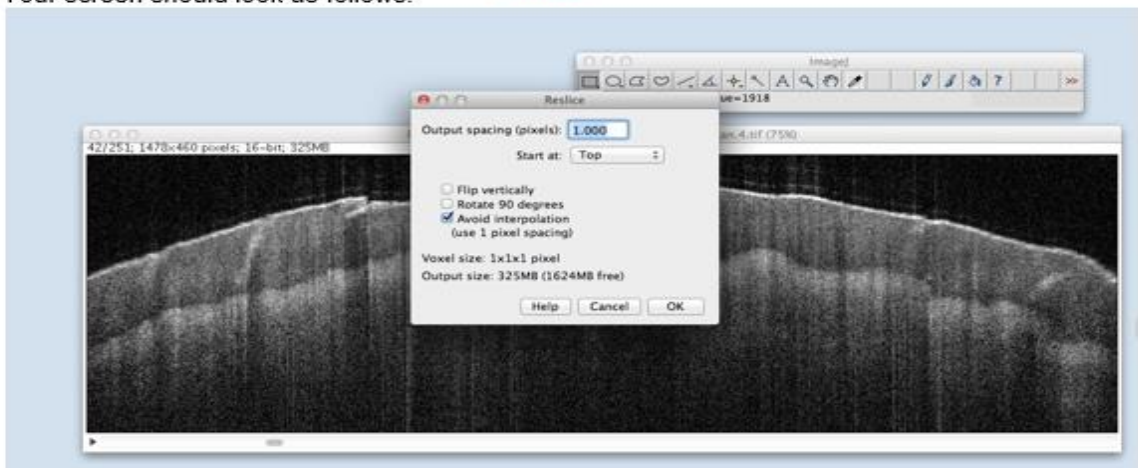
Occlusion: Class I Class II Class III Class III OJ = OB: complete / incomplete
 AOB Y/N

Dentine:
 discoloured: Y/N abscess: Y/N tooth wear: mild / mod / sev (which teeth):

19 Appendix 7 Michelson Diagnostics' Manual on manipulating OCT images in image J

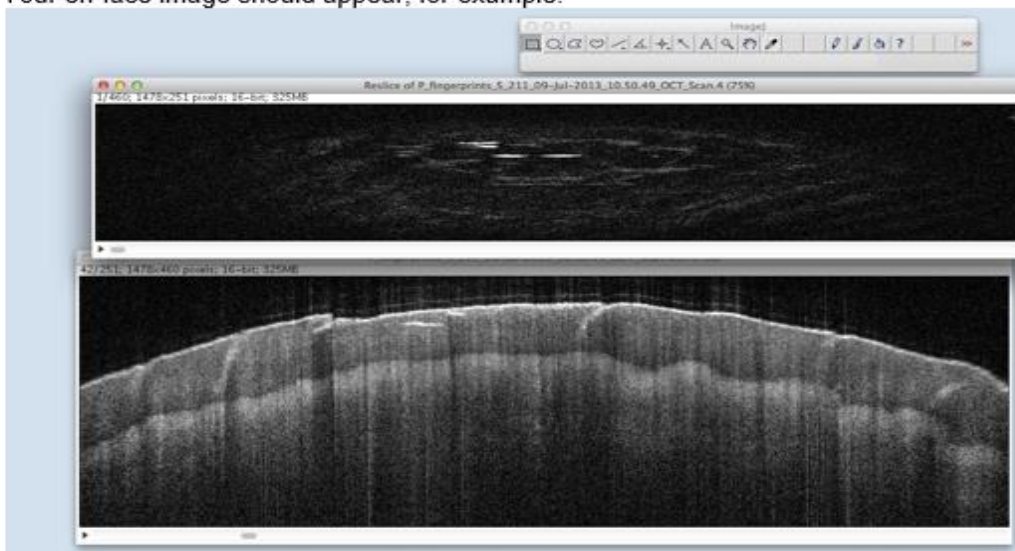
En-face Instructions:

1. Open up **imagej**
2. Drag and drop the image for en-face view or alternatively use file-open and search for the image in your directory
3. To produce the en-face go to **image-stacks-reslice**.
4. Your screen should look as follows:

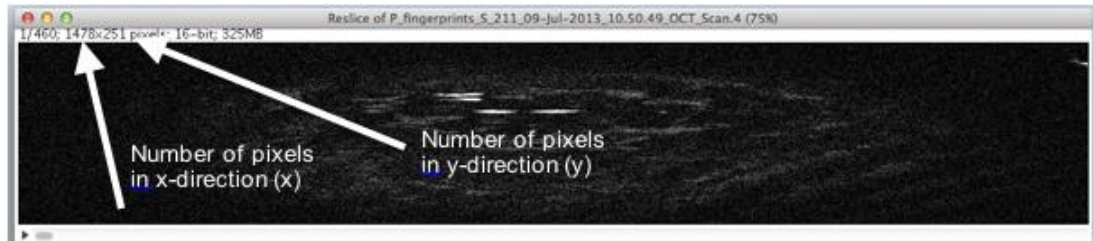


Ensure the settings are as displayed in the image above. These values in the settings should be the default. Click 'OK'

5. Your en-face image should appear, for example:



6. Once re-sliced, it is possible to scale the image. To scale the image stack, go to **Image-Scale...** Look at the pixel dimensions on the stack image, these are pointed out below:



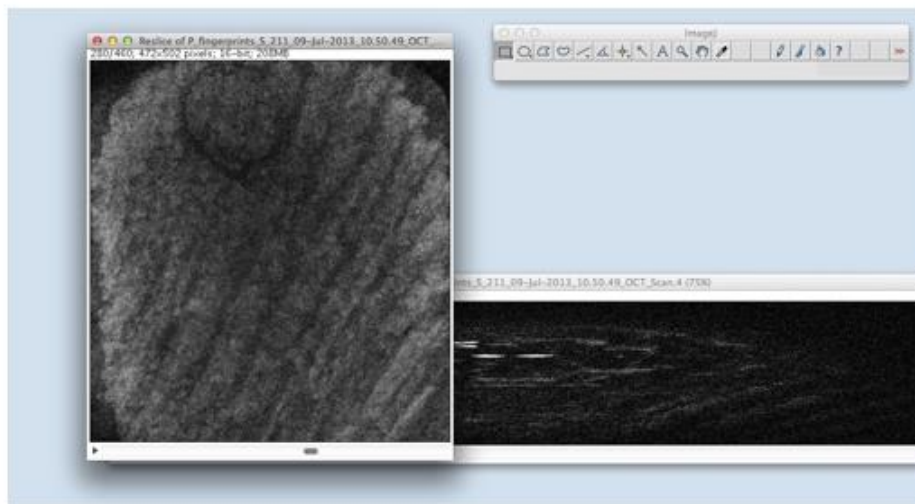
Using the formulae below:

$$X_scale = \frac{y}{x} \times \text{factor}$$

$$Y_scale = \text{factor}$$

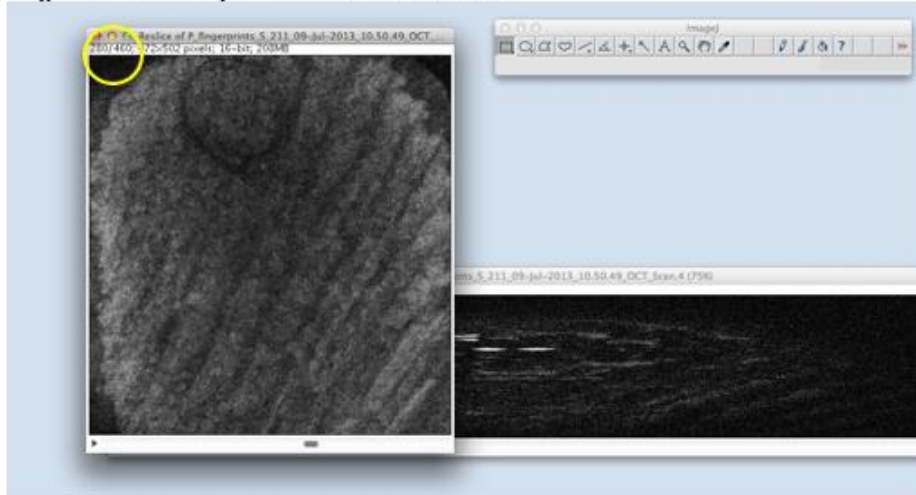
$$Z_scale = 1$$

Where x is the number of pixels in the x-direction and y is the number of pixels in the y direction. The factor is added to enlarge the image. I advise a factor around 2, but it will vary depending on the number of slices in the image.



7. The en-face scaled image can be saved using file-save as required format.

Calculating the relative depth of the en-face slices:



The values circled above can be used to calculate the relative depth. In this example, 280 is the current slice number and 460 is the total number of slices. The depth of a B scan is 2mm, therefore the relative depth in mm can be calculated as follows:

$$Depth = \frac{2}{n} \times m$$

Where n is the total number of slices and m is the current slice. In this example above m is 280 and n is 460.

Histogram instructions:

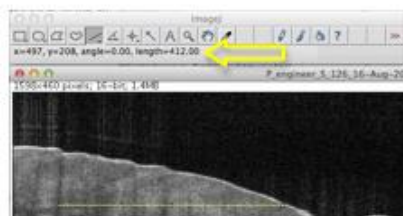
To analyze a histogram, select an area either using the box/line functions (as circled in the image below) or select the whole image by using keys "ctrl+a".



Once selected, go to "analyze" and then "Histogram".

Measuring pixels:

The distance can be measured using the "line" control (as circled in pervious image above) on Imagej. Simply select the line function, and click and drag. Values will appear at the top showing you the distances, as shown below:



Each pixel is approximately 4microns in tissue.

The area can be measured by clicking "analyze" and then "measure".

Plot profile:

Select an area or line.

Go to "analyze" "plot profile".

20 Appendix 8

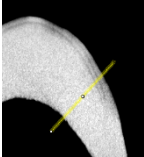
Method of MD analysis method using Image J provided by Mr Mohamed AI-Mosawi, QMUL

- **Analyse multiple images**

The micrographs were analysed using Image J 1.38 image processing software (NIH, Bethesda, MD).

- Load image file in TomView
- Click File > Export > Bitmaps > Create new folder and save into the new folder.
- Open ImageJ
- Drag the new folder and drop it into ImageJ
- An “Open folder” window will appear with two options
- Tick “Use Virtual Stack” then press “Yes”
- Select the line option
- Draw a line on the portion for analysis
- Click “Analyse” then select “Histogram”

- **Plot profile**

- Open image with ImageJ.
- Select the “Straight” icon: 
- Draw a line on the section for analysis: 
- Double click the “Straight” icon to change line width:



- Click “Analyse”.
- Go to “Plot Profile”.
- A graph will appear indicating the gray scale value.
- Press “Copy” to paste the results to Microsoft Excel (They will appear in a table).
- Press “Live” if it is preferred to see the plot while drawing the line.

- **Colour grey scale**

- Using Tomview find out the range of LAC needed (e.g. 2-3).
- Using MS Excel create a table of the LAC range with 0.05 increments (e.g. 2, 2.05, ...) (**Fig 2**).
- Multiply these ranges by the grey scale factor 75, the value must be integer, therefore the function $=INT(...*75)$ must be written in MS Excel (**Fig 2**).
- Now assign a colour to each integer by filling the cell (**Fig 2**).
- Note the Red, Green and Blue values by going to fill cell > more colours > Costume (**Fig 1**).

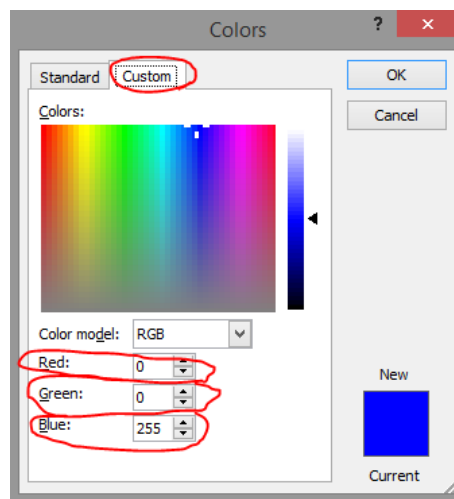


Fig 1

- You should end up with a table like this:

	A	B	C	D	E	F
1	Mineral	Gray value		Red	Green	Blue
2	3	225		255	0	255
3	2.95	221		0	50	255
4	2.9	217		0	75	255
5	2.85	213		0	100	255
6	2.8	210		0	150	255
7	2.75	206		0	200	255
8	2.7	202		0	225	255
9	2.65	198		0	255	255
10	2.6	195		0	255	200
11	2.55	191		0	255	150
12	2.5	187		0	255	0
13	2.45	183		150	255	0
14	2.4	180		200	255	0
15	2.35	176		255	255	0
16	2.3	172		255	225	0
17	2.25	168		255	200	0
18	2.2	165		255	150	0
19	2.15	161		255	100	0
20	2.1	157		255	75	0
21	2.05	153		255	50	0
22	2	150		255	0	0

Fig 2

- Open ImageJ and load XMT images as described in **Section 1 a-f**.
- Click on Image > colour > Edit LUT

- i) Assign the colours from MS Excel to LUT Editor using Gray and RGB values by clicking on each pixel (**Fig 3**).

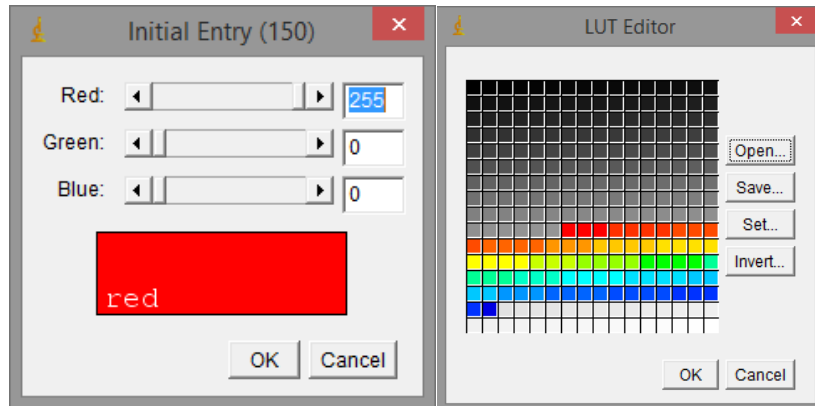


Fig 3

- j) Save it and open Tomview.
- k) In Tomoview Click the brightness icon and click colour (**Fig 4**).

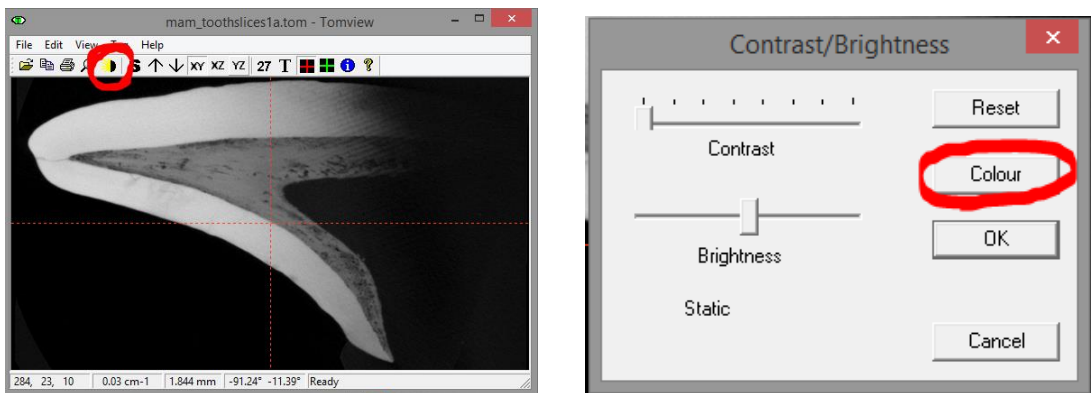


Fig 4

- l) Load the “.lut” file saved by ImageJ (**Fig 5**).

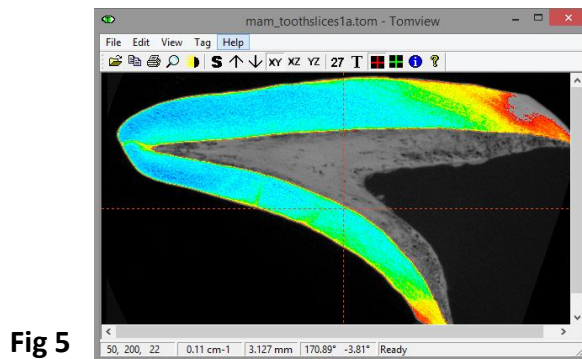


Fig 5

- m) DONE!